SOLVOTHERMAL CHEMISTRY OF EARLY TRANSITION METAL FLUORIDES

David W. Aldous

A Thesis Submitted for the Degree of PhD
at the
University of St. Andrews

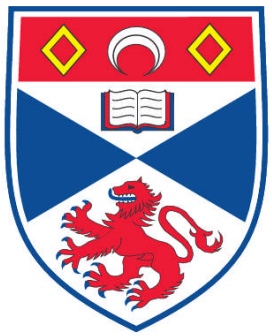

2008

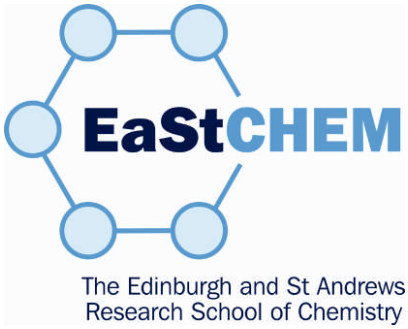

Solvothermal Chemistry of Early Transition Metal Fluorides

A thesis presented for the degree of

Doctor of Philosophy

in the Faculty of Science of the University of St. Andrews

by David W. Aldous, BSc (Hons), AMRSC

March 2008

Declaration

I, David Aldous hereby certify that this thesis, which is approximately 35,000 words in length, has been written by me, that it is the record of work carried out by me and that it has not been submitted in any previous application for a higher degree.

I was admitted as a research student in October, 2004 and as a candidate for the degree of PhD in October, 2005; the higher study for which this is a record was carried out in the University of St Andrews between 2004 and 2008.

Date……Signature of Candidate…….....

I hereby certify that the candidate has fulfilled the conditions of the Resolution and Regulations appropriate for the degree of PhD in the University of St Andrews and that the candidate is qualified to submit this thesis in application for that degree.

Date……..….Signature of Supervisor……..…….....

The following is an agreed request by candidate and supervisor regarding the electronic publication of this thesis:

Access to Printed copy and electronic publication of thesis through the University of St Andrews. Embargo on both printed copy and electronic copy for the same fixed period of 1 year on the following ground: publication would preclude future publication.

Date……Signature of Candidate…….....

Signature of Supervisor……..…….....

Abstract

In this thesis, 60 crystal structures which have been synthesised by the solvothermal method are reported, with 57 of them representing novel materials. The remaining three materials have previously been reported but have been made by a new and milder method of synthesis. Ti, Zr, Hf, V, Nb, Ta and Mo have all been used to make fluoride or oxyfluoride materials at temperatures ranging from 60 °C to 200 °C. Both inorganic and organic moieties (“templates”) have been used to direct the formation of the (oxy)fluoride materials, usually as an anionic species. These materials have then been studied for their magnetic properties, where relevant.

Initially, 10 vanadium-based compounds were made at 100 °C using a range of templates. Through variations in water content, temperature and cation ratio a further 19 compounds were synthesised. The inorganic species in these structures range from monomers, to dimers, tetramers and chains, to infinite 2D sheets.

A family of vanadium compounds has been synthesised, with piperazine as a template, which shows an increase in covalent connectivity through the increase of the reaction temperature, with a decrease in oxidation state as a result. These materials are also interrelated through the use of a “Y” shaped motif in their structural composition. Through a change in cation content a novel trigonal chain compound (related to the structure of $CsCrF_4$) has been synthesised with piperazine which possibly shows strong geometric magnetic frustration.

Vanadium oxyfluoride analogues of $(VO)_2P_2O_7$ have been made, which show interesting magnetic properties with a range of different templates, ranging from alkali metal cations to the bulky protonated template, *trans* 1,2 bis (4-pyridyl) ethene. The best fits to magnetic susceptibility data are obtained with an antiferromagnetic Heisenberg chain model.

Nine molybdenum-based structures have also been synthesised, with five of the structures being made through changes in the temperature and cation ratio of the reactions. An example of this is the formation of tetrameric units with ammonium, through the condensation of monomers as a result of an increase in the reaction temperature.

A further 22 structures have also been made with metal, M = Ti, Zr, Hf, Nb and Ta. These structures have a tendency to from isolated polyhedral units under the conditions studied in this work. Several examples of isolated $[MF_6]^{n-}$ and $[MF_7]^{n-}$ monomers are reported and also one example of a *trans*-connected $[TiOF_4]^{2-}$ infinite chain structure.

Acknowledgements

Firstly I would like to thank Phil for giving me the opportunity to work in his group, and for his guidance and expert advice.

I am grateful to several persons who without their help this thesis would not have been possible. Thank you to Prof. Alex Slawin and Dr. Yang Li for the collection of some of the single crystal data and guidance on crystallography. Prof. Paul Attfield and Dr. Richard Goff are thanked for their assistance in some of the magnetic data analysis. Dr. John Warren and Dr. Tim Prior are also thanked for their help and guidance on data collection at Daresbury.

I am also grateful to all the technical and scientific staff of the University of St Andrews for their assistance and to the EPSRC for funding this work.

On a personal note, I would like to thank all of my friends in and out of chemistry for their support, friendship and guidance. Special thanks go to Dan for the entertaining wednesday evenings, Charlotte for fixing my “i” key and to Karen, co-creator of the “Avocado Game”.

Finally, I would like to thank Vicki for all her support, companionship and keeping me supplied with lots of houmous!

Table of Contents

1.0 Introduction

The work contained within this thesis concerns the synthesis of novel transition metal (oxy)fluorides, their characterisation and a discussion of their properties. The hydrothermal chemistry of these materials will also be discussed. The following chapters describe the concept of building units, the effect of structure on material properties, some known transition metal (oxy)fluorides structures and the potential properties that these novel materials may have.

1.1 Structural Properties

1.1.1 Building Units

The concept of a building unit (BU) has been used for over 70 years but not until 2000 was the concept of building units and their effect on the topology of the bulk crystal structure fully elucidated i.e. Scale Chemistry.[1] A building unit refers to the motif from which a structure is made, regardless of symmetry, and is often confused with an asymmetric unit which could refer to crystallographic sites and therefore symmetry. BUs are often thought of as the building blocks of a structure, regardless of their size in relation to the magnitude of the final structure e.g. the difference in size of bricks used to build a three storey house.

Scale chemistry is the design of new solids from BUs. A good use of BUs, and the resulting scale chemistry, has been the design of new zeolites which are often made up of the simplest BUs; MO_4 tetrahedra, where M is either silicon of aluminium. These BUs can then be assembled into secondary building units (SBUs) such as the four ring (4R) and the double six ring (D6R) as seen in Fig 1.1.

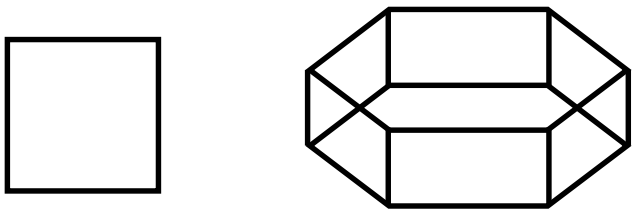

Fig. 1.1 The 4R and D6R SBUs.

1.1.2 BUs in Oxyfluorides

Fluoride and oxyfluoride BUs can be found in a variety of topologies, from the 5 co-ordinate square-based pyramid to the 8 co-ordinate square antiprism, with the most common being the 6 co-ordinate octahedron. These BUs can have an out-of-centre distortion resulting from a short oxide bond, for instance.

In MX_6 octahedra (where X = F^- or O^{2-}) out-of-centre distortions are often responsible for any interesting physical properties in the bulk material. When the octahedral co-ordination around a d^0 metal centre becomes distorted, for example in **$[NH_4][VOF_4]$**[3] (see Fig. 1.2), this causes the gap between the lowest unoccupied molecular orbitals (cationic LUMOs) and the highest occupied molecular orbitals (anionic HOMOs), to decrease.[4] If the gap between the LUMOs and HOMOs becomes sufficiently small, the two can mix and are stabilised by a second-order Jahn-Teller effect (the degenerate electronic ground state is stabilised by geometric rearrangement).[5,6] Therefore, the larger the out-of-centre distortion, the smaller the gap between these orbitals and the greater the effect this may have on the physical properties of the structure. This effect is due to the formation of dipole moments (along the direction of the axis with the shortest distance in the octahedra) which can polarise the structure when they are arranged in an unsymmetrical manner i.e. there is a net dipole moment.

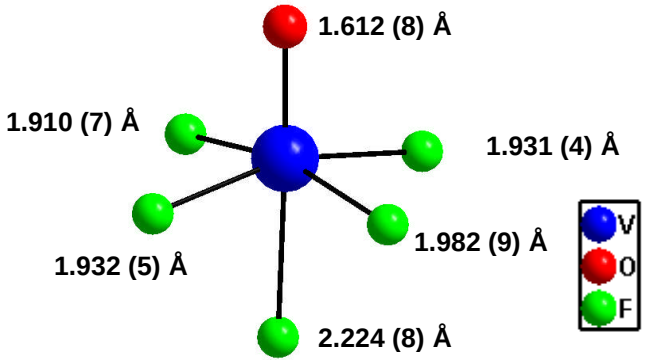

Fig. 1.2 The distorted [VOF_5] octahedra of **$[NH_4][VOF_4]$**[6].

For d^n (where n is greater than zero) the distortion is readily suppressed as the gap between LUMOs and HOMOs becomes too great. Also, the effective ionic radii and charge of the cationic metal centre has an influence on the level of distortion. For small, highly charged metals such as V^V and Mo^{VI} a greater distortion is seen than in comparison to Zr^{IV} and Hf^{IV}, which are larger and less highly charged (see Table 1.1).

Ox. State	Ti	Zr	Hf	V	Nb	Ta	Mo	W
(3+)	67.0			64	72	72	69	
(4+)	60.5	72	71	58	68	68	65	66
(5+)				54	64	64	61	62
(6+)							59	60

Table 1.1 The effective ionic radii (shown in pm) for a selection of transition metals with various oxidation states, in 6 co-ordination[7].

1.1.3 Non-Centrosymmetric Crystal Classes

Crystal structures can be either classed as centrosymmetric or non-centrosymmetric (NCS). NCS structures are of particular interest to material scientists as they posses a wide selection of properties that are dependent upon their symmetry, such as enantiomorphism, optical activity, pyroelectricity and piezoelectricity.[8] To simply classify a structure as NCS is insufficient, as there are 21 different acentric crystal classes, although these classes can be easily subdivided into two categories; polar and non-polar. A graphical representation of the sub-division of the 21 crystal classes is shown in Fig. 1.3.

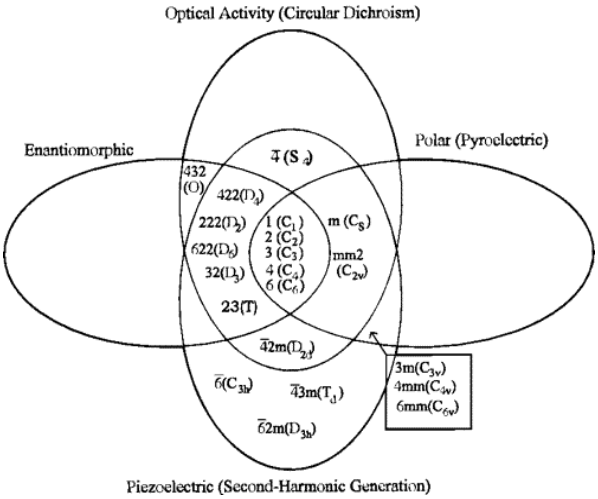

Fig 1.3 Interrelationships of non-centrosymmetric crystal classes.[8]

Many of the crystal classes possess more than one property. From the above diagram it can be seen that some of the properties shown are dependent upon others, namely an enantiomorphic sample must be optically active and a pyroelectric sample must be piezoelectric, although the converse for both is not true.

1.1.4 Existing (oxy)fluoride structures

The term monomer refers to an isolated inorganic polyhedron e.g. octahedron. In the following sub-sections, the terms monomer, dimer etc are only applied to the polyhedra MX_Y in question as either being isolated or connected to another MX_z polyhedron (where M is an early transition metal, X is either an oxygen, fluorine or nitrogen atom and Y and Z are integers above zero). An example of this is the connectivity of isolated inorganic polyhedra through organic moieties to form a chain, which would be described as a monomeric structure rather than as a chain in order to differentiate between extended inorganic compounds and those made as co-ordination compounds.

A complete review of all known structures types of fluorides and oxyfluorides for Ti, Zr, Hf, V, Nb, Ta and Mo is not intended here. Instead, select materials which are of interest for their

structural and/or physical properties have been chosen to be discussed in the following sub-sections. In the last 20 years two significant reviews have been published which, as of 2000, methodically cover most known transition metal oxyfluorides. These reviews are by Hagenmuller[9] and by Nakajima, Žemva and Tressaud[10].

1.1.4.1 Monomers

A simple example of a 5 co-ordinated metal centre occurs in **$[C_{13}H_{14}N_3]_2[VF_5]$**,[11] which consists of an isolated monomer templated through hydrogen bonding to form a 3D solid. A more interesting example of a 5 co-ordinated metal centre is that in **$[Cu(NC_5H_5)_4][VOF_4]$**.[12] The $[VOF_4]^{2-}$ square-based pyramidal anion forms a chain through the square planar $[Cu(py)_4]^{2+}$ cation as shown in Fig 1.4.

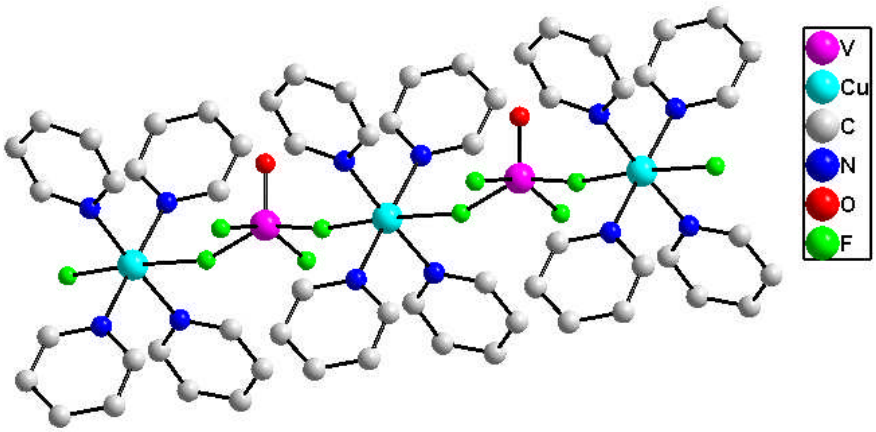

Fig 1.4 The infinite chains of **$[Cu(NC_5H_5)_4][VOF_4]$**[12].

The structure forms in the NCS space group $C222_1$ which means that it should exhibit Second Harmonic Generetion (SHG). The SHG response from the sample was measured and found to be five times less than α−quartz, which is quite low. Although this was expected, as through symmetry, the net cancellation of the V−O axis vectors in the solid occurs, leading to a net cancellation of the dipole moment.

Na_3TaF_8[13] is one of the few examples of 8 co-ordinate fluoride structures for these metals. The higher co-ordination states normally are only possible for the larger cations e.g. Zr^{4+}, Hf^{4+}, due to steric hindrance, so this is quite unusual. The $[TaF_8]^{3-}$ anion and its associated polyhedron are both shown below in Fig 1.5. The shape of the polyhedron is a near-perfect square Archimedean antiprism with the shape being only slightly distorted from that of the ideal on one of the square faces.

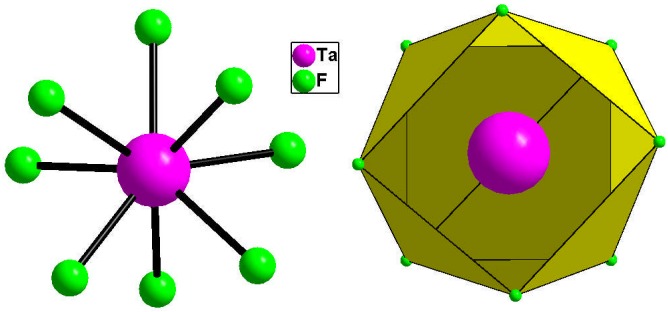

Fig 1.5 The $[TaF_8]^{3-}$ anion and polyhedron in **Na_3TaF_8**[13].

The **$[C_4H_{12}N_2][TiF_5(H_2O)]_2$**[14] structure consists of isolated octahedral $[TiF_5(H_2O)]^-$ anions templated with protonated piperazine moieties through hydrogen bonds to form the 3D structure. The anions form strong hydrogen bonds from the O−H groups to F atoms on neighbouring octahedra to make infinite zig-zag chains (see Fig 1.6).

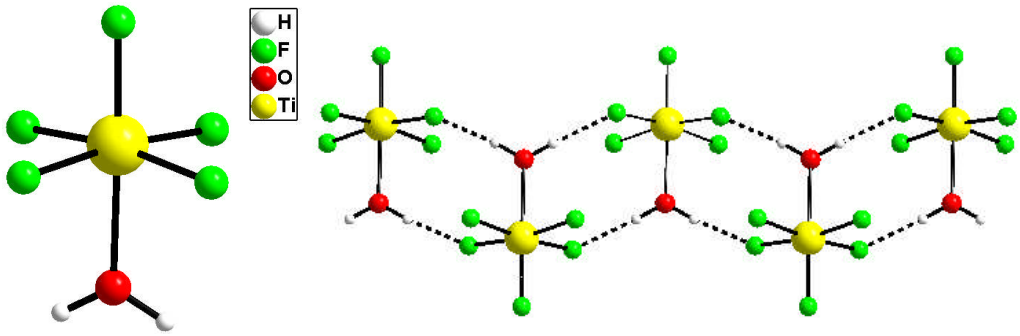

Fig 1.6 The $[TiF_5(H_2O)]^-$ anion and hydrogen bonded chain in **$[C_4H_{12}N_2][TiF_5(H_2O)]_2$**.[14]

The material **$[Ag_3MoO_3F_3][Ag_3MoO_4]Cl$**[15] is a good example of monomeric units linked together to form a chain through an intermediate species, in this case Ag^+ cations. The structure crystallises in the noncentrosymmetric space group P3m1 which is a result of the polar chains $[Ag_3MoO_3F_3]$ and $[Ag_3MoO_4]^+$ (see Fig 1.7), which run parallel to one another but do not result in the net cancellation of individual moments. The chains are held through ionic bonding from staggered Cl^- anions, which also charge balances the $[Ag_3MoO_4]^+$ unit. This material is also interesting for how it was synthesised; by serendipity. The chloride anions originally came from an impurity in one of the starting materials, Ag_2O. This resulted in a very small yield but subsequent reactions used HCl to determine the optimum conditions.

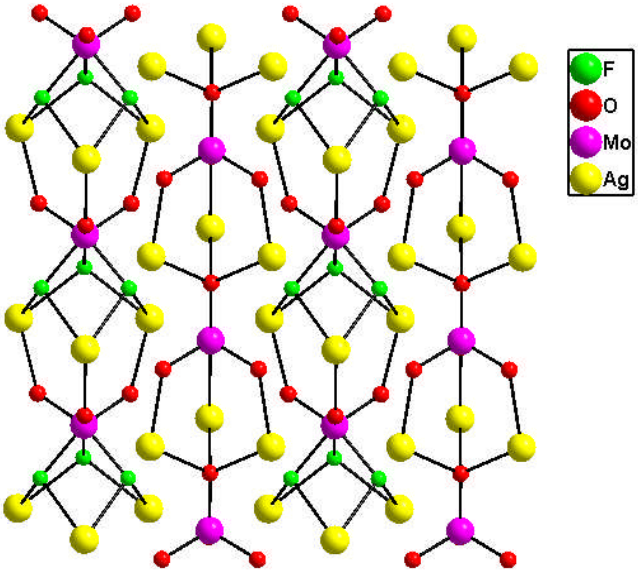

Fig 1.7 The chains of $Ag_3MoO_3F_3$ and $[Ag_3MoO_4]^+$ in **$[Ag_3MoO_3F_3][Ag_3MoO_4]Cl$**.[15]

1.1.4.2 Dimers

Dimeric structures are a good example of the building units that make up a lot of fluoride and oxyfluoride structures. The dimer in **$Na_5Zr_2F_{13}$**[16] is made up of corner sharing 7 co-ordinated prisms (see Fig 1.8). The 7 co-ordinate polyhedron can be described as consisting of a mono-capped trigonal prism. The polyhedra are joined the through the cap of the trigonal prisms to form the dimer.

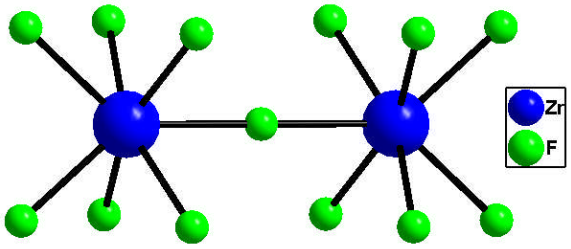

Fig 1.8 The $[Zr_2F_{13}]^{5-}$ dimer in **$Na_5Zr_2F_{13}$**.[16]

The structure is held together through strong ionic bonds between the fluorine anions and the sodium cations at an average distance of 2.35 Å. The packing around the anionic dimer is shown below in Fig 1.9. The dimers align themselves in chains parallel to the *b* axis with the sodium ions occupying the interstitial sites around them.

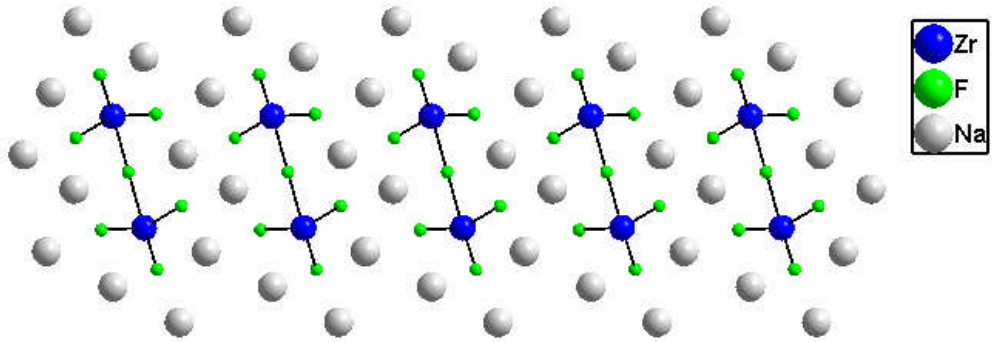

Fig 1.9 The interstitial packing of **$Na_5Zr_2F_{13}$**.[16]

In comparison the dimer in **$[NH_3OH]_6[Zr_2F_{14}]$**[17] is edge sharing instead of corner sharing. The $[Zr_2F_{14}]^{6-}$ dimer (see Fig 1.10) is completely surrounded by the protonated species; ammonium hydroxide, through which a hydrogen bonding network is established. Due to the small size of the cation, the hydrogen bonds can be quite short and therefore stronger than average, with the distance between the fluorine and oxygen atoms being as short as 2.50 (5) Å.

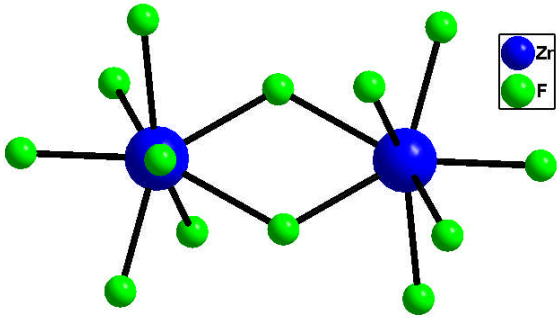

Fig 1.10 The $[Zr_2F_{14}]^{6-}$ dimer in **$[NH_3OH]_6[Zr_2F_{14}]$**.[17]

$Cs[C_4H_{12}N][V_2O_2F_8(H_2O)]$[18] is an interesting structure for several of its structural features. The anionic dimer alone is unusual, consisting of two octahedra which corner share through a fluorine bridge. Each octahedron is different (See Fig 1.11) with the left octahedron consisting of a short V=O bond (1.576 (4) Å), four V-F bonds (on average 1.822 Å) and a long V-(H_2O) (2.294 (4) Å). The V-(H_2O) bond is lengthened by a *trans* effect from the vanadyl bond, which draws more electron density away from the vanadium metal centre, causing the bond to lengthen. The same happens in the right octahedron with the bridging fluorine atom being lengthened from an average length of 1.815 Å (for the other four fluorine atoms) to 2.322 (4) Å. The vanadyl bond is again short in this octahedron, at a length of 1.581 (4) Å.

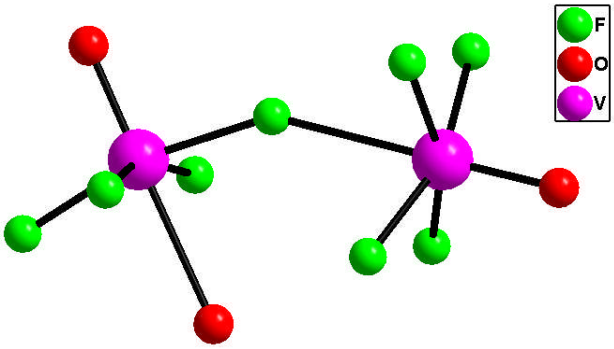

Fig 1.11 The $[V_2O_2F_8(H_2O)]^{2-}$ dimer in **$Cs[C_4H_{12}N][V_2O_2F_8(H_2O)]$**.[18]

The $[V_2O_2F_8(H_2O)]^{2-}$ dimers are linked together through inorganic hydrogen bonding from the aqua group to fluorine atoms on neighbouring octahedra to form zigzag chains (see Fig. 1.12).

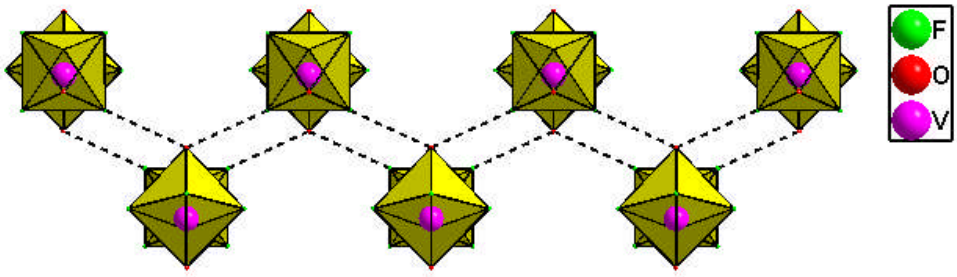

Fig 1.12 The hydrogen bonded chains in **$Cs[C_4H_{12}N][V_2O_2F_8(H_2O)]$**.[18]

These chains are then held together through ionic bonding via the caesium cations to form infinite layers (see Fig 1.13 − left). These inorganic layers are then separated by the tetramethyl ammonium cations (which hold the layers together through organic hydrogen bonding) to form the 3D structure (see Fig 1.13 − right). This structural type is also fairly uncommon owing to the fact that both inorganic and organic hydrogen bonding and ionic bonding are all being used simultaneously.

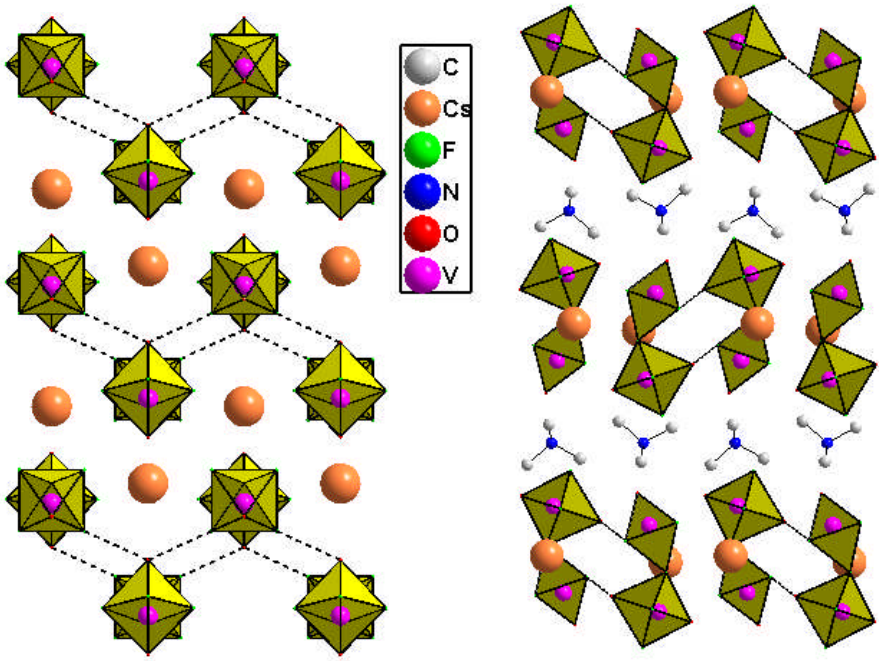

Fig 1.13 The inorganic layers (left) and the inorganic-organic sandwich (right) in **$Cs[C_4H_{12}N][V_2O_2F_8(H_2O)]$**.[18]

By comparison to $Cs[C_4H_{12}N][V_2O_2F_8(H_2O)]$, the composition of **$[C_4H_{12}N_2]_2[Ti_2OF_{10}]\cdot 2H_2O$**[19] is simple. The $[Ti_2OF_{10}]^{4-}$ dimers (see Fig 1.14) are held together a through a complex system of hydrogen bonds from the diprotonated piperazine moieties which also isolate the dimers from each other. The water molecules play little or no part in the hydrogen bonding of the structure as they are too far (O--F distance is greater than 3 Å) from the fluorine atoms to form any significant bonds.

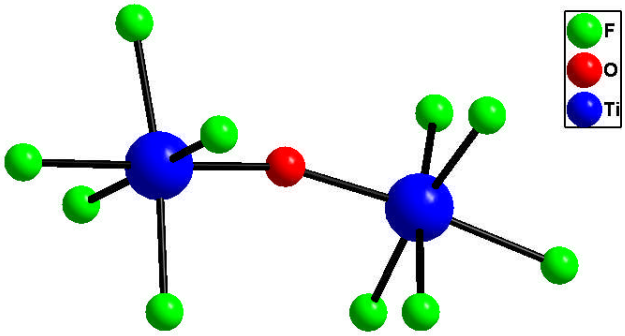

Fig 1.14 The $[Ti_2OF_{10}]^{4-}$ dimer in **$[C_4H_{12}N_2]_2[Ti_2OF_{10}]\cdot 2H_2O$**[19].

1.1.4.3 Trimers

There are very few early transition metal (oxy)fluoride trimeric structures. One such example is **$K[C_4H_{12}N][V_3O_3F_{12}]$**,[18] which is comprised of $[V_3O_3F_{12}]^{3-}$ trimeric anionic units (see Fig 1.15), potassium cations and tetramethyl ammonium cations. The trimer is built of three $[VOF_3F_{2/2}]^{2-}$ octahedra which all share two corners with the other two adjacent octahedra.

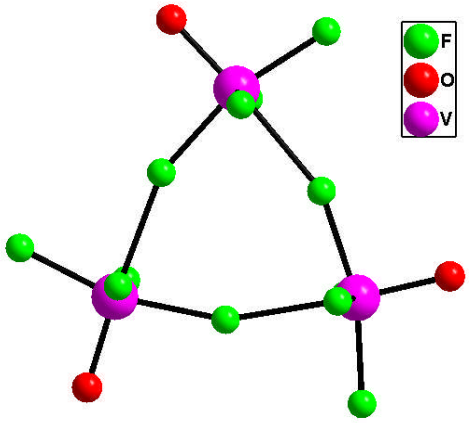

Fig 1.15 The trimeric unit of **$K[C_4H_{12}N][V_3O_3F_{12}]$**[18].

The trimeric units are joined together to form a chain by ionic bonding to the potassium cations (see Fig 1.16). These inorganic chains are then sandwiched together to form the 3D structure by hydrogen bonding from the tetramethyl ammonium cations, which completely surround the chains to isolate them from each other.

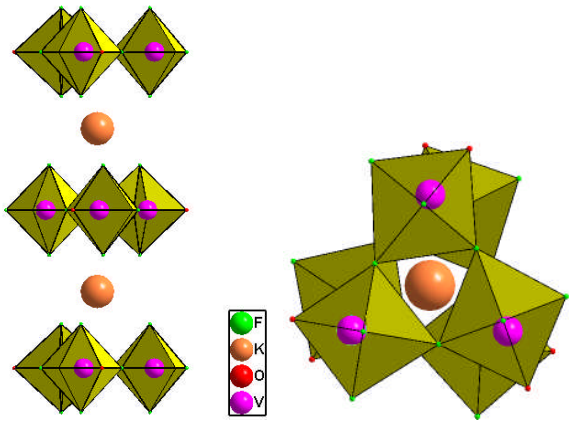

Fig 1.16 The inorganic chain of **$K[C_4H_{12}N][V_3O_3F_{12}]$**[18] viewed along the *b* axis (left) and the *c* axis (right).

1.1.4.4 Tetramers

The product **$[CH_8N_4][ZrF_6]\cdot H_2O$**[20] was first made when Abrahams *et al* were investigating the synthesis of the ferroelectric salt $[CH_8N_4][[ZrF_6]$. The structure consists of $[Zr_4F_{24}]^{8-}$ square planar tetrameric units (see Fig 1.17), diprotonated aminoguanidinium cations and water molecules. The tetramer itself consists of 4 ZrF_8 distorted Archimedean antiprisms which share square−face edges. These tetrameric units are enclosed by the aminoguanidinium cations and water molecules, through which they form an extensive hydrogen bonded network.

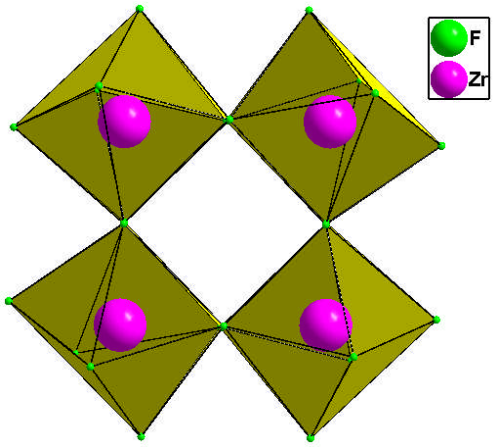

Fig 1.17 The $[Zr_4F_{24}]^{8-}$ tetramer in **$[CH_8N_4][ZrF_6]\cdot H_2O$**.[20]

$Ba_3V_2O_4F_8$[21] has a similar tetrameric unit to that of **$[CH_8N_4][ZrF_6]\cdot H_2O$**[20] but is an oxyfluoride rather than the pure fluoride structure. The tetrameric unit consists of four octahedral $V(O/F)_6$ units connected through adjacent O and F corner atoms to form $[V_4(O/F)_{20}]^{8-}$ units (see Fig 1.18).

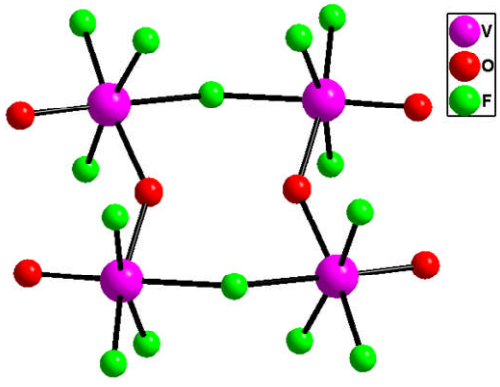

Fig 1.18 The $[V_4(O/F)_{20}]^{8-}$ tetramer in **$Ba_3V_2O_4F_8$**[21].

The tetrameric units are separated by a three-dimensional network of FBa_4 tetrahedra as shown below in Fig 1.19. The framework consists of four staggered chains, running along the *c*-axis, of bitetrahedral groups which corner share. Inside the network are large cages in which the tetramer is enclosed.

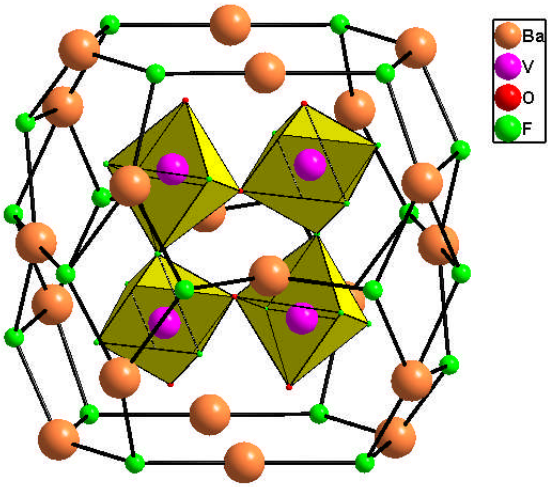

Fig 1.19 The $[V_4(O/F)_{20}]^{8-}$ tetramer in a twenty barium atom edged cage.[21]

$[TiF_2([15]crown-5)][Ti_4F_{18}]$[22] is an interesting material for several reasons. Firstly the $[Ti_4F_{18}]^{2-}$ tetrameric unit is unusual and quite uncommon. The tetramer is built up of four TiF_6 units which corner-share the three adjacent corners of a triangular face on a octahedron to make up the structure (see Fig. 1.20). Secondly the cation in the structure is another titanium fluoride complex, $[TiF_2([15]crown-5)]^{2+}$. Thirdly, the means by which the material is formed is atypical. **$[TiF_2([15]crown-5)][Ti_4F_{18}]$** is formed from a solution of [15]crown-5 and TiF_4 in acetonitrile left at room temperature for several hours, from which colourless crystals formed. The ionisation of metal species in solution usually requires an internal fluorine source, such as HF, rather than just the starting material TiF_4. This reaction presents the first autoionisation of a metal fluoride in a solution.

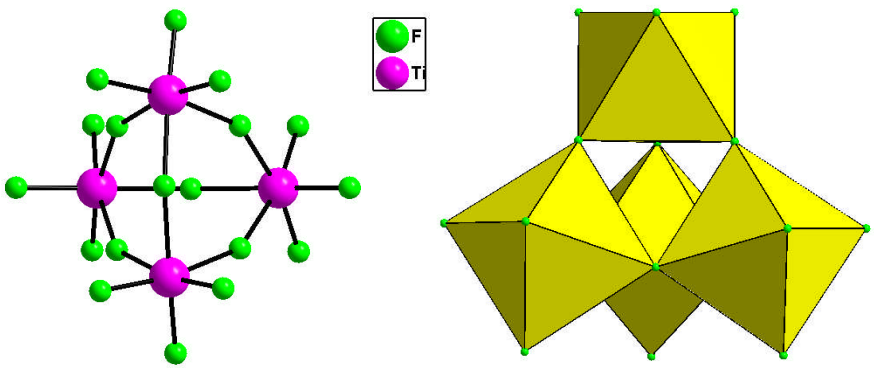

Fig 1.20 The $[Ti_4F_{18}]^{2-}$ tetramer in **$[TiF_2([15]crown-5)][Ti_4F_{18}]$**.[22]

1.1.4.5 1D Structures

In 1D structures, linear chains are one of the most common structural motifs. **$[NH_4]_2[TiOF_4]$**[23] is a simple near-linear chain structure (see Fig 1.21) held together by hydrogen bonding from the protonated ammonium species. The repeat units, $TiO_{2/2}F_4$, are connected together through the two *trans* oxygen atoms to form the kinked chains which also run parallel to one another.

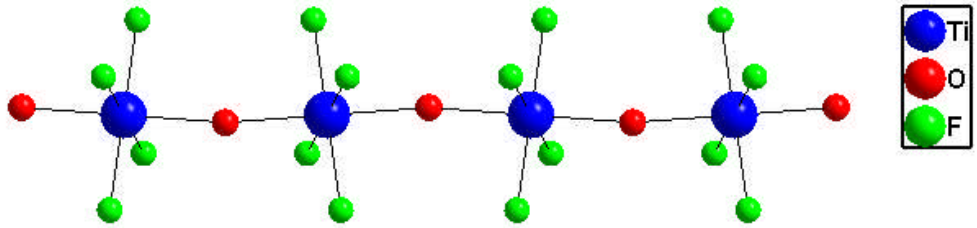

Fig 1.21 The near-linear *trans* chain in **$[NH_4]_2[TiOF_4]$**.[23]

Another common structural motif in 1D structures is the zigzag chain. A good example of this is **$K_2VO_2F_3$**[24] which comprises of *cis* zigzag chains (see Fig 1.22) held together through ionic bonding from the potassium cations. In the *cis*-chain, the bridging V-F bonds are noticeably longer than the other V-F bonds, at 2.189 (5) Å in length. This is due to the *trans* effect from the vanadyl bond.

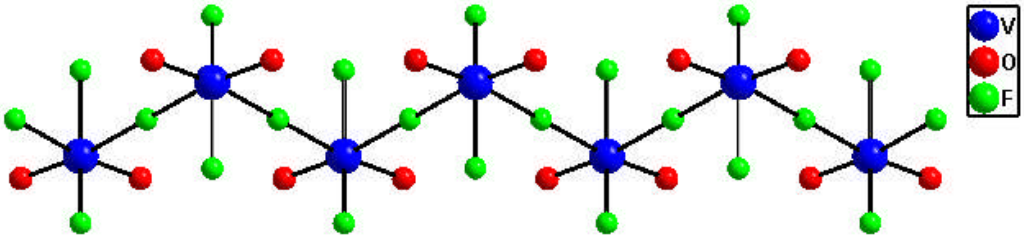

Fig 1.22 The *cis* zigzag chain in **$K_2VO_2F_3$**.[24]

Not all 1D structures follow the simple linear or zigzag motifs shown above. **$Cs[VOF_3]\cdot\frac{1}{2}H_2O$**[25] is a complex chain with several irregular features. The basic building unit of the structure is shown below in Fig 1.23 − left, which is comprised of two crystallographically unique VOF_5 octahedra which are linked through corner and edge sharing. The fluorine atoms *trans* to the vanadyl group experience a lengthening of their bonds, caused by a *trans* effect, from an average of 1.914 Å (for the other bridging fluorine atoms) to 2.164 (6) Å. The unusual trimeric repeat units are linked together through a 120° rotation to form the complex chains (see Fig 1.23 − right).

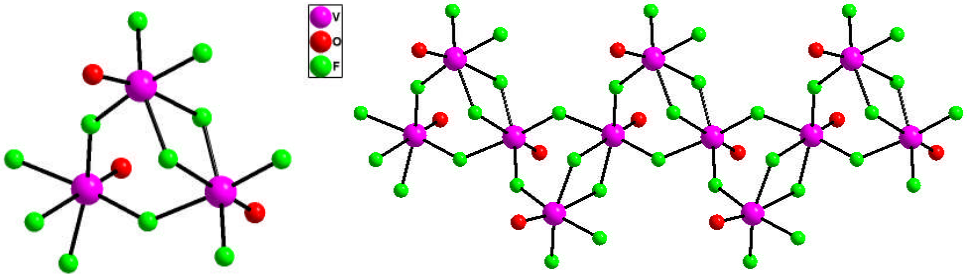

Fig 1.23 The BU (left) and complex chain (right) in **$Cs[VOF_3]\cdot\frac{1}{2}H_2O$**.[25]

1.1.4.6 2D Structures

$K_2Zr_3OF_{12}$[26] is a layered structure based around a hexamer building unit. Six $ZrOF_7$ distorted Archimedean anti-prisms share corners and edges to form the hexamer (see Fig 1.24) which comprises of an edge sharing layer and a corner sharing layer which are also connected by corner sharing.

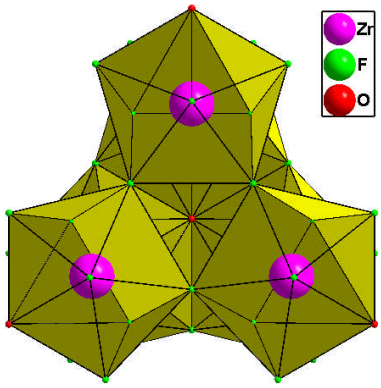

Fig 1.24 The hexamer repeat unit in **$K_2Zr_3OF_{12}$**.[26]

The hexameric units repeat to form the infinite layer by alternating their configuration by 180° in respect to one another, i.e. the corner sharing layer is on the top of the layer in one hexamer, the next adjoining hexamers are on the bottom (see Fig 1.25). Hexagonal channels reside within these layers and are filled with potassium cations. The layers are sandwiched together through ionic bonding from more potassium cations but the layers are staggered so that the channels become occluded by the other layers. **$K_2Zr_3OF_{12}$** is also an interesting material for the route by which it was synthesised: Microwave-assisted hydrothermal synthesis. This method of synthesis is relatively uncommon, with most hydrothermal reactions occurring in a standard oven at a temperature equal to or below 220°C.

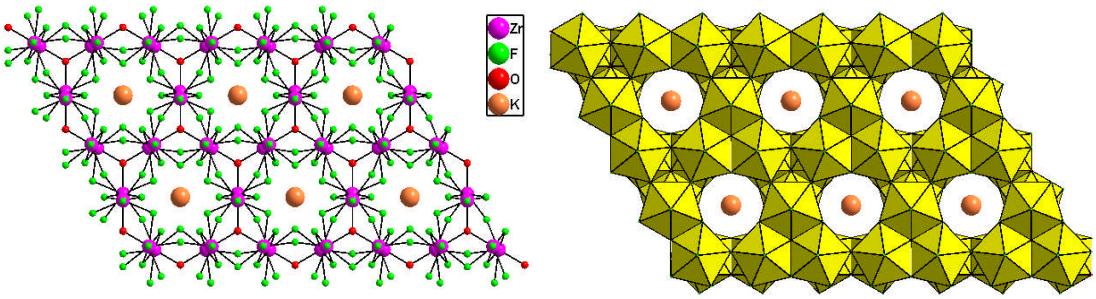

Fig 1.25 The layered motif in $\mathbf{K_2Zr_3OF_{12}}$.[26]

$\mathbf{[NH_4][HfF_5]}$[27] is one of the few layered hafnium fluoride materials. The structure consists of dimers of $[Hf_2F_{12}]^{2-}$ as the repeat unit. The dimer itself is also unusual as it features two enneahedra, which is a very curious co-ordination enviroment. The dimers corner share with each other to form the layer motif (see Fig 1.26). The channels that are left are occupied by ammonium cations, which also hold the layers together through an extensive hydrogen bonded network. The channels into which some of the ammonium cations are situated are left open by the neighbouring layers, unlike in the previously mentioned material.

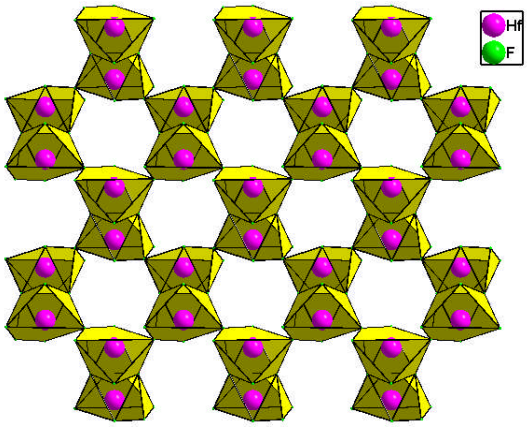

Fig 1.26 The $[HfF_5]^-$ layered motif in $\mathbf{[NH_4][HfF_5]}$.[27]

$\mathbf{KTiF_4}$[28] has the same structure as the Dion-Jacobson phases i.e. *cis* corner sharing octahedra forming an infinite 2-D lattice (see Fig 1.27 − left) and is the first reported early transition metal fluoride example of this. The structure is comprised of the $[TiF_4]^-$ layers with potassium cations sandwiched between them. The anionic layer is not perfectly regular, with octahedral tilting seen below in Fig 1.27 − right.

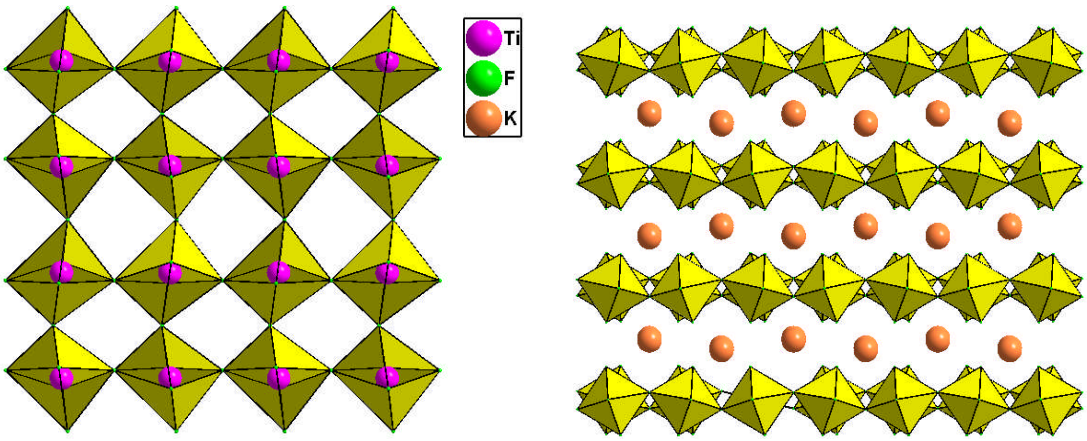

Fig 1.27 The $[TiF_4]^-$ layer motif (left) and the packing (right) in **$KTiF_4$**.[28]

$K_5Ti_3F_{14}$[29] is related to the Dion-Jacobson phases but can be more precisely described as a chiolite type structure. The structure consists of corner sharing octahedra (see Fig 1.28 − left) but in this structure, it is only every alternate octahedron that is both *cis* and *trans* corner sharing, with the other octahedra, being *trans* corner sharing. This leaves "holes" in the lattice which are occupied by potassium cations (see Fig 1.28 − right). A single layer of additional K^+ cations holds the layers together through ionic bonding. The interlayer cations are only situated above or below the *cis* corner sharing octahedra, alternately. The vanadium analogue[30] of this structure has also been synthesised and shown to have ferrimagnetic properties.[31]

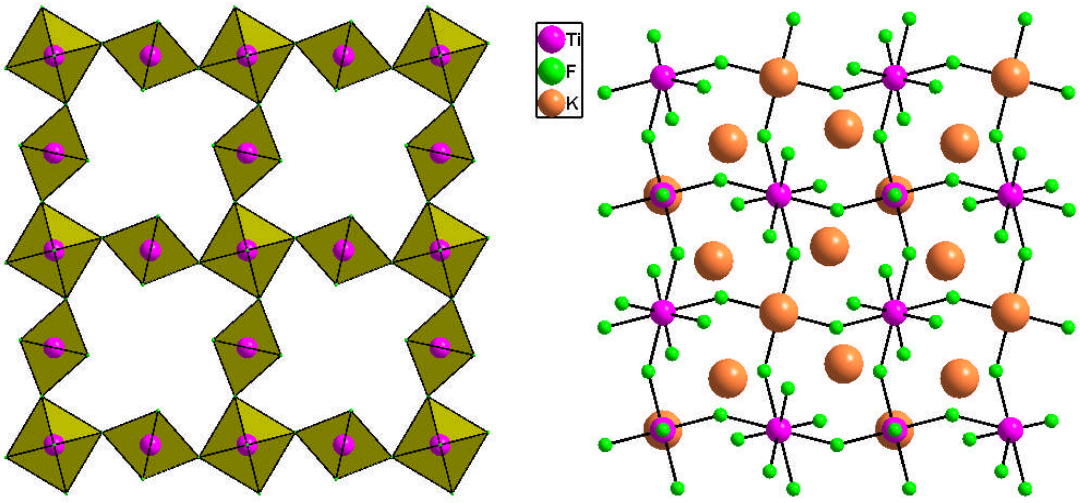

Fig 1.28 The $[Ti_3F_{14}]^{3-}$ layer motif (left) and packing (right) in **$K_5Ti_3F_{14}$**.[29]

1.1.4.7 3D Structures

$Li_3Zr_4F_{19}$[32] is a three-dimensional framework with channels along the *a* direction with a very unusual shape, all based on the topology of ZrF_7 units (see Fig 1.29). The structure consists of ZrF_7 pentagonal bypyramids which are arranged into a triangular unit through corner sharing. These units are then connected together through edge sharing dimers and by edge sharing to other triangular units to from the layered structure. The 3D structure is formed by corner sharing of one fluorine atom from the triangular motif to another similar unit. This is what precludes the formation of other channels in the solid. Materials such as this are of interest for their potential use in lithium batteries and as a nuclear reactor fuel solvent in the chemical reprocessing of spent reactor fuel elements.

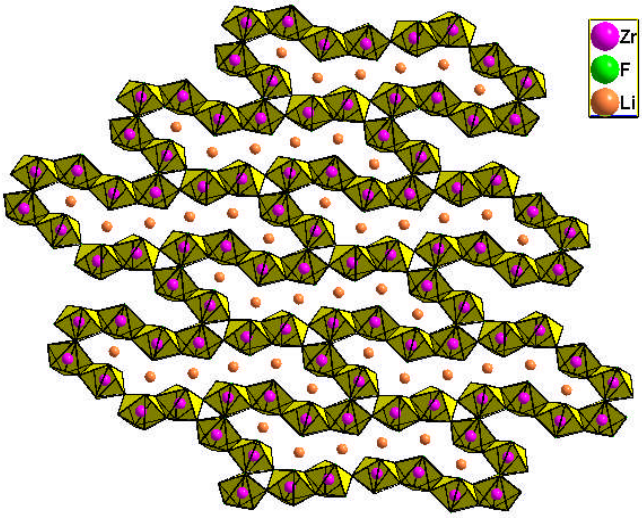

Fig 1.29 The lithium-filled channels in **$Li_3Zr_4F_{19}$**.[32]

$K_2Ta_4O_9F_4$[33] consists of $[Ta_{12}(O/F)_{54}]^{n-}$ blocks (see Fig 1.30 − left) which make up the structural motif. These blocks are the same as the ones used to make up the hexagonal tungsten bronzes and are linked together by common corners to form the lattice (see Fig 1.30 − right). The structure has open channels along the *c* axis which are occupied by charge balancing potassium cations. The oxygen and fluorine atoms are disordered across all sites and are represented as oxygen atoms in the diagrams below.

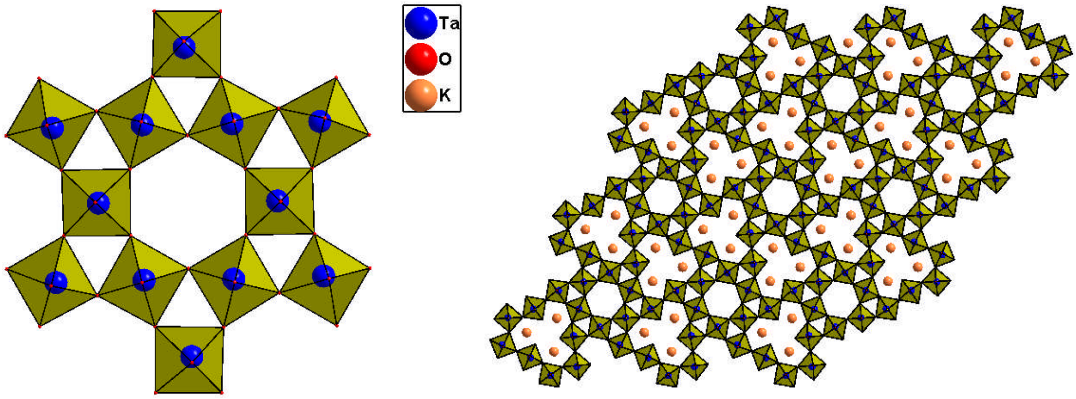

Fig 1.30 The $[Ta_{12}(O/F)_{54}]$ block (left) and a projection down the *c* axis (right) in $\mathbf{K_2Ta_4O_9F_4}$.[33]

$\mathbf{[NH_3]_{0.0267}[VF_3]}$[34] is comprised of the same $[M_{12}F_{54}]$ blocks as the structure above. The blocks are arranged in a classical hexagonal tungsten bronze array shown below (Fig 1.31). In this structure, although the lattice is neutral it still contains some guest molecules, in this case, ammonia, which is situated in the open pores along the *c* axis.

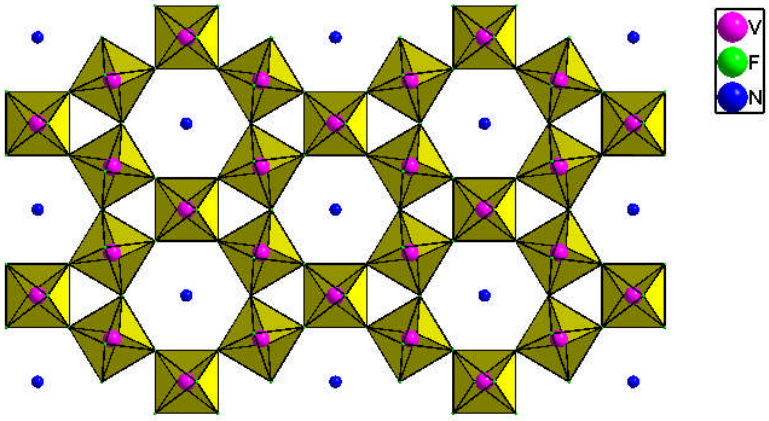

Fig 1.31 A projection down the c axis in $\mathbf{[NH_3]_{0.0267}[VF_3]}$.[34]

1.2 Physical Properties

1.2.1 Properties of Fluorides

The material family of transition metal fluorides are known for their diverse properties,[9] which range from use as textile flame retardants to tooth enamel protectants.[35,36]

These properties can be attributed to the unique nature of fluorine; its small size and high electronegativity. As a result of this, their lattice energy exceeds that of other halogenides, resulting in higher melting points. Conversely, M−F bonds are weaker than M−O bonds (due to higher electrical charge on O^{2-} and π back bonding), which can allow them to make excellent ionic conductors in a "quasi-liquid" state.[9] Fluorides also make excellent magnetic materials and they are known for their strong anti-ferromagnetic coupling between M−F−M linkages.

Some of the properties of fluorides considered in this work will now be briefly outlined.

1.2.2 Second-Harmonic Generation (SHG)

Second-harmonic generation or frequency doubling is a property of nearly all NCS materials (see section 1.1.3) and is applicable to the bulk of the whole material. When a beam of light is introduced onto a material, the emergent beam has a wavelength of precisely half of the original i.e. $\lambda_1 \rightarrow ½\ \lambda_1$. So if a Laser with a wavelength of 1064nm was introduced onto a sample thought to show SHG, any reflected light would appear green, as it would have a wavelength of 532nm. This is a simple test for SHG activity and confirms that a crystal structure is NCS. It also requires very small amounts of sample.[37]

1.2.3 Magnetism

Electrons possess a magnetic moment as a result of their spin, therefore all materials show some sort of magnetic property.[38] When these electrons are paired, the moments are effectively cancelled. When an electron is unpaired, the atom in question has a magnetic moment. The magnetic flux density, B, of a sample is given by:

$$\mathrm{B} = \mu_0 \left(H + M \right) \tag{1.1}$$

where μ_0 is the vacuum permeability, M is the sample magnetisation and H is the applied field. The magnetic susceptibility of a sample, χ, is given as:

$$\chi = \frac{M}{H} \tag{1.2}$$

The magnetic susceptibility of a sample can easily be measured as a function of temperature. It is from derivations of these data that significant information about the magnetic interactions in the sample can be extracted. Before these data are analysed they need to be corrected for diamagnetic interactions, through the use of Pascal constants.[39] Diamagnetic forces are repulsive to the magnetic field and arise from paired electrons in the sample. This contribution is very small compared to effect of paramagnetic interactions from unpaired electrons which are attracted to the magnetic field.

Unpaired electrons in a magnetic field across a range of temperatures can align in various ways. If, at a particular temperature, the alignment of the spins is random, the material is said to be paramagnetic. If the spins align parallel to one another the structure is ferromagnetic, if the alignment is anti-parallel, then the structure is anti-ferromagnetic. These properties can easily be seen in a plot of magnetic susceptibility, χ , against temperature, T, as shown below in Fig 1.32 (or as a plot of the inverse of the magnetic susceptibility, χ^{-1}, against temperature, T, in Fig 1.33).[39]

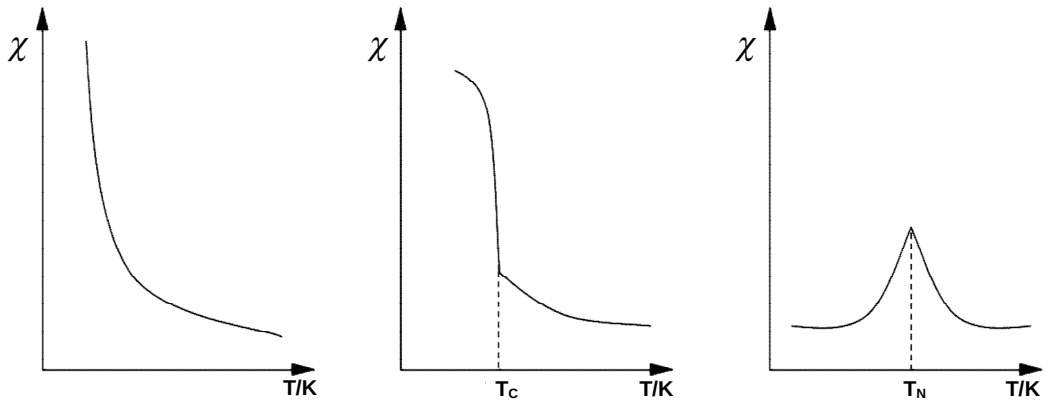

Fig. 1.32 χ vs. T, for a paramagnetic (left), ferromagnetic (centre) and an anti-ferromagnetic (right) sample.

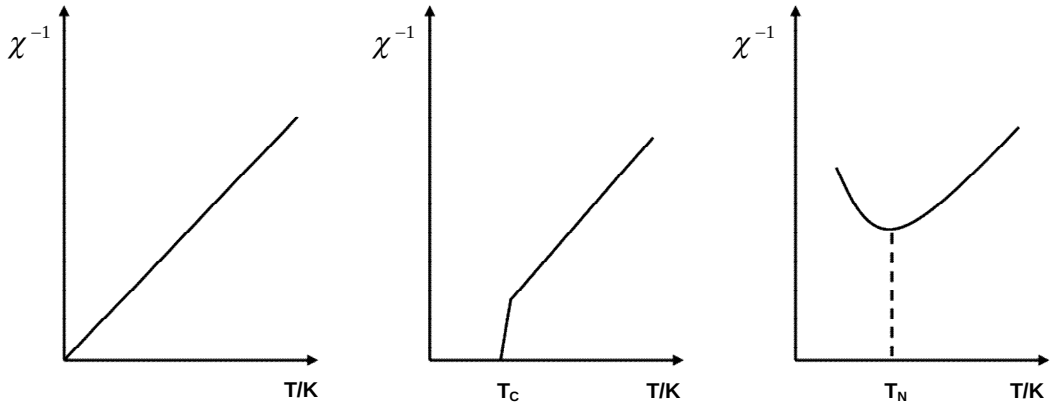

Fig. 1.33 χ^{-1} vs. T, for a paramagnetic (left), ferromagnetic (centre) and an anti-ferromagnetic (right) sample.

For ferromagnetic and anti-ferromagnetic samples there is an obvious point at which the phase transition from being paramagnetic occurs, this is called the Curie (T_C) or Néel (T_N) point respectively. A special case of anti-ferromagnetism is ferrimagnetism, which usually occurs when two moments are aligned anti-parallel to one another but have different moments. The result is a plot which looks ferromagnetic but where the Weiss constant (see equation 1.4) is negative. Ferrimagnetism can also occur because of magnetic frustration, which is caused by antagonistic geometrical constraints. In a square lattice the spins on the corners of the lattice can either align parallel or co-parallel (ferro or anti-ferromagnetically) to one another, where as in a triangular lattice if the interactions are not ferromagnetic then the system will be frustrated.[39] This is because the lattice can never totally align anti-parallel as there will always be an odd spin, as shown in Fig. 1.34. In a review by Ramirez,[40] the difference between ferrimagnetism and geometric frustration is defined. If the ratio of the Weiss constant, Θ (see equation 1.4 and Fig. 1.36), to the ordering temperature, T_N, is greater than 10, then the system is strongly geometrically frustrated. If this ratio is less than 10, it can be considered to ferrimagnetic.

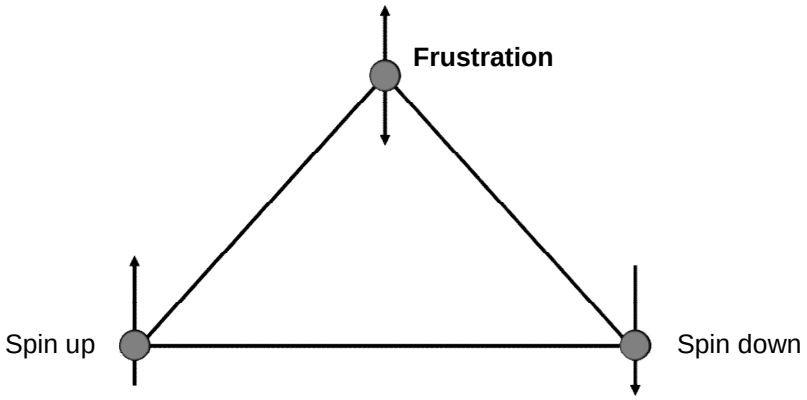

Fig. 1.34 The frustration in a triangular lattice.

These materials can also show exchange interactions. If the orbitals of the metal atoms overlap or are very close, then direct exchange can occur, which is defined by the exchange energy, *J*. If *J* is positive the interaction is ferromagnetic, with the opposite being true for anti-ferromagnetism. If the orbitals are too far apart then an indirect exchange, or superexchange, mechanism can occur. The exchange energy is still defined in the same way but the interaction occurs through an intermediate diamagnetic ligand, e.g. O^{2-}. A good example of anti-ferromagnetic superexchange is in NiO, in which the Ni^{2+} cations are able to magnetically couple with the O^{2-} anion. The overlapping electrons align anti-parallel to one another as shown in Fig 1.35.

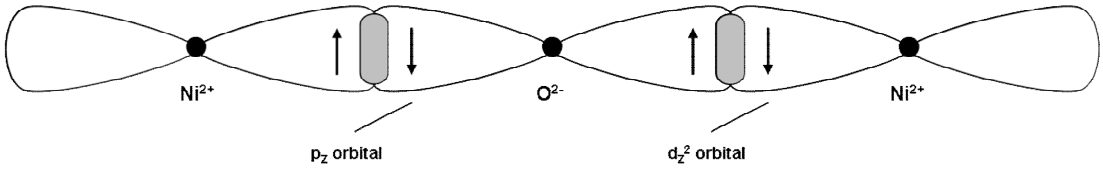

Fig. 1.35 The anti-ferromagnetic coupling of the *d* electrons in Ni^{2+}, with the *p* electrons of O^{2-} in NiO.

Above the transition point in a ferro or anti-ferromagnetic material the sample is paramagnetic and can be described as having Curie or Curie-Weiss behaviour. Curie behaviour is when the magnetic susceptibility is inversely proportional to the temperature:

$$\chi = \frac{C}{T} \tag{1.3}$$

Curie-Weiss behaviour is given by:

$$\chi = \frac{C}{T + \Theta} \tag{1.4}$$

where Θ is the Weiss constant. In both equations, *C*, is the Curie constant and is given by:

$$C = \frac{Ng^2\mu_B^2}{3k} \cdot S(S+1) \tag{1.5}$$

which is defined by a series of fundamental constants and *S*, the spin quantum number per electron.

A plot of Curie and Curie-Weiss behaviour is shown below in Fig. 1.36.

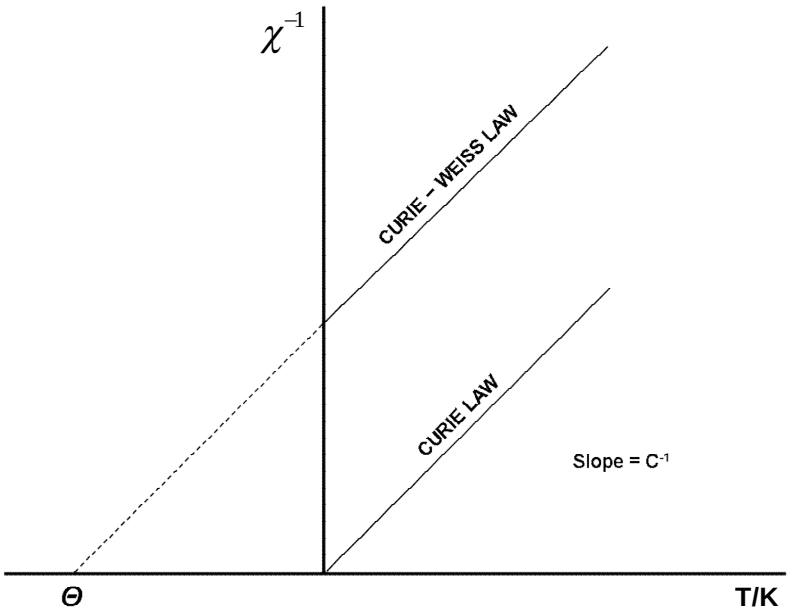

Fig. 1.36 A plot of χ^{-1} against temperature showing Curie and Curie-Weiss behaviour.

Paramagnetic materials show Curie behaviour and (anti-)ferromagnetic materials show Curie-Weiss behaviour above the respective Curie/Néel points. From a plot of this behaviour, the magnetic moment can be extracted.

The magnetic moment of a material is measured in Bohr magnetons (BM) and a single electron is said to have a spin moment of 1.73 BM. The overall spin moment, μ_s, for a material is given by:

$$\mu_s = g\sqrt{S(S+1)} \qquad (1.6)$$

where g is the gryomagnetic ratio, ~ 2.00, and S is the sum of the spin quantum numbers, ½ per electron.

The magnetic structure of a material can also be studied by neutron diffraction. Neutrons interact with unpaired electrons as they have a magnetic dipole moment, which gives rise to an extra scattering factor. A simple example is NiO which, when studied by X-rays, has a simple cubic rock salt structure. With neutron diffraction, extra peaks are observed from the unpaired *d* electrons arranged anti-parallel on alternate layers, to form a superstructure.

Magnetic structure analysis was used, in MnO, to provide the first proof for the existence of anti-ferromagnetic behaviour.

References

1. G. Férey, *J. Solid State Chem.*, **2000**, 152, 37.
2. J. Gopalakrishnan, K. Ramesha, K. Kasthuri Ranagan and S. Pandey, *J. Solid State Chem.,* **1999**, 148, 75.
3. P. Bukovec and L. Golic, *Acta Cryst.,* **1980,** B36, 1925.
4. N. S. P. Bhuvanesh and J. Gopalakrishnan, *J. Mater. Chem.*, **1997**, 7, 2297.
5. K. M. Ok and P. S. Halasyamani, *Mater. Chem.*, **2006**, 18, 3176.
6. W. Massa and D. Babel, *Chem. Rev.*, **1988**, 88, 275.
7. R. D. Shannon, *Acta Cryst*., **1976**, A32, 751.
8. P. S. Halaysamani and K. R. Poeppelmeier, *Chem. Mater.,* **1998,** 10, 2753.
9. "Inorganic Solid Fluorides"; P. Hagenmuller (Editor), Academic Press: London, 1985.
10. "Advanced Inorganic Fluorides": Synthesis, Characterisation and Applications, T. Nakajima, B. Zemva and A. Tressaud (Editors), Elsevier Science, S.A, 2000.
11. M. R. Silva, A. M. Beja, J. A. Paixao and L. A. De Veiga, *Z. Kristallogr. NCS*, **2001**, 216, 261.
12. M. E. Welk, C. L. Stern, K. R. Poeppelmeier and A. J. Norquist, *Crystal Growth & Design*, **2007**, 7, 956.
13. J. L. Hoard, W. J. Martin, M. E. Smith and J. F. Whitney, *J. Amer. Chem. Soc.*, **1954**, 76, 3820.
14. L. –Q. Tang, M. S. Dadachov and X. –D. Zou, *Z. Kristallogr. NCS*,, **2001**, 216, 259.
15. P. A. Maggard, T. S. Nault, C. L. Stern and K. R. Poeppelmeier, *J. Solid State Chem.*, **2003,** 175, 27
16. R. M. Herak, S. S. Malčić and L. M Manojlovič, *Acta Cryst.*, **1965**, 18, 520.
17. I. Ban, L. Golic, S. Milicev and B Volavsek, *Monatshefte fuer chemie und verwandte Teile anderer Wissenschaften*, **1995**, 126, 1279.
18. M. Hilbers, M. Leimkuhler and R. Mattes, *Z. Naturforschung. B – Chem. Sci*., **1989**, 44, 383.
19. M. S. Dadachov, L. –Q. Tang and X. –D. Zou, *Z. Kristallogr. NCS*,, **2001**, 216, 141.
20. C. R. Ross, B. L. Paulsen, R. M. Nielson and S. C. Abrahams*, Acta Cryst*., **1998**, B54, 417.
21. M. P. Crosnier-Lopez, H. Duroy and J. L. Fourquet, *Z. Anorg. Allg. Chem.* **1993,** 619, 1597.
22. A. Decken, H. D. B. Jenkins, C. Knapp, G. B. Nikiforov, J. Passmore and J. M. Rautiainen, *Angew. Chem. Int. Ed.*, **2005**, 44, 7958.
23. J. Patarin, F. Marcuccilli-Hofner and H. Kessler, *Eur. J. Solid State Inorg. Chem.*, **1994**, 31, 501.
24. R. Stromberg, *Acta Chem. Scand. Ser A,* **1986,** A 40, 325.
25. K Waltersson, *J. Solid State Chem.*, **1979**, 28, 121.
26. M. A. Saada, A. Hermon-Ribaud, V. Maisonneuve, L. S. Smiri and M. Leblanc, *Acta Cryst.*, **2003**, E59, 131.

27. C. Plitzko and G. Meyer, *Z. Anorg. Allg. Chem*, **1998**, 624, 169.
28. P. R. Sabatier, G. Charroin, D. Avignant and J. C. Cousseins, *Acta Cryst.*, **1979**, B35, 1333.
29. S, J. La Placa and W. Kunnmann, *American Crystallographic Association: Program Winter*, **1970**, 85.
30. B. M. Wanklyn, B. J. Garrard, F. Wondre and W. Davidson, *J. Cryst. Growth*, **1976**, 33, 165.
31. C. Cros, J-M. Dance, J-C. Claude, B. M. Wanklyn and B. J. Garrard, *Mater. Res. Bull.*, **1977**, 12, 415.
32. P. Dugat, M. El-Ghozzi, J. Metin and D. Avignant, *J. Solid State Chem.*, **1995**, 120, 187.
33. P. A. Boukhari, J. P. Chaminade, M. Vlasse and M. Pouchard, *Acta Cryst.*, **1979**, B35, 1983.
34. R. de Pape, A. Le Bail, F. Lubin and G. Férey, *Rev. Chim. Miner.,* **1987**, 24, 545.
35. M. R. Bauer, C. R. Ross, R. M. Neilson and S. C. Abrahams, *Inorg. Chem*., **1999**, 38, 1028.
36. E. Goreshnik, M. Leblanc, V. Maisonneuve, *J. Solid State Chem*., **2004**, 177, 4023.
37. K. M. Ok, E. O. Chi, P. S. Halasyamani, *Chem. Soc. Rev.*, **2006**, 35, 710.
38. "Physical Chemistry", P. W. Atkins, 6th Edition, Oxford University Press, Oxford, **1998**.
39. "Solid State Chemistry and its Applications", A. R. West, John Wiley & Sons, Singapore, 2005.
40. A. P. Ramirez, *Annu*. *Rev. Mater. Sci.*, **1994**, 24, 453.

2.0 Techniques

2.1 The Hydrothermal Method

The hydrothermal method was developed by scientists and technologists trying to emulate materials made through natural processes.[1] It was first used commercially in 1845 by Schafthaul to make quartz in a process still used today to fabricate quartz for the electronics industry.[2] Then in 1892 Bayer used the hydrothermal method to leach metal from mineral ore. This process is still used today on a host of uranium ores, sulphides of gold, copper, nickel and zinc.[3] It was not until 1948 that Barrer was the first person to produce synthetic analogues of microporous materials – zeolites, consequently opened up a whole new method of synthesising materials which has proved popular among material scientists ever since.

The definitions of a hydrothermal reaction are varied but are best summarised as "a reaction occurring under conditions of high temperature and pressure in the presence of an aqueous solvent in a closed system". The definition of a solvothermal reaction is the same but with a non-aqueous solvent. In this work the reactions above 100 °C are carried out in a Teflon-lined stainless steel autoclave, so meet the above definition. The reactions at 100 °C and below do not meet the definition as they are not under pressure and are best described as an aqueous reaction.

2.2 X-ray Diffraction

X-rays are produced when electrons, accelerated by a high voltage, strike a metal target. The electrons decelerate as they collide with the material and through multiple collisions their energy is released as a continuous X-ray spectrum called white radiation (*bremstrahlung*), as shown in Fig. 2.1. If an electron has energy above a threshold potential it ionises the target by ejecting an electron from an inner shell. When this happens, an electron from a higher orbital falls to fill the vacancy emitting a characteristic wavelength of X-ray radiation, based on the energy difference between the two shells. When the electron that fills the vacancy in the inner shell falls from an adjacent shell, the wavelength is called K_{α}. When the descending electron is from a shell that is not adjacent, i.e. two levels up; the wavelength of radiation emitted is called K_{β} and is at a shorter wavelength and less intense as it occurs more infrequently.[4] The K_{α} line actually exists as a doublet due to the spin states of the 2*p* electrons and the wavelength used is actually an average of this doublet. For example, the wavelengths of the $K_{\alpha 1}$ and $K_{\alpha 2}$ lines of molybdenum (the metal target of the electrons) are 0.7093 and 0.7135 Å, so the average of the resultant wavelength is 0.7107 Å. Different metal targets can be used for different wavelengths and are separated from the bremstrahlung by passing the generated X-rays through a monochromator or confocal optics.

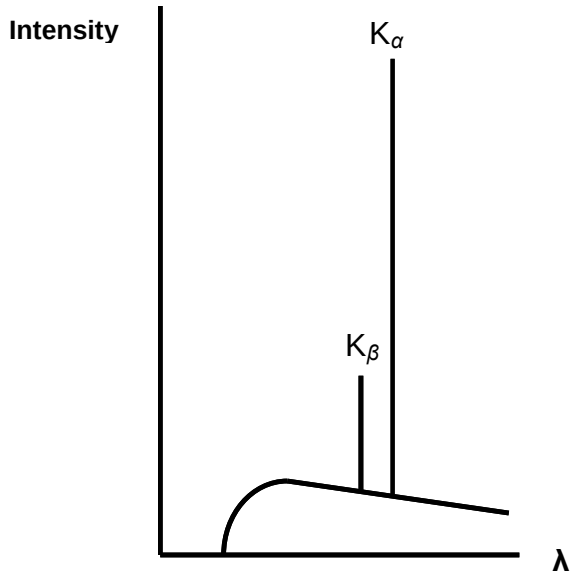

Fig. 2.1 A typical X-ray emission spectrum for a metal

There are two conventional laboratory generators of X-rays; a sealed X-ray tube and a rotating anode chamber.[5] Both consist of a high voltage power supply applied between a cathode and an anode of choice (most commonly copper or molybdenum). In a sealed X-ray tube, the anode has to be cooled to stop the target metal melting. The rate at which the anode can be cooled dictates how intense an electron beam can be used and the intensity of the X-rays generated. In a rotating anode, the target metal is rotated parallel to the direction of the generated X-rays, meaning it is continuously regenerated. As a result of this, a much higher power electron beam can hit the target and generate more intense X-rays. For copper radiation, the intensity of the X-rays from a rotating anode generator are 3-5 fold higher than those from a sealed X-ray tube.

X-rays of a much greater intensity can be obtained from a synchrotron source.[6] An example of this is the synchrotron at the Daresbury Laboratory (for the general schematic of a synchrotron see Fig. 2.2[7]). Electrons are accelerated at speeds close to the speed of light and forced to move in a circular path, causing them to be constantly accelerating. When a charged particle, e.g. an electron, moves under the influence of an accelerating field, it emits electromagnetic radiation, e.g. X-rays. A broad spectrum of radiation is created; the required radiation for each station is selected by a monochromator and focused by a magnetic field.[5] At Daresbury the electrons are initially accelerated using the linear accelerator before feeding into the booster ring where they are accelerated close to the speed of light. They are then injected into the synchrotron storage ring where the radiation is emitted tangentially to the experimental stations located around the circumference.

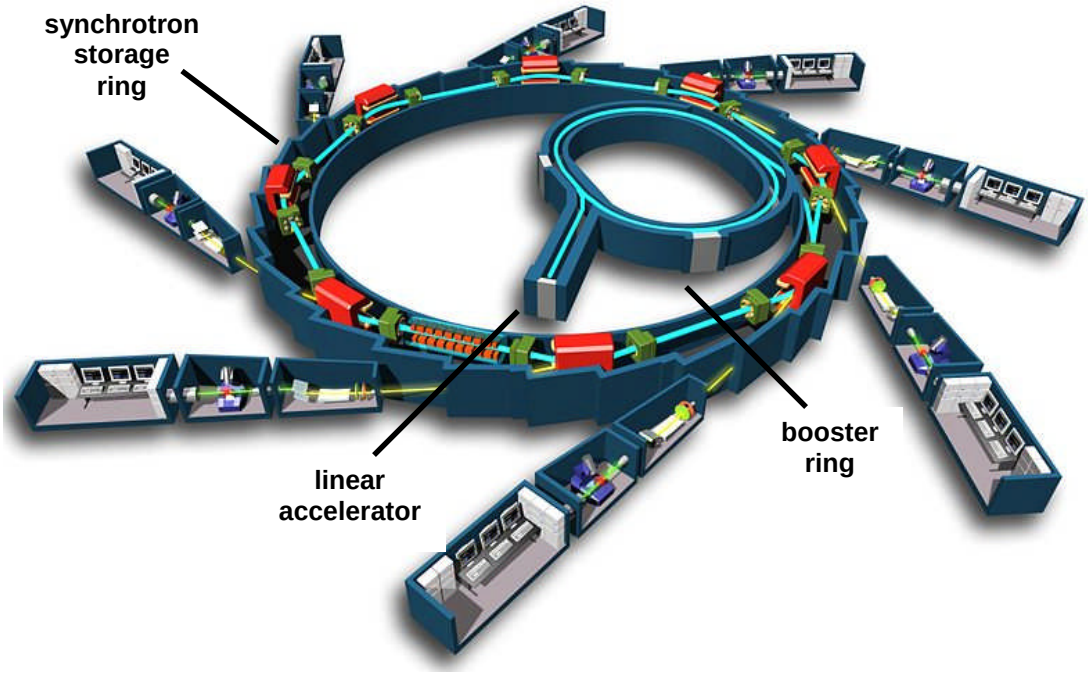

Fig. 2.2 A schematic diagram of a synchrotron facility.[7]

In 1912 von Laue realised that the spacings between atoms were comparable to the wavelength of X-rays (~ 1 Å). As such X-rays should be diffracted by a crystalline sample. The long range ordering in a crystal means that the diffracted X-rays should appear as a regular pattern, or diffraction pattern. As a result of constructive interference, the diffraction pattern appears as an array of spots. This pattern is geometrically related to the geometry of the lattice and unit cell of the crystal.[5] W. L. Bragg considered a crystal to be built up of layers or planes. As such, some X-rays will be reflected off a plane with the angle of reflection equal to the angle of incidence and the rest of the X-rays will pass through to be reflected off other planes, as shown in Fig. 2.3.

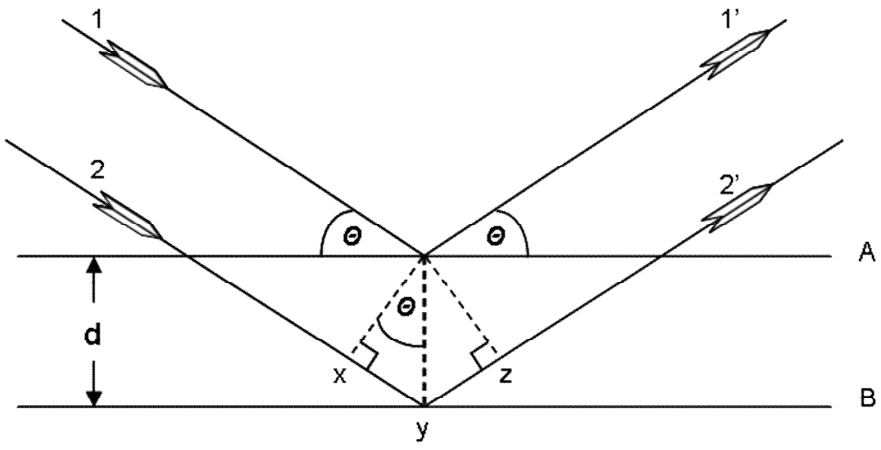

Fig. 2.3 X-rays reflecting off adjacent planes

X-ray beams, 1 and 2, are reflected off adjacent planes, A and B, within the crystal. When the reflected beams 1' and 2' are in phase, constructive interference occurs but they must fulfil certain criteria in order to be so; beam 2-2' has to travel the extra distance *xyz* which has to be equal to an integer of wavelengths. The distance, *d*, is related to the incidence angle, θ, and the distance *xy* by:

	$xy = yz = d \sin\theta$	
so	$xyz = 2d \sin\theta$	
and	$xyz = n\lambda$	
therefore	$2d \sin\theta = n\lambda$ – **Bragg's Law**	(2.1)

Bragg's law allows for the precise spots on a diffraction pattern to occur as when an incident angle is different from the angle of reflection, cancellation occurs. Bragg's law also shows that the diffraction pattern (sin *θ*) is the geometric inverse of the crystal lattice spacings, *d*. The distance between planes, *d*, can also be described as d_{hkl}. For a known value of *hkl*, the value of sin *θ* can be calculated. The simplest example of this is for a cubic system, where cell axes a, b and c are all equal, as given below:

$$\sin\Theta = \left(h^2 + k^2 + l^2\right)^{1/2} \frac{\lambda}{2a} \qquad (2.2)$$

When an X-ray is diffracted by a crystal, the X-ray does not actually reflected an individual atom, it is scattered by the electrons of that atom. The higher the atomic mass, the greater the scattering power of that atom. This gives the scattering or form factor. This term is also dependent on the incident angle of radiation, the greater the angle, the weaker the intensity of the scattered X-ray. So a diffraction pattern is not just a pattern of atomic geometry but of electron density within the crystal.[6]

Although the equation derived by Bragg is a very simplistic model consisting of only two planes it withstands mathematical scrutiny when compared to a complex model for a 3D structure. It is because of this, in the simplest of terms, we can use Bragg's law to elucidate the structure of a crystal from its diffraction pattern. This is done through the single crystal method.

2.2.1 Single Crystal Method

A Bruker SMART 1K CCD diffractometer (Daresbury Laboratories), a Rigaku SCX Mini diffractometer (in house) and a Rigaku Mercury CCD diffractometer (in house) were all used to collect data for this work. These machines use the current preferred technology in order to speed up data collection and improve data quality. These diffractometers are all equipped with area detectors which allow for faster data collection times through the collection of

multiple diffraction spots in a single image (see Fig 2.4). The Rigaku SCX Mini diffractometer collects all images twice to remove any spurious peaks (zingers) caused by cosmic radiation, which helps to improve the data quality.

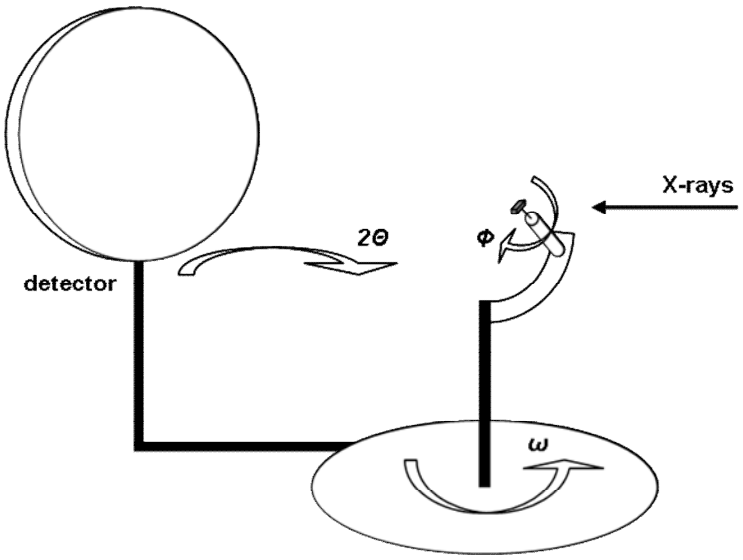

Fig. 2.4 A schematic diagram of a diffractometer
equipped with an area detector

Once the initial frames have been collected (approx. 20 frames) the crystal system and unit cell parameters are calculated. This is done for two reasons; firstly for confirmational purposes - e.g. if the crystal has a known unit cell it could be a known material, therefore not worth collecting and, secondly, for determining the orientation of the crystal to the incident beam. Once these parameters have been established the process of data collection begins. Each frame is recorded for the same length of time dictated by the scattering ability of the atomic species in question, the weaker the scattering ability of the crystal, the longer each frame is collected for. Once the data collection is complete, the data is integrated and *hkl* values attributed to each spot in the diffraction pattern. From these values, systematic absences can be found and the space group determined, as some diffraction spots are absent due to the effects of symmetry.

In order to convert the diffraction data into a 3D map of electron density i.e. the location and type of each atom, complex calculations need to be performed due to the loss of phase information (this problem is called the “phase problem”). Once these calculations have been performed, the structure factor, F_{hkl}, can be used to Fourier synthesise an electron density map, ρ_{xyz}.

$$\rho_{xyz} = \frac{1}{V}\sum_{hkl} F_{hkl} e^{-2\pi i(hx+ky+lz)} \quad (2.3)$$

2.2.1.1 Patterson Synthesis

Patterson synthesis overcomes the phase problem by using the amplitude of the square of the structure factor taken from the diffraction data.[7] This is used in the following expression:

$$P_{xyz} = \frac{1}{V}\sum_{hkl} \left|F_{hkl}\right|^2 \exp^{-2\pi i(hx+ky+lz)} \quad (2.4)$$

The map this equation creates is not of electron density but of the vectors between atoms in the unit cell. This method is particularly useful if the unit cell is mostly comprised of heavy atoms, e.g. mineral species, as the structure factor will be mostly comprised of these heavy atoms.

2.2.1.2 Direct Methods

Most modern structural analyses make use of direct methods in order to determine the crystal structure from diffraction data.[5] This method uses a statistical approach (the Sayre relationship) which assumes all the atoms are randomly distributed and their structure factors are all equal:

$$S(hkl) \sim S(h'k'l') \cdot S(h-h',\ k-k',\ l-l') \quad (2.5)$$

Where S relates to sign of the phase in question. So the phase in question can be determined (with a high statistical probability) if other phases are known. The probability that this prediction is true is given by:

$$P = \frac{1}{2} + \frac{1}{2}\tanh\left[\frac{1}{N}\left|E_{hkl} \cdot E_{h'k'l'} \cdot E_{h-h',k-k',l-l'}\right|\right] \quad (2.6)$$

So, if *Ehkl* is the 552 reflection and *Eh'k'l'* is the 111 reflection, then the difference between the two is the *E*441 reflection (*Eh−h',k−k',l−l'*) . If both the E_{552} and the E_{111} reflection are large and positive, then if the E_{441} reflection is large, it will most probably be positive. Using this, a small set of known phases is determined and used to generate the structure factors for the crystal structure. From these structure factors, a Fourier transform is applied and an electron density map created (see Equation 2.3).

2.2.1.3 Structure Refinement

The most widely used method of structure refinement is the least-squares method. This process compares the observed intensities with calculated intensities, giving a value for the difference between them. In the structure solution program SHELXL-97[8] the weighting scheme is given by:

$$w = \frac{1}{\sigma^2\left(F_0^2\right) + \left(aP\right)^2 + bP'} \tag{2.7}$$

Where σ is the standard deviation of the data, *P* is a summation used to reduce statistical bias, *P'* is a summation used to reduce statistical bias corrected for polarisation and *a* and *b* are adjustable parameters employed to keep the goodness of fit close to 1.0 (see 2.10)

The R-index for F^2 is given by:

$$wR_2 = \left\{ \frac{\sum\left[w\left(F_0^2 - F_c^2\right)\right]^2}{\sum w\left[F_0^2\right]^2} \right\}^{1/2} \tag{2.8}$$

and the R-index of *F* is given by:

$$wR_1 = \frac{\sum\left[w\left(\left|F_0\right| - \left|F_c\right|\right)\right]^2}{\sum w\left|F_0\right|^2} \tag{2.9}$$

The goodness of fit is based of F^2 and is given as:

$$GOF = S = \left\{ \frac{\sum\left[w\left(F_0^2 - F_c^2\right)\right]^2}{n - p} \right\}^{1/2} \tag{2.10}$$

where *n* is the number of reflections and *p* is the total number of refined parameters.

The R-index for F^2 should be more than double the value for *F.* If the R-index for F^2 is more than treble the value of R-index of *F*, then there maybe an error in the structure solution. This could be caused by twinning or a poorly diffracting crystal. The data should be evaluated and a re-collection considered.

Once the refinement is complete the value of *S* should be close to 1.0 and the R-index for *F* should be below 5%. If the value of *S* is too high (>1.3), additional refinement cycles may be required in order to reach convergence.

2.2.2 Powder X-ray Diffraction

Powder X-ray diffraction patterns were collected on a Stoe STADI-P powder diffractometer using a copper anode, which produced monochromated X-rays at 1.5406 Å. The samples were mounted on a sandwich of mylar discs greased with Vaseline. The resultant patterns were used to check for sample purity by comparing them to patterns simulated from solved single crystal data. The obtained patterns were also used in comparison with known materials to see if they were novel and to prevent the multiple submissions of identical samples for the collection of single crystal X-ray diffraction data.

2.3 Bond Valence Sum Calculations

Once a structure solution is complete, a bond valence sum calculation should be performed in order to help confirm that the solution is correct. It can also show if there is any atomic disorder in the structure. The bond valence, (s), from each bond surrounding a metal centre are summed together, the resultant value should be close to the hypothesised valence state of the atom in question. The calculation for an individual bond valence is based on the following equation:

$$s = \exp\left(\frac{(Ro - R)}{B}\right) \qquad (2.11)$$

Where (s) is the bond valence, (R) is the bond length and Ro and B are bond valence parameters that depend on the two atoms forming the bond. The bond valence parameters are the values determined by Brown & Altermatt[9] and O'Keeffe & Brese,[10] where the term B normally has the value of 0.37. Bond valence sum calculations in this work were performed using the VALENCE program.[11]

2.4 Magnetic Measurements

The magnetic measurements of all samples (except samples V−1 and V−2, which were collected by Prof. A. Harrison of Edinburgh University) were collected on a Quantum Design MPMS SQUID at the University of St Andrews. Data were usually recorded in a field of 5000 Oe while warming from 2 to 334 K in 4 K steps, following consecutive zero field cooling (ZFC) and field cooling (FC) cycles. All data sets were corrected for diamagnetism through the use of Pascal constants. For the theory behind magnetic measurements, refer to section 1.2.3.

2.4.1 Superconducting Quantum Interference Device (SQUID)

When a magnet is moved through a coil of wire, it induces a flow of electrons; it is this principle that is used to measure magnetisation in a SQUID device.[4] A schematic diagram of the internal workings of the SQUID machine is seen in Fig. 2.5. A magnetic field is applied parallel to a sample, which is then moved in small increments through the field. Surrounding the sample is a superconducting wire through which a change in current flows, this is detected by the SQUID. The samples magnetisation is then calculated from the change in current, detected by the SQUID.[5]

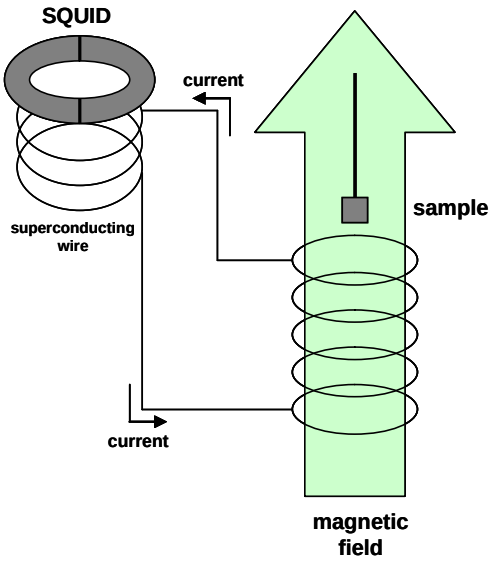

Fig. 2.5 A schematic diagram of the SQUID machine.

2.5 SHG Measurements

SHG Measurements were carried out by the research group of Prof. P. Shiv Halasyamani from the Department of Chemistry and Centre for Materials, University of Houston, Texas, USA. The samples were measured by the process Prof. Halasyamani outlined in a recent paper[12]. The sample outputs were measured against a quartz sample (which has an arbitary value of 1). The equipment has only a lower threshold for detection, at a value equivalent to half of the output from quartz.

2.6 CHN Microanalysis

CHN Microanalysis was performed using a Carlo Erba EA1110 analyser and collected by Slyvia Williamson in the School of Chemistry. The obtained values were compared to the theoretical values as a measure of sample purity.

2.7 EPR Spectroscopy

EPR spectra were collected on a Bruker EMX 10/12 spectrometer operating at 9.5 GHz with 100 KHz modulation, with a sweep width of 3300 G, field modulation amplitude of 4 Gpp and a power of 4 mW. Samples were in powder form within a 1mm o.d. glass capillary in the resonant cavity.

References

1. “Synthesis of Inorganic Materials”, U. Schubert and Hüsing, Wiley-VCH, U.S.A. **2002**.
2. R. A. Laudise, *Chemical and Engineering News*, **1987**, September 28th Edition, 30.
3. “Handbook of Hydrothermal Techniques”, K. Byrappa and M. Yoshimura, William Andrew Publishing, U.S.A. **2001**.
4. “Physical Chemistry”, P. W. Atkins, 6th Edition, Oxford University Press, Oxford, **1998**.
5. “Solid State Chemistry and its Applications”, A. R. West, John Wiley & Sons, Singapore, **2005**.
6. “Fundamentals of Crystallography”, C. Giacovazzo, (Editor), Second Edition, Oxford University Press, Oxford, **2002**.
7. Synchrotron Soleil: Schéma de Principe Copyright © Chaix & Morel et Associés, Used with Permission.
8. G. M. Sheldrick, Institüt für Anorganische Chemie der Universität, Tammanstrasse 4, D-3400 Göttingen, Germany, **1998**
9. I. D. Brown and D. Altermatt, *Acta Cryst*., **1985,** B41, 244.
10. N. E. Brese and M. O'Keeffe, *Acta Cryst*., **1991**, B47, 192.
11. VALENCE © I. D. Brown, Brockhouse Institute for Materials Research, McMaster University, Hamilton, Ontario. Canada, Used with permission.
12. K. M. Ok, E. O. Chi, P. S. Halasyamani, *Chem. Soc. Rev.*, **2006**, 35, 710.

3.0 Experimental

3.1 Synthesis

During this work, 2644 experiments were carried out resulting in 60 new crystal structures, all of which are described in later chapters. All the experiments were performed in either a polypropylene bottle or in a Teflon-lined stainless steel autoclave, depending upon the reaction temperature. Once the reaction vessels had cooled to room temperature, the contents were emptied, filtered and washed in water, or in the case of a few water soluble materials, washed in ethylene glycol. All samples were dried in air at 60 °C. A general scheme of synthesis is as follows; in a polypropylene bottle, 1 mmol of metal source (a transition metal oxide) was dissolved in 0.5 ml of HF. To this 0 to 5 ml of water is added along with 5 ml of ethylene glycol. An appropriate amount of "template" (or structure directing agent) is added (organic or inorganic) and the solution mixed until homogeneous. The bottle is either then heated at 100 °C or the contents of the bottle transferred into the Teflon-lined stainless steel autoclave and heated at a temperature above 100 °C but below or equal to 220 °C. All reactions were heated for up to a maximum of 4 days.

HF is used as a fluorine source as it also acts as the mineralising agent; different concentrations were tried but did not result in any different materials. Ethylene glycol is used as the solvent of choice for several reasons; it is cheap, soluble in water and it is also a non-aqueous polar solvent. Pyridine and butanol were both tried as alternative solvents but without any success. They at best either yielded the same products or, in the case of pyridine, which is not soluble in water, cause a bi-layer to form in the solution hampering the formation of products. At worst the reactions, which had worked in ethylene glycol, did not work in these solvents because the template could not dissolve.

A variety of metal sources were used in this work and for different reasons:

- Vanadium and molybdenum – various oxidation states possible. Known to form polar building units in aqueous solution.
- Zirconium – different co-ordination states possible. Known to have high thermal stability.
- Titanium, hafnium, niobium and tantalum – used to show the effect of periodicity and for the different co-ordination states possible.

An assortment of template species was used, both organic and inorganic. The organic templates are shown in Fig. 3.1. The inorganic species used were the alkali metals from sodium to caesium. These different cationic species were used for different reasons. The organic molecules act as structure directing agents through their geometry and as cations (once protonated). The alkali metals do not act as structure directing agents through their geometry but through their effective ionic radii. A wide selection of organic species was used

to investigate the effect of charge density and different structural features on the resultant product. Metals such as tin, bismuth and antimony were used because their lone pairs might have a structure directing effect. Chiral molecules were also tried without success, as they were not stable under the reaction conditions. These compounds would degrade into ammonia, which then formed known materials.

If the various metal sources, templates, water contents and temperature are combined, a wide selection of variables becomes available. The main synthetic strategy was to make materials at 100 °C with varying water contents, characterise them, then proceed to use exactly the same ratio of reagents but at higher temperatures. This would help to investigate the effect of concentration of the reagents in water and also the effect of temperature on the resultant structures. Once a range of structures had been synthesised and characterised, the metal/cation ratio was investigated, to see if any further new structures could be isolated from the reagents.

Fig. 3.1 Amines used as structure directing agents.

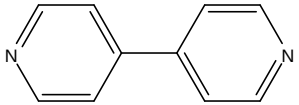

4-4’ bipyridyl

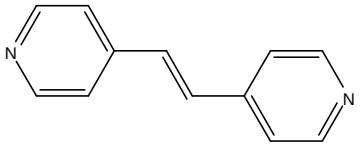

1,2 bis (4-pyridyl) ethene

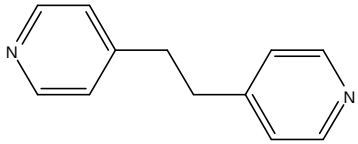

1,2 bis (4-pyridyl) ethane

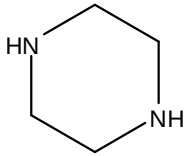

Piperazine

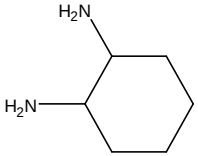

1,2 diamino cyclohexane

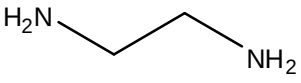

ethylene diamine

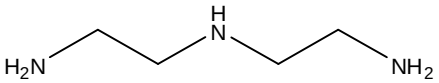

diethylene triamine

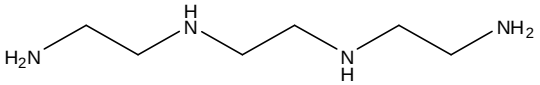

triethylene tetramine

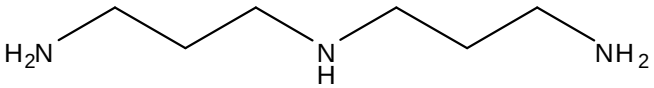

N-(3-aminopropyl)-1,3-propane diamine

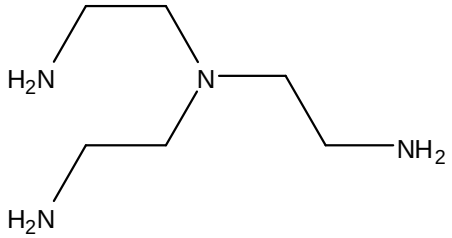

tris (2-aminoethyl) amine

4.0 Vanadium Oxyfluoride Materials

In this chapter, the crystal structures and hydrothermal chemistry of 29 vanadium (oxy)fluoride structures will be discussed. These materials have been synthesised and denoted from **V−1** to **V−29** (numbered in the chronological order in which they were syntheised). The structures range from the unusual neutral $[VOF_2]$ monomers to 2D $[VF_4]^-$ sheets. The crystallographic information for these compounds is presented in Tables 4.1 to 4.6. The synthetic conditions are given in at the end of the chapter, with the elemental analysis for each structure on the accompanying CD. Atomic co-ordinates are located in Appendix A (on the accompanying CD). Bond angles and hydrogen bonds are all contained in the appropriate CIF file (see enclosed CD).

Single crystals were analysed using either a Rigaku Mercury CCD equipped with confocal optics Mo-Kα radiation, a Rigaku SCX-Mini equipped with graphite monochromated Mo-Kα radiation or a Bruker SMART with silicon-monochromated synchrotron radiation (stations 9.8 or 16.2 at CCLRC Daresbury Laboratory), see the appropriate CIF for details. Intensity data were collected by the narrow frame method and corrected for Lorentz and polarization effects as well as absorption by Multi-Scan techniques. All structures were solved by direct methods and refined by full-matrix least-squares cycles in SHELX-97.[1] All non-hydrogen atoms were refined with anisotropic thermal parameters (except where stated). Hydrogen atoms attached to carbon and nitrogen atoms were located at geometrically calculated positions and refined with isotropic thermal parameters, while those attached to oxygen atoms were found, where possible, by Fourier techniques and refined isotropically.

The synthesis of materials **V−1** to **V−29** was carried out in a systematic manner which all started from a few simple reactions at 100°C. Simple linear amines were initially used to follow similar reactions to those done previously, to see if further novel compounds could be produced but with the variable water content as an additional, previously untested, variable. Once a few materials had been synthesised and characterised, temperature was introduced as a variable to see if more condensed structures could be produced at higher temperatures.

Once these reactions proved to be fruitful other cations were considered. By trying to duplicate a known titanium compound[2] with crown ether, sodium and vanadium oxide, novel compound **V−16** was synthesised. The absence of crown ether in the product meant that it did not need to be used in further reactions and furthermore other alkali metals may produce novel products as well.

Once a whole range of different products had been made, one further variable was still to be explored; cation ratio, i.e. the ratio of organic/inorganic cation to vanadium. Through the increase or decrease in cation ratio, three further new compounds were produced. A more

complete discussion of the synthetic aspects of the product produced is discussed in subsection 4.3

Table 4.1 Crystallographic Information for **V−1** to **V−4**.

Compound	**V−1**	**V−2**	**V−3**	**V−4**
Formula	$[C_6H_{20}N_3]_2[V_4O_4F_{14}]\cdot 2H_2O$	$[C_{12}H_{12}N_2]_{0.5}[VOF_3(H_2O)]$	$[C_{10}H_{10}N_2][V_2O_2F_6(H_2O)_2]$	$[C_4H_{12}N_2]_3[V_2O_2F_8]_2[VOF_4(H_2O)]_2$
Space Group	P-1 (2)	P-1 (2)	P-1 (2)	P-1 (2)
a/ Å	8.275(3)	3.794(3)	5.569(2)	6.891(2)
b/ Å	9.706(2)	10.408(6)	7.181(2)	8.406(2)
c/ Å	10.232(2)	11.333(6)	9.391(3)	12.706(4)
α/°	63.13(2)	63.38(4)	101.07(1)	77.57(1)
β/°	85.33(3)	81.98(3)	97.51(1)	84.46(1)
γ/°	78.59(2)	87.99(4)	95.11(1)	75.45(1)
V/ $Å^3$	718.6(4)	396.0(5)	362.9(2)	695.0(3)
Z	1	2	1	1
ρ_{calc}/ g cm^{-3}	1.937	1.963	2.023	2.084
μ/ mm^{-1}	1.392	1.269	1.378	1.453
Crystal Size/ mm	0.10 x 0.10 x 0.10	0.20 x 0.10 x 0.01	0.20 x 0.20 x 0.20	0.10 x 0.10 x 0.03
F(000)	424	234	220	438
Reflns Collected	4252	2363	2411	3892
Independent Reflns	2634	1459	1392	2394
R_{int}	0.0194	0.0815	0.0150	0.0255
Obsd data [$I > 2\sigma(I)$]	2223	597	1370	2049
Data/restraints/parameters	2634/2/196	1459/2/124	1392/0/117	2394/2/207
GOF on F^2	1.048	0.859	1.457	1.034
*R*1, *wR*2 [I > 2 *σ*(*I*)]	0.0309, 0.0796	0.0984, 0.2254	0.0317, 0.1376	0.0405, 0.0998
*R*1, *wR*2 (all data)	0.0330, 0.0806	0.1440, 0.2594	0.0321, 0.1381	0.0500, 0.1061

Table 4.2 Crystallographic Information for **V−5** to **V−9**.

Compound	**V−5**	**V−6**	**V−7**	**V−8**	**V−9**
Formula	$[C_6H_{22}N_4][VOF_4(H_2O)]_2 \cdot H_2O$	$[C_6H_{22}N_4][V_2O_2F_8]$	$[C_6H_{16}N_2]_2[V_2O_2F_8]$	$[C_4H_{16}N_3][VOF_5] \cdot H_2O$	$[C_8H_{26}N_4][V_2O_2F_8] \cdot H_2O$
Space Group	P-1 (2)	P 2_1/n (14)	P 2_1/c (14)	P 2_1/c (14)	P -1 (2)
a/ Å	8.884(4)	7.929(2)	11.645(3)	8.699(1)	7.633(3)
b/ Å	9.143(4)	10.591(3)	7.051(2)	12.558(1)	7.756(3)
c/ Å	11.951(5)	8.497(2)	12.490(3)	9.820(1)	8.501(3)
α/°	103.008(6)				78.19(1)
β/°	108.336(8)	97.834(6)	102.964(8)	100.011(3)	71.19(1)
γ/°	92.849(7)				72.19(2)
V/ $Å^3$	890.2(7)	706.9(3)	999.4(4)	1056.4(2)	450.4(3)
Z	2	2	2	4	1
ρ_{calc}/ g cm^{-3}	1.829	2.049	1.722	1.799	1.844
μ/ mm^{-1}	1.155	1.425	1.023	0.999	1.139
Crystal Size/ mm	0.10 x 0.10 x 0.10	0.20 x 0.15 x 0.10	0.10 x 0.10 x 0.10	0.04 x 0.04 x 0.04	0.10 x 0.10 x 0.10
F(000)	500	440	532	588	256
Reflns Collected	6087	4150	5259	6760	2513
Independent Reflns	4362	1290	2218	1851	2074
R_{int}	0.0284	0.0557	0.0154	0.0256	0.0221
Obsd data [$I > 2\sigma(I)$]	2793	1203	1767	1656	1487
Data/restraints/parameters	4362/6/249	1290/0/100	2218/0/127	1851/0/142	2074/2/124
GOF on F^2	1.004	1.602	1.140	1.291	1.187
*R*1, *wR*2 [I > 2 *σ*(*I*)]	0.0569, 0.1420	0.0418, 0.1325	0.0334, 0.0802	0.0338, 0.0714	0.0480, 0.1565
*R*1, *wR*2 (all data)	0.0787, 0.2354	0.0535, 0.1730	0.0383, 0.0826	0.0418, 0.0884	0.0496, 0.1619

Table 4.3 Crystallographic Information for **V−10** to **V−14**.

Compound	**V−10**	**V−11**	**V−12***	**V−13**	**V−14***
Formula	$[C_{10}H_{28}N_4][V_2O_2F_8]\cdot 2H_2O$	$[C_{10}H_{28}N_4][V_2O_2F_8]$	$[C_{12}H_{10}N_2]_{0.5}[VOF_3]$	$[C_6H_{22}N_4][VF_5(H_2O)]_2$	$[C_{10}H_8N_2][VF_3]$
Space Group	P 2_1/n (14)	P -1 (2)	C2/c (5)	P -1 (2)	I222 (23)
a/ Å	8.296(1)	7.730(3)	11.972(2)	8.660(2)	3.797(4)
b/ Å	8.625(2)	7.754(4)	15.663(3)	9.160(2)	10.769(7)
c/ Å	13.173(2)	7.786(6)	7.581(2)	11.640(3)	11.312(6)
α/°		89.741(7)		109.460(8)	
β/°	92.423(4)	73.218(5)	95.010(3)	93.610(3)	
γ/°		75.768(5)		91.860(8)	
V/ Å^3	941.8(3)	432.0(4)	1416.1(5)	867.5(4)	462.6(6)
Z	2	1	8	2	2
ρ_{calc}/ g cm^{-3}	1.856	1.885	2.027	1.831	1.896
μ/ mm^{-1}	1.095	1.178	2.485	1.186	0.966
Crystal Size/ mm	0.20 x 0.20 x 0.20	0.10 x 0.10 x 0.10	0.10 x 0.02 x 0.02	0.20 x 0.15 x 0.10	0.10 x 0.01 x 0.01
F(000)	540	250	856	484	264
Reflns Collected	6048	2968	5136	5930	3009
Independent Reflns	2005	2181	1506	3391	839
R_{int}	0.0163	0.0318	0.1054	0.0229	0.0509
Obsd data [$I > 2\sigma(I)$]	1733	1415	989	2826	713
Data/restraints/parameters	2005/2/133	2181/0/118	1506/0/98	3391/0/233	839/0/40
GOF on F^2	1.207	1.154	1.018	1.123	0.922
*R*1, *wR*2 [I > 2 $\sigma(I)$]	0.0384, 0.0942	0.0464, 0.1289	0.0712, 0.1625	0.0498, 0.1485	0.0379, 0.0848
*R*1, *wR*2 (all data)	0.0402, 0.0956	0.0602, 0.1973	0.1135, 0.1866	0.0748, 0.2400	0.0498, 0.0907

* = Collected at Daresbury Laboratories.

Table 4.4 Crystallographic Information for **V−15** to **V−19**.

Compound	**V−15***	**V−16**	**V−17**	**V−18**	**V−19***
Formula	$[C_4H_{12}N_2]_4[V_5O_3F_{20}]\cdot 2H_2O$	$Na_4V_2O_2F_8$	K_2VOF_4	$RbVOF_3$	$CsVOF_3$
Space Group	P -1 (2)	C2/c (15)	Pnma (62)	Pbam (55)	Pbam (55)
a/ Å	11.778(2)	12.662(4)	7.353(3)	8.559(4)	9.004(2)
b/ Å	12.524(2)	10.267(3)	5.611(2)	11.526(6)	11.703(2)
c/ Å	13.332(2)	6.717(2)	11.480(5)	3.859(2)	3.909(1)
α/°	86.675(2)				
β/°	84.838(2)	106.67(1)			
γ/°	67.417(2)				
V/ Å^3	1807.8(5)	836.5(4)	473.6(3)	380.7(3)	411.9(1)
Z	2	4	4	4	4
ρ_{calc}/ g cm^{-3}	1.961	3.000	3.102	3.654	4.142
μ/ mm^{-1}	2.463	2.554	3.833	15.221	19.915
Crystal Size/ mm	0.10 x 0.03 x 0.01	0.20 x 0.10 x 0.10	0.18 x 0.18 x 0.02	0.10 x 0.02 x 0.02	0.10 x 0.01 x 0.01
F(000)	1070	712	420	380	452
Reflns Collected	13387	2128	2764	2152	2846
Independent Reflns	7374	928	633	580	414
R_{int}	0.0346	0.0110	0.0242	0.0436	0.0419
Obsd data [$I > 2\sigma(I)$]	5955	775	510	340	323
Data/restraints/parameters	7374/0/481	928/0/73	633/0/46	580/0/37	414/0/37
GOF on F^2	1.019	1.176	1.216	1.134	0.997
*R*1, *wR*2 [I > 2 *σ*(*I*)]	0.0651, 0.1668	0.0191, 0.0529	0.0421, 0.0787	0.0607, 0.1414	0.0384, 0.0912
*R*1, *wR*2 (all data)	0.0776, 0.1755	0.0193, 0.0531	0.0484, 0.0808	0.0813, 0.1572	0.0458, 0.0958

* = Collected at Daresbury Laboratories.

Table 4.5 Crystallographic Information for **V−20** to **V−24**.

Compound	**V−20**	**V−21***	**V−22***	**V−23**	**V−24**
Formula	$[C_4H_{16}N_3][VF_6]$	KVF_4	$[C_4H_{12}N_2][VF_5]\cdot H_2O$	$NaVF_4$	NH_4VOF_3
Space Group	P 2_1/c (14)	Pnma (62)	P 2_1/n (14)	P 2_1/a (14)	Pbam (55)
a/ Å	8.629(1)	12.283(2)	11.447(3)	7.542(4)	8.532(4)
b/ Å	10.674(2)	7.591(1)	5.910(2)	5.292(3)	11.651(5)
c/ Å	10.777(1)	7.744(1)	13.580(6)	7.901(4)	3.836(1)
α/°					
β/°	96.651(5)		91.54(2)	101.56(2)	
γ/°					
V/ Å^3	985.9(3)	722.0(2)	918.4(6)	308.9(3)	381.3(3)
Z	4	8	4	4	4
ρ_{calc}/ g cm^{-3}	1.827	3.055	1.809	3.224	2.473
μ/ mm^{-1}	1.065	6.708	2.000	3.266	2.527
Crystal Size/ mm	0.40 x 0.40 x 0.40	0.50 x 0.50 x 0.02	0.04 x 0.005 x 0.005	0.30 x 0.05 x 0.02	0.60 x 0.05 x 0.03
F(000)	552	624	504	280	276
Reflns Collected	9622	4931	6465	1081	2430
Independent Reflns	2173	838	1936	688	536
R_{int}	0.0497	0.0228	0.0535	0.0200	0.0372
Obsd data [$I > 2\sigma(I)$]	2088	615	1612	370	566
Data/restraints/parameters	2173/0/127	838/48/61	1936/0/118	688/0/55	536/10/54
GOF on F^2	1.113	1.170	1.005	1.212	1.202
*R*1, *wR*2 [I > 2 *σ*(*I*)]	0.0351, 0.1015	0.0290, 0.0834	0.0562, 0.1305	0.0467, 0.1499	0.0451, 0.1210
*R*1, *wR*2 (all data)	0.0363, 0.1026	0.0394, 0.0894	0.0673, 0.1393	0.0476, 0.1513	0.0464, 0.1225

* = Collected at Daresbury Laboratories.

Table 4.6 Crystallographic Information for **V−25** to **V−29**.

Compound	**V−25**	**V−26**	**V−27**	**V−28**	**V−29**
Formula	$[C_{12}H_{12}N_2]_{0.5}[VOF_3]$	$[C_4H_{12}N_2][VOF_4(H_2O)]$	$[C_4H_{13}N_3][VOF_2]$	$[C_4H_{12}N_2]_3[V_7F_{27}]$	$K_5V_3F_{14}$
Space Group	C2/m (12)	P -1 (2)	Pbcm (57)	R -3c (167)	P4/mnc (128)
a/ Å	12.144(3)	5.718(1)	6.759(2)	17.367(2)	7.600(2)
b/ Å	15.668(4)	8.246(1)	10.212(2)	17.367(2)	7.600(2)
c/ Å	3.827(1)	9.811(1)	11.683(3)	19.604(2)	11.679(3)
α/°		97.444(3)			
β/°	93.873(7)	101.073(3)			
γ/°		104.340(3)			
V/ Å^3	726.5(3)	432.1(1)	806.4(3)	5120.6(9)	674.6(3)
Z	4	2	4	6	2
ρ_{calc}/ g cm^{-3}	1.966	1.914	1.714	2.136	3.024
μ/ mm^{-1}	1.365	1.187	1.214	1.997	3.727
Crystal Size/ mm	0.12 x 0.05 x 0.05	0.30 x 0.25 x 0.05	0.08 x 0.08 x 0.08	0.17 x 0.15 x 0.10	0.06 x 0.06 x 0.02
F(000)	424	254	428	3108	580
Reflns Collected	3746	4505	4950	16123	3681
Independent Reflns	828	1970	771	1316	434
R_{int}	0.1581	0.0595	0.0381	0.0781	0.0109
Obsd data [$I > 2\sigma(I)$]	612	1790	678	977	396
Data/restraints/parameters	828/16/67	1970/2/126	771/0/55	1316/0/89	434/0/32
GOF on F^2	1.225	1.110	1.086	1.346	1.230
*R*1, *wR*2 [I > 2 $\sigma(I)$]	0.1320, 0.2089	0.0446, 0.1107	0.0379, 0.0848	0.1296, 0.1909	0.0310, 0.0853
*R*1, *wR*2 (all data)	0.1749, 0.2236	0.0493, 0.1128	0.0440, 0.0883	0.1749, 0.2072	0.0332, 0.0866

4.1 New Oligomers and Polymeric Compounds

The structures in this sub-section are novel inorganic oligomers and polymeric compounds i.e. the inorganic moiety of the structure has not previously been reported. In the last 20 years two significant reviews have been published which, as of 2000, methodically cover most known transition metal oxyfluorides. These reviews are by Hagenmuller[3] and by Nakajima, Žemva and Tressaud.[4]

4.1.1 Monomers

$[C_6H_{22}N_4][VOF_4(H_2O)]_2 \cdot H_2O$ (V−5) consists of two $[VOF_4(H_2O)]^{2-}$ octahedra, which are hydrogen bonded to one another to form a dimer (see Fig. 4.1 − left). These two monomers are then connected to the rest of the structure through hydrogen bonding from the protonated amine template, triethylene tetramine, and the water molecule to form the 3D structure. The hydrogen bonded dimer in the asymmetric unit also shows *inter*-dimer bonding to a neighbouring hydrogen-bonded dimer, to form a tetramer (see Fig 4.1 − right). The two $[VOF_4(H_2O)]^{2-}$ octahedra are different from one another in the fact that one is a *trans* monomer and the other is a *cis* monomer. The *trans* monomer has been previously reported[5] but the *cis* monomer is novel. In the *trans* monomer, the aqua group is directly opposite the V=O group. This causes the bond to the aqua group to lengthen, due to a *trans* effect. This effect is also seen in the *cis* variant but with the aqua group being *cis* to the V=O, it is a V−F bond which is lengthened (see Table 4.7). The compound is also paramagnetic down to 2 K and from a plot of χ^{-1} vs. T for above 150K (see Fig 4.2) a value for μ_{eff} (μ_B) = 2.03(2) BM could be extracted which is comparable to the theoretical value of μ_{eff} (μ_B) = 1.79 BM − per V^{4+} ion.

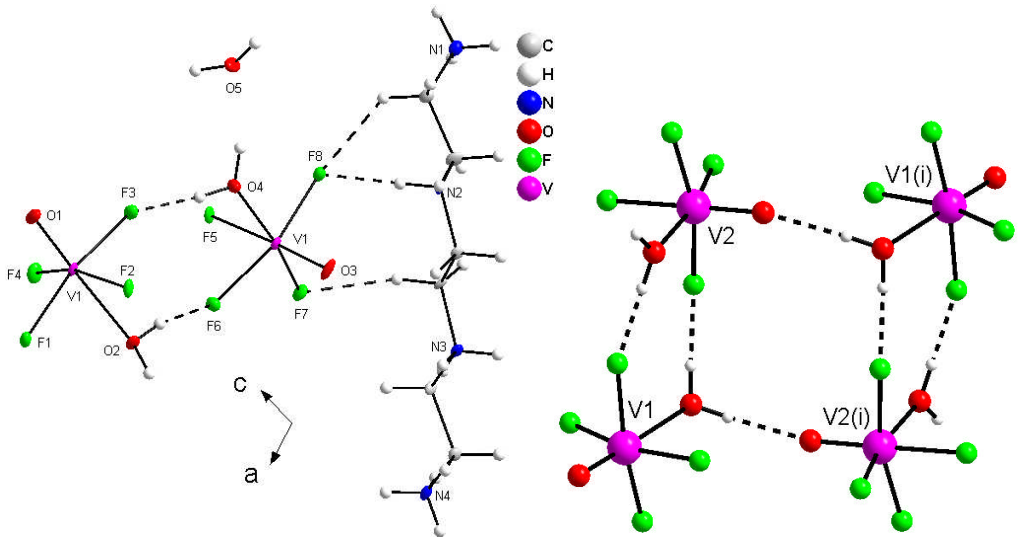

Fig 4.1 The asymmetric unit viewed down the *b*-axis (left) and the hydrogen bonded tetramer in **V−5**, symmetry operator (i) *–x*, 1−*y*, −*z*.

Bond	Bond Length (Å)	s_{ij}	Bond	Bond Length (Å)	s_{ij}
V1−O1	1.606(3)	1.600	V2−O3	1.641(3)	1.472
V1−O2	2.305(3)	0.245	V2−O4	2.035(3)	0.512
V1−F1	1.930(2)	0.534	V2−F5	2.084(3)	0.356
V1−F2	1.938(3)	0.531	V2−F6	1.958(2)	0.499
V1−F3	1.960(2)	0.497	V2−F7	1.905(3)	0.582
V1−F4	1.929(3)	0.539	V2−F8	1.905(2)	0.575
		∑V1 = **3.95**			∑V2 = **4.00**

Table 4.7 Selected bond lengths and bond valence sums for **V−5**.

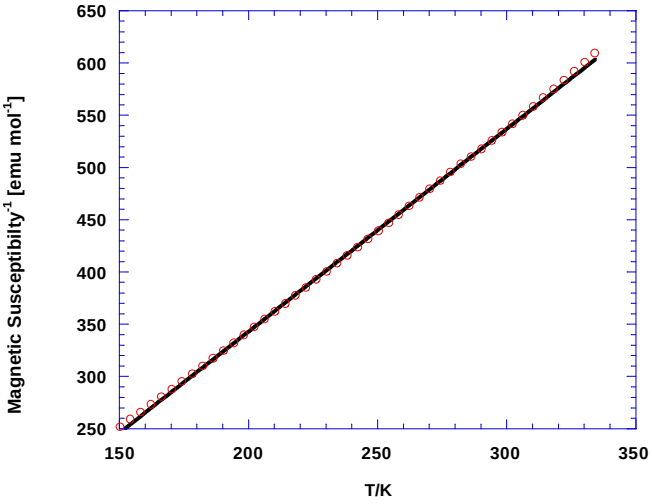

Fig 4.2 χ^{-1} vs. T for **V−5** above 150K.

$[C_4H_{13}N_3][VOF_2]$ (V−27) is a new neutral monomer compound, which is quite unusual as the inorganic moieties are usually negatively charged. The building unit of the structure consists of a single octahedral vanadium centre situated on a mirror plane, to which the diethylene triamine is bonded along with two V−F bonds and one vanadyl bond (see Fig 4.3 and Table 4.8). The structure is held together through hydrogen bonding to other neutral clusters to form the 3D network (see Fig 4.4). The sample is also paramagnetic down to 2 K and from a plot of χ^{-1} vs. T for above 150K (see Fig 4.5), a value for μ_{eff} (μ_B) = 1.47 (1) BM, which is comparable to the theoretical value of μ_{eff} (μ_B) = 1.79 BM, can be extracted.

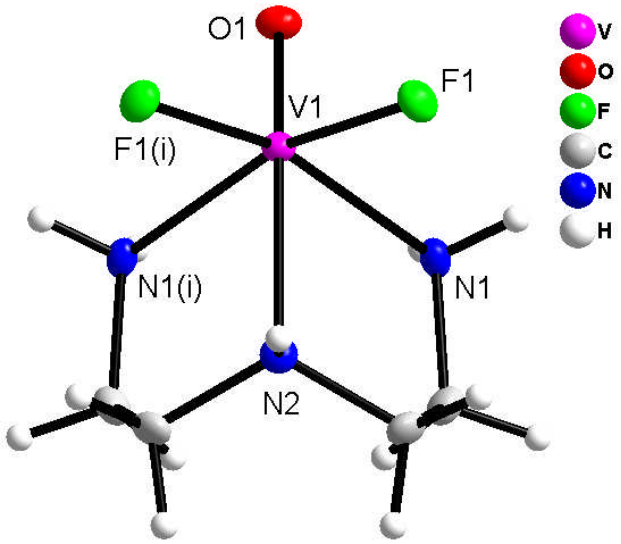

Fig 4.3 The building unit in **V−27**, symmetry operator (i) *x*, *y*, ½−*z*.

Bond	Bond Length (Å)	s_{ij}
V1−O1	1.621(2)	1.537
V1−F1	1.908(2)	0.570
V1−F1’	1.908(2)	0.570
V1−N1	2.145(2)	0.501
V1−N1’	2.145(2)	0.501
V1−N2	2.291(3)	0.338
		∑V1 = **4.02**

Table 4.8 Bond lengths and bond valence sums for **V−27**.

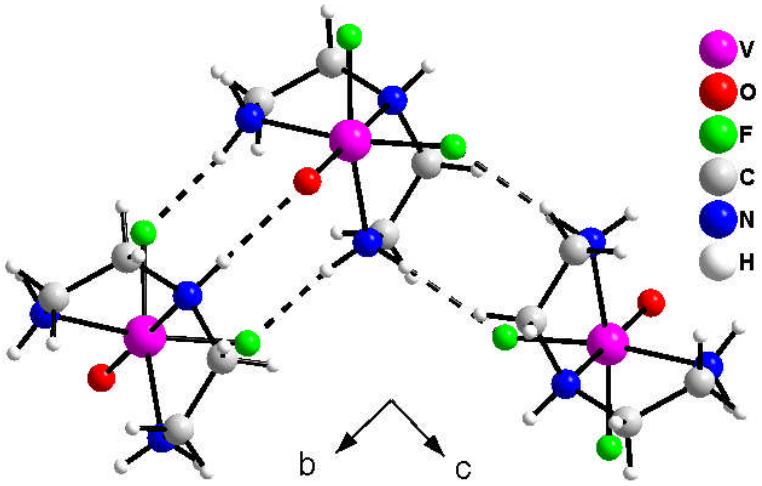

Fig 4.4 The *inter*-monomer hydrogen bonding in **V−27**.

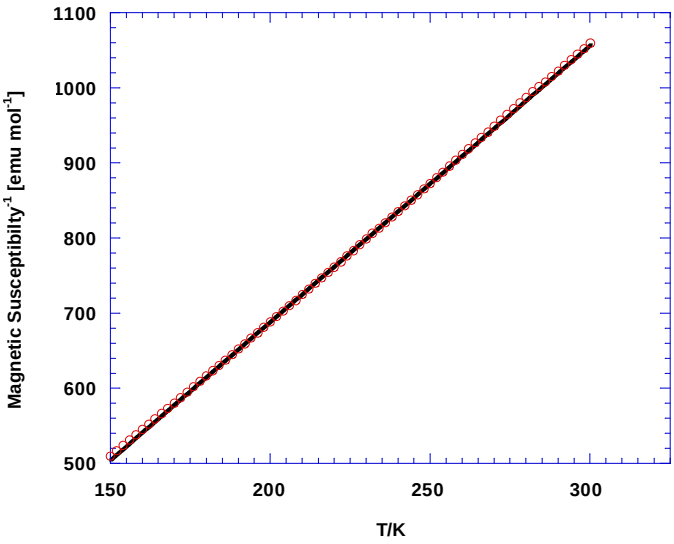

Fig 4.5 χ^{-1} vs. T for **V−27** above 150K.

4.1.2 Dimers

$[C_6H_{22}N_4][V_2O_2F_8]$ (V−6), **$[C_6H_{16}N_2]_2[V_2O_2F_8]$ (V−7)**, **$[C_8H_{26}N_4][V_2O_2F_8]\cdot H_2O$ (V−9)**, **$[C_{10}H_{28}N_4][V_2O_2F_8]\cdot 2H_2O$ (V−10)**, **$[C_{10}H_{28}N_4][V_2O_2F_8]$ (V−11) and $Na_4V_2O_2F_8$ (V−16)** are all structures based on the $[V_2O_2F_8]^{4-}$ dimer shown below in Fig 4.6, which is previously unreported. Each dimer shows the similar degree of lengthening of the V−F bond caused by the *trans* effect from the V=O unit (which range from 2.117 Å to 2.204 Å) and contains one unique vanadium atom situated about an inversion centre (see Tables 4.9 − 4.14)

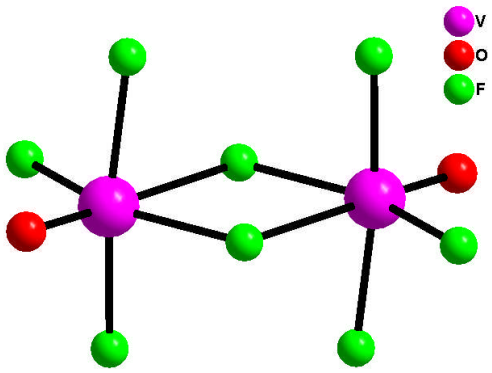

Fig 4.6 The $[V_2O_2F_8]^{4-}$ dimer in **V−6**, **V−7**, **V−9**, **V−10**, **V−11** and **V−16.**

The structure of **$[C_6H_{22}N_4][V_2O_2F_8]$ (V−6)** consists of the V^{4+} dimer (see Table 4.9) shown in Fig 4.6, completely surrounded by the tetraprotonated amine template, triethylene tetramine. It is through hydrogen bonding from the non-bridging fluorine bonds, e.g. F4 (see Fig 4.7), to the template that the complete structure is composed.

Bond	Bond Length (Å)	s_{ij}
V1−O1	1.611(3)	1.596
V1−F1	1.973(3)	0.478
V1−F2	1.969(2)	0.483
V1−F2’	2.157(2)	0.291
V1−F3	1.918(2)	0.555
V1−F4	1.917(2)	0.556
		∑V1 = **3.96**

Table 4.9 Selected bond lengths and bond valence sums for **V−6**.

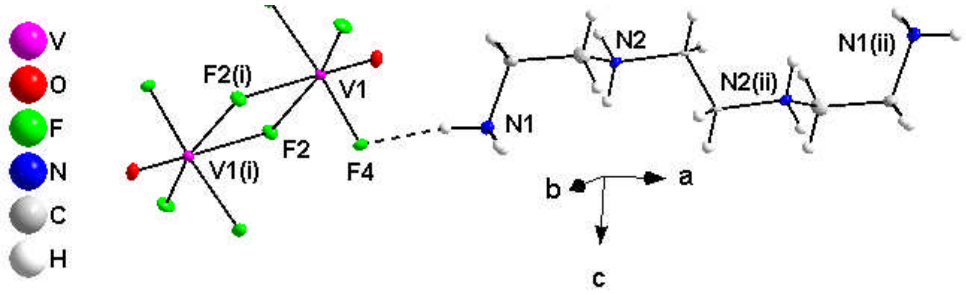

Fig 4.7 The building unit in **V−6**. Symmetry operators (i) *–x*, 1-*y*,1-*z*, (ii) 2-*x*, -*y*, 1-*z*.

$[C_6H_{16}N_2]_2[V_2O_2F_8]$ (V−7) is similar in structure to **V−6**. The structure again consists of the dimer in Fig 4.6 (see Table 4.10), but is surrounded by a different template, *trans* diamino cyclohexane (see Fig 4.8). A 3D network of hydrogen bonds holds the structure together.

Bond	Bond Length (Å)	s_{ij}
V1−O1	1.597(2)	1.640
V1−F1	1.943(1)	0.519
V1−F2	1.943(1)	0.519
V1−F3	1.944(1)	0.517
V1−F4	1.969(1)	0.483
V1−F4’	2.186(1)	0.269
		∑V1 = **3.95**

Table 4.10 Selected bond lengths and bond valence sums for **V−7**.

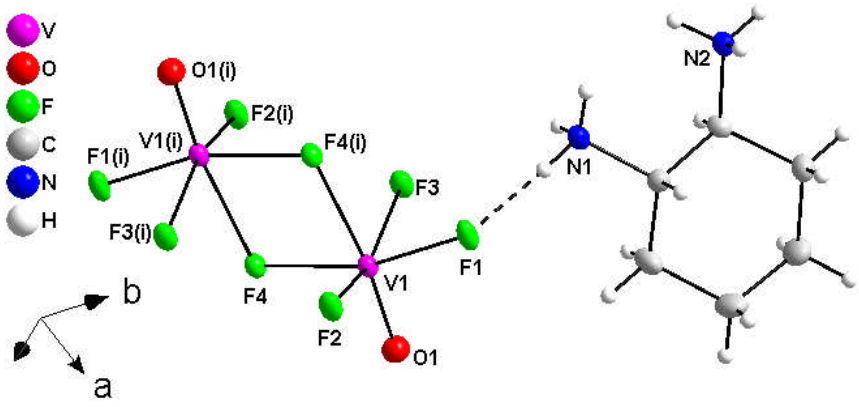

Fig 4.8 The building unit in **V−7**. Symmetry operator (i) *–x*, *–y*, *-z*.

$[C_8H_{26}N_4][V_2O_2F_8]\cdot H_2O$ (V−9) uses 1,2 bis (3-aminopropylamino) ethane (see Fig 3.1) as template, which is in the *syn* conformation. The water molecules link the V^{4+} dimers together (see Fig 4.9 and Table 4.11) to form a hydrogen-bonded chain, see Fig. 4.9. These chains are then completely surrounded by the linear template running parallel, to link the structure together through further hydrogen bonding.

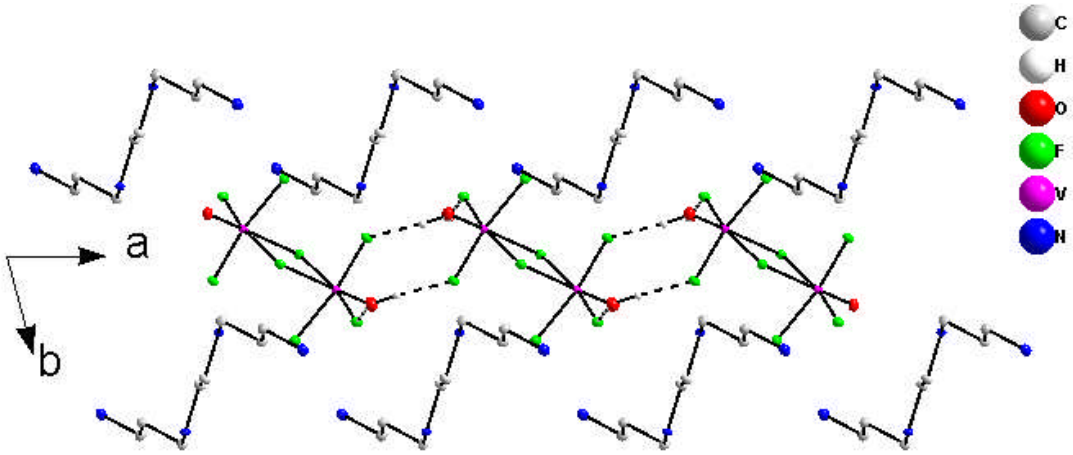

Fig 4.9 The hydrogen bonded chain in **V−9**. Some hydrogen atoms have been removed for clarity.

Bond	Bond Length (Å)	s_{ij}
V1−O1	1.625(2)	1.520
V1−F1	1.918(2)	0.555
V1−F2	1.911(2)	0.565
V1−F3	1.958(2)	0.498
V1−F4	2.018(2)	0.423
V1−F4’	2.117(2)	0.324
		∑V1 = **3.89**

Table 4.11 Selected bond lengths and bond valence sums for **V−9**.

Another hydrogen-bonded chain, again linked through water molecules (see Fig 4.10), is seen in **$[C_{10}H_{28}N_4][V_2O_2F_8]\cdot 2H_2O$ (V−10)**. A similar conformation to **V−9** occurs with the protonated template, cyclam, surrounding the linear chains. The template holds the structure together through hydrogen bonding and as such is located close to the fluorine atom which is not used for *intra*-chain hydrogen bonding.

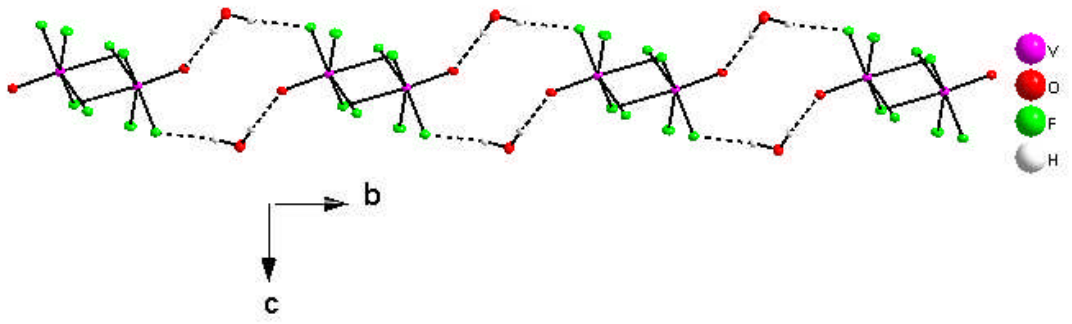

Fig 4.10 The hydrogen bonded chain in **V−10**.

Bond	Bond Length (Å)	s_{ij}
V1−O1	1.629(2)	1.504
V1−F1	1.891(2)	0.597
V1−F2	1.917(1)	0.556
V1−F3	1.950(1)	0.509
V1−F4	1.959(1)	0.497
V1−F4’	2.204(2)	0.256
		∑V1 = **3.92**

Table 4.12 Selected bond lengths and bond valence sums for **V−10**.

$[C_{10}H_{28}N_4][V_2O_2F_8]$ (V−11) is very similar to structure **V−10** (it has the same template) only in this case, without the water molecules. As a result of this the hydrogen bonded chains are not present. Instead the V^{4+} dimers (see Fig 4.6 and Table 4.13), are each surrounded by the protonated template and held together as a layer (see Fig 4.11). These layers are then staggered and held together by further hydrogen bonding to form an extensive 3D hydrogen bonding network.

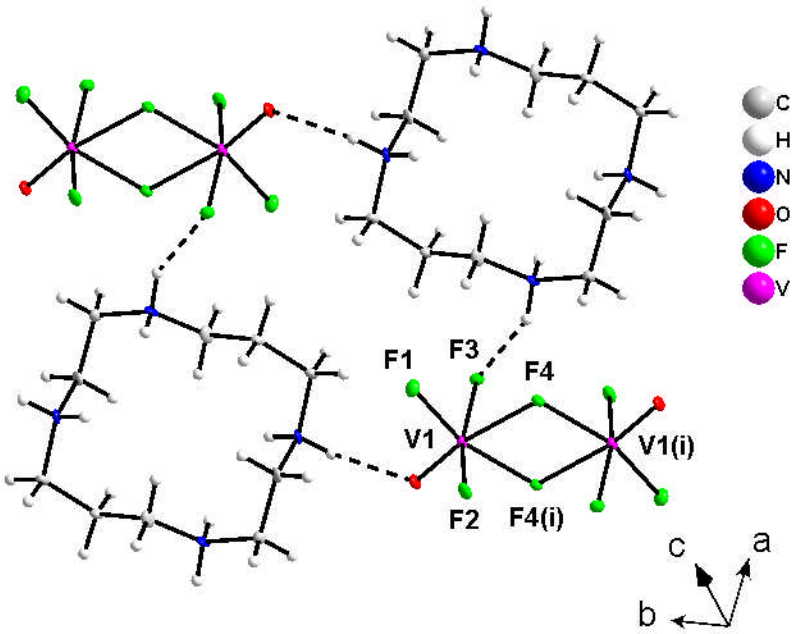

Fig 4.11 The hydrogen bonding in **V−11**. Symmetry operator (i) 1−*x*, −*y*, −*z*.

Bond	Bond Length (Å)	s_{ij}
V1−O1	1.610(3)	1.583
V1−F1	1.868(2)	0.635
V1−F2	1.981(2)	0.468
V1−F3	1.932(2)	0.534
V1−F4	2.017(2)	0.425
V1−F4’	2.166(3)	0.284
		∑V1 = **3.93**

Table 4.13 Selected bond lengths and bond valence sums for **V−11**.

$Na_4V_2O_2F_8$ (V−16) is a simple structure consisting of a dimer (see Fig 4.6) which is enclosed by sodium ions. These cations fill the interstitial voids and charge balance the negative dimer (see Fig 4.12). The structure is also paramagnetic down to 2 K and from a plot of χ^{-1} vs. T above 150K (see Fig 4.13), a value for μ_{eff} (μ_B) = 1.27 (3) BM can be extracted, which is

comparable to the theoretical value of μ_{eff} (μ_B) = 1.79 BM, but is unusually low. The V^{4+} oxidation state is also confirmed by BVS (see Table 4.14).

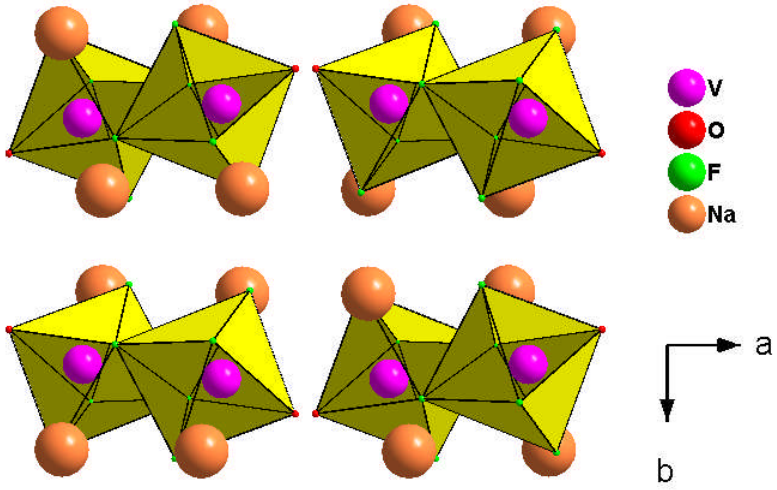

Fig 4.12 The interstitial packing in **V−16**.

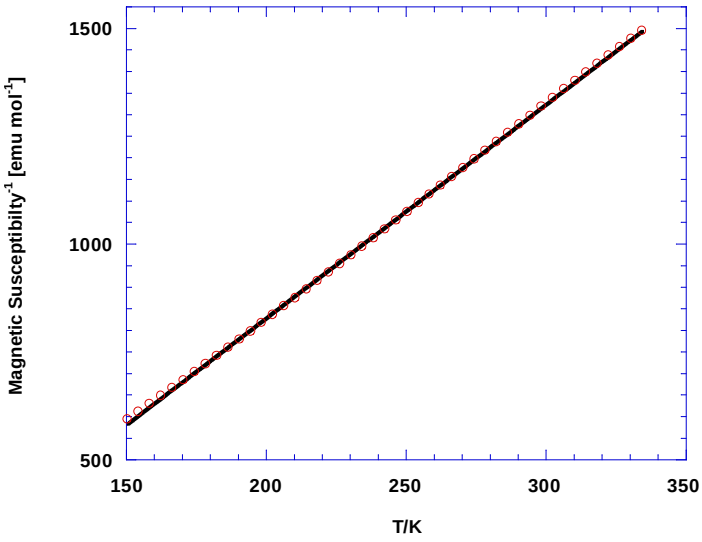

Fig 4.13 χ^{-1} vs. T for **V−16** above 150K.

Bond	Bond Length (Å)	s_{ij}
V1−O1	1.612(1)	1.575
V1−F1	1.903(1)	0.578
V1−F2	1.948(1)	0.512
V1−F3	1.941(1)	0.521
V1−F4	1.9698(1)	0.482
V1−F4’	2.214(1)	0.249
		∑V1 = **3.92**

Table 4.14 Selected bond lengths and bond valence sums for **V−16**.

4.1.3 Tetramers

$[C_6H_{20}N_3]_2[V_4O_4F_{14}]\cdot 2H_2O$ (V−1) consists of two distinct vanadium sites (both V^{4+}, see Table 4.15) which sit about an inversion centre, the protonated template *N*-(3-aminopropyl)-1,3 diaminopropane and a water molecule (see Fig 4.14). The $[V_4O_4F_{14}]^{6-}$ tetramer, as seen in Fig 4.15, could be described as an edge sharing dimeric unit, capped by two monomers situated around an inversion centre at the centre of the tetramer.

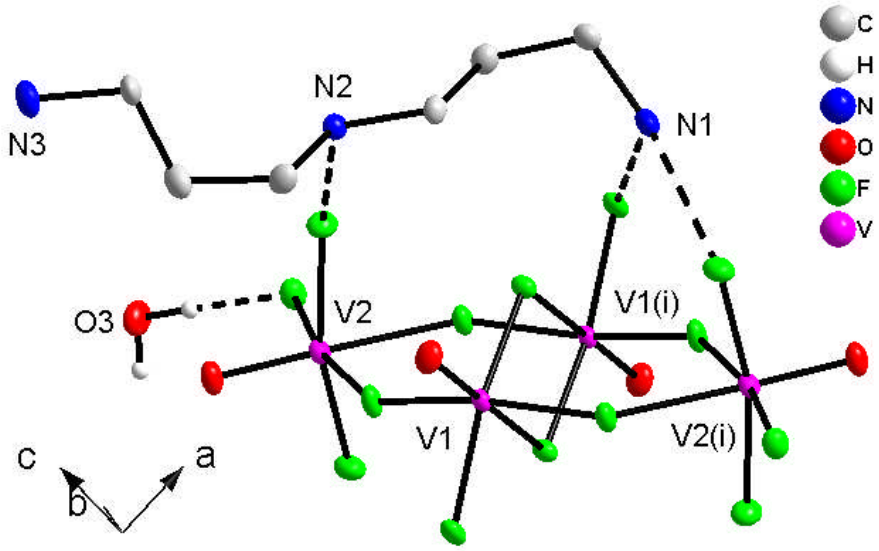

Fig 4.14 The building unit for **V−1**, some hydrogen atoms have been omitted for clarity. Symmetry operator (i) 1−*x*, −*y*, −*z*.

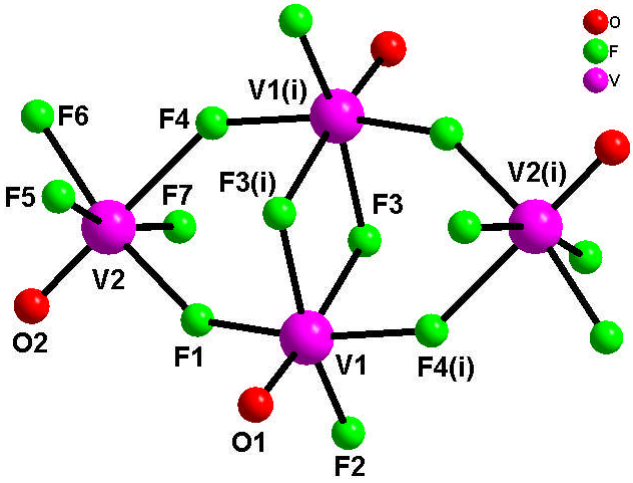

Fig 4.15 The anionic $[V_4O_4F_{14}]^{6-}$ tetramer in **V−1**. Symmetry operator (i) 1−*x*, −*y*, −*z*.

Bond	Bond Length (Å)	s_{ij}	Bond	Bond Length (Å)	s_{ij}
V1−O1	1.595(2)	1.667	V2−O2	1.619(2)	1.566
V1−F1	1.985(2)	0.463	V2−F1	1.980(2)	0.469
V1−F2	1.935(2)	0.530	V2−F4	2.144(2)	0.301
V1−F3	1.942(2)	0.520	V2−F5	1.930(2)	0.537
V1−F3’	2.150(2)	0.296	V2−F6	1.967(2)	0.486
V1−F4	1.925(2)	0.544	V2−F7	1.926(2)	0.543
		∑V1 = **4.02**			∑V2 = **3.90**

Table 4.15 Selected bond lengths and bond valence sums for **V−1**.

The tetramers are then held together through strong hydrogen bonds (2.39 Å from the water molecule to the terminal fluorine atoms, F3 and F4) to form chains (see Fig 4.16). The chains are held close together through the linear template which hydrogen bonds to the only other non-bridging fluorine atom, F2.

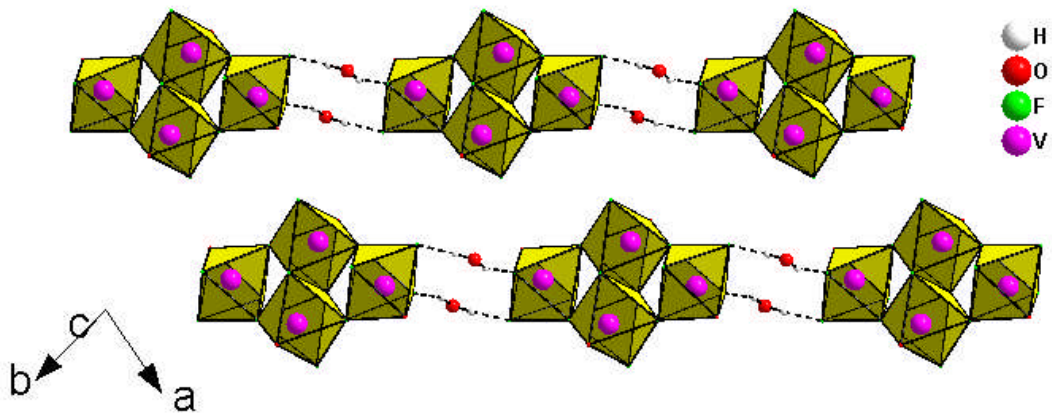

Fig 4.16 The hydrogen bonded chains in **V−1**.

V−1 also shows some interesting magnetic properties. The tetramer appears antiferromagnetic at low temperatures, with a Néel tempertature of approximately 20 K, as shown in Fig 4.17 (data collected by Prof. A. Harrison of the University of Edinburgh). The broad maximum in χ vs. T is a signature of low dimensional antiferromagnetic ordering. The structure is the only 0D material to show magnetic ordering found in this work. A search through the literature finds that it is the only vanadium oxyfluoride oligomer to show long range magnetic ordering and that, in general, magnetism in transition metal (oxy)fluoride oligomers is quite unusual with only a few examples showing antiferromagnetic interactions.[6−8] In these aquafluorometallate (III) compounds (Mn, Cr and Fe), which are similar to the structure of **V−13**, the monomers are hydrogen bonded together to form an anionic chain which shows antiferromagnetic properties through the O−H···F hydrogen bond. A similar pathway must occur in **V−1** where the antiferromagnetic interaction is mediated by the water molecule in between the tetramers.

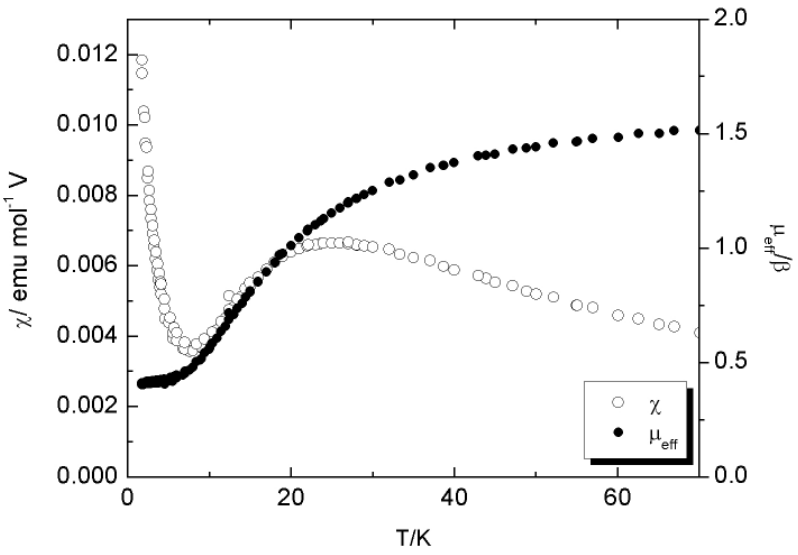

Fig 4.17 A graph of χ and μ_{eff} vs. T for **V−1** below 70 K.

4.1.4 Chain Structures

$[C_{12}H_{12}N_2]_{0.5}[VOF_3(H_2O)]$ (V−2) is a linear chain structure (which contains V^{4+}, see Table 4.16) held together by the protonated *trans* 1,2 bis (4-pyridyl) ethylene template. The building unit can be seen below in Fig 4.18 - left. The chain hydrogen bonds to the template through the non-bridging fluorine atom, F2, whilst the other non-bridging fluorine atom, F3, hydrogen bonds to another chain running parallel to it (see Fig 4.9 – right). These chains are held together through hydrogen bonding from the aqua group to F3 to form a dimeric chain, which is surrounded by the template species to form the 3D structure. The structure is also paramagnetic down to 2 K which can be seen from a plot of χ vs. T for below 60K (see Fig 4.19 − data collected by Prof. A. Harrison of the University of Edinburgh).

Bond	Bond Length (Å)	s_{ij}
V1−O1	1.600(7)	1.627
V1−O2	2.269(7)	0.267
V1−F1	1.844(5)	0.608
V1−F1'	1.991(6)	0.455
V1−F2	1.912(5)	0.564
V1−F3	1.919(5)	0.533
		∑V1 = **4.07**

Table 4.16 Selected bond lengths and bond valence sums for **V−2**.

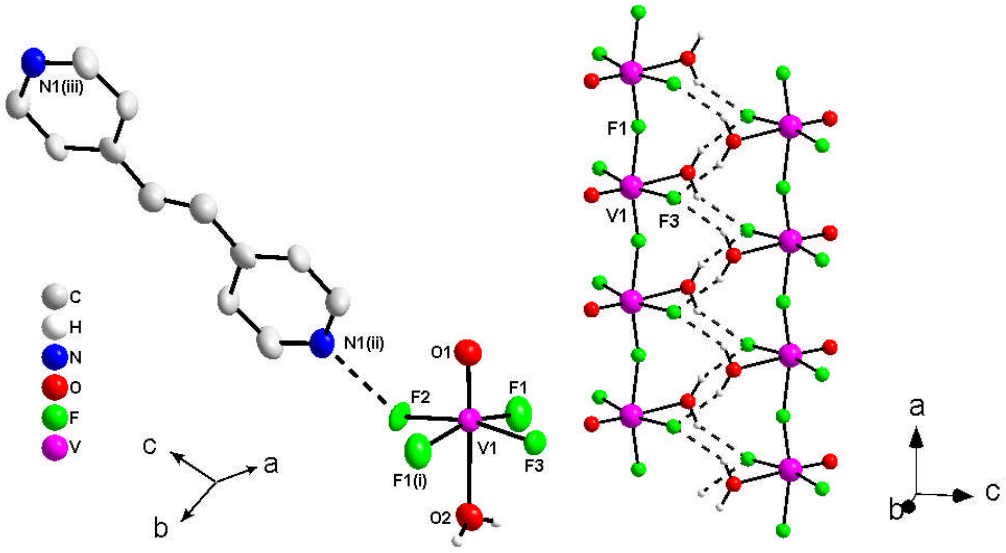

Fig 4.18 The building unit (left) and the hydrogen bonded chains (right) in **V−2**, some hydrogen atoms have been omitted for clarity. Symmetry operators (i) −1+*x*, *y*, *z*, (ii) −*x*, 1−*y*, 1−*z*, (iii) −2+*x*, −1+*y*, 1+*z*.

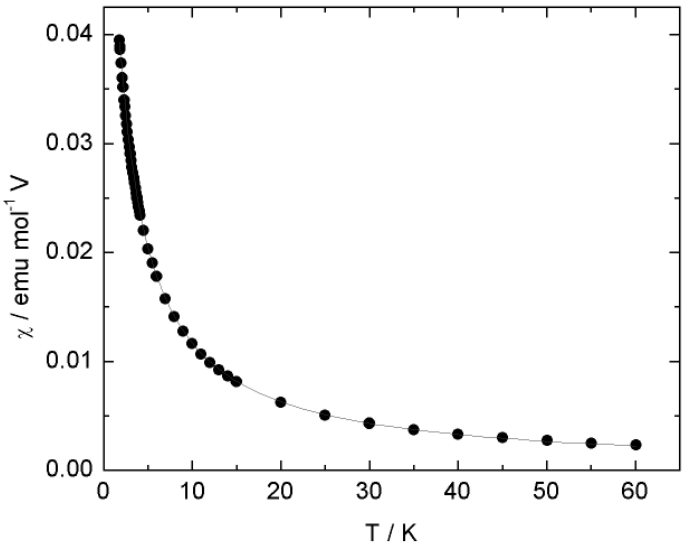

Fig 4.19 A graph of χ vs. T for **V−2** below 60 K.

$[C_{12}H_{10}N_2]_{0.5}[VOF_3]$ (V−12) is a ladder-like structure consisting of corner and edge sharing $[VOF_1F_{4/2}]$ octahedra (see Fig 4.20 – top), which shares many similarities with $(VO)_2P_2O_7$[9,10] (see Fig 4.21) but the template in this case is protonated *trans* 1,2 bis (4-pyridyl) ethylene. Further similar ladder structures have been made with a variety of different templates and will be discussed later (see **V−18**, **V−19**, **V−24** and **V−25**). The structure displays octahedral tilting along its *c* axis (see Fig 4.20 – bottom) which causes a doubling of the *c* axis in comparison to other structures (see **V−18**, **V−19** and **V−24**).

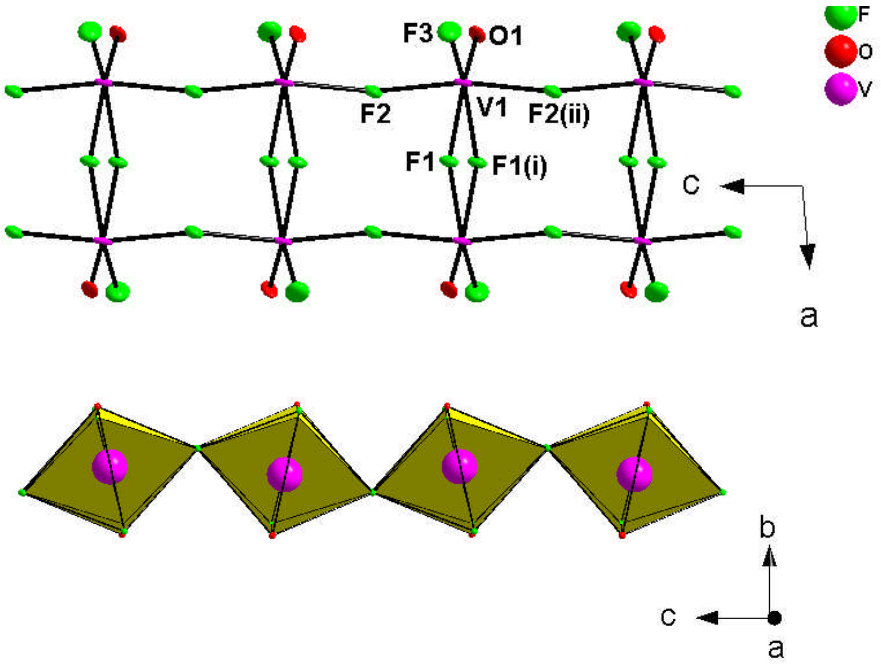

Fig 4.20 The ladder chain (top) and the octahedral tilting (bottom) in **V−12**. Symmetry operators (i) 1-*x*, 1-*y*, 1-*z*, (ii) *x*, 1-*y*, -½+*z*.

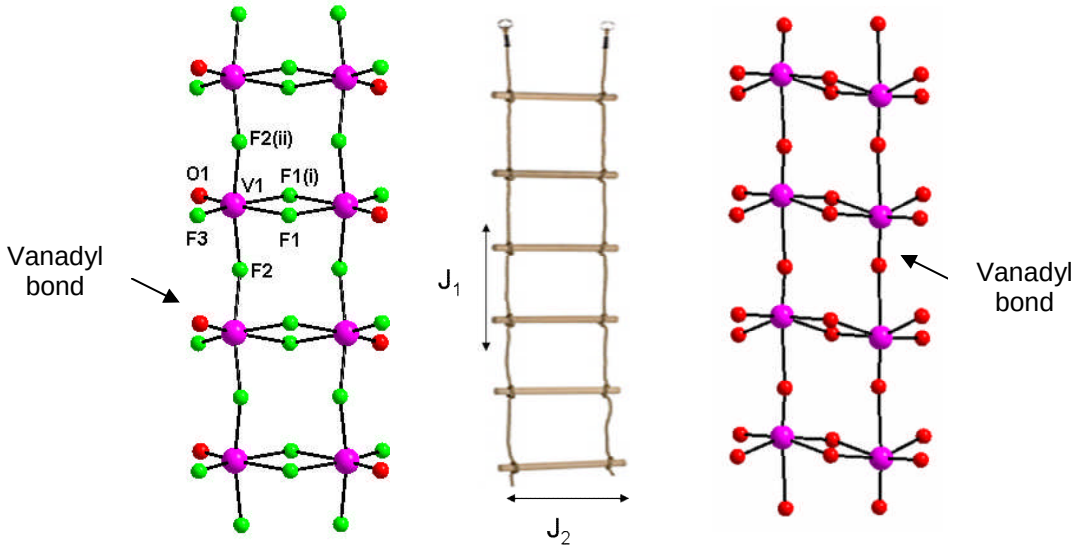

Fig 4.21 A pictorial comparison of the chain structures in **V−12** (left) and $(VO)_2P_2O_7$ (right).

In light of the comparison to $(VO)_2P_2O_7$, which is known for its interesting and well studied magnetic properties,[9,10] magnetic susceptibility data were collected and analysed. The data could be fitted with a simple Heisenberg model,[11] which proved a good fit (as seen below in Fig 4.22). The model was fitted for interactions along the rails of the ladder, J_1, only (see Fig 4.21). Interactions along the rungs of the ladder, J_2 (see Fig 4.21), were considered using the Bleaney-Bowers dimer model[12] but resulted in a value of effectively zero, confirming the choice of rail-only interactions, i.e. J_1. A further, more complex model, the Ising ½ spin ladder model,[13] which uses both sets of interactions, was tried but only proved further the rail only interactions, J_1, were present. The derived magnetic parameters were as follows, μ_{eff} (μ_B) = 1.91(5) BM(which is comparable to the theoretical value of 1.79 BM for V^{4+} which is also confirmed by BVS, (see Table 4.17), Θ = −27.4(7) K and J_1 = −20.1(3) K.

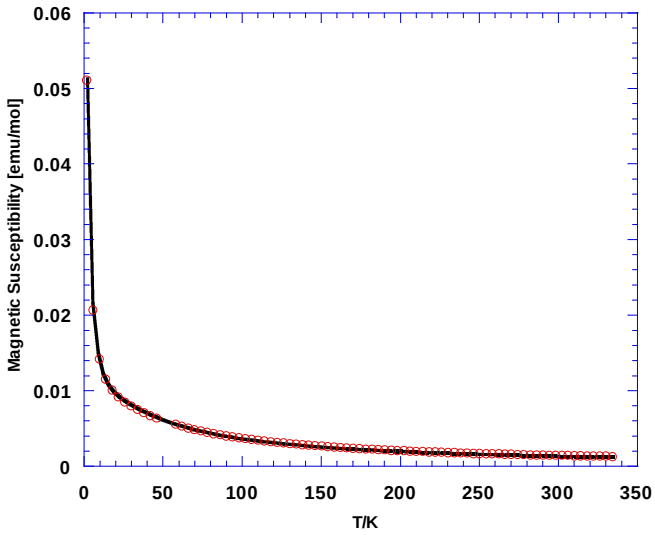

Fig 4.22 The Heisenberg fit (solid line) for χ vs. T for **V−12**.

Bond	Bond Length (Å)	s_{ij}
V1−O1	1.690(4)	1.275
V1−F1	2.022(3)	0.419
V1−F1’	2.108(3)	0.332
V1−F2	1.967(3)	0.486
V1−F2’	1.968(3)	0.485
V1−F3	1.789(4)	0.786
		∑V1 = **3.78**

Table 4.17 Selected bond lengths and bond valence sums for **V−12**.

This proved interesting as the interactions in $(VO)_2P_2O_7$ are along the rungs of the ladder. A comparison of the two structures may reveal why this difference occurs. In **V−12**, the short vanadyl bond lies *exo* to the ladder but in $(VO)_2P_2O_7$ this bond runs along the rail of the ladder (see Fig 4.21) with both sets of interactions running perpendicular to their respective vanadyl bonds. The d_{xy} orbital is the reason for the difference. This orbital is aligned perpendicular to the vanadyl bond and it is through this the interactions occurs, hence the difference occurs. The observation in $(VO)_2P_2O_7$ would have at first seemed counter-intuitive until the complete structure was considered. The ladders in $(VO)_2P_2O_7$ are linked by phosphate groups (see Fig.4.23) unlike the structure of **V−12**, which is held together through hydrogen bonding, this entirely covalently bonding allows for the alternative magnetic configuration observed even though both the structures are very similar (see Fig 4.21) i.e. the magnetic interactions are mediated by the phosphate groups, leading to an alternating antiferromagnetic chain, with two different interactions, J_A and J_B.

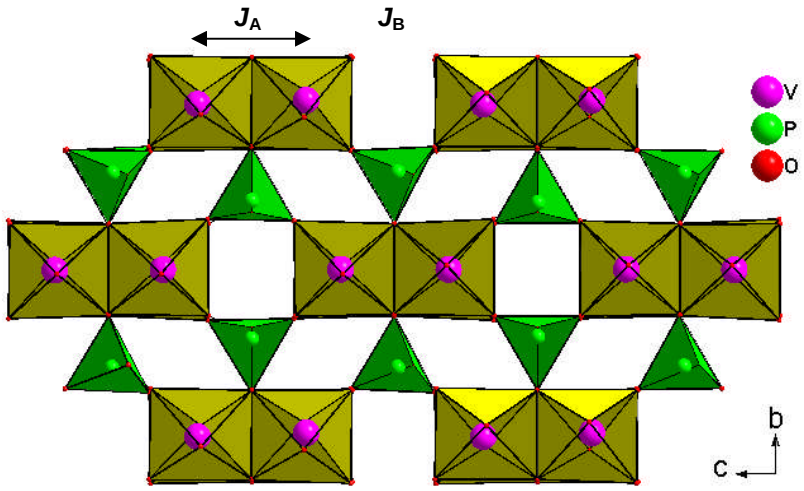

Fig 4.23 The covalently bonded structure in $(VO)_2P_2O_7$, showing the magnetic interaction pathway.

$[C_4H_{12}N_2]_4[V_5O_3F_{20}]\cdot 2H_2O$ (V−15) is a complex chain based upon a previously reported "Y-shaped" tetramer[14]. The repeat unit can be seen below in Fig 4.24 and consists of five chemically distinct vanadium sites (three V^{4+} and two V^{3+} sites − see Table 4.18) which corner and edge share with each other to form the chain structure. The three V^{4+} sites (V2, V3 and V5) are all based on a VOF_5 octahedron whilst the two V^{3+} sites (V1 and V4) are based on a VF_6 octahedron. This structural feature of a defined octahedral enviroment according to oxidation state occurs in almost all the materials in this work, with only the V^{5+} $[VOF_4(H_2O)]^-$ octahedron in **V−3** being different.

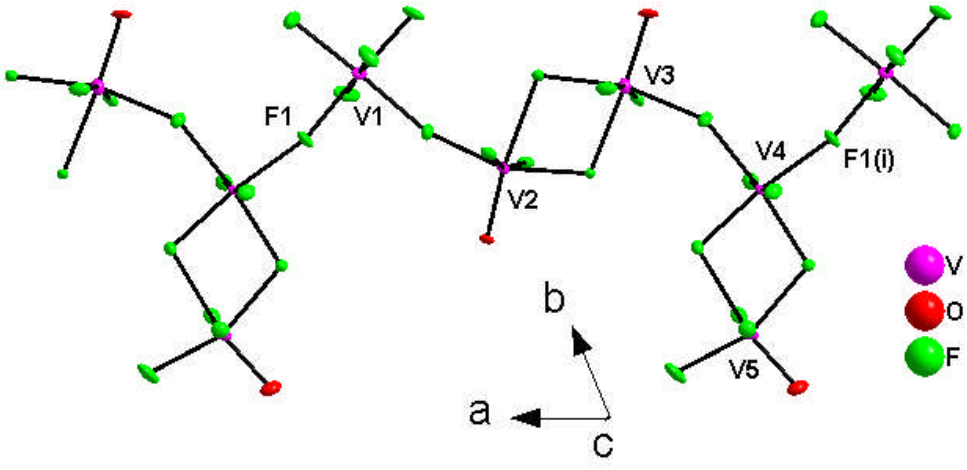

Fig 4.24 The Y-shaped chain in **V−15**. Symmetry operator (i) −1+*x*, *y*, *z*.

Bond	Bond Length (Å)	s_{ij}	Bond	Bond Length (Å)	s_{ij}
V1−F1	1.982(3)	0.467	V2−O1	1.631(3)	1.512
V1−F2	1.918(3)	0.555	V2−F4	1.930(3)	0.537
V1−F3	1.907(3)	0.572	V2−F7	1.930(3)	0.537
V1−F4	2.000(3)	0.444	V2−F8	1.906(3)	0.573
V1−F5	1.921(3)	0.550	V2−F9	2.210(3)	0.252
V1−F6	1.864(3)	0.642	V2−F10	1.972(3)	0.479
		∑V1 = **3.23**			∑V2 = **3.89**
Bond	Bond Length (Å)	s_{ij}	Bond	Bond Length (Å)	s_{ij}
V3−O2	1.699(3)	1.258	V4−F1	1.961(3)	0.494
V3−F9	1.979(3)	0.470	V4−F13	2.013(3)	0.429
V3−F10	2.101(3)	0.338	V4−F14	1.870(3)	0.632
V3−F11	1.899(3)	0.584	V4−F15	1.907(3)	0.572
V3−F12	1.924(3)	0.546	V4−F16	1.917(3)	0.556
V3−F13	1.978(3)	0.472	V4−F17	1.997(3)	0.447
		∑V3 = **3.67**			∑V4 = **3.13**

Bond	Bond Length (Å)	s_{ij}
V5−O3	1.621(4)	1.554
V5−F16	2.262(3)	0.219
V5−F17	2.027(3)	0.413
V5−F18	1.918(3)	0.555
V5−F19	1.869(3)	0.633
V5−F20	1.924(3)	0.546
		∑V5 = **3.92**

Table 4.18 Selected bond lengths and bond valence sums for **V−15**.

These chains are then held together by hydrogen bonding from the water molecules to from layers (see Fig 4.25). The layers are then sandwiched together by the protonated piperazine template to form the complete structure through an extensive hydrogen bonded network.

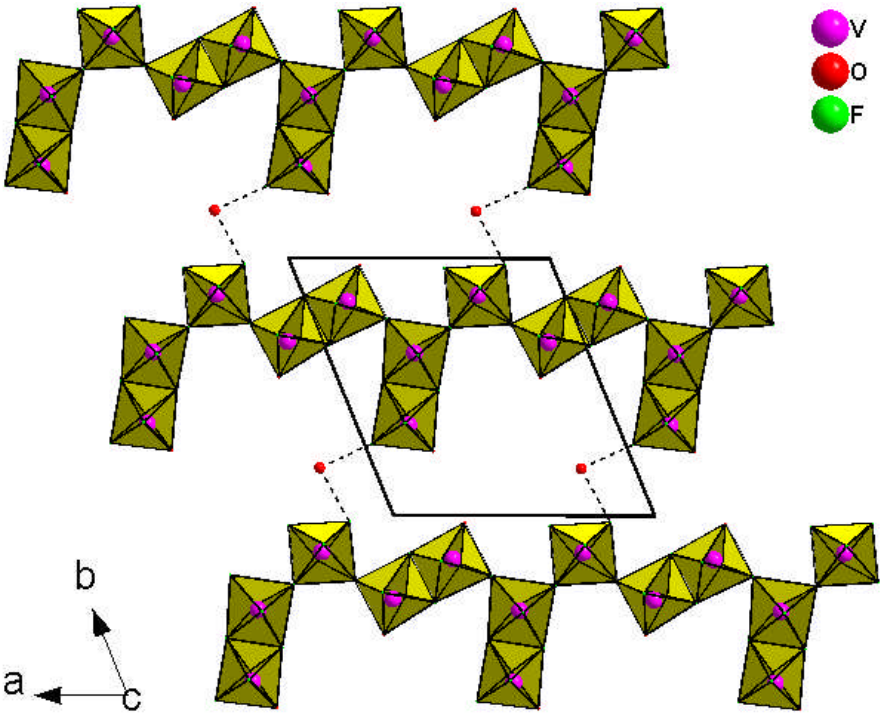

Fig 4.25 A hydrogen bonded layer in **V−15**.

The structure also proved to be antiferromagnetic (see Fig 4.26 − left). Analysis of the magnetic susceptibility showed that **V−15** had a Néel temperature of approximately 20 K and the value of *Θ* was -59.4(6) K. The value of μ_{eff} = 5.16(3) BM could be extracted (see Fig 4.26 − right) which is close to the calculated value of 5 μ_B for five non-interacting spins (three V^{4+} and two V^{3+}).

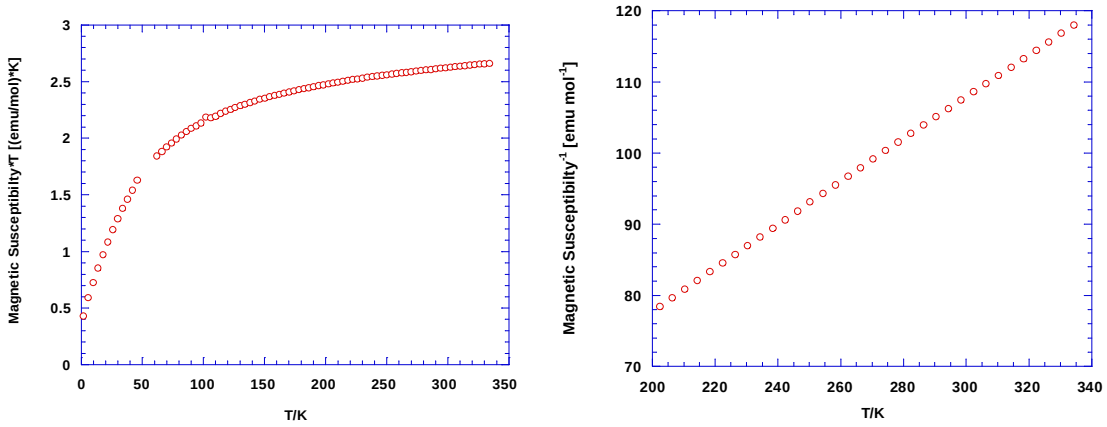

Fig 4.26 χT vs. T (left) and χ^{-1} vs. T above 150K (right) for **V−15**.

$RbVOF_3$ (V−18), $CsVOF_3$ (V−19) and **NH_4VOF_3 (V−24)** are all isostructural and are related to the ladder structure (see Fig 4.27 − top) seen in **V−12**. In this case, the ladder is “straighter” and is still based on the corner and edge sharing [$VOF_1F_{4/2}$] octahedra and does not display

the same octahedral tilting (see Fig 4.27 − bottom); as a result the *c* axis in these structures is approximately half of that in **V−12** (See Tables 4.3 − 4.5) and the overall symmetry is higher. The oxidation states of the vanadium atoms were confirmed by BVS (see Tables 4.19 − 4.21) and magnetic analysis (as their values for μ_{eff} are close to the theoretical value of 1.79 μ_B for V^{4+}, see Table 4.22)

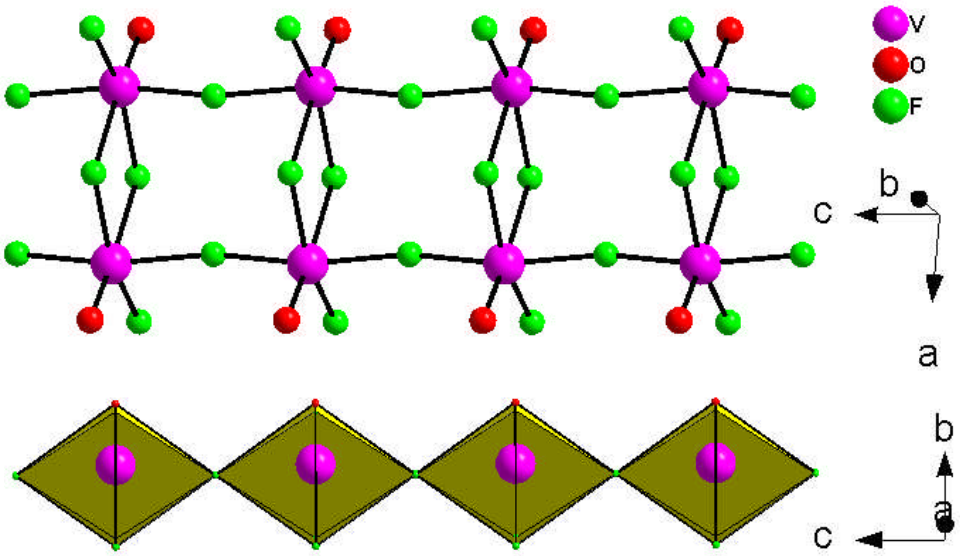

Fig 4.27 The ladder structure in **V−18**, **V−19** and **V−24**.

Bond	Bond Length (Å)	s_{ij}
V1−O1	1.584(12)	1.698
V1−F1	1.958(10)	0.498
V1−F1'	2.160(9)	0.288
V1−F2	1.948(2)	0.512
V1−F2'	1.948(2)	0.512
V1−F3	1,893(9)	0.594
		∑V1 = **4.10**

Table 4.19 Selected bond lengths and bond valence sums for **V−18.**

Bond	Bond Length (Å)	s_{ij}
V1−O1	1.600(8)	1.627
V1−F1	1.965(6)	0.501
V1−F1’	2.168(6)	0.282
V1−F2	1.972(1)	0.479
V1−F2’	1.972(1)	0.479
V1−F3	1.898(6)	0.586
		∑V1 = **3.95**

Table 4.20 Selected bond lengths and bond valence sums for **V−19**.

Bond	Bond Length (Å)	s_{ij}
V1−O1	1.596(4)	1.644
V1−F1	1.960(3)	0.495
V1−F1’	2.148(3)	0.298
V1−F2	1.887(3)	0.603
V1−F3A*	1.929(1)	0.270
V1−F3B*	1.990(2)	0.229
V1−F3A*	1.929(1)	0.270
V1−F3B*	1.990(2)	0.229
		∑V1 = **4.04**

Table 4.21 Selected bond lengths and bond valence sums for **V−24**.

* = Disordered atom sites.

These three structures also show similar magnetic interactions as **V−12**. They are all antiferromagnetic and their magnetic susceptibility data fit the same Heisenberg model as used before (see Fig 4.28 − Fig 4.30). The broad maxima in the plots of χ vs. T for the three structures are indicative of low dimensional magnetic interactions.

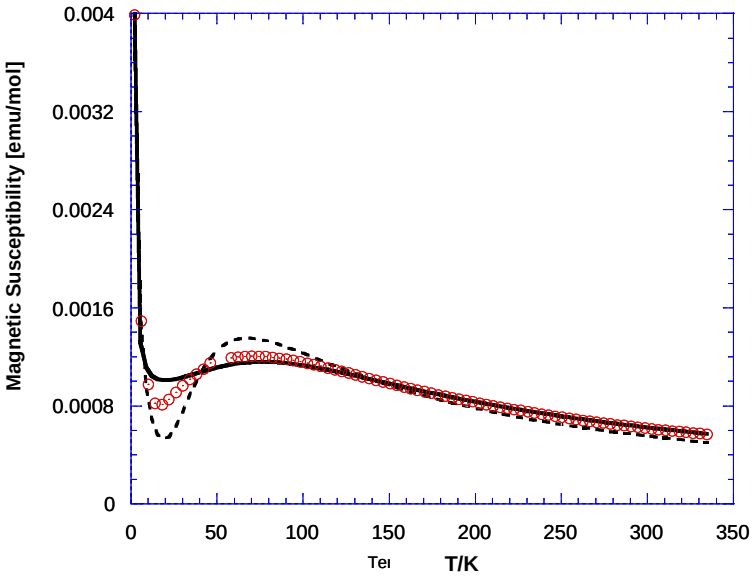

Fig 4.28 The Heisenberg (solid line) and the Bleaney-Bowers (dashed line) fits for χ vs. T for **V−18**.

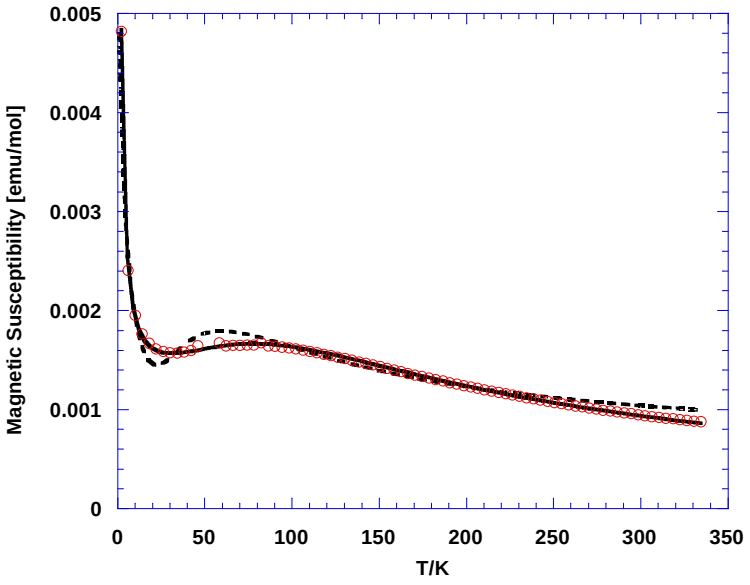

Fig 4.29 The Heisenberg (solid line) and the Bleaney-Bowers (dashed line) fits for χ vs. T for **V−19**.

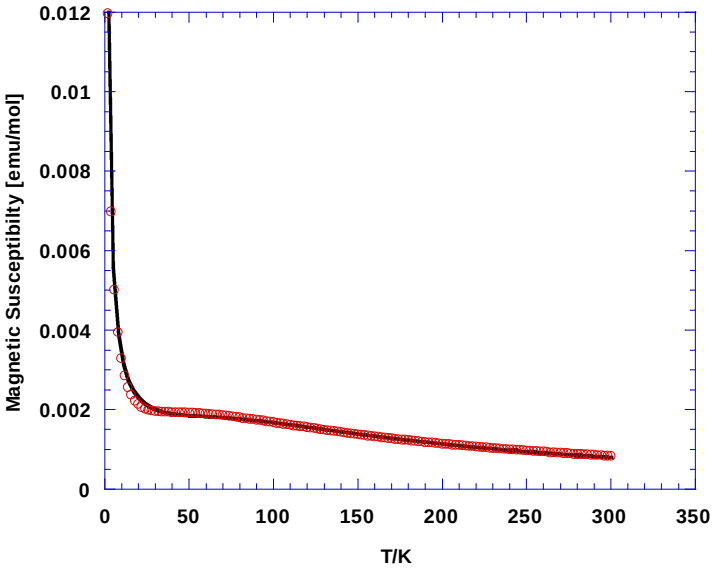

Fig 4.30 The Heisenberg fit (solid line) for χ vs. T for **V−24**.

The derived magnetic data for the three structures is similar as well (see Table 4.22). The values of J_1 are all comparable and noticeably larger than in **V−12**, where the strength of the interaction may have been reduced by the octahedral tilting, as this is the main difference between the two structure types. In **V−24** the *inter*-ladder fluorine atom, F3, is slightly disordered away from its ideal position (see Fig 4.31), which may be the cause of the slight decrease in the value of J_1.

	V−18	**V−19**	**V−24**
μ_{eff} (μ_B)	1.39(4)	1.79(4)	1.56(5)
Θ (K)	−92.2(5)	−122.9(3)	−66.1(3)
J_1 (K)	−67(3)	−65.8(2)	−60.3(4)

Table 4.22 The magnetic parameters of **V−18**, **V−19** and **V−24**.

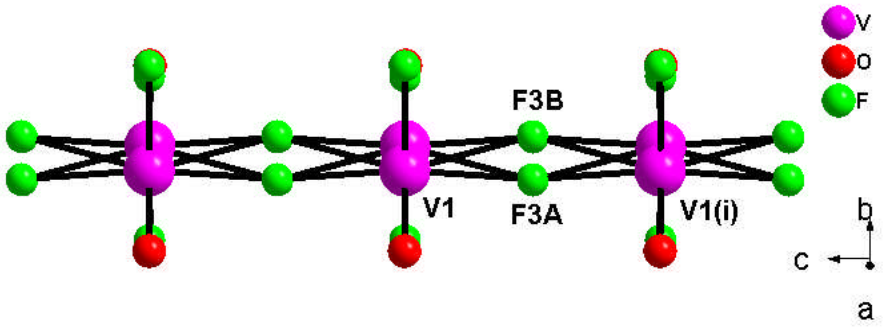

Fig 4.31 The disordered ladder in **V−24**. Symmetry operator (i) *x*, *y*, −1+*z*.

$[C_{12}H_{12}N_2]_{0.5}[VOF_3]$ (V−25) is another ladder chain structure and is isostructural with **V−24** (see Fig 4.31), although the templates used (*trans* 1,2 bis (4-pyridyl) ethane (see Chapter 3 − Fig 3.1) and ammonia for **V−25** and **V−24,** respectively) are quite different. The "ladders" both show the same disorder of the bridging fluorine atom, F3, although in **V−25** the non-bridging atoms F1 and O1 are disordered also. The similarity between **V−24** and **V−25** is surprising as it would be assumed that it would be similar to **V−12**, as they have similar templates (*trans* 1,2 bis (4-pyridyl) ethene and *trans* 1,2 bis (4-pyridyl) ethane (see Chapter 3 − Fig 3.1), for **V−12** and **V−25**, respectively) with the only difference being that **V−25** is held together with *trans* 1,2 bis (4-pyridyl) ethane rather than the ethene version used in **V−12** (which is also disordered − see Fig 4.32). As a result of the change of template the structure **V−25** no longer shows the octahedral tilting seen in **V−12** which results in the *c* axis being similar to **V−18**, **V−19** and **V−24**. The magnetic susceptibility of the sample(see Fig 4.33) was measured but showed to be paramagnetic with a value for μ_{eff} (μ_B) = 2.24(2) which is quite above the theoretical value of 1.79 μ_B (for V^{4+}, see Table 4.23). This is most unusual as all the other ladder structures have had comparable results. The only other explanation is that the sample had either degraded before the measurement was conducted or during it.

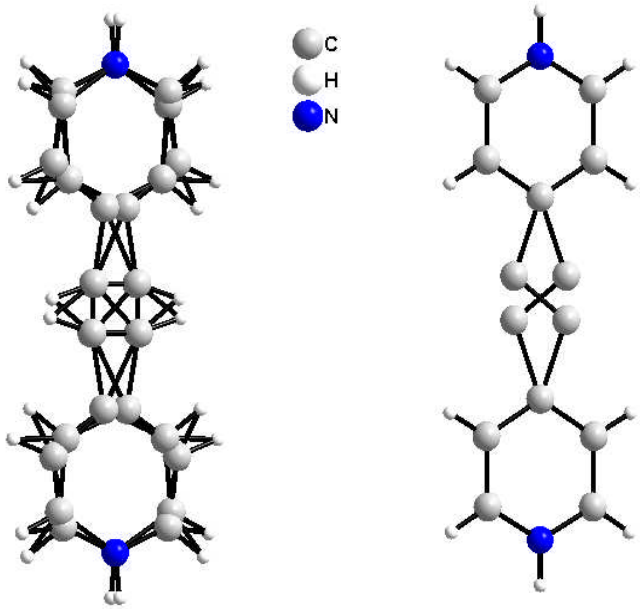

Fig 4.32 The disordered and ordered template in **V−12** and **V−25**.

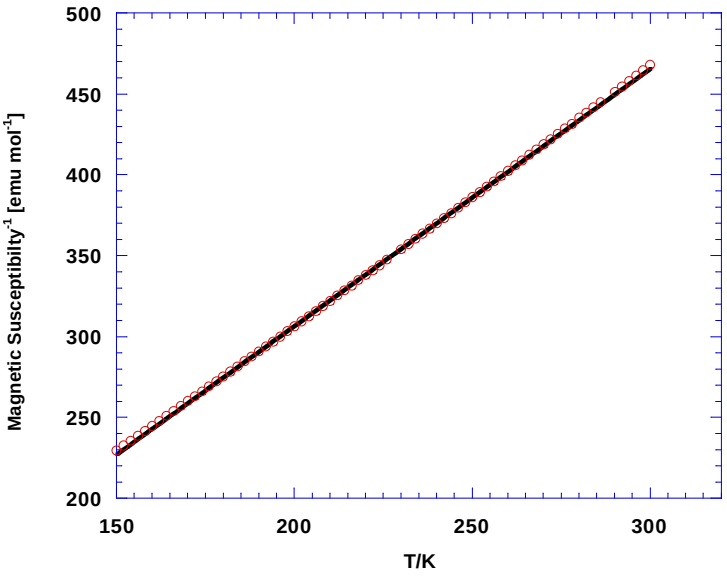

Fig 4.33 χ^{-1} vs. T for **V−25** above 150K.

Bond	Bond Length (Å)	s_{ij}
V1−O1	1.705(7)	1.225
V1−F1	1.705(7)	0.987
V1−F2	2.048(5)	0.390
V1−F2'	2.048(5)	0.390
V1−F3A*	1.971(11)	0.241
V1−F3B*	1.981(10)	0.234
V1−F3A*	1.971(11)	0.241
V1−F3B*	1.981(10)	0.234
		∑V1 = **3.94**

Table 4.23 Selected bond lengths and bond valence sums for **V−25**.
* = Disordered atom sites.

$[C_4H_{12}N_2]_3[V_7F_{27}]$ (V−28) is an unusual structure (see Fig 4.34 − top) and is related to $CsCrF_4$[15] (see Fig 4.34 − bottom). The chain structure is held together through an extensive hydrogen bonding network with piperazine as the template cations (which are situated on inversion centres), which surround the chains (see Fig 4.35). The vanadium atoms are all V^{3+} which is confirmed by BVS (see Table 4.24).

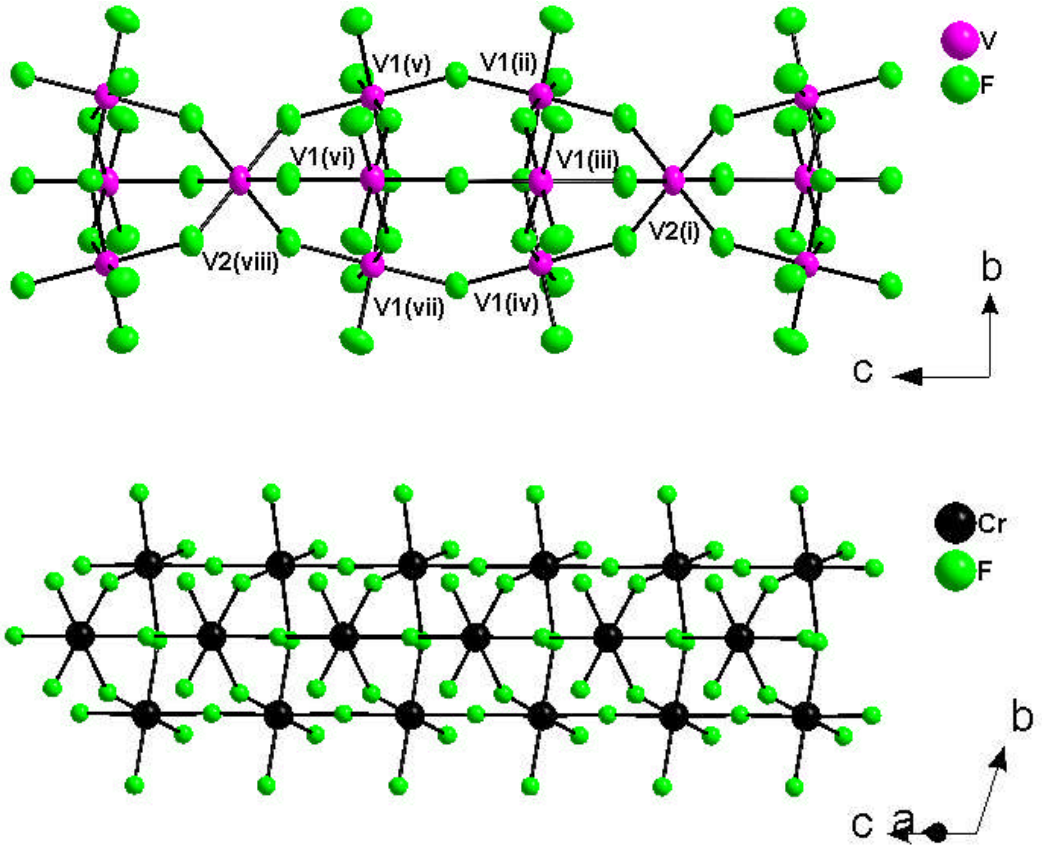

Fig 4.34 The chain structure in **V−28** (top) and $CsCrF_4$ (bottom).
Symmetry operators (i) 1/3+*x*−*y*, 2/3−*y*, 1/6−*z*, (ii) 1/3−*x*+*y*, 2/3+*y*, 1/6+*z*, (iii) 1/3+*x*, 2/3+*x*−*y*, 1/6+*z*, (iv) 1/3−*x*, 2/3−*y*, 1/6+*z*, (v) 1/3+*x*−*y*, 2/3+*y*, 2/3−*z*, (vi) 1/3+*y*, 2/3−*x*+*y*, 2/3−*z*, (vii) 1/3−*x*, 2/3−*y*, 2/3−*z*, (viii) 1/3+*x*, 2/3+*y*, 2/3+*z*.

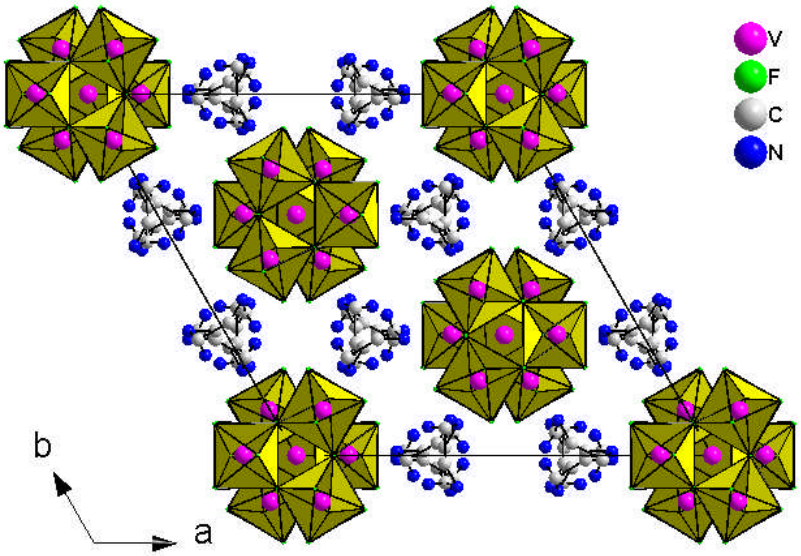

Fig 4.35 The unit cell in **V−28.**

Bond	Bond Length (Å)	s_{ij}	Bond	Bond Length (Å)	s_{ij}
V1−F1	1.981(3)	0.468	V2−F5	1.939(5)	0.524
V1−F2	1.966(5)	0.487	V2−F5	1.939(5)	0.524
V1−F2'	2.002(5)	0.442	V2−F5	1.939(5)	0.524
V1−F3	1.867(5)	0.637	V2−F5	1.939(5)	0.524
V1−F4	1.828(6)	0.708	V2−F5	1.939(5)	0.524
V1−F5	1.993(5)	0.453	V2−F5	1.939(5)	0.524
		∑V1 = **3.20**			∑V2 = **3.14**

Table 4.24 Selected bond lengths and bond valence sums for **V−28**.

The similarity between $CsCrF_4$ and **V−28** is easily seen by comparing a view down their respective *c* axes (see Fig 4.36). **V−28** has the same trigonal configuration as $CsCrF_4$ but is gathered to point by a face sharing [VF_6] monomer, reminiscent of a string of sausages! It is after this point that the structure makes a 60° rotation about the *c* axis and does so along the length of the chain to give the eclipsed effect seen in Fig 4.36 − right. $CsCrF_4$ could be considered to have a 3-3-3 octahedral repeat unit in comparison to the 3-3-1 repeat unit in **V−28**.

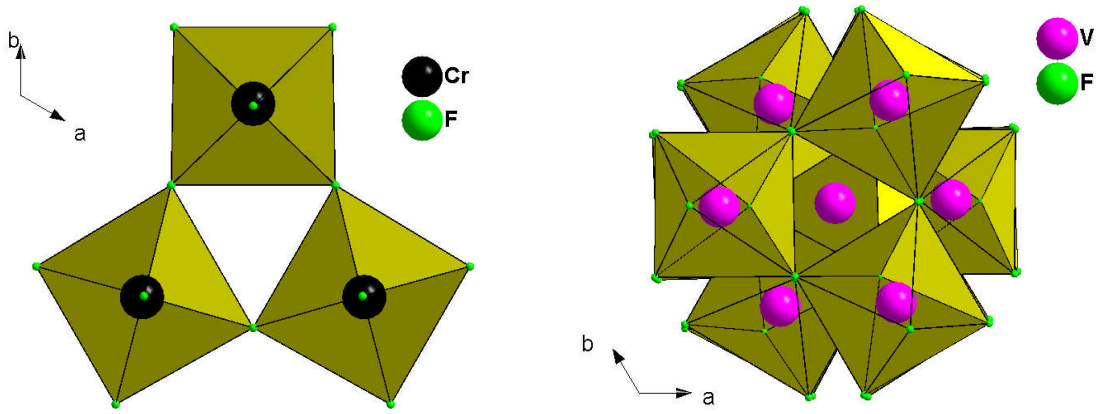

Fig 4.36 A view down the *c* axis of $CsCrF_4$ (left) and **V−28** (right).

It is because of this trigonal shape that structures such as $CsCrF_4$ are known to display magnetic frustration.[16-18] Analysis of the magnetic susceptibility of **V−28** proved inconclusive for ferrimagnetism and magnetic frustration and possibly only shows weak antiferromagnetism. A plot of χ^{-1} vs. T (see Fig 4.37) shows that *Θ* will have a negative intercept (which is indicative of antiferromagnetism) and at a low temperature the data tends towards zero or even a positive intercept (which is indicative of ferromagnetism). The combination of these two parameters would clearly show ferrimagnetism and magnetic frustration in the structure but as the data tends towards zero and not a positive intercept, the

data could just be weakly antiferromagnetic. One possible conclusion is that the magnetic frustration is localised and separated by the face sharing [VF_6] monomer to create compartments or "sausages" of magnetic frustration. The magnetic parameters obtained for **V−28** were μ_{eff} = 2.92(2) BM (which is close to the theoretical value of 2.82 BM per V^{3+} atom) and Θ = −77.7(5) K. The ratio of the ordering temperature (below 2 K) and the value of Θ is therefore 38.9 or greater. This value was used in a review by Ramirez[19] as a method of differentiating between ferrimagnetism and strongly geometrically frustrated magnets. A value of above 10 indicates geometric frustration. He cites the example of kagome-lattice jarosite compound, $KCr_3(OH)_6(SO_4)_2$, as an example where the ratio is 34 or greater as a result of an ordering temperature below 2 K and Θ = −67.5 K

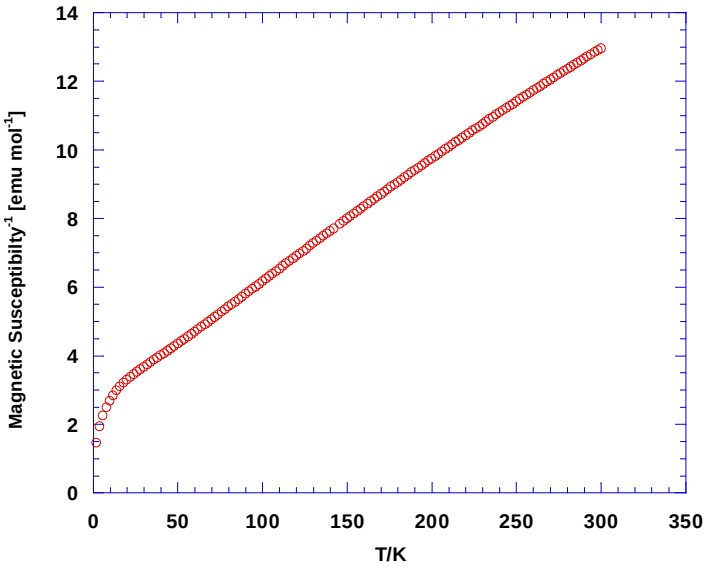

Fig 4.37 χ^{-1} vs. T for **V−28**.

4.1.5 Layer Structures

$[C_{10}H_8N_2][VF_3]$ (V−14) is a novel layered hybrid material. The structure is based around a [$VF_2F_{2/2}$] corner sharing octahedral chain backbone. From this, two 4,4 bipyridyl groups are linked to two further vanadium centres and from this the infinite layered lattice is formed (see Fig 4.38). The structure is closely related to [$C_{10}H_8N_2$][MnF_3].[20] The structure has an identical topology but experiences phase transitions across a range of temperatures.

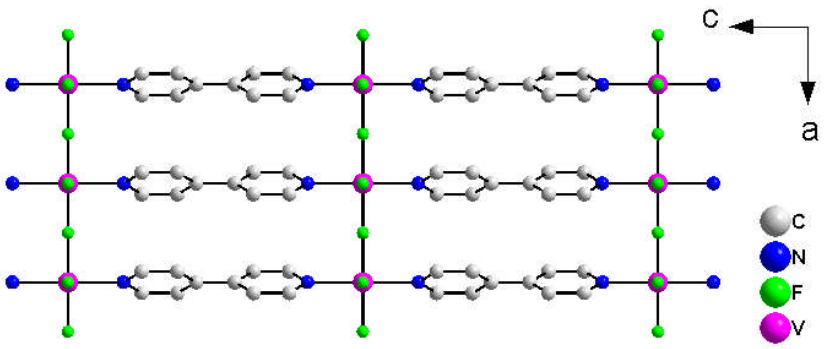

Fig 4.38 The infinite 2D lattice in **V−14**. Hydrogen atoms have been removed for clarity.

The structure was measured for its magnetic susceptibility (see Fig 4.39 − left) and found to be weakly antiferromagnetic (see Fig 4.39 − right) with the following magnetic parameters: μ_{eff} = 1.92(7) BM and Θ = −4.73(3) K with an approximate Néel point at 8 K. The low value of μ_{eff} (from the theoretical value of 2.83 BM for V^{3+}) may be caused by the vanadium site being mixed valence V^{3+}/V^{4+} as indicated by the BVS calculation (see Table 4.25). There was no crystallographic evidence for this other than a slight elongation of the ellipse of the bridging fluorine atom which could be due to partial oxygen/fluorine atom disorder. To determine further the correct oxidation state of the vanadium site, an EPR spectrum was collected for the sample and for two known reference samples: **V−19** (V^{4+}) and **V−22** (V^{3+}). Unfortunately, only broad spectra could be collected due to the concentration of the unpaired spins being measured. Fig 4.40 shows the three spectra: (i) **V−14** at the top, (ii) **V−19** in the middle and (iii) **V−22** at the bottom. It can be seen that the broad band seen in both spectra (ii) and (iii) are present in spectrum (i) but that spectra (ii) and (i) are more similar. This tentatively suggests that the sample is predominantly V^{3+} but by no means gives a definitive answer.

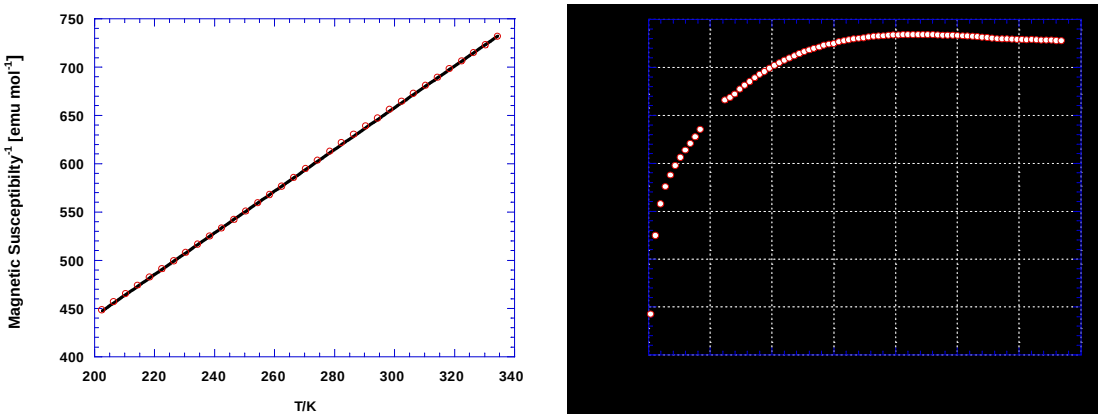

Fig 4.39 χ^{-1} vs. T above 200K (left) and χT vs. T (right) for **V−14**.

Bond	Bond Length (Å)	s_{ij}
V1−F1	1.842(2)	0.680
V1−F1’	1.842(2)	0.680
V1−F2	1.899(2)	0.584
V1−F2’	1.899(2)	0.584
V1−N1	2.129(2)	0.523
V1−N1’	2.129(2)	0.523
		∑V1 = **3.57**

Table 4.25 Selected bond lengths and bond valence sums for **V−14**.

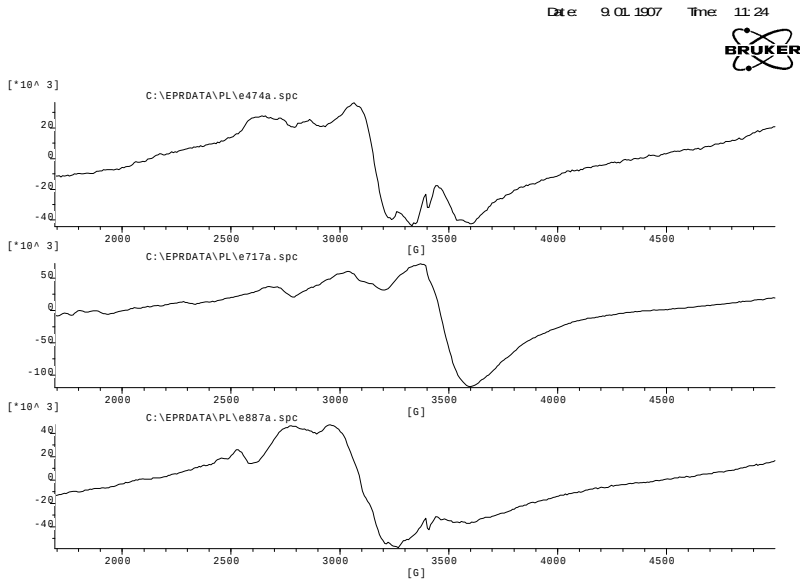

Fig 4.40 The EPR spectra of **V−14** (top), **V−19** (middle) and **V−22** (bottom).

4.2 Existing Oligomers and Polymeric Structures

The novel crystal structures contained in this sub-section are inorganic oligomers or polymeric compounds which have either been made by a different route of synthesis to that previously reported or made with a different organic/inorganic cation.

4.2.1 Monomers

$[C_4H_{12}N_2]_3[V_2O_2F_8]_2[VOF_4(H_2O)]_2$ (V−4) is a polyanionic structure consisting of a novel $[V_2O_2F_8]^{4-}$ dimer (see previous Fig 4.6) situated around an inversion centre and two $[VOF_4(H_2O)]^-$ monomers, which have previously been reported.[5] The monomer shows the expected lengthening of the aqua bond due to the *trans* effect from the V=O bond. The structure consists of a strong hydrogen bonded inorganic chain (see Fig 4.41). These chains are then separated from one another by the protonated piperazine template, which hold the

structure together through an extensive hydrogen bonded network. The structure is also mixed valence with the monomers being V^{5+} and the dimers being V^{4+} as confirmed by BVS (see Table 4.26)

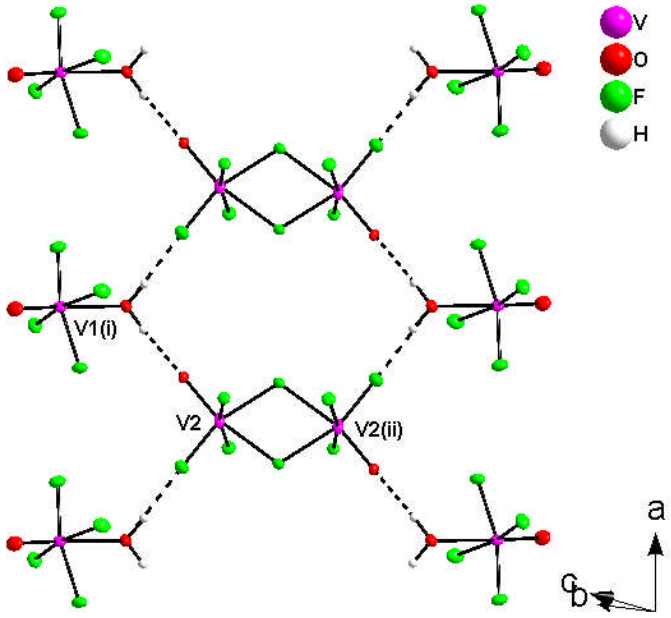

Fig 4.41 The hydrogen bonded chain in **V−4**. Symmetry operators (i) *x*, 1+*y*, *z* (ii) −*x*, 2−*y*, 1−*z*.

Bond	Bond Length (Å)	s_{ij}	Bond	Bond Length (Å)	s_{ij}
V1−O1	1.578(3)	1.745	V2−O3	1.672(2)	1.354
V1−O2	2.274(3)	0.280	V2−F5	1.933(2)	0.533
V1−F1	1.836(2)	0.692	V2−F6	1.886(2)	0.605
V1−F2	1.837(2)	0.691	V2−F7	2.052(2)	0.386
V1−F3	1.795(2)	0.774	V2−F7’	2.160(2)	0.288
V1−F4	1.843(2)	0.679	V2−F8	1.806(2)	0.751
		∑V1 = **4.95**			∑V2 = **3.92**

Table 4.26 Selected bond lengths and bond valence sums for **V−4**.

$[C_4H_{16}N_3][VOF_5]\cdot H_2O$ (V−8) is a structure that is based on a $[VOF_5]^{3-}$ monomer which has previously been reported,[21] however in this case the organic template (protonated diethylene triamine) has not been used with this monomer before. The structure consists of hydrogen bonded chains (see Fig 4.42) which run anti-parallel to one another, but share hydrogen bonds to the template to from the complete structure. The monomer is V^{4+} which is confirmed by BVS (see Table 4.27).

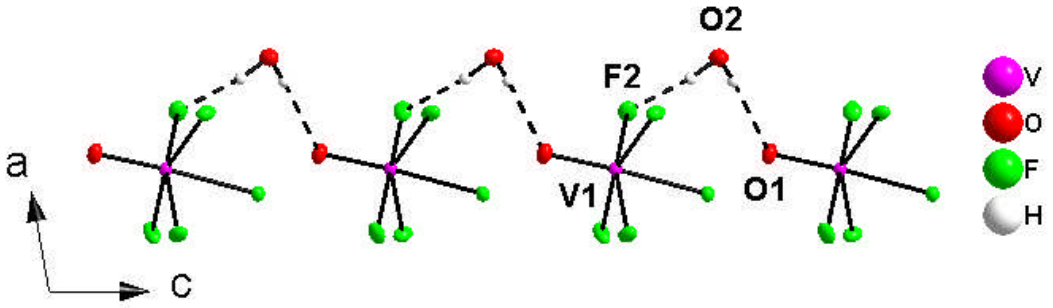

Fig 4.42 The hydrogen bonded chain in **V−8**.

Bond	Bond Length (Å)	s_{ij}
V1−O1	1.617(2)	1.570
V1−F1	1.939(1)	0.524
V1−F2	1.944(1)	0.517
V1−F3	1.941(1)	0.521
V1−F4	1.927(1)	0.541
V1−F5	2.123(1)	0.319
		∑V1 = **3.99**

Table 4.27 Selected bond lengths and bond valence sums for **V−8**.

$[C_6H_{22}N_4][VF_5(H_2O)]_2$ (V−13) consists of two crystallographically different V^{3+} monomers (confirmed by BVS, see Table 4.28) $[VF_5(H_2O)]^{2-}$ and the protonated organic cation, triethylene tetramine in the asymmetric unit (see Fig 4.43). The previously reported monomer[23] hydrogen bonds to the adjoining monomers to form an inorganic chain (see Fig 4.44). These chains are separated by the template which runs parallel to the inorganic chain and forms an extensive hydrogen bonded network as a result.

Bond	Bond Length (Å)	s_{ij}	Bond	Bond Length (Å)	s_{ij}
V1−O1	2.073(3)	0.413	V2−O2	2.063(3)	0.413
V1−F1	1.970(2)	0.482	V2−F6	1.976(2)	0.469
V1−F2	1.831(2)	0.704	V2−F7	1.876(2)	0.632
V1−F3	1.909(2)	0.567	V2−F8	1.912(2)	0.567
V1−F4	1.956(2)	0.495	V2−F9	1.945(2)	0.509
V1−F5	1.931(2)	0.537	V2−F10	1.911(2)	0.567
		∑V1 = **3.20**			∑V2 = **3.16**

Table 4.28 Selected bond lengths and bond valence sums for **V−13**.

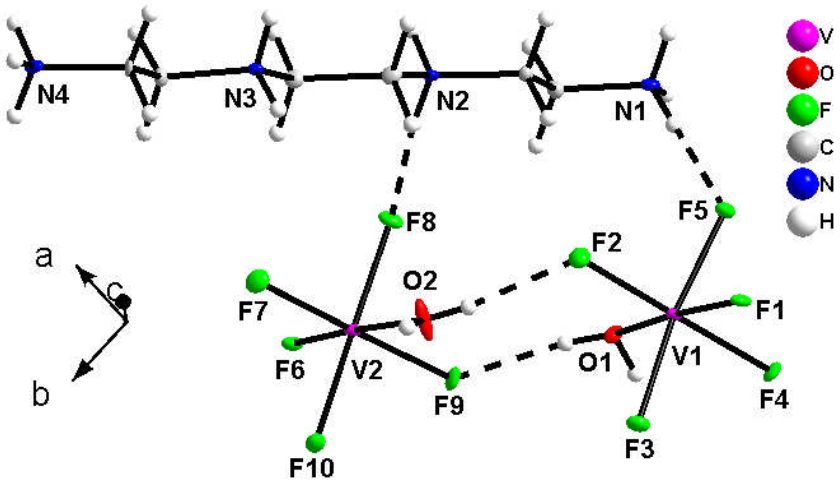

Fig 4.43 The asymmetric unit in **V−13**.

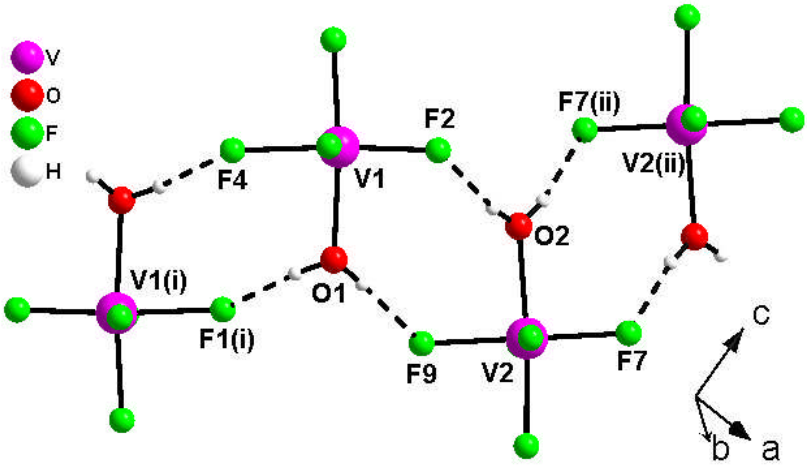

Fig 4.44 The hydrogen bonded chain in **V−13**. Symmetry operators (i) −*x*, 1−*y*, 1−*z*, (ii) 1−*x*, 2−*y*, 2−*z*.

The asymmetric unit for **$[C_4H_{16}N_3][VF_6]$ (V−20)** consists of a single $[VF_6]^{3-}$ monomer (V^{3+} confirmed by BVS, see Table 4.29) and the protonated template, diethylene triamine (see Fig 4.45). The overall structure consists of an extensive hydrogen bond network from all six of the fluorine atoms on the previously reported monomer[23] to the template species.

Bond	Bond Length (Å)	s_{ij}
V1−F1	2.018(1)	0.426
V1−F2	1.899(1)	0.587
V1−F3	1.945(1)	0.519
V1−F4	1.998(1)	0.449
V1−F5	1.967(1)	0.489
V1−F6	1.969(1)	0.486
		∑V1 = **2.96**

Table 4.29 Selected bond lengths and bond valence sums for **V−20**.

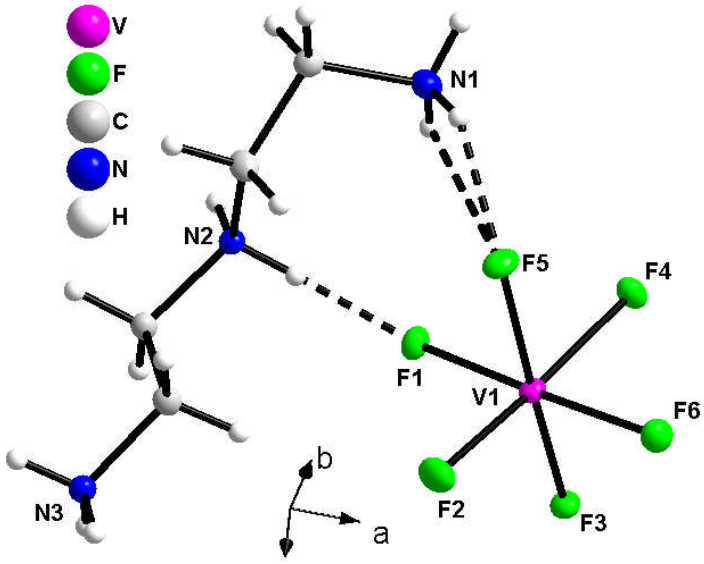

Fig 4.45 The asymmetric unit in **V−20**.

$[C_4H_{12}N_2][VOF_4(H_2O)]$ V−26 is a structure based on the previously reported monomer,[5] $[VOF_4(H_2O)]^{2-}$ as seen in the asymmetric unit (see Fig 4.46). This monomer is similar to that shown in Fig 4.1 but unlike the previously reported monomer, in this case the metal centre is V^{4+} (confirmed by BVS, see Table 4.30). The monomer hydrogen bonds to its adjoining monomers to form an inorganic chain (see Fig 4.47 − left). These chains are then kept separate from one another by the protonated template species, piperazine, which acts to hold the chains together as part of the complete hydrogen bonded network. The inorganic chain is comparable to the polar inorganic chain seen in $[C_2H_{10}N_2][VOF_4(H_2O)]$.[24] Instead of the chain being centrosymmetric, the $[VOF_4(H_2O)]^{2-}$ octahedra align in a uniform direction along the direction of the *b* axis (see Fig 4.47 − right). As a result, the structure crystallises in the space group $P2_1$ and has a SHG activity of approximately 15-30 times less than that of $LiNbO_3$.

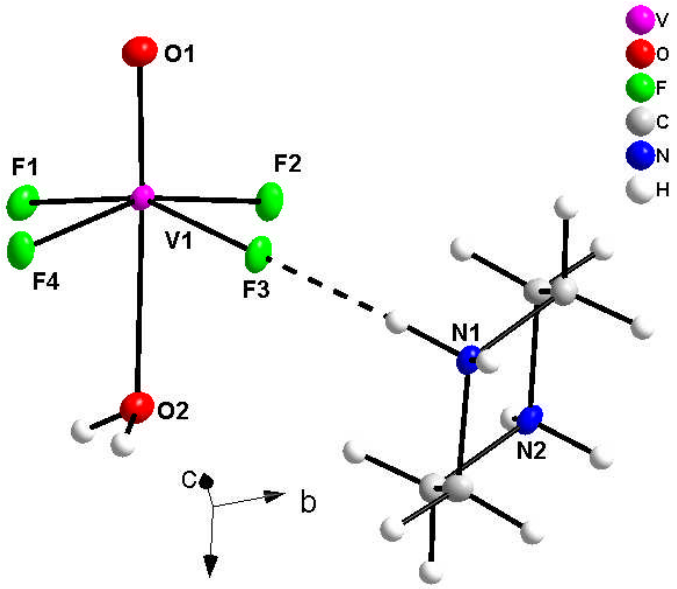

Fig 4.46 The asymmetric unit in **V−26**.

Bond	Bond Length (Å)	s_{ij}
V1−O1	1.620(2)	1.558
V1−O2	2.357(2)	0.213
V1−F1	1.966(2)	0.487
V1−F2	1.932(1)	0.534
V1−F3	1.919(1)	0.553
V1−F4	1.921(1)	0.550
		∑V1 = **3.90**

Table 4.30 Selected bond lengths and bond valence sums for **V−26**.

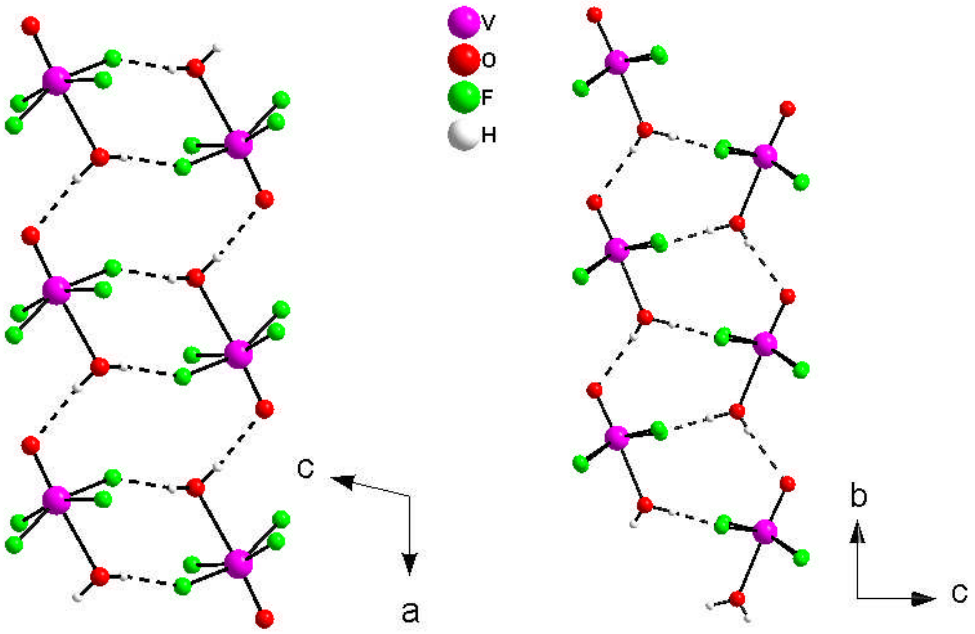

Fig 4.47 The hydrogen bonded chains in **V−26** (left) and $[C_2H_{10}N_2][VOF_4(H_2O)]$[24] (right).

4.2.2 Dimers

$[C_{10}H_{10}N_2][V_2O_2F_6(H_2O)_2]$ V−3 is a structure comprising the known dimer[25] (see Fig 4.48 − left) $[V_2O_2F_6(H_2O_2]^{2-}$ but this is held together through an extensive hydrogen bonded network with a new template, the protonated 4,4 bipyridyl. The asymmetric unit consists of half the dimer (one unique vanadium site) and half the template, which are related by symmetry to form the building unit shown below (see Fig 4.48 − right). The bridging fluorine atoms *trans* to the vanadyl bond display the expected lengthing caused by the *trans* effect. The unique vanadium atom is V^{4+} as confirmed by BVS (see Table 4.31).

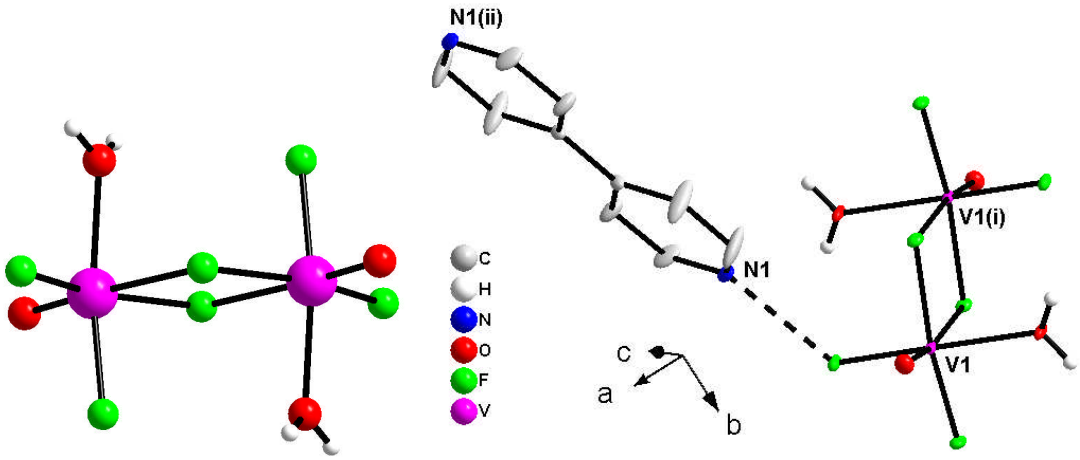

Fig 4.48 The dimer (left) and the building unit (right) in **V−3**. Some hydrogen atoms have been removed for clarity. Symmetry operators (i) −*x*, 1−*y*, 1−*z* (ii) 1−*x*, −*y*, 2−*z*.

Bond	Bond Length (Å)	s_{ij}
V1−O1	1.606(2)	1.618
V1−O2	2.022(2)	0.528
V1−F1	1.954(1)	0.506
V1−F1’	2.178(2)	0.275
V1−F2	1.947(2)	0.513
V1−F3	1.898(2)	0.589
		∑V1 = **4.03**

Table 4.31 Selected bond lengths and bond valence sums for **V−3**.

The dimer hydrogen bonds to its neighbouring dimers to form an inorganic continuous plane (see Fig. 4.49). These layers are separated by the organic cation to form alternating organic−inorganic layers.

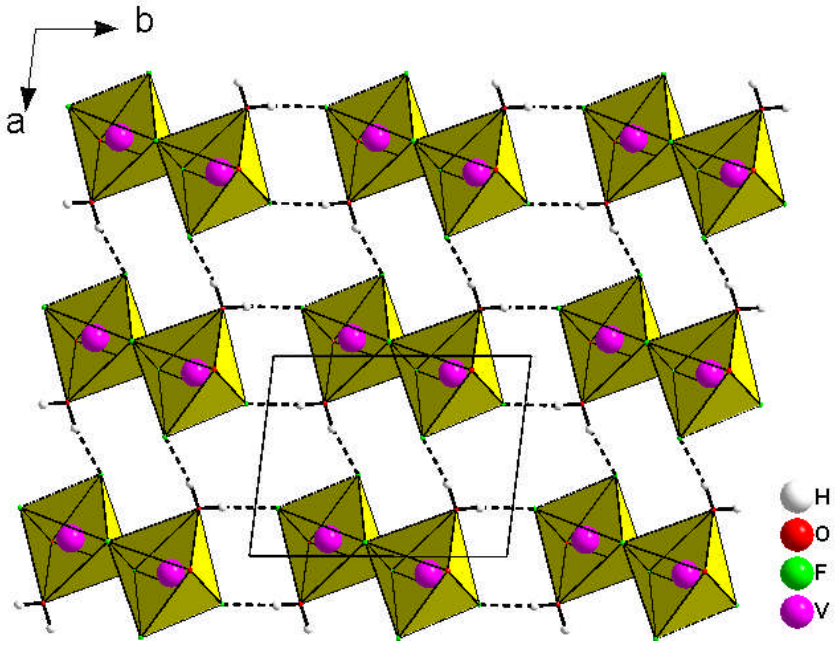

Fig 4.49 The hydrogen bonded sheet in **V−3**.

4.2.3 Chain Structures

K_2VOF_4 (V−17) is a known inorganic chain structure[26] which is comprised of a zig-zag chain (see Fig 4.50) surrounded by potassium cations. The non-bonding fluorine and oxygen atoms, F4 and O1, which lie in the plane of the chain are disordered, having an average length of 1.757 Å. This structure was solved in a centrosymmetric space group, Pnma. The original paper by Karlason, solved the structure in non-centrosymmetric space group $Pn2_1a$ (which does not show the disorder of atoms O1 and F4) and cited a piezoelectric measurement, in a

PhD thesis by Carpy,[27] as proof that the space group was correct. A sample was sent to Prof. Halasyamani's group in Houston, University of Texas to confirm this by measuring the SHG output from the sample. A reasonable output was expected from the sample as the distortion around the vanadium site was comparable to that of a known SHG material, $[C_2H_{10}N_2][VOF_4(H_2O)]$.[24] What Prof. Halasyamani's group discovered was that the material was not even SHG active, which is very unlikely if the structure is non-centrosymmetric. This measurement suggests that the solution in space group Pnma given in this work is correct. Both solutions may be correct, as the exact method of synthesis is not mentioned in the paper; subtle differences between the reactions may yield similar but ultimately different results. The structure is also paramagnetic down to 2 K and gives a value of μ_{eff} = 1.42(3) BM (see Fig 4.51), which is below the theoretical value of 1.79 BM for V^{4+} (which is confirmed by BVS, see Table 4.32).

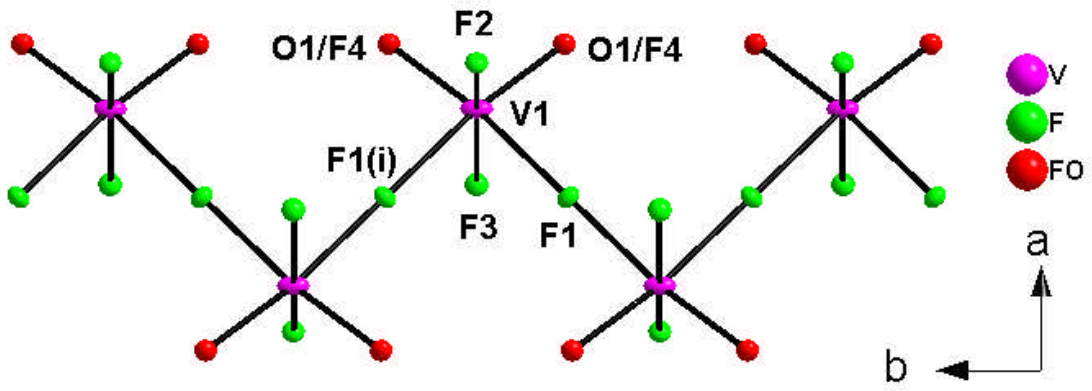

Fig 4.50 The disordered chain in **V−17**. Symmetry operator (i) 1/2+*x*, 1/2-*y*, 3/2-*z*.

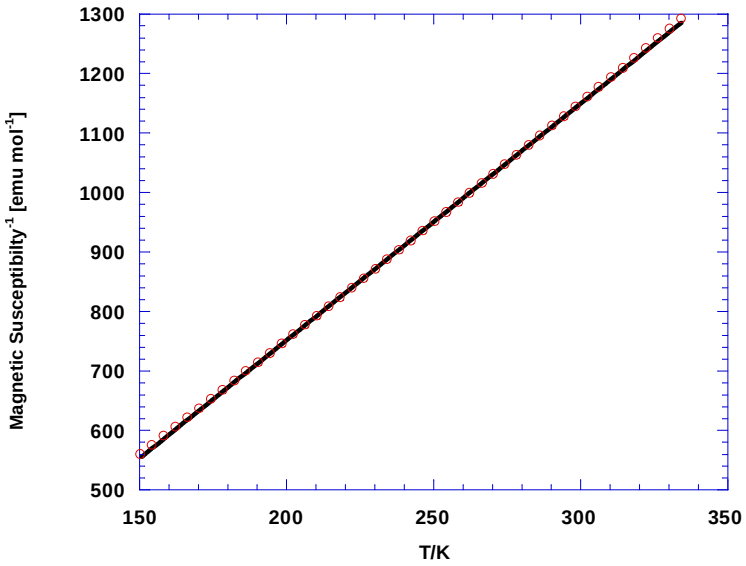

Fig 4.51 χ^{-1} vs. T for **V−17** above 150K.

Bond	Bond Length (Å)	s_{ij}
V1−O1	1.758(2)	1.061
V1−F1	2.088(1)	0.350
V1−F1’	2.088(1)	0.350
V1−F2	1.932(3)	0.534
V1−F3	1.896(3)	0.589
V1−F4	1.758(2)	0.865
		∑V1 = **3.75**

Table 4.32 Selected bond lengths and bond valence sums for **V−17**.

$[C_4H_{12}N_2][VF_5]\cdot H_2O$ (V−22) is a *cis*-connected chain structure (see Fig 4.51) similar to those found in VF_5[28] and $BaVF_5$[2] and based on the $[VF_4F_{2/2}]$ octahedra. The chains are kept separate by a protonated template piperazine which also, via complex hydrogen bond network, holds the structure together.

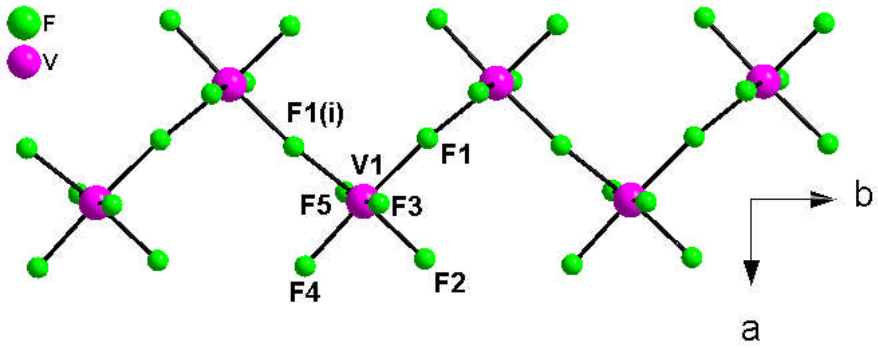

Fig 4.51 The zig-zag chain in **V−22**. Symmetry operator (i) 3/2-*x*, -1/2+*y*, 1/2-*z*.

The magnetic susceptibility for the sample was measured (see Fig 4.52 − left) and showed to be antiferromagnetic (see Fig 4.52 − right). The following magnetic parameters were derived from the data; μ_{eff} (μ_B) = 2.54(4) BM and Θ = −67.1(6) K. An approximate Néel temperature is estimated at 40 K because of a sharp upturn in the value of χ at low temperatures because of a small paramagnetic impurity made an accurate observation impossible in a plot of χ vs. T. The calculated value of 2.54(4) BM is close to the theoretical value of 2.83 BM for V^{3+} (confirmed by BVS, see Table 4.38).

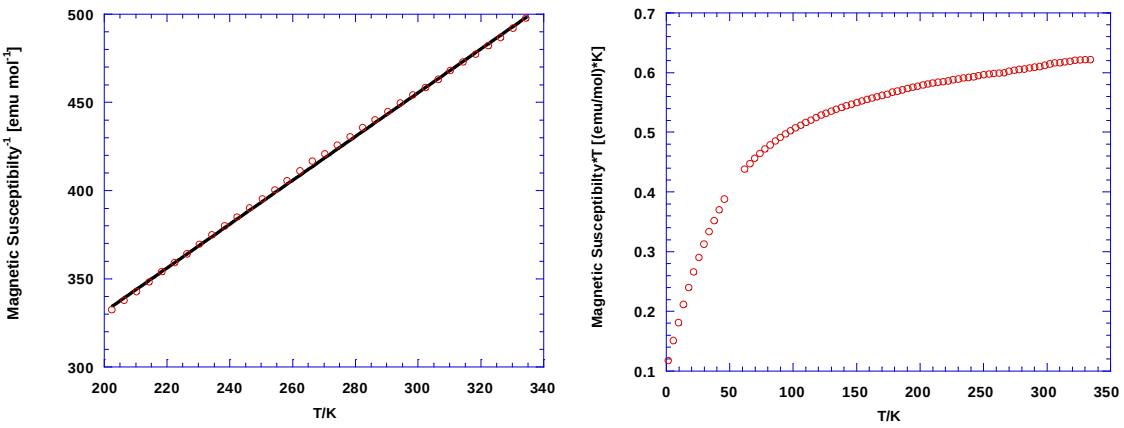

Fig 4.52 χ^{-1} vs. T above 200K(left) and χT vs. T (right) for **V−22**.

Bond	Bond Length (Å)	s_{ij}
V1−F1	1.991(2)	0.455
V1−F1'	1.999(2)	0.446
V1−F2	1.898(2)	0.586
V1−F3	1.901(2)	0.581
V1−F4	1.935(2)	0.530
V1−F5	1.908(2)	0.570
		∑V1 = **3.17**

Table 4.33 Selected bond lengths and bond valence sums for **V−22**.

4.2.4 Layer Structures

KVF_4 (V−21) and **$NaVF_4$ (V−23)** are both related to the Dion-Jacobson phases and have been reported previously.[29,30] The continuous inorganic sheets consist of a *cis* corner sharing V^{3+} (confirmed by BVS, see Table 4.34 and 4.35) $[VF_2F_{4/2}]$ octahedra (see Fig 4.53). In between the layers are the respective potassium and sodium ions, which hold the layers together through ionic bonding (see Fig 4.53 bottom left and bottom right). The sheet structure for **V−23** (see Fig 4.31 – top right) is different to the potassium analogue (see Fig 4.31 – top left) due to the difference in size of the sodium ion. As Na^+ is smaller the sheet needs to become "puckered" in order to establish the ionic contacts, to hold the structure together. What makes these two materials unique is the method by which they were synthesised. Previously they had been made through a high temperature flux process on a bed of molten lead salt as the solvent, at 600°C. **V−21** and **V−23** were made hydrothermally in an autoclave at 200°C. This discovery opens the potential for further traditional solid state materials to be made in this way, which is cheaper and also easier; an example of which could be the synthesis of multiferroic materials such as $BaMnF_4$.[31]

Bond	Bond Length (Å)	s_{ij}
V1−F1	1.879(1)	0.616
V1−F2	1.881(1)	0.614
V1−F3	1.973(1)	0.478
V1−F4	1.967(1)	0.486
V1−F5	1.964(2)	0.489
V1−F5’	1.966(2)	0.488
		∑V1 = **3.17**

Table 4.34 Selected bond lengths and bond valence sums for **V−21**.

Bond	Bond Length (Å)	s_{ij}
V1−F1	1.950(3)	0.509
V1−F1’	1.967(3)	0.486
V1−F2	1.977(3)	0.473
V1−F2’	1.982(3)	0.467
V1−F3	1.861(3)	0.647
V1−F4	1.888(3)	0.647
		∑V1 = **3.18**

Table 4.35 Selected bond lengths and bond valence sums for **V−23**.

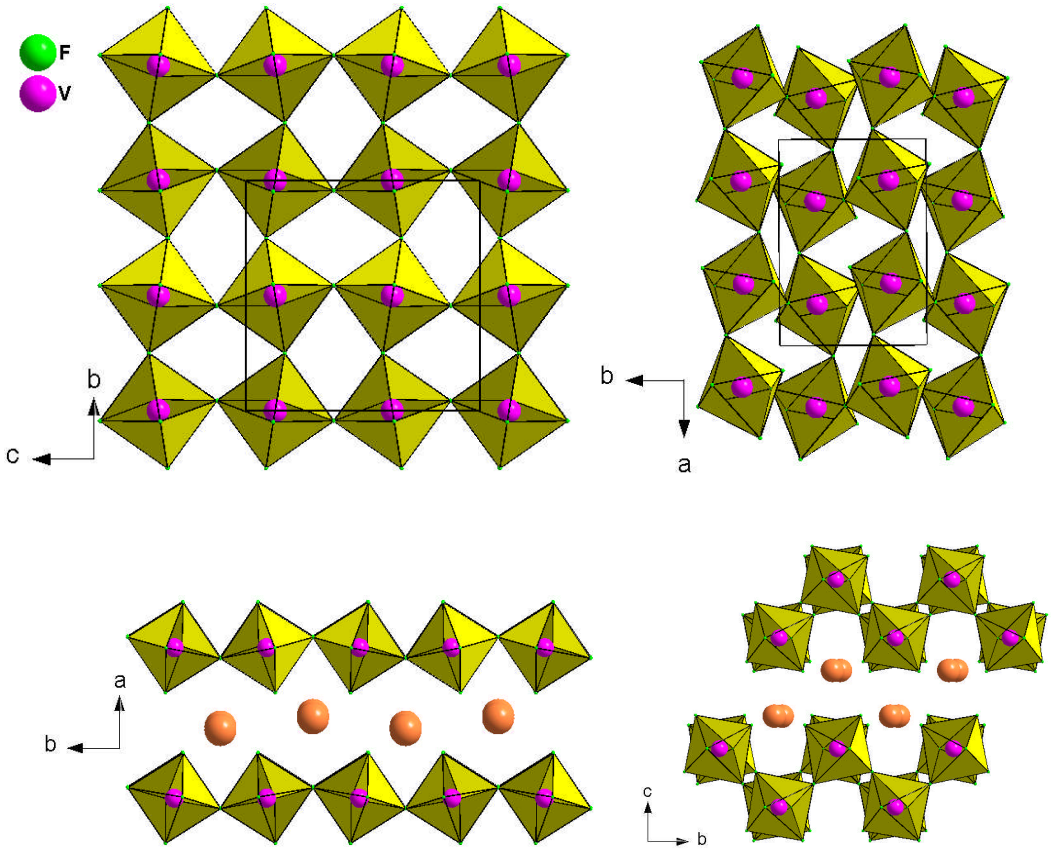

Fig 4.53 The continuous sheets in **V−21** (top left), **V−23** (top right) and the inorganic layers in **V−21** (bottom left) and **V−23** (bottom right).

$K_5V_3F_{14}$ (V−29) has previously been reported[32] but its actual crystal structure was not published. The structure is related to the chiolite phases and consists of alternating *cis* $[VF_2F_{4/2}]$ and *trans* $[VF_4F_{2/2}]$ octahedra (see Fig 4.54 − top). The potassium ions occupy the holes in the lattice and are also situated in between the $[V_3F_{14}]^{5-}$ layers where they hold the lattice together through ionic bonding (see Fig 4.54 − bottom). $K_5V_3F_{14}$, like $NaVF_4$ and KVF_4, was made by a high temperature flux process on a bed of molten lead salt as the solvent, at 600°C with **V−29** being made hydrothermally in a similar process to **V−21** and **V−23** (see Appendix B for the synthesis conditions). Since $K_5V_3F_{14}$ is also a known ferrimagnetic structure[33] with magnetic parameters of μ_{eff} = 2.93 BM and Θ = −77 K; a comparison of these values to those extracted from **V−29** would see if it is the same material. Magnetic susceptibility data were collected for **V−29** (see Fig 4.55) and the results proved to be very close to those published, with magnetic parameters of μ_{eff} = 2.82(1) BM and Θ = −70.8(4) K. The value for μ_{eff} is very close to the theoretical value of 2.83 BM for V^{3+} (Also confirmed by BVS, see Table 4.36). The literature also states that the ordering temperature was at 21±2 K, with the ordering temperature in **V−29** being close at 16 K. This helps to show that both the structural and physical properties of known compounds made by solid state methods can be replicated by hydrothermal reactions.

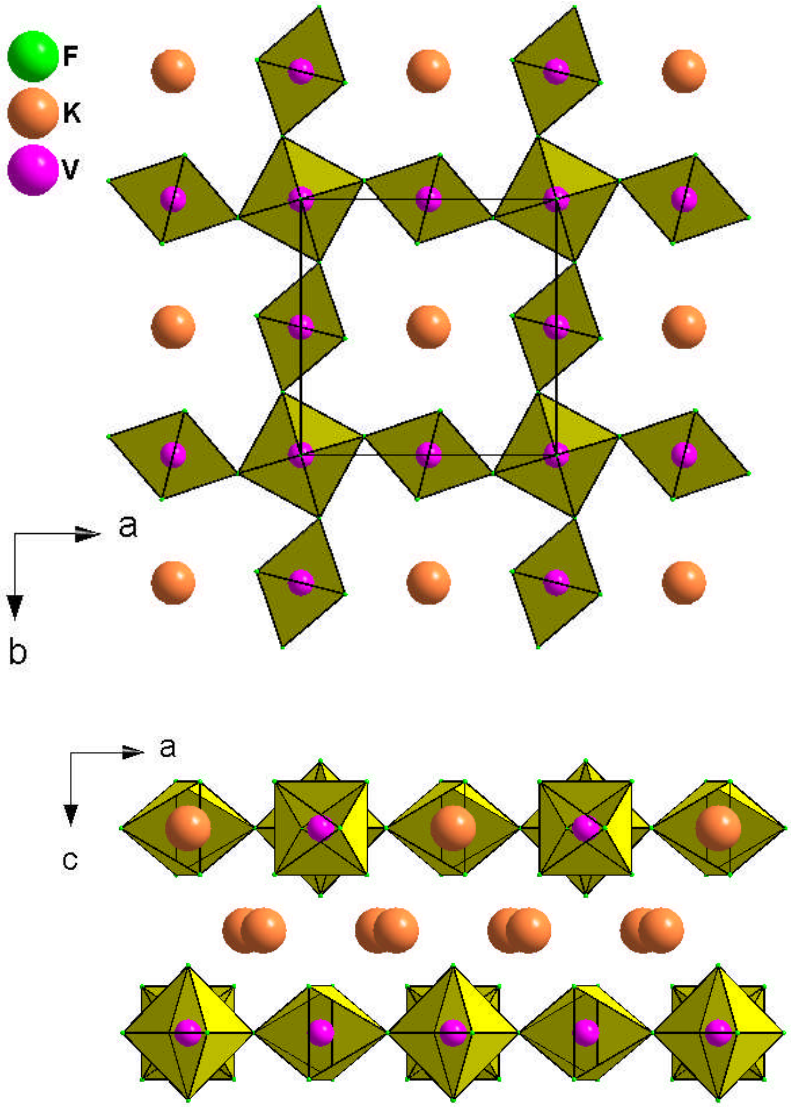

Fig 4.54 The inorganic sheet (top) and layered structure (bottom) in **V−29**

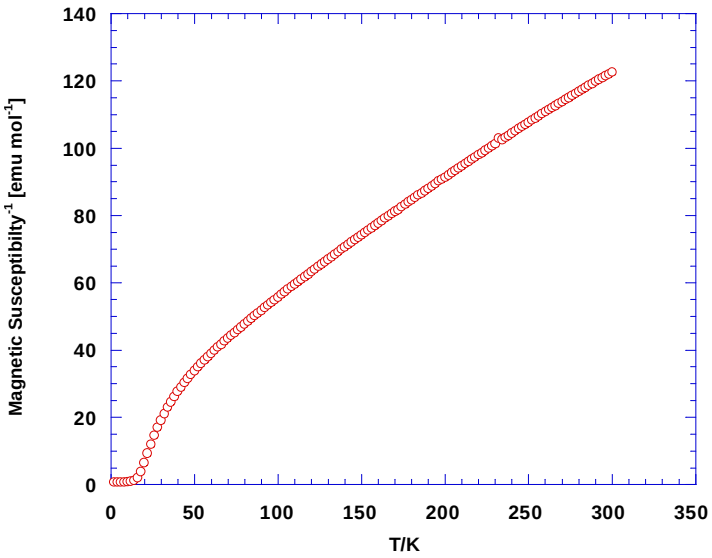

Fig 4.55 χ^{-1} vs. T for **V−29**.

Bond	Bond Length (Å)	s_{ij}	Bond	Bond Length (Å)	s_{ij}
V1−F1	1.903(3)	0.575	V2−F2	1.956(2)	0.501
V1−F1'	1.903(3)	0.575	V2−F2'	1.956(2)	0.501
V1−F1'	1.903(3)	0.575	V2−F2'	1.956(2)	0.501
V1−F1'	1.903(3)	0.575	V2−F2'	1.956(2)	0.501
V1−F2	2.000(2)	0.444	V2−F3	1.920(3)	0.552
V1−F2'	2.000(2)	0.444	V2−F3'	1.920(3)	0.552
		∑V1 = **3.18**			∑V2 = **3.11**

Table 4.36 Selected bond lengths and bond valence sums for **V−29**.

4.3 Synthetic Aspects

4.3.1 Effect of Water Content on Synthesis

The effect of water content on a synthetic reaction can be huge. Too much water and the solution could become too dilute to react or too little water and the solution may form unwanted dense phases, if any at all. All the reactions in this work contained a mix of ethylene glycol and water. If no ethylene glycol was added and pure water solution was used, then no products were formed. Even if no water was added, there would always be some present from the aqueous HF acid used (52% water by volume) and this is displayed in **V−1** where in the reaction conditions there is no added water but it is present in the product. What follows are a few examples of where a simple change in water content can yield different products.

4.3.1.1 Cyclam System

Products **V−10** and **V−11,** are very closely linked with both possessing the same $[V_2O_2F_8]^{4-}$ dimer (see Fig 4.6). Both structures were made from identical solutions except for the water content (see synthetic conditions in Appendix B). **V−10** was made with 2.5 ml of water whilst **V−11** was made with 0.5 ml of water. The noticeable difference this caused was that in the first structure, **V−10**, water is incorporated into the structure where it hydrogen bonds the dimers into a chain (see Fig 4.10). In **V−11**, without water present, the dimers are isolated from one another by the protonated template. The structure of **V−11** is also more condensed with the *intra* V−V dimer-dimer distance being 5.59 Å compared to 6.54 Å in **V−10**.

4.3.1.2 Triethylene Tetramine System

Structures **V−5** and **V−6** both came from almost identical reaction solutions (see synthetic condition in Appendix B), with the only difference being 2 ml of water between them. In **V−5**, 5ml of water was used, to make the *cis* and *trans* $[VOF_4(H_2O)]^{2-}$ monomers (see Fig 4.1). If

the water content in the reaction mixture is reduced by 2 ml, the monomers condense into the $[V_2O_2F_8]^{4-}$ unit in **V−6** (see Fig 4.6).

4.3.1.3 Piperazine System

$[C_4H_{12}N_2]_4[V_4O_3F_{17}]\cdot 4H_2O$ is a structure previously reported in the thesis by N. Stephens.[14] If the same reaction mixture is used but with 3ml less water, instead of the Y-shaped tetramer being formed, the *trans* aqua monomer $[VOF_5(H_2O)]^{2-}$ in **V−26** is produced instead (see synthetic conditions in Appendix B). The simple monmeric unit (see Fig 4.46) consists of a V^{4+} metal centre, unlike the $[V_4O_3F_{17}]^{8-}$ which has a mixture of V^{4+} and V^{3+} in a 3:1 ratio. Why this material does not undergo partial or complete reduction to V^{3+} is unclear but may be due to the rate of formation of the product. The material is also counter-intuitive as since a lower water content was used in the synthesis, a more condensed product would be expected.

4.3.2 Effect of Temperature on Synthesis

Heat can display an enormous effect on the products formed in reactions. In hydrothermal reactions the pressures generated by elevated temperatures can lead to the condensation of structures and also the extra heat can increase the reactivity of reagents. A common feature of the materials in this work is the relationship between the reduction of vanadium and temperature. Several of the examples that follow show this trend as well as the condensation of products at increased temperatures.

4.3.2.1 Piperazine System

The piperazine system is one of the most interesting, with several interrelated products ranging from 0D to 1D structures, all with a Y-shaped motif, as a result of increasing temperature and all with exactly the same ratio of reagents (see synthetic conditions in Appendix B). The start of this at 60 °C is **V−4** (see Fig 4.41), from the hydrogen bonded chains a Y-shaped motif can be seen from the two monomers which hydrogen bond to one end of the dimer. This structure is also only partly reduced, with the monomers having a V^{5+} centre and the dimers having a V^{4+} (average oxidation state is 4.5). If the same reaction solution was heated to 100 °C, the monomers and dimers condensed to produce a Y-shaped tetramer,[14] where further reduction had occurred to bring the average oxidation state down to 3.75. Even further reduction and condensation occurred when the solution was heated to 160 °C, where upon a complex chain, **V−15** (see Fig 4.24), was formed (with an average oxidation state of 3.6) based on the Y-shaped tetramer. A schematic diagram of this is shown below in Fig 4.56. This system continues further when the temperature is increased to 190 °C, where the structure becomes completely reduced to V^{3+} and the zig-zag chain structure of **V−22** is formed (see Fig 4.51). This chain could be considered to be the further condensation of the *cis* corner sharing octahedral elements of the chain, which are already V^{3+}, through the loss of oxide ligands. This system in many ways is analogous to the cobalt succinate system[34] where dimensionality was found to increase proportionally with temperature.

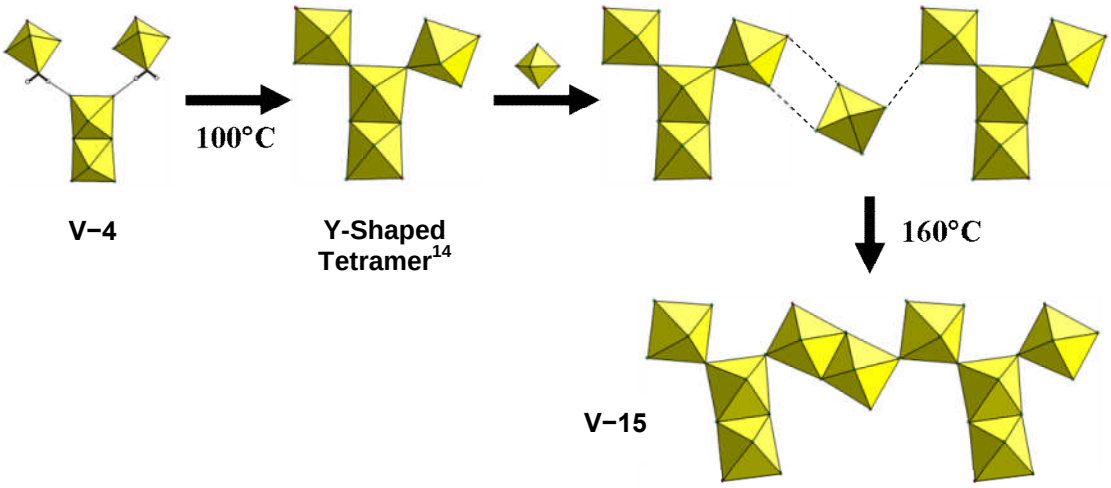

Fig 4.56 A schematic diagram of the progressive condensation and reduction of the piperazine system from 0D to 1D.

4.3.2.2 *Trans* 1,2 Bis (4-Pyridyl) Ethylene System

When the temperature of reaction used to synthesise **V−2** is increased from 100 °C to 160 °C, **V−12** is formed (see synthetic conditions in Appendix B). The structural motif of **V−12** (see Fig 4.20 − top) originates from the chains in **V−2** (see Fig 4.18). If the structures are both viewed down their respective "rails" of the ladder, it is clear to see the link between them (see Fig 4.57). The ladder motif in **V−12** comes from the condensation of the hydrogen bonded chains in **V−2**.

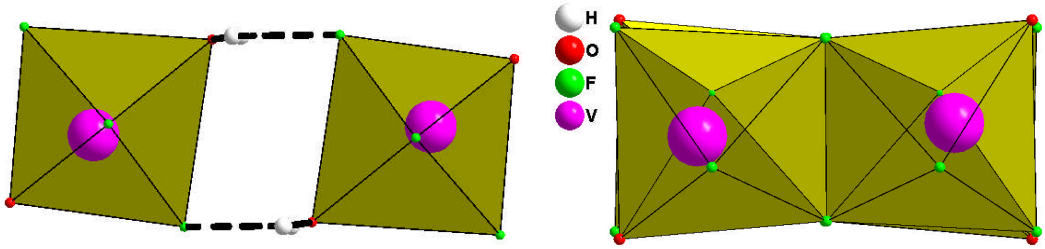

Fig 4.57 The hydrogen bonded and the covalently bonded chains in **V−2 and V−12** respectively.

4.3.2.3 4-4 Bipyridyl System

The hybrid layered material, **V−14**, is formed when the reaction solution used to synthesise **V−3**, is heated to 160 °C (see synthetic conditions in Appendix B). This causes the vanadium to reduce further to V^{3+} and the plane structure is formed (see Fig. 4.38), through the elevated pressures generated above 100 °C.

4.3.2.4 Triethylene Tetramine System

At 100 °C the *trans* aqua monomer $[VOF_5(H_2O)]^{2-}$ in **V−5** is formed (see Fig 4.1), when the temperature of reaction is increased to 160 °C (see synthetic conditions in Appendix B). The vanadium is reduced from V^{4+} to V^{3+}, and the *trans* aqua monomer $[VF_5(H_2O)]^{2-}$ in **V−13**, is formed (see Fig 4.43).

4.3.2.5 Diethylene Triamine System

This system is comparable with the triethylene tetramine system, as a similar reduction occurs upon elevated heating. At 100 °C the mononuclear $[VOF_5]^{3-}$ unit in **V−8** is formed (see Fig 4.42). When the reactants are heated to 160 °C the V^{4+} is reduced to V^{3+} and the $[VF_6]^{3-}$ monomer in **V−20** is formed (see Fig 4.45 and synthetic conditions in Appendix B).

4.3.2.6 Sodium System

The novel dimer in **V−16** (see Fig 4.6) was synthesised at 100 °C, if the reaction solution is heated to 220 °C, then the vanadium centres become reduced and the Dion-Jacobson phase, **V−23**, is formed (see Fig 4.53 − top right and synthetic conditions in Appendix B). The structure has become more condensed as a result of the elevated temperature and resultant pressure.

4.3.2.7 Potassium System

The system is analogous to the sodium system, with the reduction and condensation of the chain in **V−17** at 100 °C (see Fig 4.50) to the Dion-Jacobsen phases in **V−21** at 220 °C (see Fig 4.53 − top left and synthetic conditions in Appendix B). The only difference between the two systems is the dimensionality of the 100 °C material. In the sodium system it is a dimer that is made at 100 °C, where as in the potassium system it is a 1D covalent chain, although both are based around the $[VOF_5]$ monomer motif.

4.3.3 Effect of Cation Ratio on Synthesis

The counter-cation to vanadium ratio is an important variable to consider in these reactions. Higher dimensionality products can be achieved if the ratio is decreased (i.e. lower cation content) as any resultant structure will have to compensate for the loss of charge balancing ions and become more condensed, even if the reaction temperature remains constant. Likewise if the ratio is raised (cation content increased) the inorganic moieties can become more isolated from each other caused by separation from the increased cation content within the structure.

4.3.3.1 Piperazine System

The use of piperazine continues to bear fruit for its astute choice as a counter-cation. If the amount of piperazine is reduced to one third and heated at 190 °C, the zig-zag chain structure

in **V−22** (see Fig 4.51) is no longer formed. Instead, the complex magnetic material, **V−28** (see Fig 4.34 − top), is formed (see synthetic conditions in Appendix B). As the vanadium can no longer be reduced below its current V^{3+} oxidation state, the structure has had to become more condensed and share more fluorine atoms to compensate for the reduction in charge balancing cations in order for the material to remain neutral.

4.3.3.2 Potassium System

The products of reactions can be influenced by the stoichiometric ratio of cations. Originally in the synthesis of **V−21** a mixture of products was produced. After this was discovered the materials were targeted in a more systematic way. So if the potassium content used to synthesise **V−21** (see Fig 4.53 − top left), is increased to the ratio required to form $K_5M^{(III)}{}_3F_{14}$ then the product **V−29** is made (see Fig 4.54 − top) and synthetic conditions in Appendix B). The increase in potassium content is included into the structure through the formation of holes in the layers into which the K^+ ions sit.

4.3.3.3 Diethylene Triamine System

In the piperazine system, where the decrease in the cation content causes the structure to become more condensed, the converse can be said for increasing the cation content in this system. Product **V−27** is formed when the cation content is increased four fold, from the original reaction solution used to create the isolated monomer $[VOF_5]^{3-}$ in **V−8** (see Fig 4.42 and synthetic conditions in Appendix B). The result is the isolated neutral monomer complex, **V−27**, where the diethylene triamine template is bonded to the metal centre via the V−N bonds (see Fig 4.3).

4.4 Structure Summary

Below is a table summarising all the structures in this chapter, the mean vanadium oxidation state and their dimensionality.

Structure	Average Ox. State	Dimensionality
V−1	4	0D
V−2	4	1D
V−3	4	0D
V−4	4.5	0D
V−5	4	0D
V−6	4	0D
V−7	4	0D
V−8	4	0D
V−9	4	0D
V−10	4	0D
V−11	4	0D
V−12	4	1D
V−13	3	0D
V−14	3	2D
V−15	3.6	1D
V−16	4	0D
V−17	4	1D
V−18	4	1D
V−19	4	1D
V−20	3	0D
V−21	3	2D
V−22	3	1D
V−23	3	2D
V−24	4	1D
V−25	4	1D
V−26	4	0D
V−27	4	0D
V−28	3	1D
V−29	3	2D

Table 4.37 A summary of the vanadium (oxy)fluoride structures in this chapter.

4.5 Publications

The work in this chapter has so far resulted in the following publications:

- **Novel vanadium (IV) oxyfluorides with 'spin-ladder'-like structures, and their relationship to $(VO)_2P_2O_7$,** D. W. Aldous, R. J. Goff, J. P. Attfield and P. Lightfoot, *Inorg. Chem*., **2007**, *46*, 1277-1282.

- **Hydrothermal vanadium fluoride chemistry: Four new V^{3+} chain structures,** D. W. Aldous, N. F. Stephens and P. Lightfoot, *Inorg. Chem.,* **2007**, *46*, 3996-4001.

- **Hydrothermal chemistry of oligomeric vanadium oxyfluorides,** D. W. Aldous, N. F. Stephens and P. Lightfoot, *Dalton Trans.,* **2007,** 2271-2282.

- **The role of temperature in the solvothermal synthesis of hybrid vanadium oxyfluorides,** D. W. Aldous, N. F. Stephens and P. Lightfoot, *Dalton Trans.*, **2007**, 4207-4213.

4.6 Synthetic Conditions for V−1 to V−29

Product	V_2O_5 (g)	HF (ml)	H_2O (ml)	EG (ml)	Template	Template Quantity	Temp (°C)	Time (days)
V−1	0.182	1.0	0.0	5.0	(3-aminopropyl) 1,3 propane diamine	0.500ml	60	2
V−2	0.182	1.0	5.0	5.0	Trans 1,2 bis (4-pyridyl) ethylene	0.534g	60	2
V−3	0.182	1.0	3.0	5.0	4-4 Bipyridyl	0.463g	60	4
V−4	0.182	1.0	2.0	5.0	Piperazine	0.258g	60	4
V−5	0.182	1.0	5.0	5.0	Triethylene Tetramine	0.500ml	100	1
V−6	0.182	1.0	3.0	5.0	Triethylene Tetramine	0.500ml	100	1
V−7	0.182	1.0	5.0	5.0	1,2 diamino Cyclohexane	0.500ml	100	1
V−8	0.182	1.0	2.0	5.0	Diethylene Triamine	0.500ml	100	1
V−9	0.182	1.0	0.0	5.0	1,2 Bis (3-aminopropylamino) ethane	0.500ml	100	3
V−10	0.091	0.5	2.5	2.5	Cyclam	0.296g	100	⅛
V−11	0.091	0.5	0.5	2.5	Cyclam	0.296g	100	⅛
V−12	0.182	1.0	5.0	5.0	Trans 1,2 bis (4-pyridyl) ethylene	0.534g	160	1
V−13	0.182	1.0	3.0	5.0	Triethylene tetramine	0.500ml	160	1
V−14	0.182	1.0	3.0	5.0	4-4 Bipyridyl	0.463g	160	1
V−15	0.182	1.0	2.0	5.0	Piperazine	0.258g	160	1
V−16	0.091	0.5	0.0	2.5	Sodium Carbonate	0.160g	100	1
V−17	0.182	0.5	5.0	5.0	Potassium Nitrate	0.300g	100	1
V−18	0.182	0.5	2.0	5.0	Rubidium Chloride	0.360g	100	1
V−19	0.182	0.5	0.0	5.0	Caesium Chloride	0.500g	100	1
V−20	0.182	0.5	4.0	5.0	Diethylene Triamine	0.500ml	190	1
V−21	0.182	0.5	1.0	5.0	Potassium Chloride	0.300g	220	1
V−22	0.182	0.5	3.0	5.0	Piperazine	0.258g	190	1
V−23	0.182	0.5	4.0	5.0	Sodium Nitrite	0.200g	220	1
V−24	0.182	0.5	0.0	5.0	Pyrazine Carboxamide	0.370g	100	1
V−25	0.182	0.5	1.0	5.0	Trans 1,2 bis (4-pyridyl) ethane	0.550g	160	1
V−26	0.182	0.5	1.0	5.0	Piperazine	0.258g	100	1
V−27	0.182	0.5	0.0	5.0	Diethylene Triamine	2.000ml	100	1
V−28	0.182	0.5	0.0	5.0	Piperazine	0.086g	190	1
V−29	0.182	0.5	5.0	5.0	Potassium Chloride	0.350g	220	1

References

1. G. M. Sheldrick, Institüt für Anorganische Chemie der Universität, Tammanstrasse 4, D-3400 Göttingen, Germany, **1998**.
2. T. S. Cameron, A. Decker, E. G. Ilyin, G. B. Nikiforov and J. Passmore, *Eur. J. Inorg. Chem.*, **2004**, 3865.
3. "Inorganic Solid Fluorides"; P. Hagenmuller (Editor), Academic Press: London, 1985.
4. "Advanced Inorganic Fluorides": Synthesis, Characterisation and Applications, T. Nakajima, B. Zemva and A. Tressaud (Editors), Elsevier Science, S.A, 2000.
5. H. Rieskamp and R. Mattes, *Z. Naturforschung. B – Chem. Sci*., **1976**, 31, 541.
6. R. L. Carlin, R. Burriel, J. A. Rojo and F. Palacio, *Inorg. Chem.*, **1984**, 2213.
7. L. Schroeder, G. Frenzen, W. Massa and D.-H. Menz, *Z. Anorg. Allg. Chem.*, **1993**, 619, 1307.
8. L. Schroeder, *Thesis*, University of Marburg, 1995.
9. D. C. Johnston, J. W. Johnson, D. P. Goshorn and A. J. Jacobson, *Phys. Rev. B*, **1987**, 35, 219.
10. H. J. Hoo, M. H. Whangbo, P. D. VerNooy, C. C. Torardi and W. J. Marshall, *Inorg. Chem.*, **2002**, 41, 4664.
11. E. E. Kaul, H. Rosner, V. Yushankai, J. Sichelschmidt, R. V. Shpanchenko and C. Geibel, *Phys. Rev. B*, **2003**, 67, 174417.
12. "Magnetochemistry"; R. L. Carlin, Springer, Berlin, 1986.
13. C. P. Landee, M. M. Turbill, C. Galeriu, J. Giantsidis and F. M. Woodward, *Phys. Rev. B*, **2001**, 63, 100402.
14. N. F. Stephens, *Thesis*, University of St Andrews, 2006.
15. D.Babel and G. Knoke, *Z. Anorg. Allg. Chem.*, **1978**, 442, 151.
16. O. Kampe, C. Frommen and J. Pebler, *Naturforschung. B – Chem. Sci*., **1993**, 48, 1112.
17. P. Lacorre, M. Leblanc, J. Pannetier and G. Férey, *J. Magn. Mag. Mater.*, **1991**, 94, 337.
18. P. Lacorre, M. Leblanc, J. Pannetier and G. Férey, *J. Magn. Mag. Mater.,* **1987**, 66, 337.
19. A. P. Ramirez, *Annu*. *Rev. Mater. Sci.*, **1994**, 24, 453.
20. J. Darriet, W. Massa, J. Pebler and R. Stoef, *Solid State Sci*., **2002**, 4, 1499.
21. G. Pausewang and W. Ruedoff, *Z. Anorg. Allg. Chem.*, **1969**, 364, 69.
22. R. Pirani, *Gazzetta Chimica Italiana*, **1932**, 62, 380.
23. R. Pirani, *Gazzetta Chimica Italiana*, **1932**, 62, 381.
24. N. F. Stephens, M. Buck and P. Lightfoot, *J. Mater. Chem.*, **2005**, 15, 4298.
25. P. Bukovec, S. Milicev, A. Demsar and L. Golic, *Dalton Trans.*, **1981**, 1802.
26. K. Walterson and B. Karlason, *Cryst. Struct. Comm.*, **1978**, 7, 459.
27. A. Carpy, *Thesis*, University of Bordeaux, 1973.
28. A. J. Edwards and G. R. Jones, *J. Chem. Soc. A*, **1969**, 1651.

29. B. J. Garrard, S. H. Smith, B. M. Wanklyn and G. Garton, *J. Cryst. Growth*, **1975**, 29, 301.
30. D. Babel and B. Peschel., *Z. Anorg. Allg. Chem.*, **1997**, 623, 1614.
31. M. Yoshimura, M. Hidaka, T. Mizushima, J. Sakurai, T. Tsuboi and W. Kleeman, *J. Magn. Mag. Mater.,* **2006**, 299, 404.
32. B. M. Wanklyn, B. J. Garrard, F. Wondre and W. Davidson, *J. Cryst. Growth*, **1976**, 33, 165.
33. C. Cros, J-M. Dance, J-C. Claude, B. M. Wanklyn and B. J. Garrard, *Mater. Res. Bull.*, **1977**, 12, 415.
34. P. M. Forster, A. R. Burbank, C. Livage, G. Férey and A. K. Cheetham, *Chem. Comm.*, **2004**, 368.

5.0 Molybdenum Oxyfluoride Materials

In this chapter, the crystal structures and hydrothermal chemistry of 9 molybdenum oxyfluoride structures will be discussed. These materials have been synthesised and denoted from **Mo−1** to **Mo−9** (numbered in chronological order in which they were synthesised). The structures range from the unusual neutral $[Mo_2O_4F_2]$ dimer to 1D $[Mo_2O_2F_6]^{2-}$ chains. The crystallographic information for these compounds is presented in Tables 5.1 and 5.2. The synthetic conditions are given at the end of the chapter with the elemental analysis for each structure in Appendix C (on the accompanying CD). Atomic co-ordinates are located in Appendix A (on the accompanying CD). Bond angles and hydrogen bonds are all contained in the appropriate CIF file (see enclosed CD).

Single crystals were analysed using either a Rigaku Mercury CCD equipped with confocal optics Mo-Kα radiation or a Rigaku SCX-Mini equipped with graphite monochromated Mo-Kα radiation, see the appropriate CIF for details. Intensity data were collected by the narrow frame method and corrected for Lorentz and polarization effects as well as absorption by Multi-Scan techniques. All structures were solved by direct methods and refined by full-matrix least-squares cycles in SHELX-97[1]. All non-hydrogen atoms were refined with anisotropic thermal parameters (except where stated). Hydrogen atoms attached to C and N were located at geometrically calculated positions and refined with isotropic thermal parameters, while those attached to O were found, where possible, by Fourier techniques and refined isotropically.

The synthesis of materials **Mo−1** to **Mo−9** was carried out in a systematic manner which started from a few simple reactions at 100°C. Simple linear amines and alkali metals were used to carry on similar reactions to those done previously (see Chapter 4). Water content was again used as the main variable at 100°C.

Once a novel (or known) compound was synthesised at 100°C, the effect of variation in temperature and cation ratio was explored, which produced a further five new structures. The only exception to this rule was the synthesis of structure **Mo−9**, which did not yield any products below 190°C. Further reactions were carried out after the choice of template, piperazine, had proved to be very successful in the synthesis of several novel vanadium oxyfluoride materials (see **V−4**, **V−15**, **V−21**, **V−26** and **V−28** in Chapter 4). A more detailed discussion of the synthetic aspects is given in subsection 5.3.

Table 5.1 Crystallographic Information for **Mo−1** to **Mo−5**.

Compound	**Mo−1**	**Mo−2**	**Mo−3**	**Mo−4**	**Mo−5**
Formula	$[C_2H_{10}N_2]_2[Mo_2O_5F_6]$	$[C_6H_{21}N_4]_2[MoO_2F_4]_2[F]_2{\cdot}H_2O$	$[C_{10}H_{10}N_2][MoO_2F_4]$	$[C_{12}H_{12}N_2][MoO_2F_4]$	$[NH_4]_6[Mo_4O_8F_{10}]$
Space Group	C 2/c (15)	C 2/c (15)	P 2_1/a (14)	P -1 (2)	Pmnn (58)
a/ Å	17.686(3)	25.735(3)	6.891(1)	8.174(1)	6.309(1)
b/ Å	6.326(1)	11.025(1)	23.695(5)	8.953(2)	9.457(2)
c/ Å	13.510(2)	21.586(2)	7.094(1)	10.509(2)	14.957(3)
α/°				114.139(3)	
β/°	108.485(4)	111.846(3)	93.097(5)	91.636(2)	
γ/°				105.372(4)	
V/ Å^3	1433.6(4)	5683.3(10)	1156.7(4)	668.5(2)	892.4(3)
Z	4	8	4	2	2
ρ_{calc}/ g cm^{-3}	2.364	1.777	2.079	1.929	2.924
μ/ mm^{-1}	1.844	0.985	1.187	1.034	2.889
Crystal Size/ mm	0.2 x 0.2 x 0.2	0.25 x 0.12 x 0.12	0.10 x 0.05 x 0.02	0.15 x 0.08 x 0.08	0.10 x 0.03 x 0.03
F(000)	1000	3072	712	384	728
Reflns Collected	4566	26571	7921	4629	5428
Independent Reflns	1775	6510	2983	3288	898
R_{int}	0.0226	0.0897	0.0365	0.0145	0.0221
Obsd data [$I > 2\sigma(I)$]	1304	3907	2066	2322	868
Data/restraints/parameters	1775/0/96	6510/0/335	2983/0/172	3288/0/190	898/0/76
GOF on F^2	1.128	1.151	1.073	1.082	1.249
*R*1, *wR*2 [$I > 2\sigma(I)$]	0.0247, 0.0608	0.0927, 0.1655	0.0553, 0.1190	0.0291, 0.0605	0.0320, 0.0810
*R*1, *wR*2 (all data)	0.0281, 0.0635	0.1478, 0.1694	0.0660, 0.1275	0.0332, 0.0643	0.0333, 0.0819

Table 5.2 Crystallographic Information for **Mo−6** to **Mo−9**.

Compound	**Mo−6**	**Mo−7**	**Mo−8**	**Mo−9**
Formula	$[C_2H_8N_2]_2[Mo_2O_4F_2]\cdot C_2H_6O_2$	$K_6Mo_4O_8F_{10}$	$K_{14}[Mo_2O_2F_9]_2[MoOF_5]_4\cdot 2C_2H_6O_2$	$[C_4H_{12}N_2]_{0.5}[MoOF_3]$
Space Group	C 2/c (15)	Pmnn (58)	Immm (71)	C 2/c (15)
a/ Å	21.006(3)	6.047(1)	6.076(1)	15.616(9)
b/ Å	6.056(1)	9.351(1)	11.170(1)	8.355(5)
c/ Å	11.272(1)	14.487(2)	19.088(2)	9.517(6)
α/°				
β/°	97.324(4)			118.467(7)
γ/°				
V/ Å^3	1422.3(3)	819.4(2)	1295.5 (1)	1091.6(11)
Z	4	2	1	8
ρ_{calc}/ g cm^{-3}	2.252	3.795	2.919	2.592
μ/ mm^{-1}	1.827	4.656	3.172	2.370
Crystal Size/ mm	0.22 x 0.15 x 0.08	0.10 x 0.10 x 0.03	0.44 x 0.35 x 0.23	0.19 x 0.17 x 0.15
F(000)	952	872	1064	816
Reflns Collected	7260	4889	6580	6598
Independent Reflns	1693	1030	876	1925
R_{int}	0.1131	0.0274	0.0455	0.0226
Obsd data [$I > 2\,\sigma(I)$]	1248	896	853	1656
Data/restraints/parameters	1693/0/95	1030/0/76	876/53/61	1925/0/73
GOF on F^2	1.231	1.260	1.448	1.106
*R*1, *wR*2 [$I > 2\,\sigma(I)$]	0.0985, 0.1436	0.0419, 0.0840	0.0899, 0.2194	0.0285, 0.0663
*R*1, *wR*2 (all data)	0.1393, 0.1517	0.0456, 0.0852	0.0931, 0.2207	0.0321, 0.0682

5.1 New Oligomers and Polymers

The structures in this sub-section are new inorganic oligomers and polymeric compounds i.e. the inorganic moiety of the structure has not previously been reported. In the last 20 years two significant reviews have been published which, as of 2000, methodically cover most known transition metal oxyfluorides. These reviews are by Hagenmuller[2] and by Nakajima, Žemva and Tressaud[3].

5.1.1 Dimers

$[C_2H_{10}N_2]_2[Mo_2O_5F_6]$ (Mo−1) is based on one crystallographically unique Mo^{6+} site (see Table 5.3) related to another Mo^{6+} site through a 2-fold axis to form a corner-sharing dimer (see Fig 5.1). The dimer in **Mo−1** is very similar to that in $Ag_3Mo_2O_4F_7(C_4H_4N_2)_3$[4] (see Table 5.4 and Fig 5.2 − left) with the main difference being the bridging atom in the $[Mo_2O_4F_7]^{3-}$ dimer is fluorine and in **Mo−1** it is oxygen. The dimers in $Ag_3Mo_2O_4F_7(C_4H_4N_2)_3$ go on to form a layers with the Ag^+ cations, which are then bonded to the pyrazine template to make the 3D structure which consists of inorganic layers pillared by pyrazine (see Fig 5.3). The dimers in **Mo−1** are isolated from one another by the template and the complete structure is held together through hydrogen bonding from the protonated template, ethylene diamine, to the non-bridging atoms e.g. F1. A *trans* effect is seen from O1 and O2 on F1 and F3 with their bonds being lengthened to 2.084 Å and 2.151 Å respectively, as a result.

Bond	Bond Length (Å)	s_{ij}
Mo1−O1	1.707(2)	1.720
Mo1−O2	1.702(2)	1.743
Mo1−O3	1.901(1)	1.009
Mo1−F1	2.084(2)	0.474
Mo1−F2	2.007(2)	0.584
Mo1−F3	2.151(2)	0.396
		∑Mo1 = 5.94

Table 5.3 Selected bond lengths and bond valence sums for **Mo−1**.

Bond	Bond Length (Å)
Mo1−O1	1.705(3)
Mo1−O2	1.749(3)
Mo1−F1	2.185(4)
Mo1−F2	1.928(2)
Mo1−F3	1.978(2)
Mo1−F4	1.904(3)

Table 5.4 Selected bond lengths for $Ag_3Mo_2O_4F_7(C_4H_4N_2)_3$.[4]

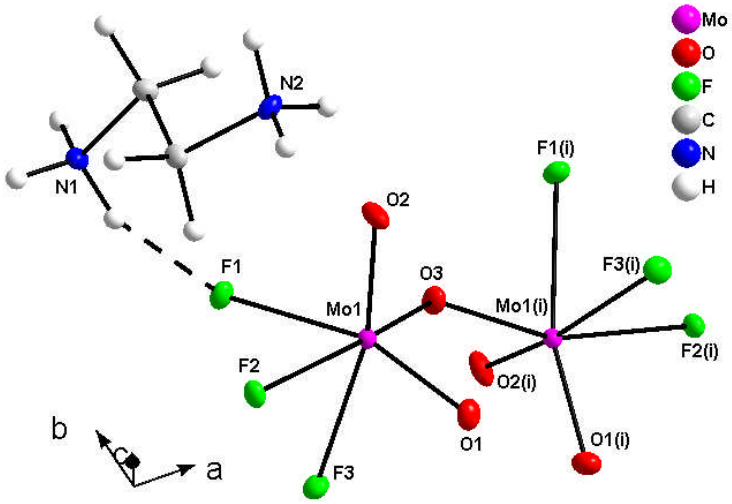

Fig 5.1 The building unit in **Mo−1**. Symmetry operator (i) 1-*x*, *y*, 1/2-*z*.

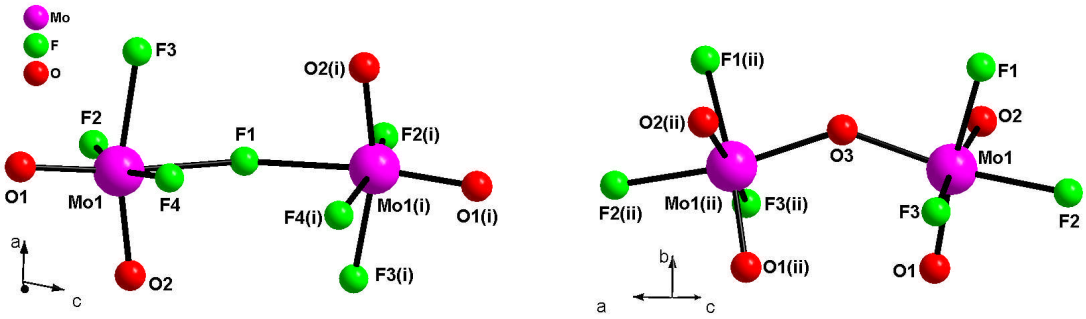

Fig 5.2 The dimers in $Ag_3Mo_2O_4F_7(C_4H_4N_2)_3$[4] and **Mo−1** respectively .
Symmetry operator (i) 5/2-*x*, *y*, 1/2-*z*, (ii) 1-*x*, *y*, 1/2-*z*.

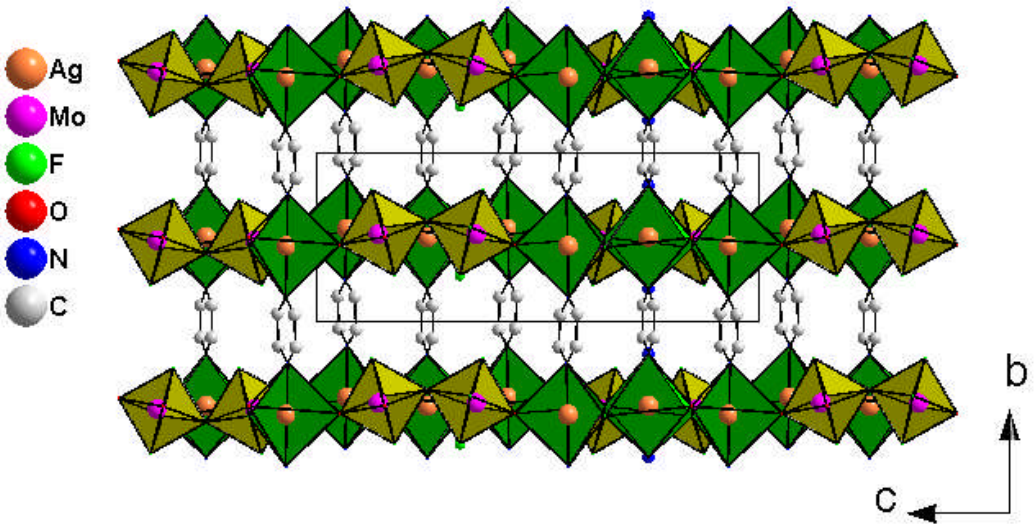

Fig 5.3 The pyrazine-bridged layers in $Ag_3Mo_2O_4F_7(C_4H_4N_2)_3$.[4]

$[C_2H_{18}N_2]_2[Mo_2O_4F_2]\cdot C_2H_6O_2$ (Mo−6) is an unusual compound and can be compared to **V−27** (see Chapter 4.1.1) for its neutral inorganic component; the $[Mo_2O_4F_2]$ dimer (see Fig 5.4). The structure is based on one crystallographically unique Mo^{5+} metal centre (see Table 5.5) which is related to another Mo^{5+} metal centre through a centre of symmetry. The dimer consists of two edge-sharing monomers, with two of the ligands on the Mo atom being nitrogen atoms from the ethylene diamine template. The dimer is disordered with F1 and F2 being a mix of fluorine and oxygen (although for simplicity they are labelled as fluorine in Fig 5.4). The disordered atoms cannot be purely oxygen as the bond lengths are too long for a vanadyl bond and there is also no evidence of OH groups either. There is also a short Mo-Mo distance in the dimer at 2.522(4) Å which indicates that there may be some metal-metal bonding in the structure. In comparison, the face-sharing dimer[5] in $[Cu(3\text{-apy})_4]_3[Mo_2O_6F_3]_2$ has a Mo-Mo distance of 3.171(1) Å, which is too far for a metal-metal interaction.

The dimers hydrogen bond to one another through the nitrogen atoms, N1 and N2, to the fluorine atoms, F1 and F2, to form an inorganic layer in the *bc* plane (see Fig 5.5). These layers are then held together by the additional organic species, ethylene glycol, to form an inorganic-organic sandwich as seen in Fig 5.6. The organic species is confirmed as ethylene glycol and not ethylene diamine through CHN analysis (calc (%): C 14.95, H 4.60, N 11.62, found (%): C 13.62, H 4.45, N 11.76), as an additional molecule of ethylene diamine would give elemental percentages of C 15.20, H 5.10, N 17.72.

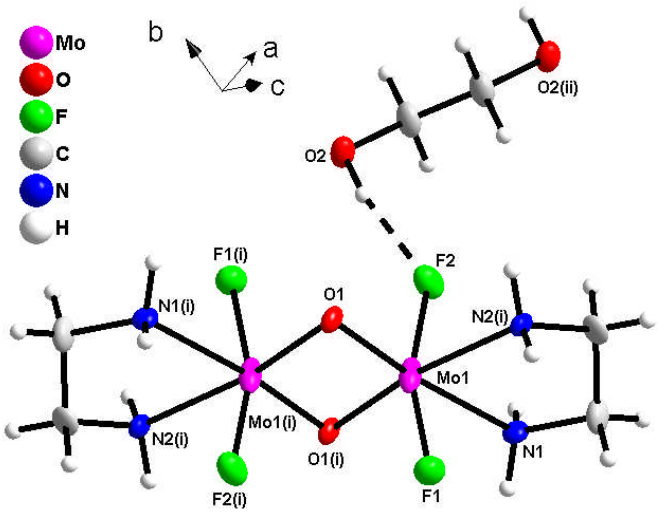

Fig 5.4 The building unit in **Mo−6**. Symmetry operators (i) 1/2-*x*, 1/2-*y*, 1-*z*, (ii) 1-*x*, 1-*y*, 1-*z*.

Bond	Bond Length (Å)	s_{ij}
Mo1−O1	1.877(6)	1.086
Mo1−O1’	1.934(6)	0.931
Mo1−F1*	1.842(5)	0.456
Mo1−F2*	1.885(5)	0.406
Mo1−O2*	1.842(5)	0.597
Mo1−O3*	1.885(5)	0.532
Mo1−N1	2.227(7)	0.555
Mo1−N2	2.149(6)	0.685
		∑Mo1 = 5.25

Table 5.5 Selected bond lengths and bond valence sums for **Mo−6**.
* = Disordered atoms.

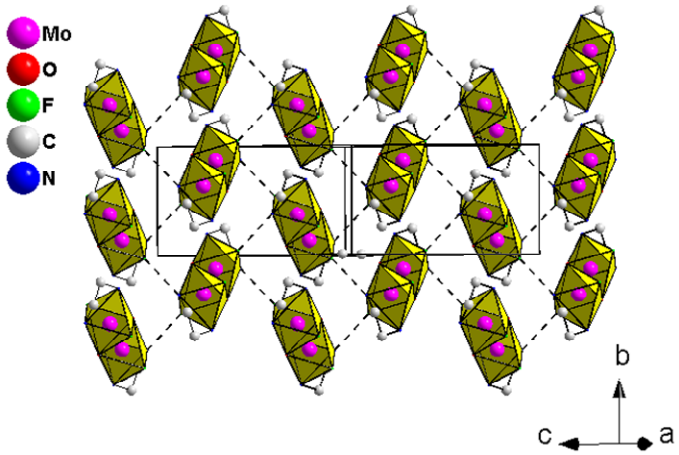

Fig 5.5 The hydrogen bonded layer in **Mo−6**.
Hydrogen atoms have been removed for clarity.

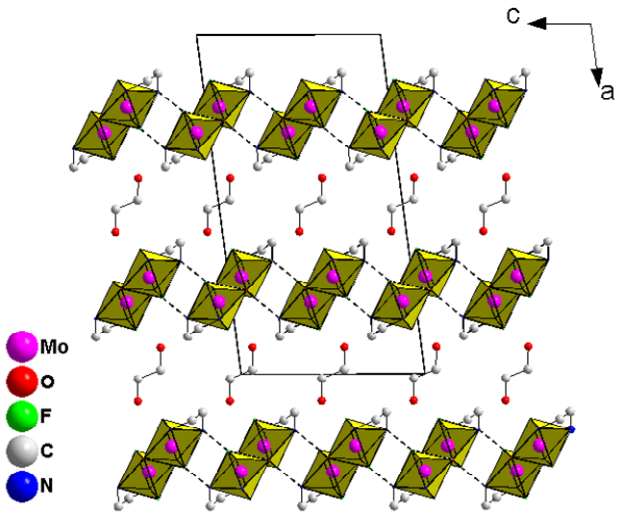

Fig 5.6 The ethylene glycol templated layers in **Mo−6**.
Hydrogen atoms have been removed for clarity.

5.1.2 Tetramers

$[NH_4]_6[Mo_4O_8F_{10}]$ (Mo−5) and $K_6Mo_4O_8F_{10}$ (Mo−7) are isostructural with one another and are based on the tetramer in Fig 5.7 which is composed of two corner sharing $[Mo_2F_4F_{2/2}O_2O_{2/2}]$ dimers. The two Mo^{5+} metal centres (see Tables 5.6 and 5.7) are related to another two Mo^{5+} metal centres through an inversion centre to form the tetramer. The Mo1−F3 and Mo2−F3 bonds are lengthened to 2.152(5) Å and 2.173(4) Å respectively by a *trans* effect from the short Mo1−O1 and Mo2−O2 bonds. The tetramers may also contain some metal-metal bonding through the molybdenum atoms connected by an edge, as they are close together at a distance of 2.552(1) Å and 2.542(1) Å for **Mo−5** and **Mo−7**, respectively.

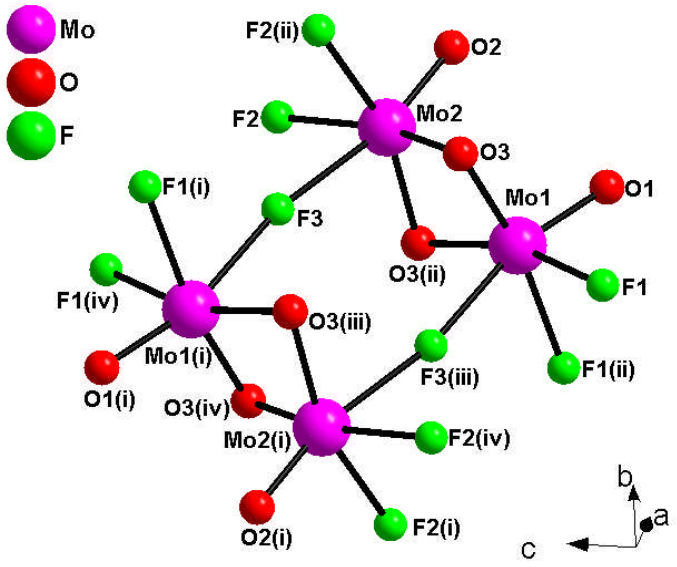

Fig 5.7 The tetramer in **Mo−5** and **Mo−7**. Symmetry operators (i) *x*, *-y*, 1-*z*, (ii) *–x*, *y*, *z*, (iii) *x*, *-y*, 1-*z*, (iv) *–x*, *-y*, 1-*z*.

Bond	Bond Length (Å)	s_{ij}	Bond	Bond Length (Å)	s_{ij}
Mo1−O1	1.690(5)	1.801	Mo2−O2	1.674(5)	1.881
Mo1−O3	1.948(4)	0.897	Mo2−O3	1.950(4)	0.892
Mo1−O3	1.948(4)	0.897	Mo2−O3	1.950(4)	0.892
Mo1−F1	2.040(3)	0.534	Mo2−F2	2.049(3)	0.521
Mo1−F1	2.040(3)	0.534	Mo2−F2	2.049(3)	0.521
Mo1−F3	2.152(4)	0.395	Mo2−F3	2.173(4)	0.373
		∑Mo1 = 5.06			**∑Mo2 = 5.08**

Table 5.6 Selected bond lengths and bond valence sums for **Mo−5**.

Bond	Bond Length (Å)	s_{ij}	Bond	Bond Length (Å)	s_{ij}
Mo1−O1	1.689(6)	1.806	Mo2−O2	1.679(6)	1.855
Mo1−O3	1.938(4)	0.921	Mo2−O3	1.948(4)	0.897
Mo1−O3	1.938(4)	0.921	Mo2−O3	1.948(4)	0.897
Mo1−F1	2.016(3)	0.570	Mo2−F2	2.041(3)	0.533
Mo1−F1	2.016(3)	0.570	Mo2−F2	2.041(3)	0.533
Mo1−F3	2.153(5)	0.394	Mo2−F3	2.156(4)	0.390
		∑Mo1 = 5.18			**∑Mo2 = 5.11**

Table 5.7 Selected bond lengths and bond valence sums for **Mo−7**.

The main building unit of these structures is shown in Fig 5.8, with **Mo−5** being used as an example. The ammonium cations are all fairly close to the non-bridging fluorine atoms at a range 2.795 Å to 2.936 Å (these distances are also typical for the K^+ analogue, **Mo−7**). The material is then comprised of either hydrogen bonding or ionic bonding for **Mo−5** or **Mo−7** respectively, to form the 3D structure for which the interstitial packing is shown in Fig 5.9 (with **Mo−7** being used as the example).

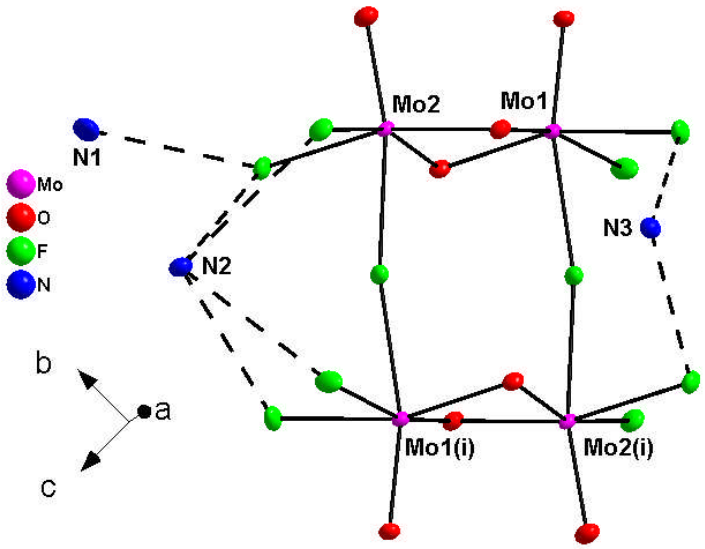

Fig 5.8 The building unit in **Mo−5**. Symmetry operator (i) *x*, *-y*, 1-*z*. Hydrogen atoms have been removed for clarity.

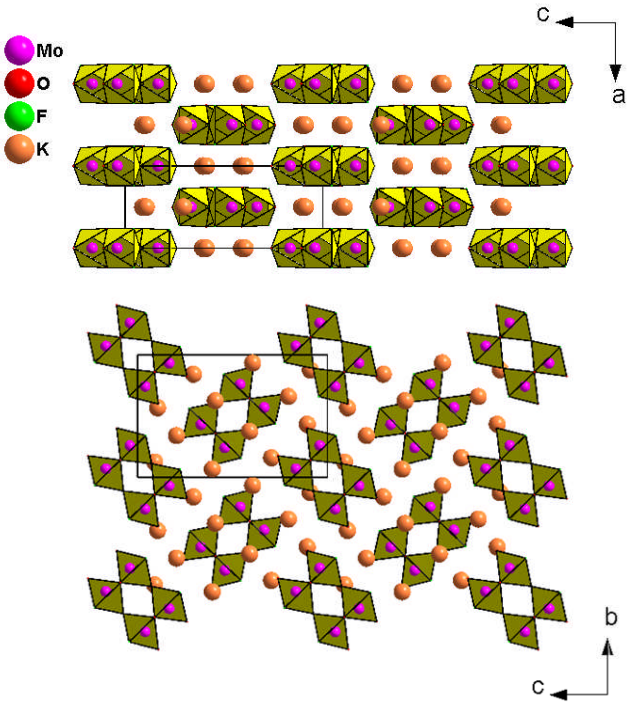

Fig 5.9 The interstitial packing in **Mo−7**.

5.1.3 Chain Structures

$[C_4H_{12}N_2]_{0.5}[MoOF_3]$ (Mo−9) is an elongated zig-zag chain structure (see Fig 5.10) based on a *cis* corner-sharing $[MoO_1F_1F_{4/4}]$ monomer. The asymmetric unit consists of a Mo^{4+} metal centre (see Table 5.8), three fluorine atoms and one oxygen atom and half the piperazine template (which is situated on an inversion centre). The chains run parallel to the *c*-axis (see Fig 5.11) and are surrounded along their length by the protonated template, piperazine. The structure is held together through hydrogen bonding from the non-bridging fluorine atom, F1, to the template. The chain also experiences metal-metal interactions through the edge mediated by F3 and its symmetry equivalent. The resulting Mo-Mo distance is 2.544(8) Å which causes the Mo-F3 bond to become slightly shortened as a result. In contrast the Mo-Mo distance in the dimer mediated by F2 is 3.629(4) Å, signifying no direct interaction.

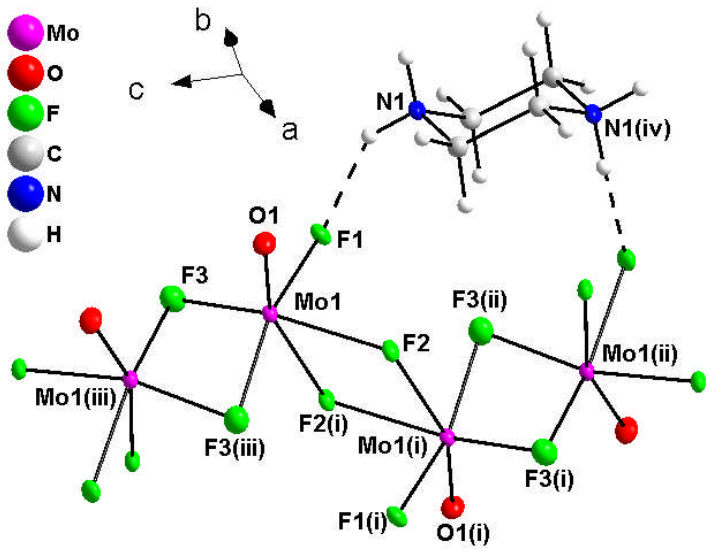

Fig 5.10 The building unit in **Mo−9**. Symmetry operators (i) 1-*x*, 1-*y*, -*z*, (ii) *x*, 1-*y*, -1/2-*z*, (iii) 1-*x*, *y*, 1/2-*z*, (iv) 1/2-*x*, 3/2-*y*, -1-*z*.

Bond	Bond Length (Å)	s_{ij}
Mo1−O1	1.685(2)	1.825
Mo1−F1	2.118(2)	0.433
Mo1−F2	2.174(2)	0.372
Mo1−F2’	2.214(2)	0.334
Mo1−F3	1.973(2)	0.640
Mo1−F3’	2.043(2)	0.530
		∑Mo1 = 4.13

Table 5.8 Selected bond lengths and bond valence sums for **Mo−9**.

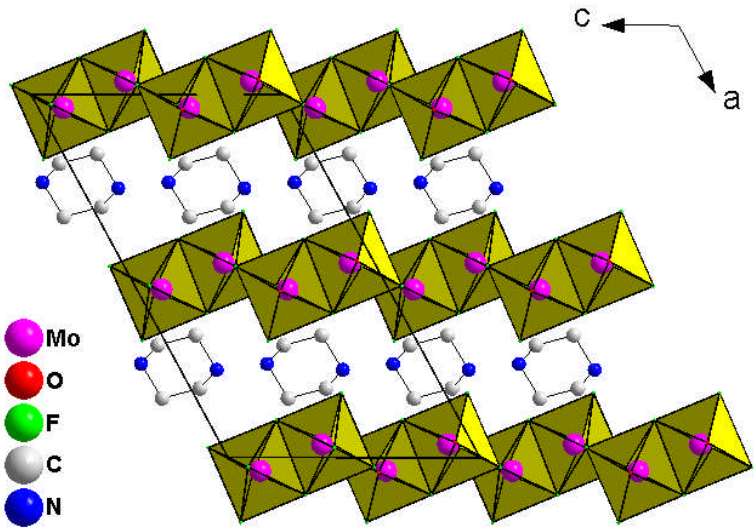

Fig 5.11 The lattice packing in **Mo−9**. Hydrogen atoms have been removed for clarity.

5.2 Existing Oligomers

The novel crystal structures contained in this sub-section are inorganic oligomers which have either been made by a different route of synthesis to that previously reported or made with a different organic/inorganic cation. The table below is a list of the first examples of some different known structure types for molybdenum (oxy)fluorides.

Chemical Formula	Structure Type	Ox. State	Ref
KRb_2MoF_6	Monomer	III	6
Li_2MoF_6	Monomer	IV	7
$NaMoF_6$	Monomer	V	8
$K_2(MoOF_5)\cdot H_2O$	Monomer	V	9
$K_2Na(MoO_3F_3)$	Monomer	VI	10
$K_2(MoO_2F_4)\cdot H_2O$	Monomer	VI	11
$CsMoF_7$	Monomer	VI	12
$(C_{10}H_8N_2)MoO_2F_2$	Monomer	VI	13
$K_2(C_4H_{12}N)(Mo_2OF_9)\cdot H_2O$	Dimer	V	14
$(NH_4)_2(Mo_2O_4F_4(H_2O)_2)$	Dimer	V	15
$(NH_4)_3(Mo_2O_2F_9)\cdot 0.9H_2O$	Dimer	V	16
$(C_5H_5N)_4Mo_2F_6$	Dimer	III	17
$Ag_3Mo_2O_4F_7(C_4H_4N_2)_3$	Dimer	VI	4
MoF_5	Tetramer	V	18
$CsMoO_2F_3$	Zig-Zag Chains	VI	19
MoO_2F	3D	V	20

Table 5.9 Some of the known structure types of molybdenum (oxy)fluorides.

5.2.1 Monomers

$[C_6H_{21}N_4]_2[MoO_2F_4]_2[F]_2{\cdot}H_2O$ (Mo−2), **$[C_{10}H_{10}N_2][MoO_2F_4]$ (Mo−3)** and **$[C_{12}H_{12}N_2][MoO_2F_4]$ (Mo−4)** are all based on the previously reported[11] $[MoO_2F_4]^{2-}$ monomer shown in Fig 5.12.

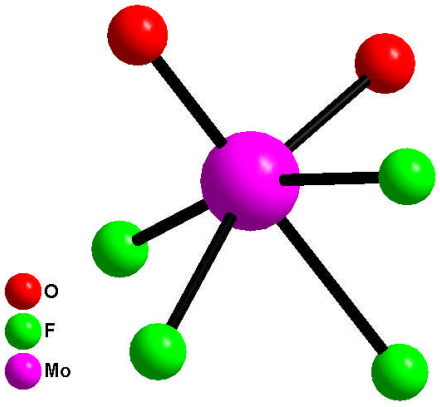

Fig 5.12 The $[MoO_2F_4]^{2-}$ monomer[11] in **Mo−2**, **Mo−3** and **Mo−4**.

The asymmetric unit in **$[C_6H_{21}N_4]_2[MoO_2F_4]_2[F]_2{\cdot}H_2O$ (Mo−2)** consists of two crystallographically different Mo^{6+} $[MoO_2F_4]^{2-}$ monomers (see Table 5.10), two moieties of the protonated template, tris (2-aminoethyl) amine (see Chapter 3 − Fig 3.1), a molecule of water and two fluoride anions (see Fig 5.13). The four Mo−F bonds (Mo1−F1, Mo1−F3, Mo2−F5 and Mo2−F7), *trans* to the vanadyl bonds on Mo1 and Mo2 (Mo1−O1, Mo1−O2, Mo2−O3 and Mo2−O4) are all lengthened as a result to 2.019(5) Å, 2.093(6) Å, 2.086(6) Å and 1.985(5) Å respectively.

The structure is comprised of a complex network of hydrogen bonds as a result of the water molecules and free fluoride anions. Firstly the two monomers are hydrogen bonded to one another via the water molecule (O5) to form a dimer through O1 and F7 at distance of 2.88(1) Å and 2.762(9) Å, respectively (see Fig 5.14). Then the “dimers” are held together as a sheet in the *bc* plane (see Fig 5.15) by the protonated template. The template itself also hydrogen bonds to the free fluoride anions which only lie in the plane of the template where they help to fill the interstitial voids and strengthen the template layer through further hydrogen bonding. The water molecules and fluoride anions were distinguished crystallographically and through chemical intuition. The fluoride and oxygen atoms were clearly distinguishable in the structure solution process, also their proximity to the other moieties gave an indication of their elemental species. An atom located close to oxygen and fluorine was most likely to be water (for hydrogen bonding) and “free” atoms located near organic templates, were most likely to be anions, in this case fluoride anions. Also the number of fluoride ions was determined through charge balancing.

The partially reduced Mo^{5+} compound, $[C_6H_{21}N_4]_2[MoOF_5]_2[F]_2 \cdot H_2O$, has also recently been reported by Maisonneuve *et al*[21]. In their reaction they used the same reagents as those used to synthesise **Mo−2** except that ethanol was used as a solvent instead of a water/ethylene glycol mix. These reagents were then heated in a microwave at 190°C, with the product forming in 1 hour. Experiments at 190°C were tried hydrothermally using the tris (2-aminoethyl) amine but it was found to decompose to ammonia at temperatures above 160°C. Microwave synthesis maybe a gentler route to achieving products at higher temperatures where template degradation is an issue. The structure is similar to **Mo−2** in that it also forms a hydrogen bonded "dimer" (see Fig 5.16) but in this case the monomers are symmetrically equivalent and related to one another through an inversion centre. Also instead of forming inorganic/organic layers (see Fig 5.15), the dimers are separated from each other through the template species enclosing them.

Bond	Bond Length (Å)	s_{ij}	Bond	Bond Length (Å)	s_{ij}
Mo1−O1	1.686(5)	1.821	Mo2−O3	1.780(6)	1.412
Mo1−O2	1.790(5)	1.374	Mo2−O4	1.653(6)	1.990
Mo1−F1	2.019(4)	0.565	Mo2−F5	2.086(5)	0.472
Mo1−F2	1.796(5)	1.033	Mo2−F6	1.978(4)	0.632
Mo1−F3	2.093(4)	0.463	Mo2−F7	1.985(5)	0.620
Mo1−F4	2.001(4)	0.594	Mo2−F8	1.825(5)	0.955
		∑Mo1 = 5.85			**∑Mo2 = 6.08**

Table 5.10 Selected bond lengths and bond valence sums for **Mo−2**.

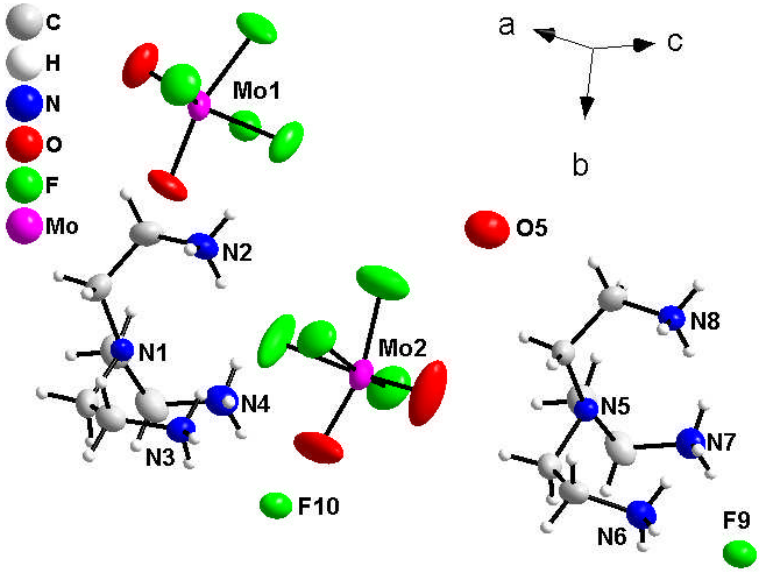

Fig 5.13 The asymmetric unit in **Mo−2**.

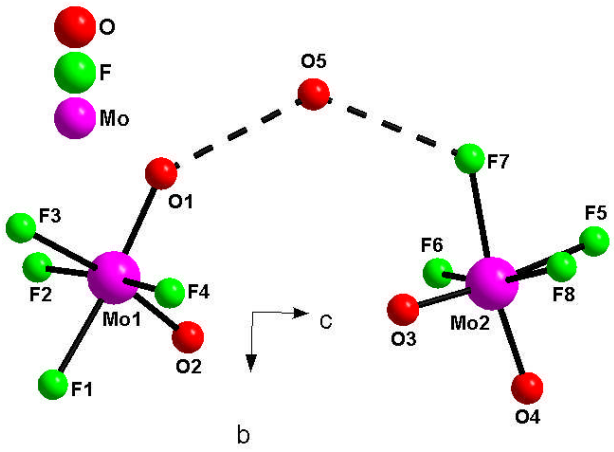

Fig 5.14 The hydrogen bonding between monomers in **Mo−2**.

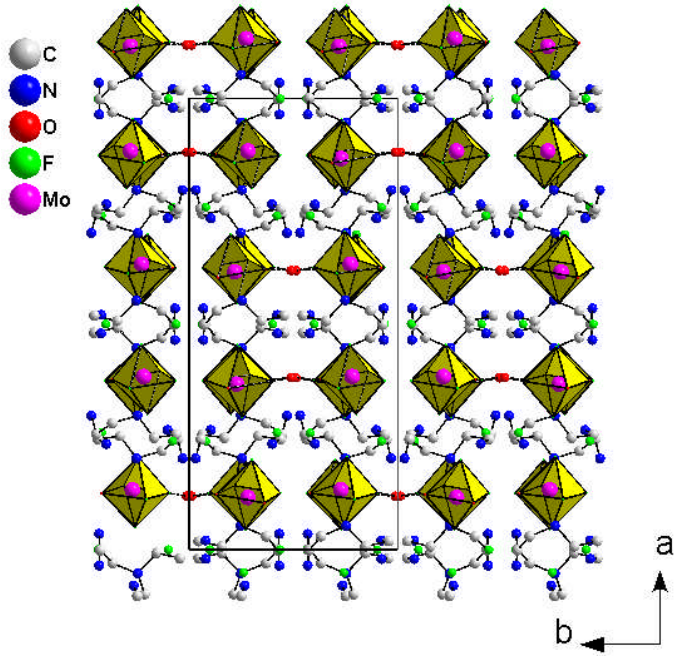

Fig 5.15 The inorganic-organic layers in **Mo−2**.
Hydrogen atoms have been omitted for clarity.

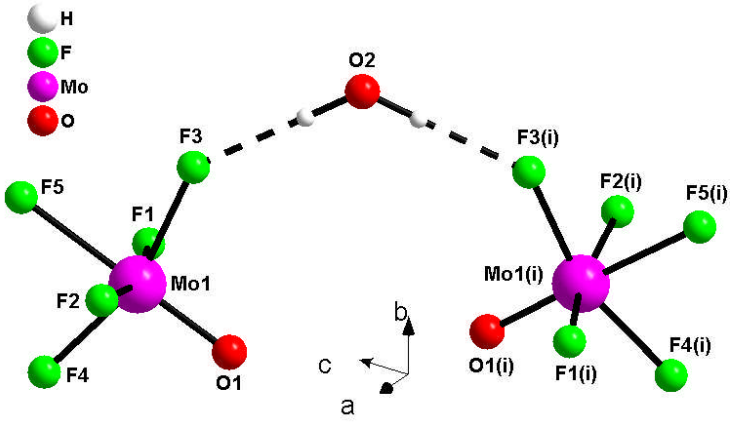

Fig 5.16 The hydrogen bonding between monomers in $[C_6H_{21}N_4]_2[MoOF_5]_2[F]_2{\cdot}H_2O$.[21] Symmetry operator (i) 1-*x*, *y*, ½-*z*.

$[C_{10}H_{10}N_2][MoO_2F_4]$ (Mo−3) consists of the Mo^{6+} $[MoO_2F_4]^{2-}$ monomer (see Table 5.11) as seen in Fig 5.10. The asymmetric unit (as shown in Fig 5.15) consists of the $[MoO_2F_4]^{2-}$ monomer and the protonated template, 4,4 bipyridyl. The 3D structure is built up of hydrogen bonding from the 4,4 bipyridyl template to the fluorine atoms. The hydrogen bond network is much simpler than in comparison to **Mo−2**, with the monomers and the template forming an infinite hydrogen-bonded lattice in the *bc* plane (see Fig 5.16). These layers are then built up on top of each other in a staggered fashion to ensure strong hydrogen bonding throughout the structure.

Bond	Bond Length (Å)	s_{ij}
Mo1−O1	1.699(4)	1.758
Mo1−O2	1.788(4)	1.382
Mo1−F1	2.195(3)	0.351
Mo1−F2	1.928(3)	0.723
Mo1−F3	1.969(3)	0.647
Mo1−F4	1.875(3)	0.834
		∑Mo1 = 5.70

Table 5.11 Selected bond lengths and bond valence sums for **Mo−3**.

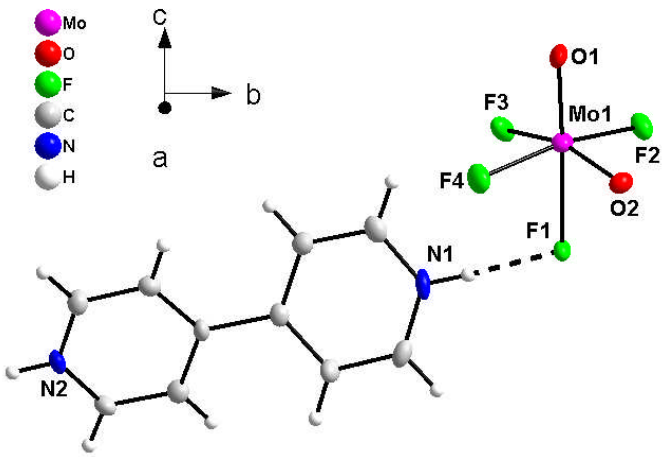

Fig 5.15 The asymmetric unit in **Mo−3**.

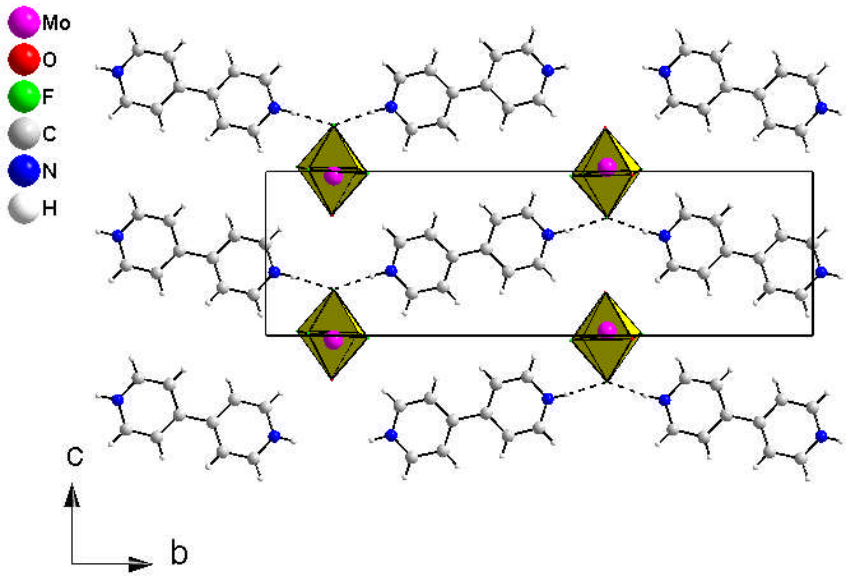

Fig 5.16 The planar packing in **Mo−3**.

$[C_{12}H_{12}N_2][MoO_2F_4]$ (Mo−4) is structurally similar to **Mo−3** with the asymmetric unit for **Mo−4** being constructed in a comparable manner (as seen in Fig 5.17), consisting of the Mo^{6+} $[MoO_2F_4]^{2-}$ monomer (see Table 5.12) and the protonated template, *trans* 1,2 bis (4-pyridyl) ethylene. The structure is held together through a complex hydrogen bonding network which is different to the packing seen in **Mo−3**, this is unexpected since the templates are very similar. Instead of the regular linear array seen in **Mo−3** (see Fig 5.16) the templates overlap with one another to accommodate for the bulkier cation (see Fig 5.18) and maintain the strong hydrogen bonds needed to hold the structure together. As a result the symmetry is reduced from monoclinic (**Mo−3** is in the space group $P2_1/a$) to triclinic (P-1 for **Mo−4**).

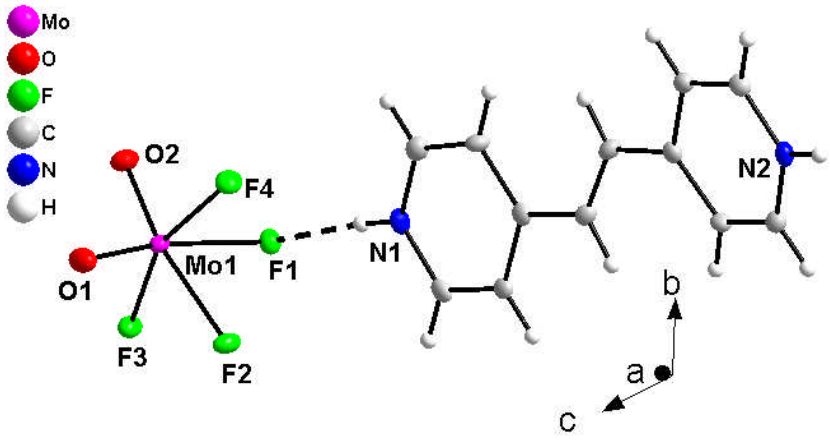

Fig 5.17 The asymmetric unit in **Mo−4**.

Bond	Bond Length (Å)	s_{ij}
Mo1−O1	1.697(2)	1.767
Mo1−O2	1.700(2)	1.751
Mo1−F1	2.125(2)	0.425
Mo1−F2	2.113(2)	0.439
Mo1−F3	1.902(2)	0.776
Mo1−F4	1.941(2)	0.698
		∑Mo1 = 5.86

Table 5.12 Selected bond lengths and bond valence sums for **Mo−4**.

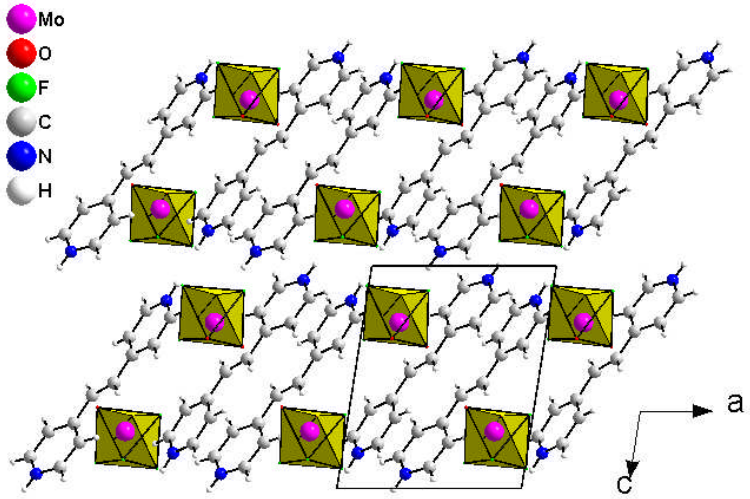

Fig 5.18 The packing in **Mo−4**.

The building unit for **$K_{14}[Mo_2O_2F_9]_2[MoOF_5]_4 \cdot 2C_2H_6O_2$ (Mo−8)** can be seen below in Fig 5.19 and consists of two known oligomers; the monomer[9] $[MoOF_5]^{2-}$ and the dimer[16] $[Mo_2O_2F_9]^{3-}$, three potassium cations and a disordered molecule of ethylene glycol. Both the monomer and the dimer are partially reduced to Mo^{5+} (see Table 5.13).

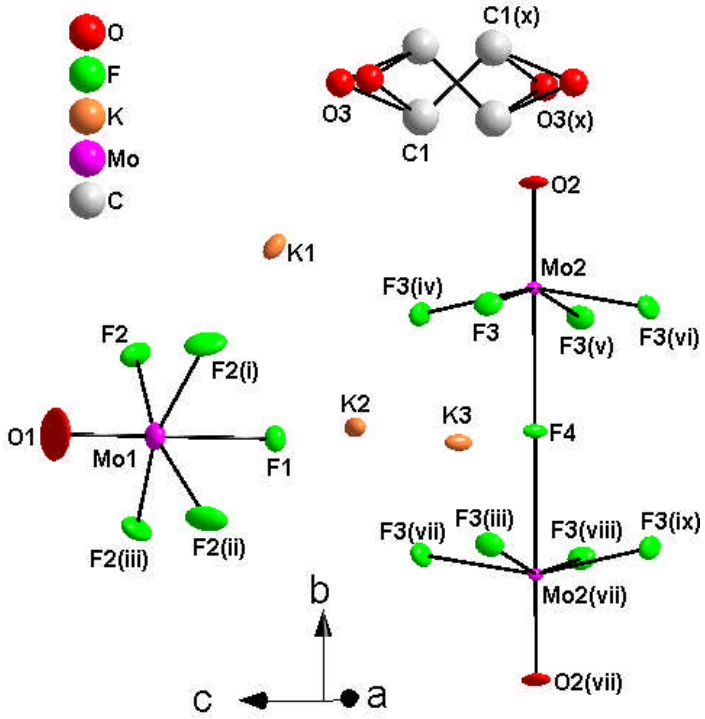

Fig 5.19 The building unit in **Mo−8**. Symmetry operators (i) -1-*x*, *y*, *z*, (ii) -1-*x*, -*y*, *z*, (iii) *x*, -*y*, *z*, (iv) -*x*, *y*, *z*, (v) -*x*, *y*, -*z*, (vi) *x*, *y*, -*z*, (vii) -*x*, -*y*, *z*, (viii) -*x*, -*y*, -*z*, (ix) *x*, -*y*, -*z*, (x) *x*, 1-*y*, -*z*,

Bond	Bond Length (Å)	s_{ij}	Bond	Bond Length (Å)	s_{ij}
Mo1−O1	1.68(2)	1.850	Mo2−O2	1.64(2)	2.078
Mo1−F1	2.02(2)	0.568	Mo2−F3	1.943(7)	0.694
Mo1−F2	1.962(8)	0.660	Mo2−F3	1.943(7)	0.694
Mo1−F2(i)	1.962(8)	0.660	Mo2−F3(iv)	1.943(7)	0.694
Mo1−F2(ii)	1.962(8)	0.660	Mo2−F3(v)	1.943(7)	0.694
Mo1−F2(iii)	1.962(8)	0.660	Mo2−F4(vi)	2.221(2)	0.328
		∑Mo1 = 5.06			**∑Mo2 = 5.18**

Table 5.13 Selected bond lengths and bond valence sums for **Mo−8**

The structure is built up of a complex system of ionic and hydrogen bonding and can be considered to consisting of two parts; an inorganic layer and an organic/inorganic layer (see Fig 5.20). The inorganic layer consists of the $[MoOF_5]^{2-}$ monomer and potassium cations which hold the layer together in the *ab* plane through ionic bonding (see Fig 5.20 − A). This

layer then alternates with the organic/inorganic layer which is comprised of the $[Mo_2O_2F_9]^{3-}$ dimer, ethylene glycol and potassium cations (see Fig 5.20 − B) and is also held together through ionic bonding. The ethylene glycol plays no part in the bonding of the organic/inorganic layer but does penetrate the layer to provide additional hydrogen bonding (see Fig 5.20 − C) to the monomers on either of the layer in the neighbouring inorganic layers.

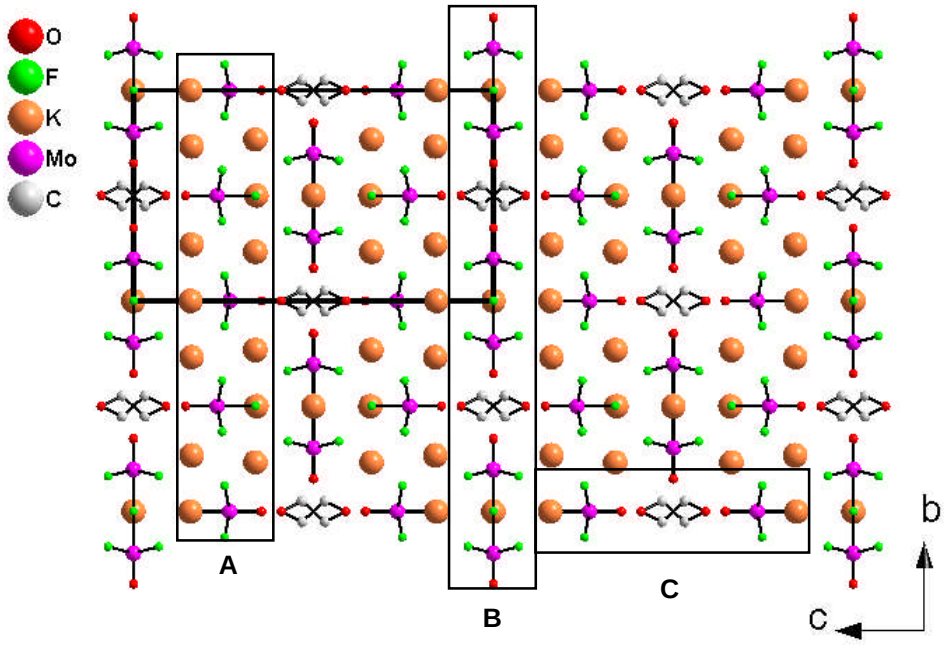

Fig 5.20 The packing of inorganic (A) and organic/inorganic layers (B) in **Mo−8**

5.3 Synthetic Aspects

5.3.1 Effect of Temperature on Synthesis

Heat can display an enormous effect on the products formed in reactions. In hydrothermal reactions the pressures generated by elevated temperatures can lead to the condensation of structures and also the extra heat can increase the reactivity of reagents. A common feature of the materials in this work is the relationship between the reduction of molybdenum and temperature.

5.3.1.1 Ethylene Diamine System

In this system, when the temperature used to synthesize the dimer in **Mo−1** (see Fig 5.21 − left) is increased from 100 °C to 140 °C (see synthetic conditions − Appendix C) the dimer becomes more condensed, going from corner-sharing to edge-sharing (see Fig 5.21), and the molybdenum is reduced from Mo^{6+} to Mo^{5+} and **Mo−6** is produced (see Fig 5.21 − right). The structure becomes more condensed as the template is no longer hydrogen bonded to the dimer but is covalently bonded to the Mo metal centre instead.

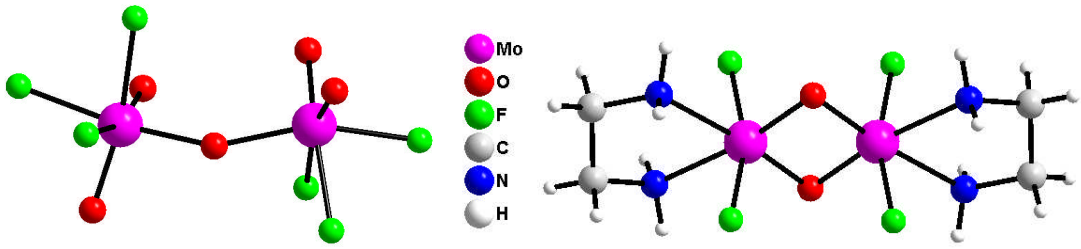

Fig 5.21 The dimers in **Mo−1** (left) and **Mo−6** (right).

5.3.1.2 Ammonium System

When ammonium cations from ammonium hydroxide were used as a template at 100 °C (see synthetic conditions − Appendix C), the known compound $[NH_4]_2[MoOF_5]$ was synthesised[16] (see Fig 5.22 − left). When the reaction temperature was increased to 160 °C the structure becomes more condensed and the tetramer in **Mo−5** is formed (see Fig 5.22 − right).

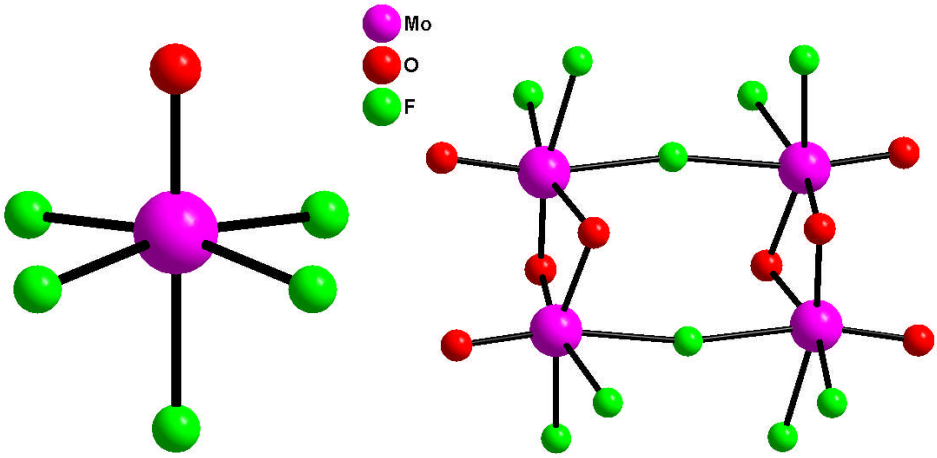

Fig 5.22 The $[MoOF_5]^{2-}$ monomer[9] (left) and $[Mo_4O_8F_{10}]^{6-}$ tetramer in **Mo−5** (right).

5.3.1.3 Potassium System

At 100 °C with potassium chloride as a starting reagent (see synthetic conditions − Appendix C), the known monomeric compound $K_2[MoO_2F_4]\cdot H_2O$ was synthesised[9] (see Fig 5.23 − left). When the reaction temperature was increased to 160 °C the molybdenum became reduced to Mo^{5+} and the structure became more condensed forming the tetramer in **Mo−7** (see Fig 5.23 − right). This system is analogous to ammonium system mentioned previously, with both systems starting from known monomeric compounds at 100 °C and going on to form the same tetramer at 160 °C.

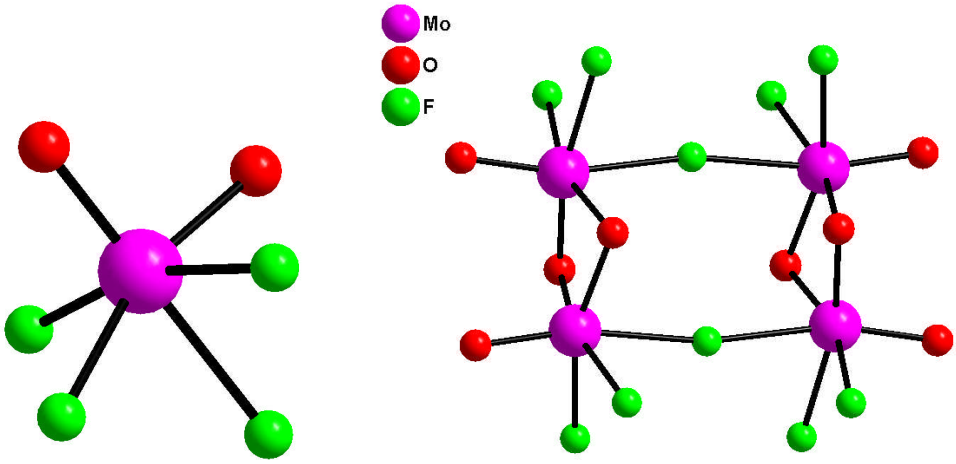

Fig 5.23 The $[MoO_2F_4]^{2-}$ monomer[6] (left) and $[Mo_4O_8F_{10}]^{6-}$ tetramer in **Mo−7** (right).

5.3.2 Effect of Cation Ratio on Synthesis

The counter-cation to molybdenum ratio is an important variable to consider. Higher dimensionality products should be achieved if the ratio is decreased (i.e. lower cation content) as any resultant structure will have to compensate for the loss of charge balancing ions and become more condensed, even if the reaction temperature remains constant. Likewise if the ratio is raised (cation content increased) the inorganic moieties should become more isolated from each other caused by separation from the increased cation content within the structure. This is not the case in the below system which, with the decrease of the cation content, causes the covalent connectivity to become reduced.

5.3.2.1 Potassium System

Mo−7 (see Fig 5.7) and **Mo−8** (see Fig 5.18) were both synthesised at 160 °C although the template content used to make **Mo−8** was a third of that in **Mo−7** (see synthetic conditions − Appendix C). The decrease in cation content usually forms more condensed structures such as chains and layered structures (see chapter 4.3.3.1 and chapter 4.3.3.2) but in this system the opposite appears to be true. Although the connectivity remains 0D, the structure changes from a tetramer to a structure comprised of monomers and dimers, so a reduction in the covalent connectivity of the inorganic moieties occurs with a reduction in cation content in the reaction conditions although the ratio of potassium to molybdenum stays similar at 6:4 and 7:4 for the products, **Mo−7** and **Mo−8**, respectively. The other difference between these two materials is the oxygen to fluorine ratio in the products. In **Mo−7**, the O/F ratio is 4:5 but in **Mo−8** the O/F ratio is 4:19, nearly four times as much. It is this increase in O/F ratio that causes the decrease in covalent connectivity, although the cause for this increase is still unknown.

5.4 Structure Summary

Below is a table summarising all the structures in this chapter, their oxidation state and their dimensionality.

Structure	Average Ox. State	Dimensionality	Oligomeric Unit (if applicable)
Mo−1	6	0D	Dimer
Mo−2	6	0D	Monomer
Mo−3	6	0D	Monomer
Mo−4	6	0D	Monomer
Mo−5	5	0D	Tetramer
Mo−6	5	0D	Dimer
Mo−7	5	0D	Tetramer
Mo−8	5	0D	Monomer and Dimers
Mo−9	4	1D	−

Table 5.14 A summary of the molybdenum oxyfluoride structures in this chapter.

5.5 Synthetic Conditions for Mo−1 to Mo−9

Product	MoO_3 (g)	HF (ml)	H_2O (ml)	EG (ml)	Template	Template Quantity	Temp (°C)	Time (days)
Mo−1	0.14	0.5	1	5	Ethylene diamine	0.500ml	100	1
Mo−2	0.14	0.5	2	5	Tris (2-aminoethyl) amine	0.500ml	100	1
Mo−3	0.14	0.5	0	5	4-4 Bipyridyl	0.463g	100	1
Mo−4	0.14	0.5	2	5	Trans 1,2 bis (4-pyridyl) ethylene	0.534g	100	1
Mo−5	0.14	0.5	1	5	Ammonium Hydroxide (33%)	1.000ml	160	1
Mo−6	0.14	0.5	5	5	Ethylene diamine	0.500ml	140	1
Mo−7	0.14	0.5	2	5	Potassium Nitrate	0.300g	160	1
Mo−8	0.14	0.5	0	5	Potassium Nitrate	0.100g	160	1
Mo−9	0.14	0.5	1	5	Piperazine	0.258g	190	1

References

1. G. M. Sheldrick, Institüt für Anorganische Chemie der Universität, Tammanstrasse 4, D-3400 Göttingen, Germany, **1998**.
2. “Inorganic Solid Fluorides”; P. Hagenmuller (Editor), Academic Press: London, 1985.
3. “Advanced Inorganic Fluorides”: Synthesis, Characterisation and Applications, T. Nakajima, B. Zemva and A. Tressaud (Editors), Elsevier Science, S.A, 2000.
4. H. Lin, B. Yan, P. D. Boyle and P. A. Maggard, *J. Solid State Chem.*, **2006**, 179, 217.
5. J. E. Kirsch, H. K. Izumi, C. L. Stern and K. R. Poeppelmeier, *Inorg. Chem.*, **2005**, 44, 4586.
6. R. Hoppe and K. Lehr, *Z. Anorg. Allg. Chem.*, **1975**, 416, 240.
7. G. Brunton, *Mater. Res. Bull.*, **1971**, 6, 555.
8. A. J. Edwards and R. D. Peacock, *J. Chem. Soc.*, **1961**, 4253.
9. D. Grandjean and R. Weiss, *Bull. Soc. Chim. Fr.*, **1967**, 3054.
10. G. Pausewang and W. Ruedoff, *Z. anorg. Allg. Chem.*, **1969**, 364, 269.
11. D. Grandjean and R. Weiss, *Bull. Soc. Chim. Fr.*, **1967**, 3049.
12. K. Gise and K. Seppelt, *Angew. Chem.*, **1994**, 106, 473.
13. I. Sens, H. Stenger, U. Muller and K. Dehnicke, *Z. Anorg. Allg. Chem.*, **1992**, 610, 117.
14. M. Leimkuhler, N. Buchholz and R. Mattes, *Z. Naturforsch. B – Chemical Sciences*, **1989**, 44, 389.
15. R. Mattes and G. Lux, *Z. Anorg. Allg. Chem.*, **1976**, 424, 173.
16. R. Mattes, K. Menneman, N. Jaekel, H. Rieskamp and H. J. Brockmeyer, *J. Less-Common Met.*, **1980**, 76, 199.
17. L. Kiriazis, R. Mattes and F. Obst, *Inorg. Chim. Acta*, **1991**, 181, 157.
18. A. J. Edwards, R. D. Peacock and R. W. H. Small, *J. Chem. Soc.*, **1962**, 4486.
19. R. Mattes, G. Mueller and H. J. Becher, *Z. Anorg. Allg. Chem.*, **1972**, 389, 177.
20. H. G. Nieder-Varenholz, *Thesis*, University of Wilhelm, Munster, **1967**, 18.
21. K. Adil, J. Marriot, M. Leblanc, and V. Maisonneuve, *Acta. Cryst.*, **2007**, E63, M1511.

6.0 Miscellaneous (Oxy)Fluoride Structures

In this chapter, the crystal structures and hydrothermal chemistry of 22 titanium, zirconium, hafnium, niobium and tantalum (oxy)fluoride structures will be discussed. These materials have been synthesised and denoted from **Ti−1** to **Ti−5**, **Zr−1** to **Zr−3**, **Hf−1** to **Hf−6**, **Nb−1** to **Nb−5** and **Ta−1** to **Ta−3** (numbered in chronological order in which they were synthesised). The structures range from a collection of $[MF_6]^{n-}$ and $[MF_7]^{n-}$ monomers (where M = Ti, Zr, Hf, Nb and Ta) to the 1D $[TiOF_4]^-$ chain. In the last 20 years two significant reviews have been published which, as of 2000, methodically cover most known transition metal oxyfluorides. These reviews are by Hagenmuller[1] and by Nakajima, Žemva and Tressaud[2].

The crystallographic information for these compounds is presented in Tables 6.1 to 6.5. The synthetic conditions are given at the end of each subsection with the elemental analysis for each structure given in Appendix D (on the accompanying CD). Atomic co-ordinates are located in Appendix A (on the accompanying CD). Bond angles and hydrogen bonds are all contained in the appropriate CIF file (see enclosed CD).

Single crystals were analysed using either a Rigaku Mercury CCD equipped with confocal optics Mo-Kα radiation, a Rigaku SCX-Mini equipped with graphite monochromated Mo-Kα radiation or a Bruker SMART with silicon-monochromated synchrotron radiation (stations 9.8 or 16.2 at CCLRC Daresbury Laboratory), see the appropriate CIF for details. Intensity data were collected by the narrow frame method and corrected for Lorentz and polarization effects as well as absorption by Multi-Scan techniques. All structures were solved by direct methods and refined by full-matrix least-squares cycles in SHELX-97[3]. All non-hydrogen atoms were refined with anisotropic thermal parameters (except where stated). Hydrogen atoms attached to C and N were located at geometrically calculated positions and refined with isotropic thermal parameters, while those attached to O were found, where possible, by Fourier techniques and refined isotropically.

The synthesis of materials of these Ti, Zr, Hf, Nb and Ta compounds was carried out in a systematic manner which started from a few simple reactions at 100°C. Simple linear amines and alkali metals were used to carry on similar reactions to those done previously (see Chapters 4 and 5). Water content was again used as the main variable at 100 °C (see synthetic conditions − Appendix D).

Once a novel compound was synthesised at 100 °C, the effect of variation in temperature was explored. These experiments produced only one new compound, **Hf−6**. For which, a more through discussion of the synthetic conditions is given in subsection 6.3.3.

Table 6.1 Crystallographic Information for **Ti−1** to **Ti−5**.

Compound	**Ti−1**	**Ti−2**	**Ti−3**	**Ti−4**	**Ti−5**
Formula	$[C_{10}H_{10}N_2][TiF_6]$	$[C_2H_{10}N_2][TiOF_4]$	$[C_4H_{12}N_2][TiF_6]$	$[C_{12}H_{12}N_2][TiF_6]$	Cs_2TiF_6
Space Group	Ibam (72)	P4/ncc (130)	P-1 (2)	P-1 (2)	P –3m1 (164)
a/ Å	7.106(2)	12.773(2)	5.753(2)	6.429(3)	6.162(4)
b/ Å	11.853(4)	12.773(2)	5.991(2)	7.085(3)	6.162(4)
c/ Å	13.169(4)	7.974(1)	6.426(2)	7.265(3)	4.950(3)
α/°			95.497(8)	75.60(2)	
β/°			94.696(8)	87.04(2)	
γ/°			105.985(7)	85.67(2)	
V/ Å^3	1109.3(6)	1301.0(3)	210.6(1)	319.4(2)	162.8(2)
Z	4	8	1	1	1
ρ_{calc}/ g cm^{-3}	1.917	2.062	1.972	1.799	4.363
μ/ mm^{-1}	0.840	1.332	1.074	0.737	12.367
Crystal Size/ mm	0.15 x 0.08 x 0.04	0.10 x 0.10 x 0.03	0.2 x 0.06 x 0.02	0.10 x 0.10 x 0.05	0.10 x 0.10 x 0.07
F(000)	640	816	126	174	186
Reflns Collected	3402	11158	1183	1853	721
Independent Reflns	537	593	898	1405	161
R_{int}	0.0339	0.0143	0.0147	0.0147	0.0145
Obsd data [$I > 2\sigma(I)$]	443	592	645	976	128
Data/restraints/parameters	537/0/50	593/0/57	898/0/61	1405/0/97	161/0/12
GOF on F^2	1.086	1.267	1.356	1.103	1.600
*R*1, *wR*2 [I > 2 *σ*(*I*)]	0.0367, 0.0891	0.0573, 0.1500	0.0587, 0.2219	0.0394, 0.0959	0.0296, 0.1034
*R*1, *wR*2 (all data)	0.0484, 0.0964	0.0573, 0.1500	0.0614, 0.2256	0.0444, 0.0983	0.0485, 0.1781

Table 6.2 Crystallographic Information for **Zr−1** to **Zr−3**.

Compound	**Zr−1***	**Zr−2**	**Zr−3**
Formula	$[C_{12}H_{12}N_2][ZrF_6]$	$[C_6H_{20}N_3][ZrF_7]$	$[C_2H_{10}N_2]_5[ZrF_7]_3[F]$
Space Group	P -1 (2)	P 2_1 2_1 2_1 (19)	P -1 (2)
a/ Å	6.727(1)	8.200(1)	12.449(3)
b/ Å	6.895(1)	10.602(1)	12.893(3)
c/ Å	7.707(2)	13.606(2)	13.262(3)
α/°	99.366(2)		92.26(1)
β/°	92.799(2)		116.75(1)
γ/°	99.105(2)		114.80(1)
V/ $Å^3$	347.2(1)	1182.9(3)	1655.9(7)
Z	1	4	2
ρ_{calc}/ g cm^{-3}	1.862	2.013	2.010
μ/ mm^{-1}	6.910	1.005	1.073
Crystal Size/ mm	0.04 x 0.04 x 0.02	0.20 x 0.15 x 0.05	0.15 x 0.15 x 0.10
F(000)	192	720	996
Reflns Collected	3207	8356	8957
Independent Reflns	1982	1523	7552
R_{int}	0.0598	0.0267	0.0309
Obsd data [$I > 2\sigma(I)$]	1634	1436	4565
Data/restraints/parameters	1982/0/98	1523/0/154	7552/103/406
GOF on F^2	1.042	1.196	1.128
*R*1, *wR*2 [I > 2 *σ*(*I*)]	0.0596, 0.1464	0.0253, 0.0512	0.0482, 0.1134
*R*1, *wR*2 (all data)	0.0642, 0.1541	0.0295, 0.0537	0.0596, 0.1197

* = Collected at Daresbury Laboratories.

Table 6.3 Crystallographic Information for **Hf−1** to **Hf−6**.

Compound	**Hf−1**	**Hf−2**	**Hf−3**	**Hf−4**	**Hf−5**	**Hf−6**
Formula	$Na_4Hf_2F_{12}$	$[C_4H_{16}N_3][HfF_7]\cdot H_2O$	$[C_6H_{22}N_4][Hf_2F_{12}]$	$[C_4H_{12}N_2][HfF_6]$	$[C_{10}H_{10}N_2][HfF_6]$	$Na_5Hf_2F_{13}$
Space Group	P 2_1/c (14)	P 2_1/c (14)	P 2_1/n (14)	P -1 (2)	Ibam (72)	C 2/m (12)
a/ Å	5.547(1)	8.9324(6)	6.982(2)	5.921(2)	6.9907(5)	11.554(4)
b/ Å	5.388(1)	12.1601(8)	10.331(2)	6.131(3)	12.0649(8)	5.486(2)
c/ Å	16.000(2)	10.3979(7)	11.215(3)	6.528(3)	13.7339(9)	8.401(3)
α/°				101.29(1)		
β/°	95.753(3)	94.581(2)	94.708(6)	91.08(1)		97.39(1)
γ/°				101.66(1)		
V/ $Å^3$	475.75(9)	1125.8(1)	806.2(3)	227.2(2)	1158.4(1)	528.1(3)
Z	2	4	2	1	4	2
ρ_{calc}/ g cm^{-3}	4.726	2.571	3.029	2.768	2.584	4.251
μ/ mm^{-1}	22.147	9.348	12.994	11.535	9.084	20.015
Crystal Size/ mm	0.22 x 0.07 x 0.06	0.07 x 0.07 x 0.07	0.10 x 0.10 x 0.03	0.30 x 0.10 x 0.10	0.30 x 0.20 x 0.16	0.01 x 0.13 x 0.14
F(000)	592	824	676	176	840	616
Reflns Collected	4696	11661	4730	1453	5680	1410
Independent Reflns	1079	2487	1777	775	695	567
R_{int}	0.0291	0.0524	0.0264	0.0130	0.0141	0.600
Obsd data [$I > 2\sigma(I)$]	1036	2025	1379	775	600	564
Data/restraints/parameters	1079/47/82	2487/2/151	1777/0/109	775/0/61	695/11/50	567/0/25
GOF on F^2	1.405	1.124	1.436	1.154	1.124	1.179
*R*1, *wR*2 [I > 2 *σ*(*I*)]	0.0243, 0.0600	0.0392, 0.0617	0.0303, 0.0447	0.0108, 0.0297	0.0249, 0.0501	0.0787, 0.2022
*R*1, *wR*2 (all data)	0.0243, 0.0606	0.0566, 0.0635	0.0380, 0.0457	0.0108, 0.0297	0.0309, 0.0524	0.0803, 0.2024

Table 6.4 Crystallographic Information for **Nb−1** to **Nb−5**.

Compound	**Nb−1**	**Nb−2**	**Nb−3**	**Nb−4**	**Nb−5***
Formula	$[C_{12}H_{12}N_2][NbOF_5]$	$[C_6H_{22}N_4][NbOF_5]_2$	$[C_{10}H_{28}N_4][NbOF_5]_2 \cdot 2H_2O$	$[C_6H_{16}N_2][NbOF_5]$	$[C_4H_{12}N_2][NbOF_5]$
Space Group	P -1 (2)	P -1 (2)	P 2_1/c (14)	P -1 (2)	P -1 (2)
a/ Å	6.611(3)	6.366(1)	8.253(1)	6.629(2)	7.7796(5)
b/ Å	6.835(3)	8.178(2)	11.460(2)	7.878(2)	7.8144(5)
c/ Å	7.741(3)	8.923(2)	11.645(2)	11.451(2)	8.5209(5)
α/°	99.821(11)	85.268(7)		89.53(2)	70.217(1)
β/°	92.502(8)	71.460(6)	108.329(3)	74.95(2)	71.5420(1)
γ/°	98.698(13)	72.695(6)		81.16(2)	67.811(1)
V/ Å^3	339.8(3)	420.5(2)	1045.6(2)	570.4(2)	440.62(5)
Z	1	1	2	2	2
ρ_{calc}/ g cm^{-3}	1.911	2.204	2.059	1.858	2.201
μ/ mm^{-1}	0.949	1.475	1.209	1.100	14.712
Crystal Size/ mm	0.15 x 0.10 x 0.03	0.20 x 0.10 x 0.08	0.20 x 0.20 x 0.20	0.15 x 0.10 x 0.04	0.04 x 0.01 x 0.01
F(000)	193	274	648	318	288
Reflns Collected	2357	2339	5328	2882	3165
Independent Reflns	1667	1890	2419	2598	1952
R_{int}	0.0197	0.0111	0.0165	0.0193	0.0116
Obsd data [$I > 2\sigma(I)$]	1270	1388	1864	1693	1682
Data/restraints/parameters	1667/0/98	1890/0/110	2419/2/142	2598/0/145	1952/0/118
GOF on F^2	1.053	1.092	1.121	1.047	1.083
*R*1, *wR*2 [I > 2 $\sigma(I)$]	0.0266, 0.0725	0.0215, 0.0573	0.0255, 0.0652	0.0535, 0.1343	0.0385, 0.1006
*R*1, *wR*2 (all data)	0.0276, 0.0732	0.0223, 0.0577	0.0283, 0.0669	0.0586, 0.1390	0.0398, 0.1022

* = Collected at Daresbury Laboratories.

Table 6.5 Crystallographic Information for **Ta−1** to **Ta−3**.

Compound	**Ta−1**	**Ta−2**	**Ta−3**
Formula	$[C_6H_{22}N_4][TaF_7][F]$	$[C_4H_{16}N_3]_2[TaF_7]_3$	$[C_4H_{12}N_2][TaF_7]$
Space Group	P 2_1/c (14)	P 2_1 (4)	C 2/c (15)
a/ Å	10.506(6)	5.818(5)	12.730(4)
b/ Å	8.225(3)	12.608(7)	8.785(3)
c/ Å	15.962(9)	17.573(7)	8.708(3)
α/°			
β/°	108.73(1)	93.956(7)	113.306(9)
γ/°			
V/ Å^3	1284.2(11)	1286.0(14)	894.4(5)
Z	4	2	4
ρ_{calc}/ g cm^{-3}	2.499	2.981	2.986
μ/ mm^{-1}	8.651	12.894	12.367
Crystal Size/ mm	0.20 x 0.20 x 0.20	0.11 x 0.03 x 0.01	0.10 x 0.10 x 0.02
F(000)	924	1060	744
Reflns Collected	10701	8193	2343
Independent Reflns	2344	3541	997
R_{int}	0.0614	0.0897	0.0141
Obsd data [$I > 2\sigma(I)$]	2280	3309	737
Data/restraints/parameters	2344/46/172	3541/107/343	997/0/65
GOF on F^2	1.183	1.051	1.084
*R*1, *wR*2 [$I > 2\sigma(I)$]	0.1086, 0.2800	0.0518, 0.1238	0.0148, 0.0338
*R*1, *wR*2 (all data)	0.1108, 0.2809	0.0563, 0.1292	0.0155, 0.0340

6.1 Titanium (Oxy)Fluoride Structures

6.1.1 Existing Oligomers and Polymeric Structures

The novel crystal structures contained in this sub-section are inorganic oligomers or polymeric compounds which have either been made by a different route of synthesis to that previously reported or made with a different organic/inorganic cation. The table below is a list of the first examples of some different known structure types for titanium (oxy)fluorides.

Chemical Formula	Structure Type	Ox. State	Ref
$K_2NaTiOF_5$	Monomer	IV	4
K_2TiF_6	Monomer	IV	5
Rb_3TiF_7	Monomer	IV	6
$Cs_2KTiO_2F_3$	Monomer	IV	7
$(C_4H_{12}N_2)[TiF_5(H_2O)]_2$	Monomer	IV	8
$(C_4H_{12}N_2)(Ti_2F_{10})\cdot 2H_2O$	Dimer	IV	9
$(C_4H_{12}N_2)Ti_2OF_{10}\cdot 2H_2O$	Dimer	IV	10
$(C_5H_6N)(Ti_2F_{11})(H_3O)\cdot H_2O$	Dimer	IV	11
K_2TiOF_4	Chain	IV	12
$NaTiF_4$	Layered	III	13
$K_5Ti_3F_{14}$	Layered	III	14
$CsTi_8F_{33}$	Layered	IV	15
$TiOF_2$	3D	IV	16
TiOF	3D	III	17

Table 6.6 Some of the known structure types of titanium (oxy)fluorides.

6.1.1.1 Monomers

$[C_{10}H_{10}N_2][TiF_6]$ (Ti−1), $[C_4H_{12}N_2][TiF_6]$ (Ti−3), $[C_{12}H_{12}N_2][TiF_6]$ (Ti−4) and **Cs_2TiF_6 (Ti−5)** are all based on the previously reported[5] $[TiF_6]^{2-}$ monomer (see Fig 6.1).

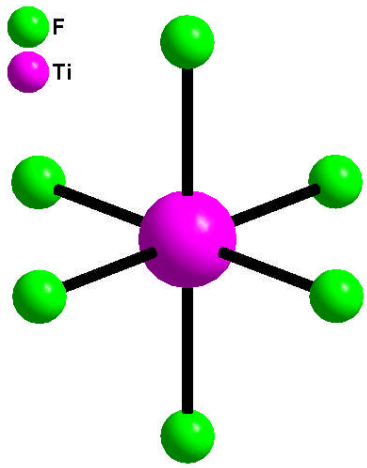

Fig 6.1 The known $[TiF_6]^{2-}$ monomer in **Ti−1**, **Ti−3**, **Ti−4** and **Ti−5**.

$[C_{10}H_{10}N_2][TiF_6]$ (Ti−1) consists of one crystallographically unique Ti^{4+} metal centre, six fluorine bonds and the protonated template 4,4 bipyridyl, which is situated about an inversion centre (see Fig 6.2). The three non-symmetry related fluorine atoms, F1, F2 and F3, are all bonded to the Ti^{4+} metal centre (confirmed by BVS, see Table 6.7) at a range of 1.850 Å to 1.889 Å. The structure is held together through a complex network of hydrogen bonds from the fluorine atoms to the cationic template.

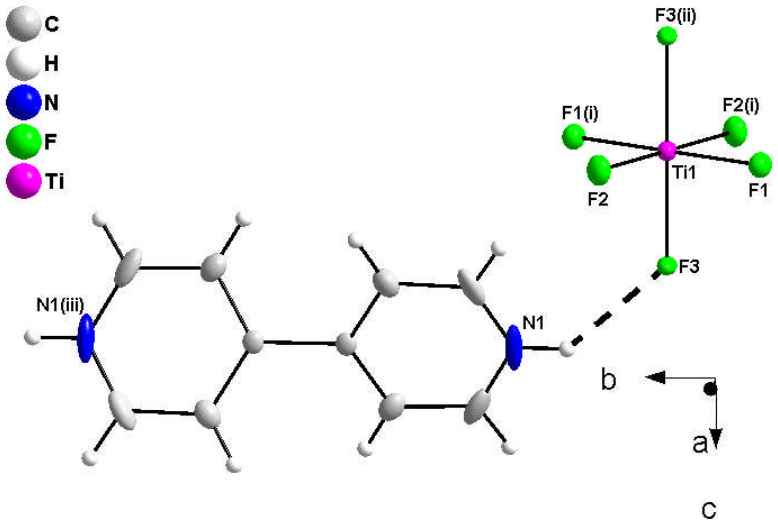

Fig 6.2 The building unit in **Ti−1**. Symmetry operators (i) *–x*, *-y*, *z*, (ii) *–x*, *-y*, *-z*, (iii) *–x*, 1-*y*, *z*.

Bond	Bond Length (Å)	s_{ij}
Ti1−F1	1.852(2)	0.780
Ti1−F1’	1.852(2)	0.780
Ti1−F2	1.850(2)	0.784
Ti1−F2’	1.850(2)	0.784
Ti1−F3	1.889(2)	0.706
Ti1−F3’	1.889(2)	0.706
		∑Ti1 = 4.54

Table 6.7 Selected bond lengths and bond valence sums for **Ti−1**.

$[C_4H_{12}N_2][TiF_6]$ (Ti−3) consists of one crystallographically unique Ti^{4+} metal centre, six fluorine bonds and the protonated template piperazine, which is situated about an inversion centre (see Fig 6.3). The three non-symmetry related fluorine atoms, F1, F2 and F3, are all bonded to the Ti^{4+} metal centre (confirmed by BVS, see Table 6.8) at a range of 1.846 Å to 1.880 Å. The structure is held together through a complex network of hydrogen bonds from the fluorine atoms to the cationic template.

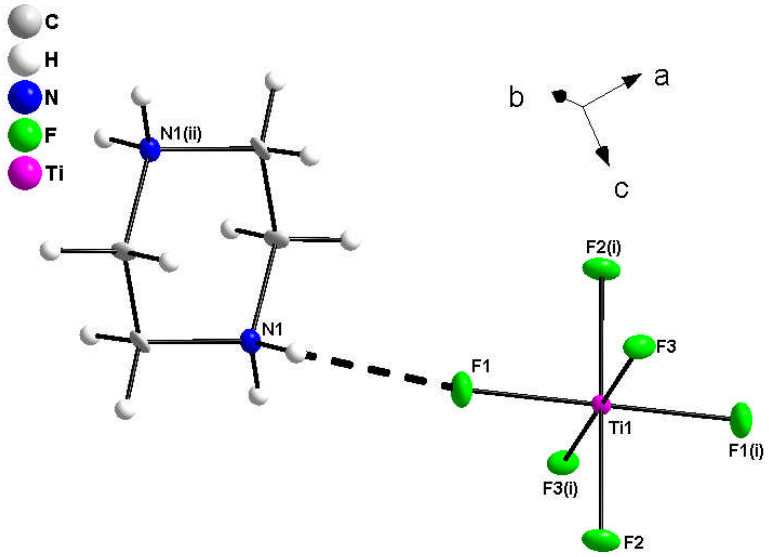

Fig 6.3 The building unit in **Ti−3**. Symmetry operators (i) 2–*x*, -*y*, 2-*z*, (ii) 1–*x*, 1-*y*, 1-*z*.

Bond	Bond Length (Å)	s_{ij}
Ti1−F1	1.846(3)	0.793
Ti1−F1'	1.846(3)	0.793
Ti1−F2	1.873(3)	0.737
Ti1−F2'	1.873(3)	0.737
Ti1−F3	1.880(3)	0.723
Ti1−F3'	1.880(3)	0.723
		∑Ti1 = 4.51

Table 6.8 Selected bond lengths and bond valence sums for **Ti−3**.

$[C_{12}H_{12}N_2][TiF_6]$ (Ti−4) consists of one crystallographically unique Ti^{4+} metal centre, six fluorine bonds and the protonated template *trans* 1,2 bis(4-pyridyl) ethene, which is situated about an inversion centre (see Fig 6.4). The three non-symmetry related fluorine atoms, F1, F2 and F3, are all bonded to the Ti^{4+} metal centre (confirmed by BVS, see Table 6.9) at a range of 1.851 Å to 1.876 Å. The structure is held together through a complex network of hydrogen bonds from the fluorine atoms to the cationic template.

Structures **Ti−1**, **Ti−3** and **Ti−4** are all very similar in their monomeric units (they are all situated upon an inversion centre and have comparable bond lengths) and the building unit as a whole. The protonated templates used in each structure are also closely related and can be considered related to one another i.e. the template species being a cyclic compound (or derivative thereof) with the protonated nitrogen species being situated within the ring.

It is also worth noting the bond valence sums, which all come in considerably higher than the expected value of 4. The BVS calculations are performed using the VALENCE[18] program with variables determined either by Brown & Altermatt[19] or O'Keeffe & Brese.[20] The difference between the two sets of variables is that those supplied by Brown & Altermatt are calculated, whilst those by O'Keeffe & Brese are partially derived, although the values used in this work were calculated which leaves the question open as to the reason for the discrepancy. The values used for the BVS calculations of **Ti−1**, **Ti−3** and **Ti−4** were by O'Keeffe & Brese.

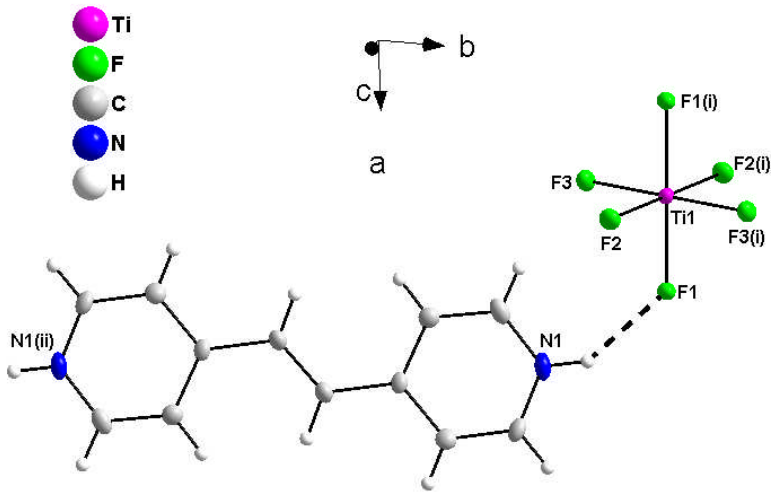

Fig 6.4 The building unit in **Ti−4**. Symmetry operators (i) -*x*, -*y*, -*z*, (ii) 1–*x*, -2-*y*, 1-*z*.

Bond	Bond Length (Å)	s_{ij}
Ti1−F1	1.876(2)	0.731
Ti1−F1'	1.876(2)	0.731
Ti1−F2	1.865(2)	0.753
Ti1−F2'	1.865(2)	0.753
Ti1−F3	1.851(2)	0.782
Ti1−F3'	1.851(2)	0.782
		∑Ti1 = 4.53

Table 6.9 Selected bond lengths and bond valence sums for **Ti−4**.

Although the monomeric structure of **Cs_2TiF_6 (Ti−5)** is similar to those shown previously (see Fig 6.5), the symmetry has been raised as a result of the more symmetrical counter-cation, to the trigonal space group P-3m1. As a result there is only unique V−F bond at a distance of 1.865(6) Å in the building unit and one unique caesium atom, Cs1. The Ti metal centre is Ti^{4+} as confirmed by BVS (see Table 6.10). The structure is held together through a network of ionic bonding from the fluorine atoms and the caesium cations (see Fig 6.6).

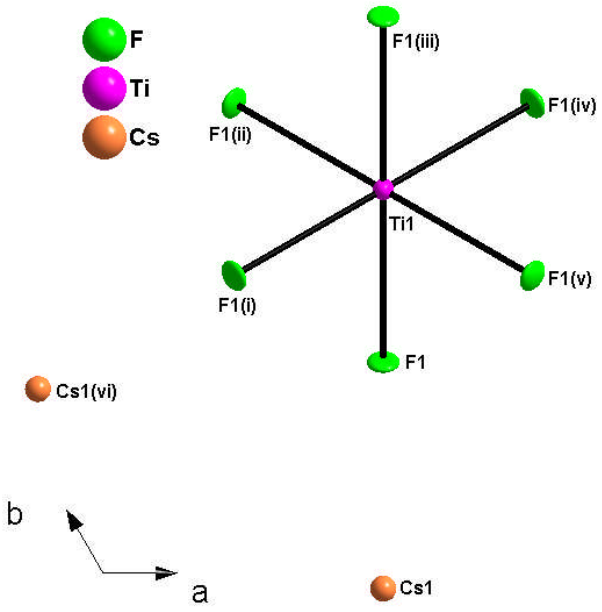

Fig 6.5 The building unit in **Ti−5**. Symmetry operators (i) *y*, *x*, 1-*z*, (ii) 1-*x*+*y*, 2-*x*, *z*, (iii) 1+*x*-*y*, 2-*y*, 1-*z*, (iv) 2-*y*, 1+*x*-*y*, *z*, (v) 2-*x*, 1-*x*+*y*, 1-*z*, (vi) *x*-*y*, 1-*y*, 1-*z*.

Bond	Bond Length (Å)	s_{ij}
Ti1−F1	1.865(8)	0.753
Ti1−F1’	1.865(8)	0.753
Ti1−F1’	1.865(8)	0.753
Ti1−F1’	1.865(8)	0.753
Ti1−F1’	1.865(8)	0.753
Ti1−F1’	1.865(8)	0.753
		∑Ti1 = 4.52

Table 6.10 Selected bond lengths and bond valence sums for **Ti−5**.

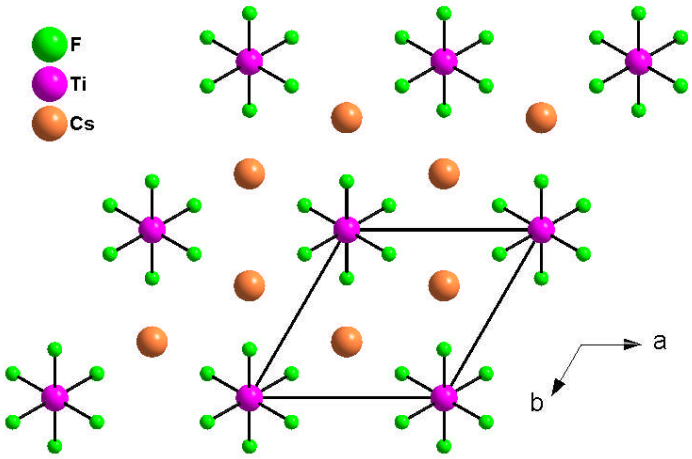

Fig 6.6 The packing in **Ti−5**.

6.1.1.2 Chain Structures

$[C_2H_{10}N_2][TiOF_4]$ (Ti−2) is based on the previously reported trans-connected $[TiOF_4]^{2-}$ chain[12] (see Fig 6.7); the same structure type has also been synthesised for $[ScF_5]^{2-}$ and $[VF_5]^{2-}$, respectively.[21,22] The building unit contains two crystallographically unique Ti^{4+} sites and a protonated molecule of the template species, ethylene diamine, which is situated on an inversion centre (see Fig 6.8). The Ti metal centres are both Ti^{4+} as confirmed by BVS (see Table 6.11). The fluorine atoms around Ti2 are also disordered and correspond to two slightly different conformations of the $[TiOF_4]^{2-}$ repeat unit as can be seen in Fig 6.7. The complete structure (see Fig 6.9) is held together through a complex network of hydrogen bonding from the protonated ethylene diamine template to the fluorine atoms on the $[TiOF_4]^{2-}$ chains. **Ti−2** was synthesised at 100 °C (see synthetic conditions − Appendix D) in a similar manner to $[C_2N_2H_{10}]_{1.5}[TiF_6][F]$, which was made at 190 °C but with 1.5 times the amount of HF and 5 times more water (the solution was also left to stand for two weeks for the product to form).[23] Although the temperature has been increased, which normally leads to more condensed structures, the monomeric structure (similar to that in **Ti−1**, **Ti−3**, **Ti−4** and **Ti−5**) $[C_2N_2H_{10}]_{1.5}[TiF_6][F]$, is produced as a result of the increased fluorine, water content and as a result of the solution being left to evaporate at room temperature for the product to form. These mild synthesis conditions lead to the $[TiF_6]^{2-}$ monomer forming rather than the $[TiOF_4]^{2-}$ chain.

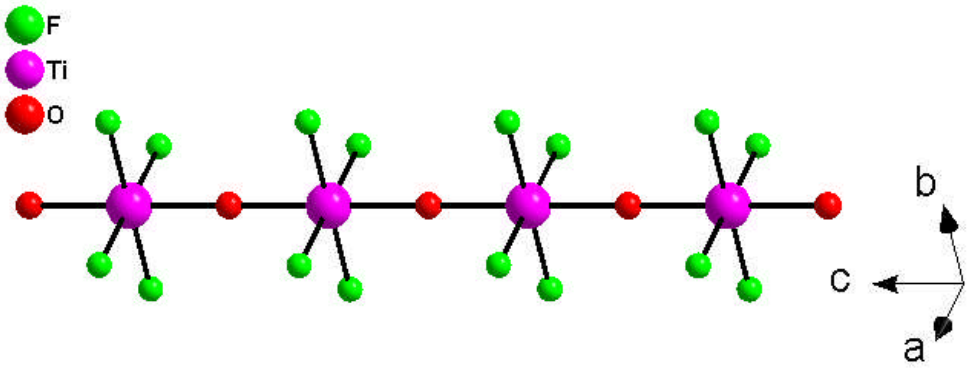

Fig 6.7 The $[TiOF_4]^{2-}$ chain in **Ti−2**.

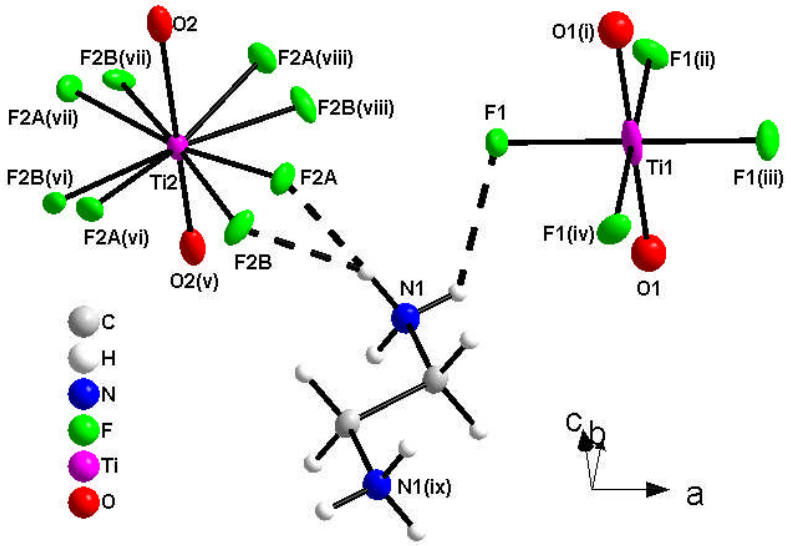

Fig 6.8 The building unit in **Ti−2**. Symmetry operators (i) ½+*y*, -1/2+*x*, ½-*z*, (ii) 1-*y*, 1-*x*, ½-*z*, (iii) 1½-*x*, ½-*y*, *z*, (iv) ½+*y*, -½+*x*, ½-*z*, (v) ½-*x*, *y*, -½+*z*, (vi) *y*, ½-*x*, *z*, (vii) ½-*x*, ½-*y*, *z*, (viii) ½-*y*, *x*, *z*, (ix) 1-*x*, -*y*, -*z*.

Bond	Bond Length (Å)	s_{ij}	Bond	Bond Length (Å)	s_{ij}
Ti1−O1	1.994(1)	0.615	Ti2−O2	1.787(6)	1.077
Ti1−O1’	1.994(1)	0.615	Ti2−O2	2.200(6)	0.353
Ti1−F1	1.900(2)	0.685	Ti2−F2A*	1.924(3)	0.321
Ti1−F1’	1.900(2)	0.685	Ti2−F2A*	1.924(3)	0.321
Ti1−F1’	1.900(2)	0.685	Ti2−F2A*	1.924(3)	0.321
Ti1−F1’	1.900(2)	0.685	Ti2−F2A*	1.924(3)	0.321
		∑Ti1 = 3.97	Ti2−F2B*	1.929(12)	0.317
			Ti2−F2B*	1.929(12)	0.317
			Ti2−F2B*	1.929(12)	0.317
			Ti2−F2B*	1.929(12)	0.317
					∑Ti2 = 3.98

Table 6.11 Selected bond lengths and bond valence sums for **Ti−2**.

* = Disordered atoms.

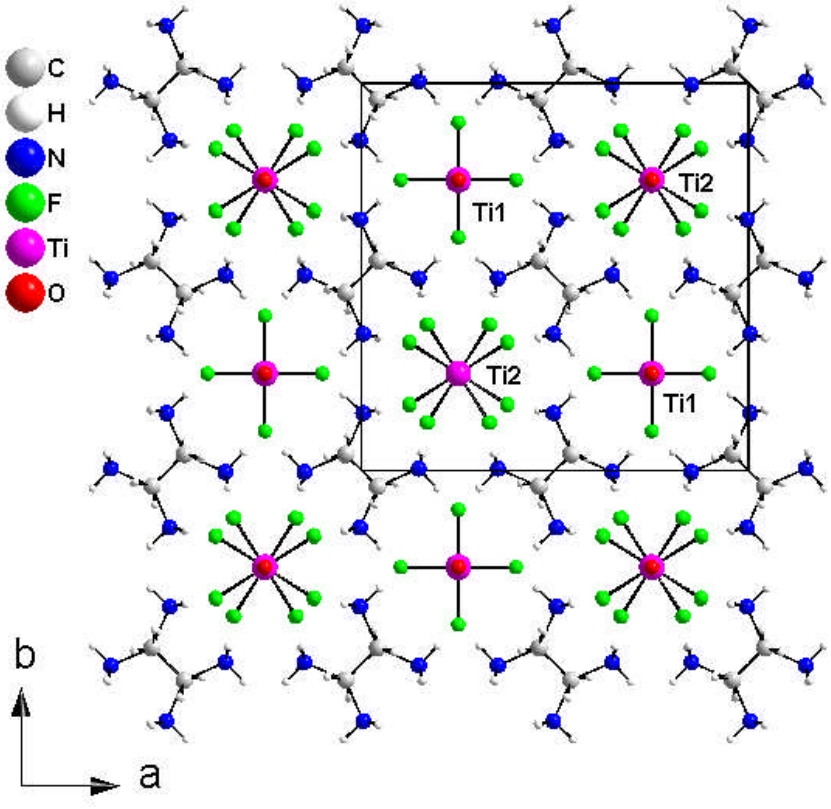

Fig 6.9 The packing in **Ti−2** as viewed down the *c* axis.

6.1.2 Synthetic Conditions for Ti−1 to Ti−5

Product	TiO_2 (g)	HF (ml)	H_2O (ml)	EG (ml)	Template	Template Quantity	Temp (°C)	Time (days)
Ti−1	0.08	0.5	4	5	4-4 Bipyridyl	0.463g	100	1
Ti−2	0.08	0.5	1	5	Ethylene Diamine	0.500ml	100	1
Ti−3	0.08	0.5	2	5	Piperazine	0.258g	100	1
Ti−4	0.08	0.5	3	5	Trans 1,2 bis (4-pyridyl) Ethylene	0.534g	100	1
Ti−5	0.08	0.5	4	5	Caesium Chloride	0.500g	100	1

6.2 Zirconium Fluoride Structures

6.2.1 Existing Oligomeric Compounds

The novel crystal structures contained in this sub-section are inorganic oligomers which have either been made by a different route of synthesis to that previously reported or made with a different organic/inorganic cation. The table below is a list of the first examples of some of the different known structure types of zirconium fluorides.

Chemical Formula	Structure Type	Ox. State	Ref
Li_4ZrF_8	Monomer	IV	24
K_3ZrF_7	Monomer	IV	25
Rb_2ZrF_6	Monomer	IV	26
$Na_5Zr_2F_{13}$	Dimer	IV	27
$(C_2H_{10}N_2)Zr_2F_{12}$	Dimer	IV	28
$Li_3Zr_4F_{19}$	Bent Chains	IV	24
$(N_2H_6)ZrF_6$	Chain	IV	29
$(CN_4H_7)ZrF_5$	Chain	IV	30
$Rb_5Zr_4F_{21}$	Layered	IV	31
$NH_4Zr_5F_{21}$	Layered	IV	32
$NH_4Zr_2F_9$	Layered	IV	32
$Na_7Zr_6F_{31}$	3D	IV	33

Table 6.12 Some of the known structure types of zirconium fluorides.

6.2.1.1 Monomers

$[C_{12}H_{12}N_2][ZrF_6]$ (Zr−1) is based on the previously reported $[ZrF_6]^{2-}$ monomer.[26] The building unit consists of one unique zirconium site and half a molecule of *trans* 1,2 bis(4-pyridyl) ethene, both of which are located about an inversion centre (see Fig 6.10). The zirconium metal centre is confirmed as Zr^{4+} by BVS (see Table 6.13). The structure is held together through an extensive hydrogen bonding network between the fluorine atoms of the $[ZrF_6]^{2-}$ monomer and the protonated *trans* 1,2 bis(4-pyridyl) ethene template.

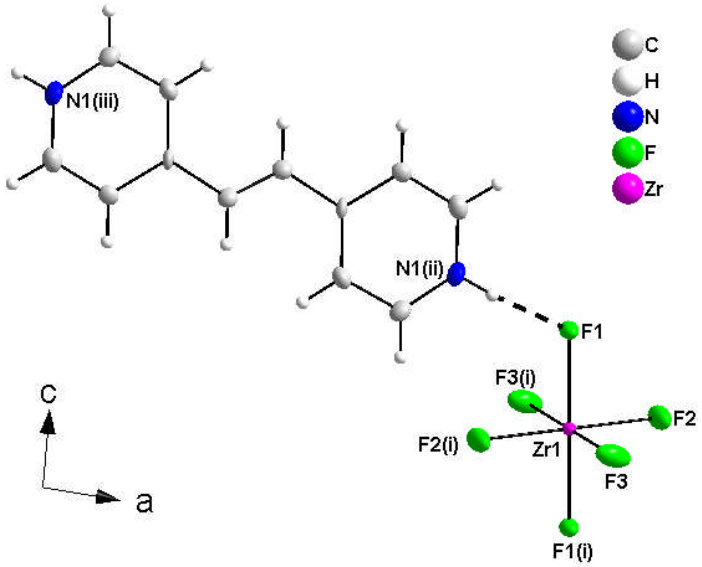

Fig 6.10 The building unit in **Zr−1**. Symmetry operators (i) –*x*, 1-*y*, -*z*, (ii) -1+*x*, *y*, *z*, (iii) -1-*x*, -*y*, 1-*z*.

Bond	Bond Length (Å)	s_{ij}
Zr1−F1	2.047(3)	0.584
Zr1−F1’	2.047(3)	0.584
Zr1−F2	1.994(3)	0.673
Zr1−F2’	1.994(3)	0.673
Zr1−F3	1.997(3)	0.668
Zr1−F3’	1.997(3)	0.668
		∑Zr1 = 3.85

Table 6.13 Selected bond lengths and bond valence sums for **Zr−1**.

$[C_6H_{20}N_3][ZrF_7]$ (Zr−2) and **$[C_2H_{10}N_2]_5[ZrF_7]_3[F]$ (Zr−3)** both contain the previously reported $[ZrF_7]^{3-}$ monomer[25] (see Fig 6.11).

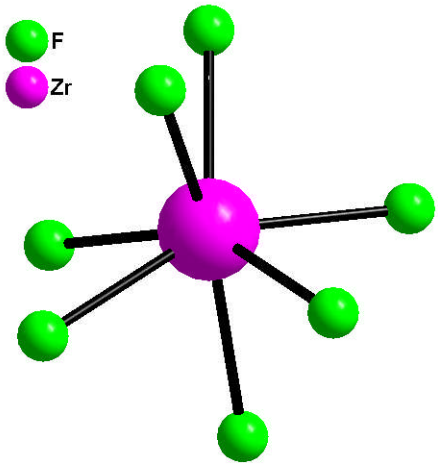

Fig 6.11 The $[ZrF_7]^{3-}$ monomer[8] in **Zr−2** and **Zr−3**.

$[C_6H_{20}N_3][ZrF_7]$ (Zr−2) has a simple building unit shown in Fig 6.12, consisting of one of unique Zr metal centre surrounded by seven unique fluorine atoms and one molecule of the protonated template, diethylene triamine. The Zr metal centre is confirmed as Zr^{4+} by BVS (see Table 6.14). The structure is held together through an extensive hydrogen bonded network from the protonated nitrogen atoms to the fluorine atoms to from the 3D network.

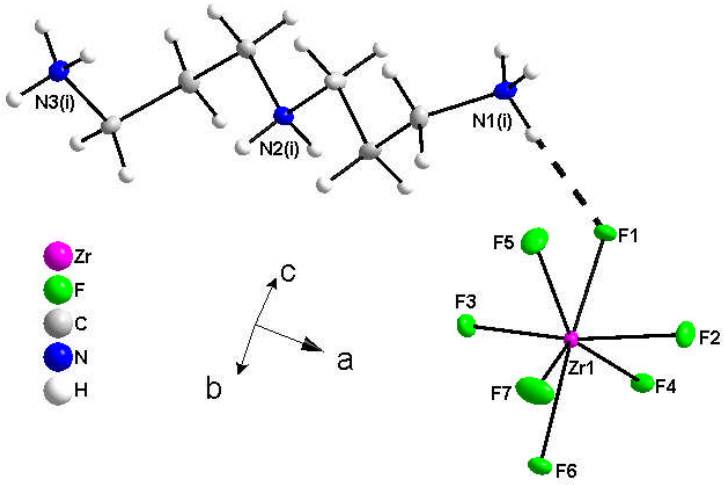

Fig 6.12 The building unit in **Zr−2**. Symmetry operator (i) 1½-*x*, 1-*y*, ½+*z*.

Bond	Bond Length (Å)	s_{ij}
Zr1−F1	2.131(2)	0.465
Zr1−F2	2.042(2)	0.619
Zr1−F3	1.998(2)	0.666
Zr1−F4	2.103(2)	0.502
Zr1−F5	2.025(2)	0.619
Zr1−F6	2.123(2)	0.475
Zr1−F7	2.056(2)	0.570
		∑Zr1 = 3.92

Table 6.14 Selected bond lengths and bond valence sums for **Zr−2**.

$[C_2H_{10}N_2]_5[ZrF_7]_3[F]$ (Zr−3) has three unique Zr metal centres in the building unit which also consists of seven molecules of the protonated template, ethylene diamine, of which four are based around an inversion centre (see Fig 6.13). The three Zr metal sites are confirmed as Zr^{4+} by BVS (see Table 6.15). The structure is held together through a very complex hydrogen bonding network between the protonated amine cation and the zirconium-bonded fluorine atoms. The lone fluorine anion fills an interstitial void and adds an extra degree of strength to the hydrogen bonding network through hydrogen bonding to the amine templates.

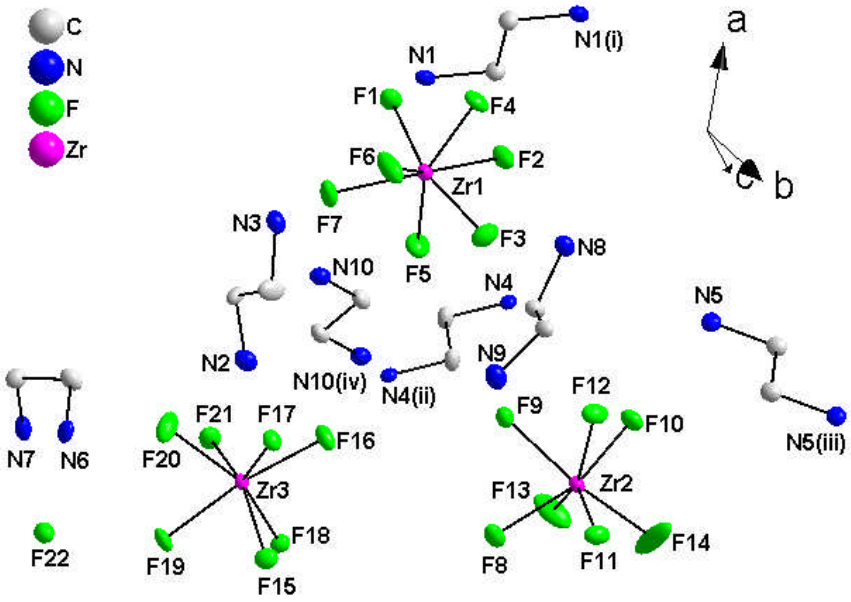

Fig 6.13 The building unit in **Zr−3**. Symmetry operator (i) 1-*x*, 1-*y*, -*z*, (ii) –*x*, 1-*y*, -*z*, (iii) 1-*x*, 2-*y*, 1-*z*, (iv) –*x*, -*y*, 1-*z*. Hydrogen atoms have been omitted for clarity.

Bond	Bond Length (Å)	s_{ij}	Bond	Bond Length (Å)	s_{ij}
Zr1−F1	2.027(4)	0.616	Zr2−F8	2.067(4)	0.553
Zr1−F2	2.098(4)	0.508	Zr2−F9	2.102(4)	0.503
Zr1−F3	2.050(4)	0.579	Zr2−F10	2.102(4)	0.503
Zr1−F4	2.059(4)	0.565	Zr2−F11	2.072(4)	0.545
Zr1−F5	2.064(4)	0.557	Zr2−F12	2.049(4)	0.580
Zr1−F6	2.090(4)	0.520	Zr2−F13	2.059(4)	0.565
Zr1−F7	2.068(4)	0.551	Zr2−F14	2.012(5)	0.641
		∑Zr1 = 3.90			**∑Zr2 = 3.89**

Bond	Bond Length (Å)	s_{ij}
Zr3−F15	2.013(4)	0.640
Zr3−F16	2.050(4)	0.579
Zr3−F17	2.072(3)	0.545
Zr3−F18	2.134(3)	0.461
Zr3−F19	2.076(3)	0.540
Zr3−F20	2.056(4)	0.570
Zr3−F21	2.074(4)	0.543
		∑Zr3 = 3.88

Table 6.15 Selected bond lengths and bond valence sums for **Zr−3**.

6.2.2 Synthetic Conditions for Zr−1 to Zr−3

Product	ZrO_2 (g)	HF (ml)	H_2O (ml)	EG (ml)	Template	Template Quantity	Temp (°C)	Time (days)
Zr−1	0.12	0.5	1	5	Trans 1,2 bis (4-pyridyl) ethylene	0.534g	100	1
Zr−2	0.12	0.5	0	5	(3-aminopropyl) 1,3 propane diamine	0.500ml	100	1
Zr−3	0.12	0.5	1	5	Ethylene Diamine	0.500ml	100	1

6.3 Hafnium Fluoride Structures

6.3.1 New Oligomeric Compounds

The structures in this sub-section contain new inorganic oligomers i.e. the inorganic moiety of the structure has not previously been reported.

6.3.1.1 Dimers

$Na_5Hf_2F_{13}$ (Hf−6) is a dimeric structure based on two corner sharing $[HfF_7]^{3-}$ monomers. The building unit consists of one crystallographically unique Hf metal centre, four unique fluorine atoms and three sodium cations (see Fig 6.14) related to each other by symmetry to create the complete $[Hf_2F_{13}]^{5-}$ dimer. The Hf metal centre is confirmed as Hf^{4+} by BVS (see Table 6.16). The structure is held together through a network of ionic bonding from the sodium cations surrounding the $[Hf_2F_{13}]^{5-}$ dimer (see Fig 6.15). The structure is isostructural with the known material, $Na_5Zr_2F_{13}$,[27] and crystallises in the same space group, C 2/m. The single crystal data collected for this structure proved to be insufficient for a full anisotropic refinement, so the refinement has been left isotropic as a result.

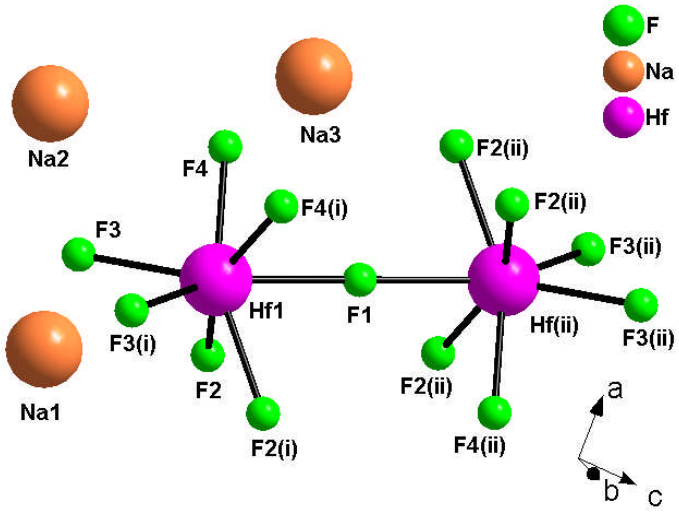

Fig 6.14 The building unit in **Hf−6**. Symmetry operators (i) *x*, -*y*, *z*, (ii) 2-*x*, *y*, 1-*z*.

Bond	Bond Length (Å)	s_{ij}
Hf1−F1	2.109(1)	0.497
Hf1−F2	2.053(7)	0.575
Hf1−F2’	2.053(7)	0.575
Hf1−F3	2.042(7)	0.595
Hf1−F3’	2.042(7)	0.595
Hf1−F4	2.039(9)	0.600
Hf1−F4’	2.039(9)	0.600
		$\sum Hf_1$ = 4.04

Table 6.16 Selected bond lengths and bond valence sums for **Hf−6**.

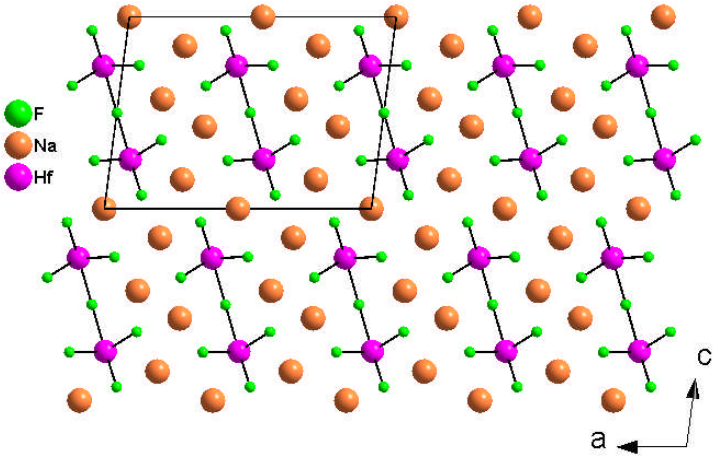

Fig 6.15 The packing in **Hf−6**.

6.3.2 Existing Oligomeric Compounds

The novel crystal structures contained in this sub-section contain inorganic oligomers which have either been made by a different route of synthesis to that previously reported or made with a different organic/inorganic cation. The table below is a list of some first examples of the different known structure types for hafnium fluorides.

Chemical Formula	Structure Type	Ox. State	Ref
Na_3HfF_7	Monomer	IV	34
Rb_2HfF_6	Monomer	IV	26
$(C_{10}H_8N_2)_2HfF_4$	Monomer	IV	35
$(C_4H_{18}N_2)_2(Hf_2F_{12})$	Dimer	IV	36
$K_5(Hf_3F_{17})\cdot H_2O$	Zig-Zag Chain	IV	37
$(NH_4)Hf_2F_9$	Layered	IV	32
$(NH_3)HfF_4$	Layered	IV	38
$(NH_4)HfF_5$	Layered	IV	39

Table 6.17 Some of the known structure types of hafnium fluorides.

6.3.2.1 Monomers

$[C_4H_{16}N_3][HfF_7]\cdot H_2O$ (Hf−2) is based on the previously reported $[HfF_7]^{3-}$ monomer[34] shown below in Fig 6.16, along with the rest of the contents of the asymmetric unit which comprise of a molecule of water and the protonated template species, diethylene triamine. The monomers are linked together into a "dimer" mediated by the water molecules (as shown in Fig 6.17). These hydrogen bonded dimers are then surrounded by the cationic template, which separates them from each other and holds the structure together through an extensive hydrogen bonded network. The Hf metal centre is confirmed as Hf^{4+} by BVS (see Table 6.18).

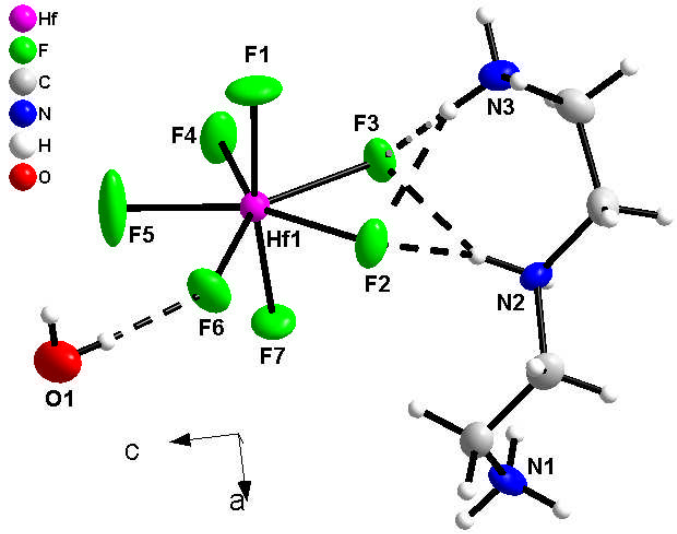

Fig 6.16 The asymmetric unit in **Hf−2**.

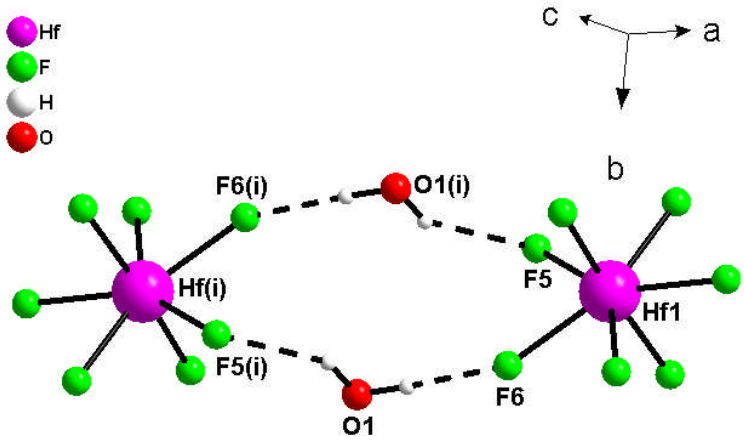

Fig 6.17 The hydrogen bonded "dimer" in **Hf−2**.
Symmetry operator (i) 1-*x*, 1-*y*, 1-*z*.

Bond	Bond Length (Å)	s_{ij}
Hf1−F1	1.975(4)	0.713
Hf1−F2	2.094(3)	0.517
Hf1−F3	2.128(3)	0.472
Hf1−F4	2.049(4)	0.584
Hf1−F5	2.029(4)	0.616
Hf1−F6	2.051(4)	0.581
Hf1−F7	1.975(4)	0.713
		∑Hf1 = 4.13

Table 6.18 Selected bond lengths and bond valence sums for **Hf−2**.

$[C_4H_{12}N_2][HfF_6]$ (Hf−4) and $[C_{10}H_{10}N_2][HfF_6]$ (Hf−5) are both based on the previously reported $[HfF_6]^{2-}$ monomer[26] shown below in Fig 6.18.

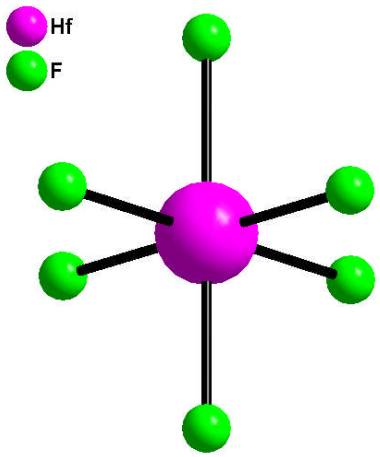

Fig 6.18 The $[HfF_6]^{2-}$ monomer in **Hf−4** and **Hf−5**.

The building unit of **$[C_4H_{12}N_2][HfF_6]$ (Hf−4)** consists of a crystallographically unique $[HfF_6]^{2-}$ monomer and a molecule of protonated piperazine which both sit about inversion centres (see Fig 6.19). The Hf metal centre is confirmed as Hf^{4+} by BVS (see Table 6.19). The fluorine atoms are bonded to the Hf metal centre at a range of distances from 1.991(2) Å to 2.008(2) Å. The 3D structure is comprised of an extensive hydrogen bonding network from the protonated cationic template to the fluorine atoms of the $[HfF_6]^{2-}$ monomer.

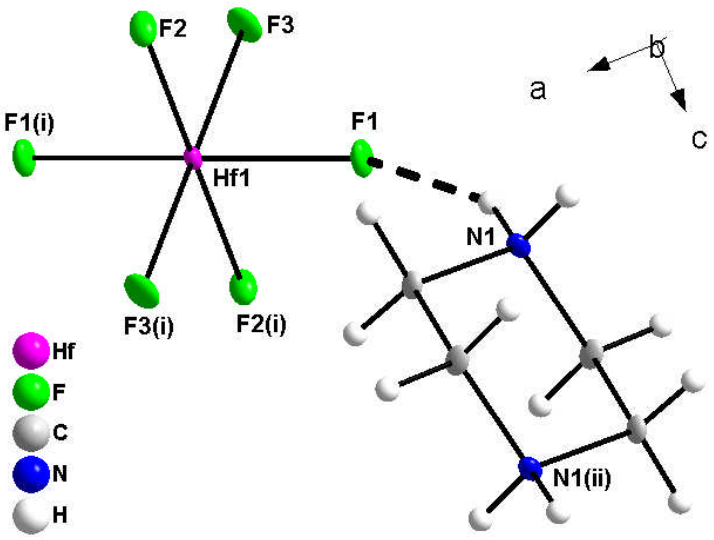

Fig 6.19 The building unit in **Hf−4**. Symmetry operator (i) 1-*x*, -*y*, 1-*z*, (ii) –*x*, -1-*y*, 2-*z*.

Bond	Bond Length (Å)	s_{ij}
Hf1−F1	2.004(2)	0.660
Hf1−F1’	2.004(2)	0.660
Hf1−F2	2.008(2)	0.652
Hf1−F2’	2.008(2)	0.652
Hf1−F3	1.991(2)	0.683
Hf1−F3’	1.991(2)	0.683
		∑Hf1 = 3.99

Table 6.19 Selected bond lengths and bond valence sums for **Hf−4**.

$[C_{10}H_{10}N_2][HfF_6]$ (Hf−5) consists of a crystallographically unique $[HfF_6]^{2-}$ monomer and a molecule of the protonated 4,4 bipyridyl template which both sit about inversion centres in the building unit (see Fig 6.20). The Hf metal centre is confirmed as Hf^{4+} by BVS (see Table 6.20). The fluorine atoms are bonded to the Hf metal centre at a range of distances from 1.971(4) Å to 2.005(4) Å. The 3D structure is comprised of an extensive hydrogen bonding network from the protonated cationic template to the fluorine atoms of the $[HfF_6]^{2-}$ monomer. The template also shows some lateral movement or disorder in the *bc* plane, causing the anisotropic ellipsoids to become elongated (see Fig 6.20).

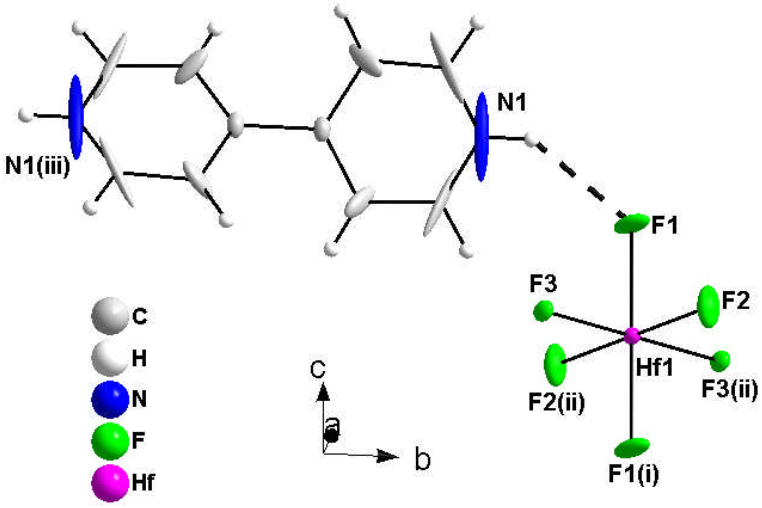

Fig 6.20 The building unit in **Hf−5**. Symmetry operators (i) –*x*, -*y*, -*z*, (ii) –*x*, -*y*, *z*, (iii) –*x*, -1-*y*, *z*.

Bond	Bond Length (Å)	s_{ij}
Hf1−F1	2.005(4)	0.658
Hf1−F1(i)	2.005(4)	0.658
Hf1−F2	1.971(4)	0.721
Hf1−F2'(iii)	1.971(4)	0.721
Hf1−F3	1.979(4)	0.706
Hf1−F3(ii)	1.979(4)	0.706
		∑Hf1 = 4.17

Table 6.20 Selected bond lengths and bond valence sums for **Hf−5**.

6.3.2.2 Dimers

$Na_4Hf_2F_{12}$ (Hf−1) and **$[C_6H_{22}N_4][Hf_2F_{12}]$ (Hf−3)** are both based on the previously reported $[Hf_2F_{12}]^{4-}$ dimer[37] shown below in Fig 6.21.

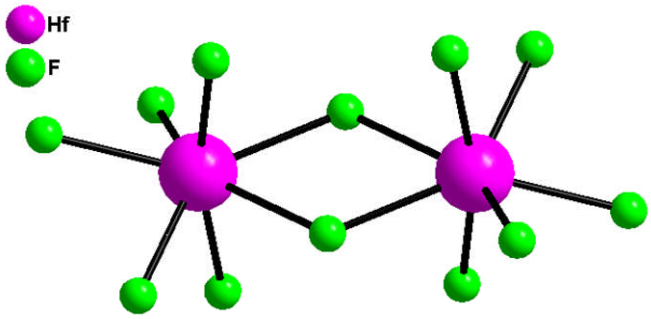

Fig 6.21 The $[Hf_2F_{12}]^{4-}$ dimer[37] in **Hf−1** and **Hf−3**.

$Na_4Hf_2F_{12}$ (Hf−1) has one crystallographically unique $[HfF_7]^{3-}$ monomer which shares a common edge with another $[HfF_7]^{3-}$ monomer, to which it is related by an inversion centre, to form the $[Hf_2F_{12}]^{4-}$ dimer in the building unit shown below in Fig 6.22. The building unit also contains two crystallographically unique sodium cations and it is through ionic bonding from the anionic dimer to these cations that the 3D structure is composed. The unique Hf metal centre is confirmed as Hf^{4+} by BVS (see Table 6.21).

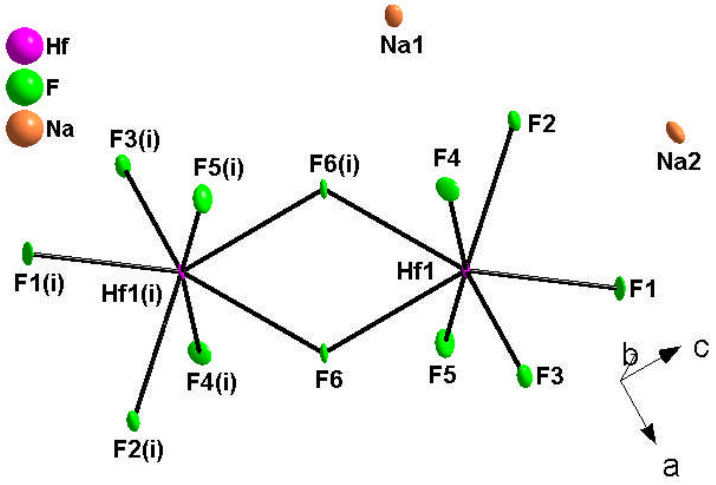

Fig 6.22 The building unit in **Hf−1**. Symmetry operator (i) *–x*, *-y*, *-z*.

Bond	Bond Length (Å)	s_{ij}
Hf1−F1	2.047(4)	0.587
Hf1−F2	2.042(4)	0.595
Hf1−F3	2.000(4)	0.667
Hf1−F4	2.032(4)	0.611
Hf1−F5	1.993(4)	0.679
Hf1−F6	2.126(4)	0.474
Hf1−F6’	2.178(4)	0.412
		∑Hf1 = 4.03

Table 6.21 Selected bond lengths and bond valence sums for **Hf−1**.

The $[Hf_2F_{12}]^{4-}$ dimer in **$[C_6H_{22}N_4][Hf_2F_{12}]$ (Hf−3)** shares many similarities to that in **Hf−1**; it too is based around a crystallographically unique $[HfF_7]^{3-}$ monomer which shares a common edge with another $[HfF_7]^{3-}$ monomer, to which it is related by an inversion centre, to form the $[Hf_2F_{12}]^{4-}$ dimer in the building unit shown below in Fig 6.23. The protonated template, triethylene tetramine, is also situated about an inversion centre in the building unit and it is through hydrogen bonding from this template to the fluorine atoms of the $[Hf_2F_{12}]^{4-}$ dimer that the 3D structure is formed. The Hf metal centre is confirmed as Hf^{4+} by BVS (see Table 6.22).

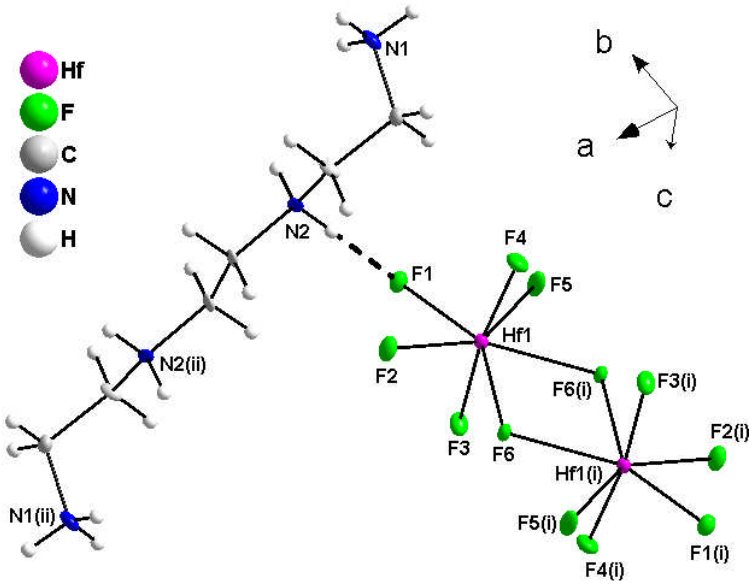

Fig 6.23 The building unit in **Hf−3**. Symmetry operator (i) *–x*, 1-*y*, -*z*, (ii) 1-*x*, 2-*y*, -*z*.

Bond	Bond Length (Å)	s_{ij}
Hf1−F1	2.050(3)	0.582
Hf1−F2	2.033(3)	0.610
Hf1−F3	1.982(3)	0.700
Hf1−F4	1.992(3)	0.681
Hf1−F5	2.042(3)	0.595
Hf1−F6	2.124(3)	0.477
Hf1−F6’	2.182(3)	0.408
		∑Hf1 = 4.05

Table 6.22 Selected bond lengths and bond valence sums for **Hf−3**.

6.3.3 Synthetic Aspects

6.3.3.1 Effect of Temperature on the Sodium System

Heat can display an enormous effect on the products formed in reactions. In hydrothermal reactions the pressures generated by elevated temperatures can lead to the condensation of structures and also the extra heat can increase the reactivity of reagents.

When the temperature used to synthesize **Hf−1** is increased from 100 °C to 220 °C, the product **Hf−6** is formed (see synthetic conditions − Appendix D). Normally an increase in temperature would correlate to an increase in connectivity. This is not the case in this system

as the both products contain a dimer although the dimer in **Hf−1** is an edge-sharing dimer whilst the dimer in **Hf−6** is corner sharing (see Fig 6.24). Intuitively this does not seem to be an increase in connectivity but could be a more condensed method of packing in the structure of **Hf−6** caused by the elevated temperature and pressure of synthesis.

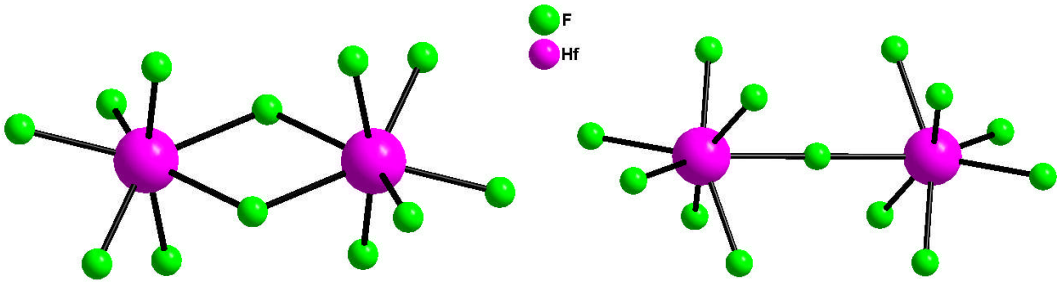

Fig 6.24 The $[Hf_2F_{12}]^{4-}$ and $[Hf_2F_{13}]^{5-}$ dimers in **Hf−1** and **Hf−6** respectively.

6.3.4 Synthetic Conditions for Hf−1 to Hf−6

Product	HfO_2 (g)	HF (ml)	H_2O (ml)	EG (ml)	Template	Template Quantity	Temp (°C)	Time (days)
Hf−1	0.315	0.75	0	2.5	Sodium Nitrite	0.100g	100	1
Hf−2	0.315	0.75	2.5	2.5	Diethylene Triamine	0.250ml	100	1
Hf−3	0.315	0.75	2.5	2.5	Triethylene Tetramine	0.250ml	100	1
Hf−4	0.315	0.75	2.0	2.5	Piperazine	0.129g	100	1
Hf−5	0.315	0.75	0	2.5	4-4 Bipyridyl	0.232g	100	1
Hf−6	0.315	0.75	1.5	2.5	Sodium Nitrite	0.100g	220	1

6.4 Niobium OxyFluoride Structures

6.4.1 Existing Oligomeric Compounds

The novel crystal structures contained in this sub-section contain inorganic oligomers which have either been made by a different route of synthesis to that previously reported or made with a different organic/inorganic cation. The table below is a list of some of the first examples of the different known structure types for niobium oxyfluorides.

Chemical Formula	Structure Type	Ox. State	Ref
$K_2(NbOF_5)(KHF_2)$	Monomer	V	40
K_3NbOF_6	Monomer	V	41
$K_2NaNbO_2F_4$	Monomer	V	4
$(N_2H_6)_2NbOF_7$	Monomer	V	42
$(C_6H_{16}N)NbOF_4(H_2O)$	Monomer	V	43
$K_5Nb_3O_3F_{14}(H_2O)$	Monomers & Dimers	V	44
$(C_2H_{10}N_2)_2[Nb_2O_3F_8]$	Dimer	V	45
$(NH_4)NbOF_4$	Linear Chain	V	46
NbO_2F_1	3D	V	47

Table 6.23 Some of the known structure types of niobium oxyfluorides

6.4.1.1 Monomers

$[C_{12}H_{12}N_2][NbOF_5]$ (Nb−1), **$[C_6H_{22}N_4][NbOF_5]_2$ (Nb−2)**, **$[C_{10}H_{28}N_4][NbOF_5]_2{\cdot}2H_2O$ (Nb−3)**, **$[C_6H_{16}N_2][NbOF_5]$ (Nb−4)** and **$[C_4H_{12}N_2][NbOF_5]$ (Nb−5)** are all based on the previously reported $[NbOF_5]^{2-}$ monomer[40] shown below in Fig 6.25. It is also worth noting the bond valence sums, which all come in considerably higher than the expected value of 5. The BVS calculations are performed using the VALENCE[18] program with variables determined either by Brown & Altermatt[19] or O'Keeffe & Brese.[20] The difference between the two sets of parameters is that those supplied by Brown & Altermatt are calculated, whilst those by O'Keeffe & Brese are partially derived, although those used in this work were calculated which leaves the question open as to the cause of the discrepancy. The values used for the BVS calculations of **Nb−1**, **Nb−2**, **Nb−3**, **Nb−4** and **Nb−5** were by O'Keefe & Brese.

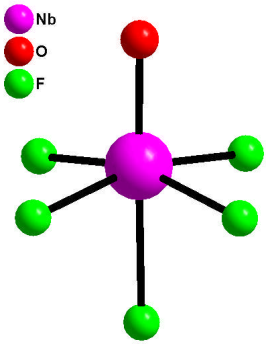

Fig 6.25 The $[NbOF_5]^{2-}$ monomer[12] in **Nb−1**, **Nb−2**, **Nb−3**, **Nb−4** and **Nb−5**.

$[C_{12}H_{12}N_2][NbOF_5]$ (Nb−1) is comprised of one crystallographically unique niobium site and half a molecule of the protonated template, *trans* 1,2 bis (4-pyridyl) ethane, both of which are situated around inversion centres to make the complete building unit shown below in Fig 6.26. The niobium metal centre is confirmed as Nb^{5+} by BVS (see Table 6.24) even though it is disordered. There is a partial O/F disorder of the F1 and F2 sites in the monomer. The structure is held together through a complex network of hydrogen bonding.

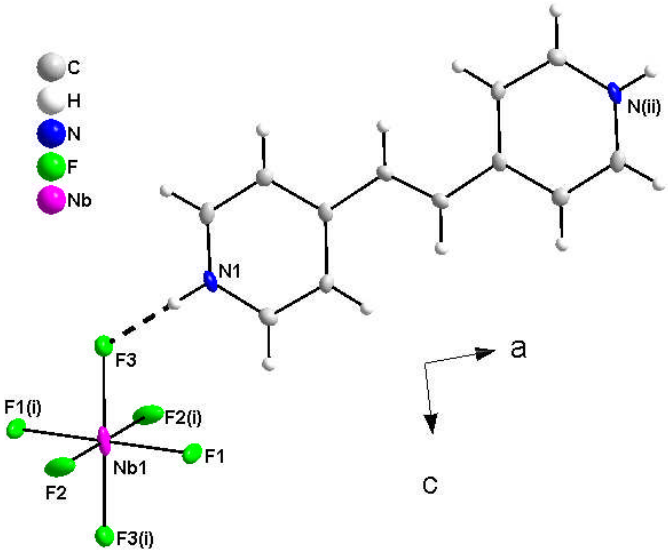

Fig 6.26 The building unit in **Nb−1**. Symmetry operator (i) -*x*, -*y*, 1-*z*, (ii) 2-*x*, 1-*y*, -*z*.

Bond	Bond Length (Å)	s_{ij}
Nb1−O1*	1.924(1)	0.241
Nb1−O1*	1.924(1)	0.241
Nb1−O1*	1.922(1)	0.243
Nb1−O1*	1.922(1)	0.243
Nb1−F1*	1.924(1)	0.648
Nb1−F1*	1.924(1)	0.648
Nb1−F2*	1.922(1)	0.652
Nb1−F2*	1.922(1)	0.652
Nb1−F3	1.940(1)	0.828
Nb1−F3’	1.940(1)	0.828
		∑Nb1 = 5.22

Table 6.24 Selected bond lengths and bond valence sums for **Nb−1**.
* = Disordered atom.

$[C_6H_{22}N_4][NbOF_5]_2$ (Nb−2) has one crystallographically unique niobium site and half a molecule of protonated triethylene tetramine which sits on an inversion centre to make the complete molecule in the building unit (see Fig 6.27). An extensive network of hydrogen bonding holds the 3D structure together. The Nb metal centre is confirmed as Nb^{5+} through BVS (see Table 6.25).

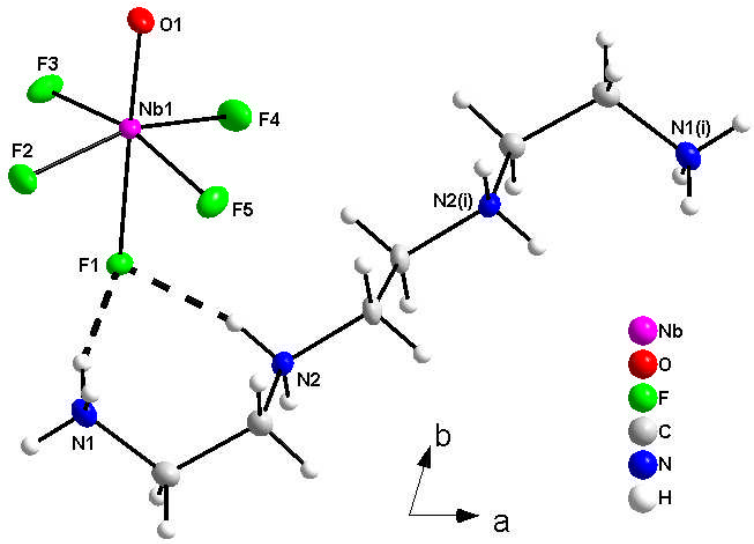

Fig 6.27 The building unit in **Nb−2**. Symmetry operator (i) 2-*x*, 1-*y*, 1-*z*.

Bond	Bond Length (Å)	s_{ij}
Nb1−O1	1.729(2)	1.635
Nb1−F1	2.150(2)	0.469
Nb1−F2	1.930(2)	0.850
Nb1−F3	1.957(2)	0.790
Nb1−F4	1.925(2)	0.862
Nb1−F5	1.966(2)	0.771
		∑Nb1 = 5.38

Table 6.25 Selected bond lengths and bond valence sums for **Nb−2**.

$[C_{10}H_{28}N_4][NbOF_5]_2 \cdot 2H_2O$ (Nb−3) has one crystallographically unique niobium site, half a molecule of the protonated template species; cyclam (which sits on an inversion centre to form the complete template) and a molecule of water in the building unit (see Fig 6.28). The Nb metal centre is confirmed as Nb^{5+} through BVS (see Table 6.26). An extensive network of hydrogen bonding holds the 3D structure together. The monomers are linked at each end (F1 and O1) directly and indirectly (via the water molecule) to two different template molecules (see Fig 6.29). The complete packing can be seen in a view upon the *bc* plane (see Fig 6.30).

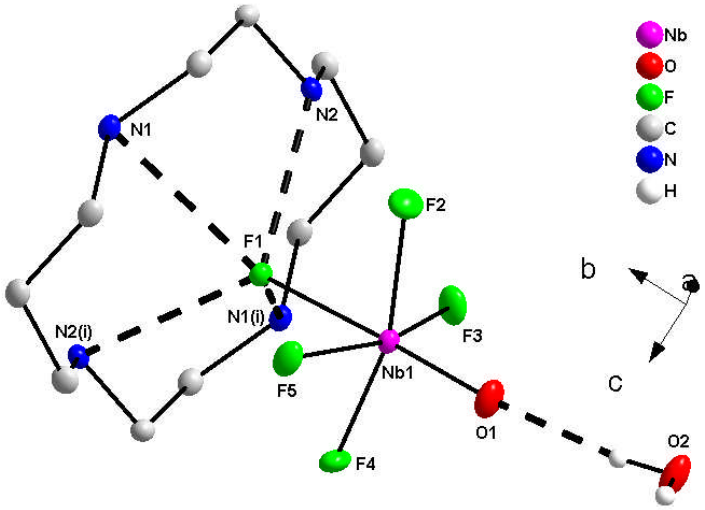

Fig 6.28 The building unit in **Nb−3**. Symmetry operator (i) -x, *2*-y, *-z*.
Some hydrogen atoms have been omitted for clarity.

Bond	Bond Length (Å)	s_{ij}
Nb1−O1	1.727(2)	1.644
Nb1−F1	2.120(2)	0.509
Nb1−F2	1.939(2)	0.830
Nb1−F3	1.927(2)	0.857
Nb1−F4	1.958(2)	0.788
Nb1−F5	1.940(2)	0.828
		∑Nb1 = 5.46

Table 6.26 Selected bond lengths and bond valence sums for **Nb−3**.

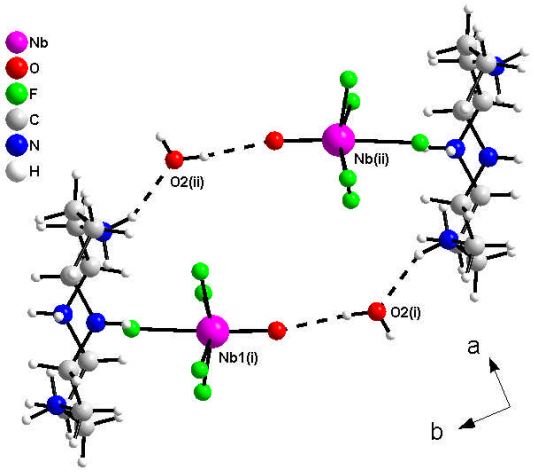

Fig 6.29 The hydrogen bonding in **Nb−3**. Symmetry operators (i) *-x*, -½+*y*, -½-*z*, (ii) *x*, ½-*y*, -½+*z*.

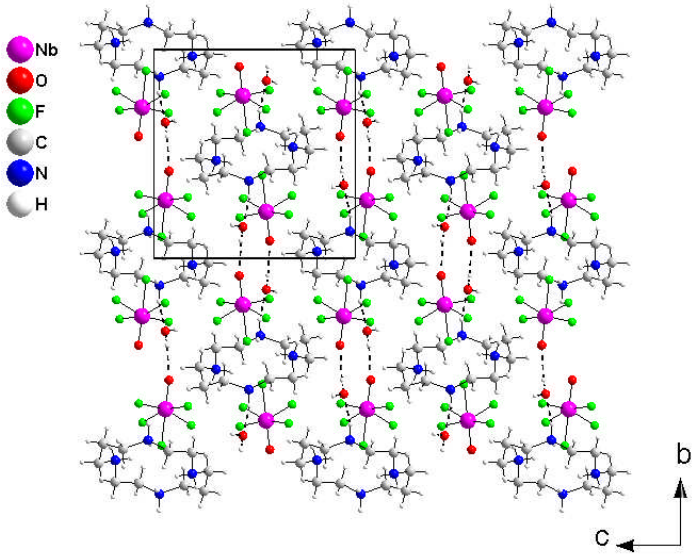

Fig 6.30 The packing in the *bc* plane in **Nb−3**.

$[C_6H_{16}N_2][NbOF_5]$ (Nb−4) has one crystallographically unique niobium site and one molecule of protonated template 1,2 diamino cyclohexane to make the complete molecule in the building unit (see Fig 6.31). The template is both the *cis* and *trans* version of 1,2 diamino cyclohexane, which causes a disorder of the amine group, N2 (see Fig 6.31). An extensive network of hydrogen bonding holds the 3D structure together. The Nb metal centre is confirmed as Nb^{5+} through BVS (see Table 6.27).

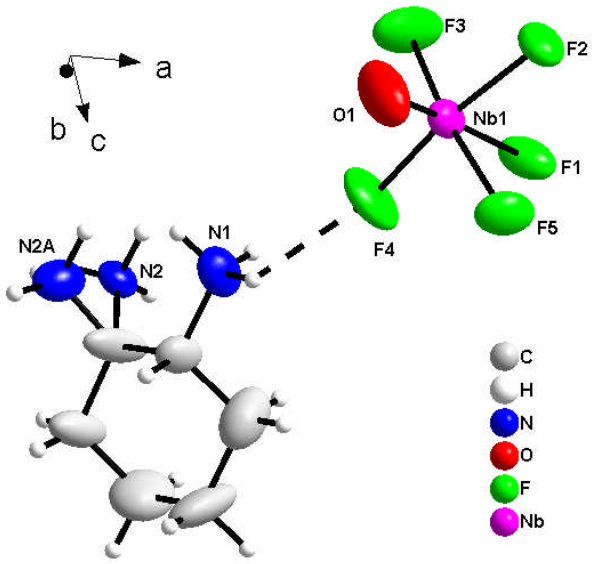

Fig 6.31 The asymmetric unit in **Nb−4**.

Bond	Bond Length (Å)	s_{ij}
Nb1−O1	1.732(6)	1.622
Nb1−F1	2.126(4)	0.501
Nb1−F2	1.927(4)	0.857
Nb1−F3	1.946(5)	0.814
Nb1−F4	1.916(4)	0.883
Nb1−F5	1.949(4)	0.808
		∑Nb1 = 5.49

Table 6.27 Selected bond lengths and bond valence sums for **Nb−4**.

$[C_4H_{12}N_2][NbOF_5]$ (Nb−5) has one crystallographically unique niobium site and two molecules of protonated template piperazine (both situated around inversion centres) to make the complete building unit (see Fig 6.32). An extensive network of hydrogen bonding holds the 3D structure together. The Nb metal centre is confirmed as Nb^{5+} through BVS (see Table 6.28). The product was synthesised at both 100 °C and 160 °C, with the higher temperature route of synthesis providing better single crystals for diffraction studies.

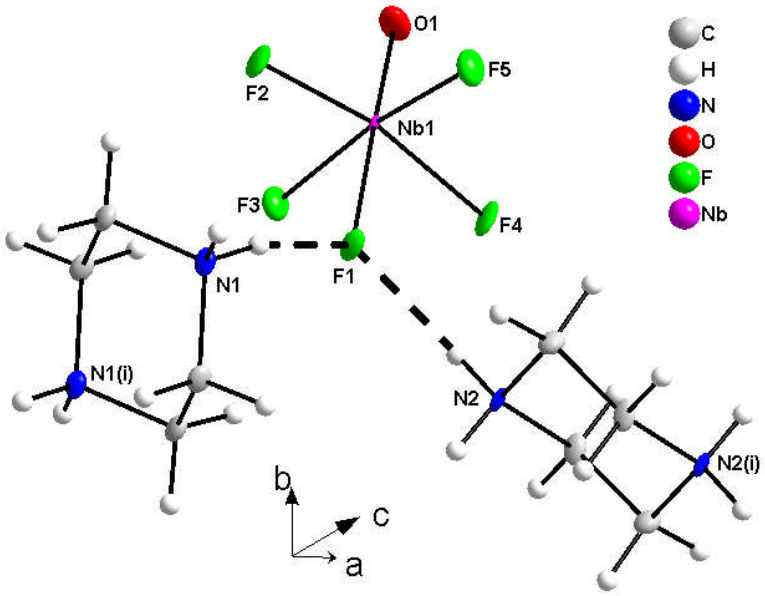

Fig 6.32 The building unit in **Nb−5**. Symmetry operator (i) *-x*, *-y*, *-z*, (ii) 1-*x*, -1-*y*, 1-*z*.

Bond	Bond Length (Å)	s_{ij}
Nb1−O1	1.736(3)	1.605
Nb1−F1	2.120(2)	0.509
Nb1−F2	1.925(2)	0.862
Nb1−F3	1.929(2)	0.853
Nb1−F4	1.965(2)	0.774
Nb1−F5	1.947(2)	0.774
		∑Nb1 = 5.42

Table 6.28 Selected bond lengths and bond valence sums for **Nb−5**.

6.4.2 Synthetic Conditions for Nb−1 to Nb−5

Product	Nb_2O_5 (g)	HF (ml)	H_2O (ml)	EG (ml)	Template	Template Quantity	Temp (°C)	Time (days)
Nb−1	0.39	0.5	2.5	2.5	Trans 1,2 bis (4-pyridyl) Ethylene	0.534g	100	1
Nb−2	0.39	0.5	1.5	2.5	Triethylene Tetramine	0.250ml	100	1
Nb−3	0.39	0.5	0	2.5	Cyclam	0.296g	100	1
Nb−4	0.27	1.0	0	5	1,2 Diamino Cyclohexane	0.500ml	100	1
Nb−5	0.27	0.5	2	5	Piperazine	0.258g	160	1

6.5 Tantalum Fluoride Structures

6.5.1 Existing Oligomeric Compounds

The novel crystal structures contained in this sub-section contain inorganic oligomers which have either been made by a different route of synthesis to that previously reported or made with a different organic/inorganic cation. The table below is a list of some of the first examples of the different known structure types for tantalum fluorides.

Chemical Formula	Structure Type	Ox. State	Ref
Na_3TaF_8	Monomer	V	48
K_2TaF_7	Monomer	V	48
NH_4TaF_6	Monomer	V	49
TaF_5	Tetramer	V	50
TaF_3	3D	III	51

Table 6.29 Some of the known structure types of tantalum fluorides.

6.5.1.1 Monomers

$[C_6H_{22}N_4][TaF_7][F]$ (Ta−1), **$[C_4H_{16}N_3]_2[TaF_7]_3$ (Ta−2)** and **$[C_4H_{12}N_2][TaF_7]$ (Ta−3)** are all based on the previously reported $[TaF_7]^{2-}$ monomer[48] shown below in Fig 6.33. It is also worth noting the bond valence sums, which all come in considerably higher than the expected value of 5. The BVS calculations are performed using the VALENCE[18] program with parameters determined either by Brown & Altermatt[19] or O'Keeffe & Brese.[20] The difference between the two sets of variables is that those supplied by Brown & Altermatt are calculated, whilst those by O'Keeffe & Brese are partially derived, which leaves the question open as to the discrepancy. The values used for the BVS calculations of **Ta−1**, **Ta−2** and **Ta−3** were by O'Keeffe & Brese.

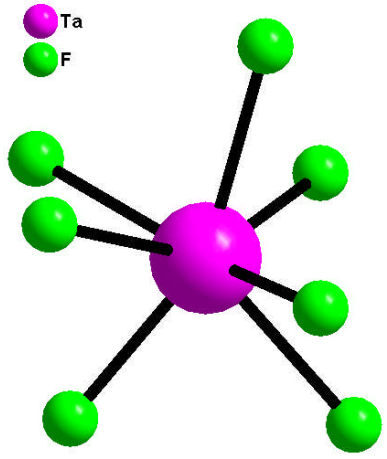

Fig 6.33 The $[TaF_7]^{2-}$ monomer[13] in **Ta−1**, **Ta−2** and **Ta−3**.

$[C_6H_{22}N_4][TaF_7][F]$ (Ta−1) has one crystallographically unique tantalum site, one molecule of protonated template; tris (2-aminoethyl) amine and a fluoride anion to make the complete molecule in the building unit (see Fig 6.34). An extensive network of hydrogen bonding holds the 3D structure together with the fluoride anion filling some of the interstitial voids and strengthening the hydrogen bonded network. The Ta metal centre is confirmed as Ta^{5+} through BVS (see Table 6.30).

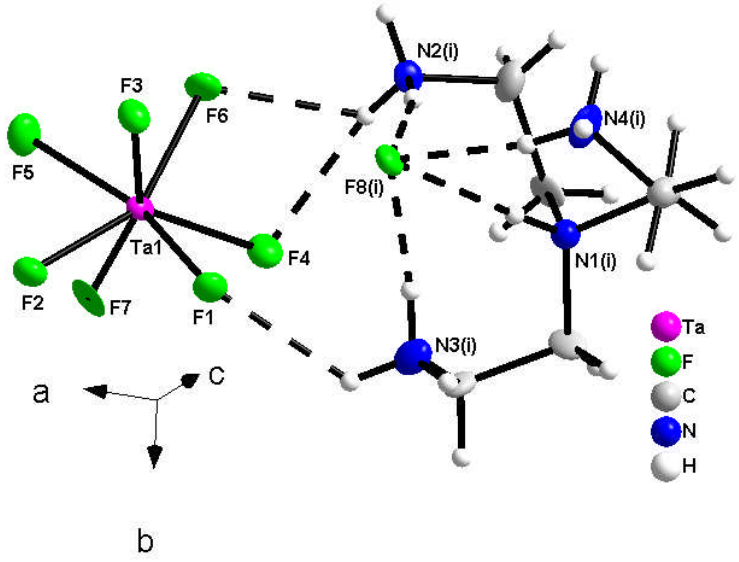

Fig 6.34 The building unit in **Ta−1**. Symmetry operator (i) -1-*x*, *y*, *z*.

Bond	Bond Length (Å)	s_{ij}
Ta1−F1	1.939(17)	0.853
Ta1−F2	1.993(18)	0.737
Ta1−F3	1.971(17)	0.782
Ta1−F4	1.985(18)	0.753
Ta1−F5	1.967(18)	0.790
Ta1−F6	1.917(17)	0.905
Ta1−F7	1.807(19)	1.218
		∑Ta1 = 6.04

Table 6.30 Selected bond lengths and bond valence sums for **Ta−1**.

$[C_4H_{16}N_3]_2[TaF_7]_3$ (Ta−2) has three crystallographically unique tantalum sites and two molecules of protonated template; diethylene triamine in the asymmetric unit (see Fig 6.35). An extensive network of hydrogen bonding holds the 3D structure together. The Ta metal centre is confirmed as Ta^{5+} through BVS (see Table 6.31). The two molecules of the template

are in different conformations to one another; with one in the *syn* conformation and the other being “bent” around the centre of the template at N2 by an angle of 117.3(2)° which as a result causes the material crystallise in the space group P 2_1. As the structure is non-centrosymmetric it should be SHG active and was sent to Prof. Shiv Halasyamani of the University of Houston, Texas for analysis. The material proved to be not SHG active or the SHG signal was too low to be measured. This is not surprising as the three different monomers have, if any, very slight out-of-centre distortions with the difference in bond lengths from the shortest to the longest being around 0.10 Å. The material was also soluble in excess water and was able to be used as a starting reagent. If the material was dissolved in water and piperazine was added along with ethylene glycol, the material **Ta−3** was formed. No extra HF needed to be added to form single crystal products.

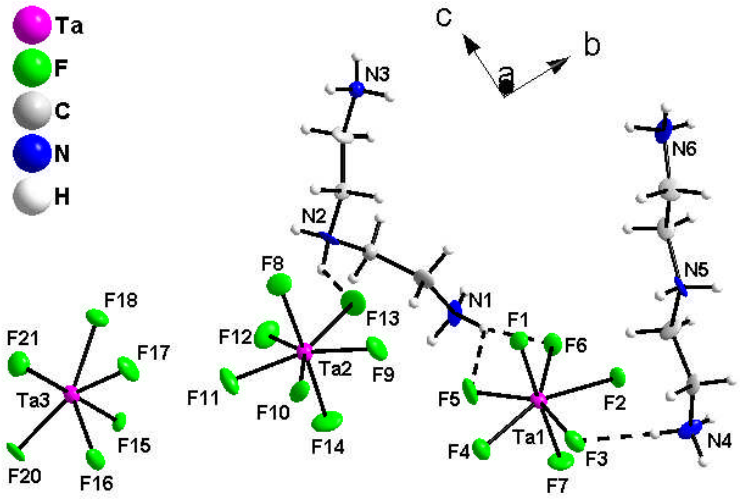

Fig 6.35 The asymmetric unit in **Ta−2**.

Bond	Bond Length (Å)	s_{ij}	Bond	Bond Length (Å)	s_{ij}
Ta1−F1	1.890(11)	0.973	Ta2−F8	1.924(11)	0.888
Ta1−F2	1.956(12)	0.814	Ta2−F9	1.940(13)	0.850
Ta1−F3	1.996(11)	0.731	Ta2−F10	1.978(11)	0.767
Ta1−F4	1.973(12)	0.778	Ta2−F11	1.937(14)	0.857
Ta1−F5	1.925(12)	0.885	Ta2−F12	1.986(12)	0.751
Ta1−F6	1.971(11)	0.782	Ta2−F13	1.948(13)	0.832
Ta1−F7	1.910(11)	0.922	Ta2−F14	1.910(12)	0.922
		∑Ta1 = 5.89			**∑Ta2 = 5.87**

Bond	Bond Length (Å)	s_{ij}
Ta1−F15	1.895(11)	0.960
Ta1−F16	1.948(11)	0.832
Ta1−F17	1.960(12)	0.806
Ta1−F18	1.973(12)	0.778
Ta1−F19	1.974(11)	0.776
Ta1−F20	1.941(11)	0.848
Ta1−F21	1.895(11)	0.960
		∑Ta3 = 5.96

Table 6.31 Selected bond lengths and bond valence sums for **Ta−2**.

$[C_4H_{12}N_2][TaF_7]$ (Ta−3) has one crystallographically unique tantalum site and one molecule of protonated template; piperazine (which is situated around an inversion centre) in the building unit (see Fig 6.36). An extensive network of hydrogen bonding holds the 3D structure together. The Ta metal centre is confirmed as Ta^{5+} through BVS (see Table 6.32).

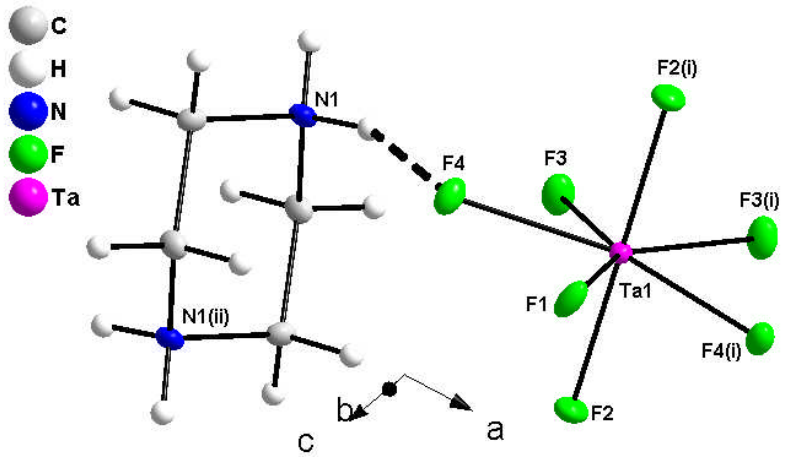

Fig 6.36 The building unit in **Ta−3**. Symmetry operator (i) –*x*, *y*, 1½-*z*, (ii) -½-*x*, ½-*y*, 2-*z*.

Bond	Bond Length (Å)	s_{ij}
Ta1−F1	1.972(3)	0.780
Ta1−F2	1.909(2)	0.925
Ta1−F2’	1.909(2)	0.925
Ta1−F3	1.954(2)	0.819
Ta1−F3’	1.954(2)	0.819
Ta1−F4	1.995(2)	0.733
Ta1−F4’	1.995(2)	0.733
		∑Ta1 = 5.73

Table 6.32 Selected bond lengths and bond valence sums for **Ta−3**.

6.5.2 Synthetic Conditions for Ta−1 to Ta−3

Product	Ta_2O_5 (g)	HF (ml)	H_2O (ml)	EG (ml)	Template	Template Quantity	Temp (°C)	Time (days)
Ta−1	0.22	0.75	0.5	2.5	Tris (2-aminoethyl) amine	0.250ml	100	1
Ta−2	0.22	0.75	0	2.5	Diethylene Triamine	0.250ml	100	1
Ta−3	0.22	0.75	2.5	2.5	Piperazine	0.139g	100	1

6.6 Summary

In total, 22 different titanium, zirconium, hafnium, niobium and tantalum (oxy)fluoride structures have been synthesised. It is clear that although a wide range of structures has been made, these are mostly comprised of similar $[MF_6]^n$ and $[MF_7]^n$ monomers (where M = Ti, Zr, Hf, Nb, Ta). A 1D chain based on $[TiOF_4]^-$ was synthesized with ethylene diamine, although the chain itself had previously been reported but with a different template.[12] Further experiments should also be performed to see if a change in cation to metal ratio produces any further novel products. A decrease in HF content with an increase in temperature could also be explored to see if more condensed structures could be synthesized.

What can be utilized from these structures is the idea of a toolbox of monomeric units which could be used in further reactions as building units. **Ta−2** being a prime example of this idea, as it can be dissolved in excess water and used in the synthesis of **Ta−3**. In theory these monomeric units, if they can be dissolved, could be inserted in other frameworks to provide novel properties in the host framework, such as optical or magnetic properties.

References

1. “Inorganic Solid Fluorides”; P. Hagenmuller (Editor), Academic Press: London, 1985.
2. “Advanced Inorganic Fluorides”: Synthesis, Characterisation and Applications, T. Nakajima, B. Zemva and A. Tressaud (Editors), Elsevier Science, S.A, 2000.
3. G. M. Sheldrick, Institüt für Anorganische Chemie der Universität, Tammanstrasse 4, D-3400 Göttingen, Germany, **1998**.
4. G. Pausewang and W. Ruedoff, *Z. Anorg. Allg. Chem.,* **1969**, 364, 69.
5. S. Siegel, *Acta Cryst*., **1952**, 5, 683.
6. B. Hoffman, *Z. Anorg. Allg. Chem.,* **1979**, 458, 151.
7. A. Vedrine, J. P. Besse, M. Capestan, *Revue de Chimie Minerale*, **1971**, 663.
8. L.-Q. Tang, M. S. Dadachov and X. –D. Zou, *Z. Krist. – NCS.*, **2001**, 216, 259.
9. M. S. Dadachov, L.-Q. Tang and X. –D. Zou, *Z. Krist. – NCS.*, **2000**, 215, 605.
10. M. S. Dadachov, L.-Q. Tang and X. –D. Zou, *Z. Krist. – NCS.*, **2001**, 216, 141.
11. L.-Q. Tang, M. S. Dadachov and X. –D. Zou, *Z. Krist. – NCS.*, **2001**, 216, 387.
12. M.Schabert and G. Pausewang, *Z. Anorg. Allg. Chem.,* **1988**, 559, 143.
13. P. R. Sabatier, G. Charroin, D. Avignant and J. C. Cousseins, *Acta Cryst.*, **1979**, B35, 1333.
14. S, J. La Placa and W. Kunnmann, *American Crystallographic Association: Program Winter*, **1970**, 85.
15. H. Bialowons and B. G. Mueller, *Z. Anorg. Allg. Chem.,* **1995**, 621, 1223.
16. K. Vorres and J. Donhue, *Acta Cryst*., **1955**, 8, 25.
17. B. L. Chamberland, *J. Solid State Chem.*, **1970**, 2, 49.
18. VALENCE © I. D. Brown, Brockhouse Institute for Materials Research, McMaster University, Hamilton, Ontario. Canada, Used with permission.
19. I. D. Brown and D. Altermatt, *Acta Cryst*., **1985,** B41, 244.
20. N. E. Brese and M. O'Keeffe, *Acta Cryst*., **1991**, B47, 192.
21. N. F. Stephens and P. Lightfoot, *Solid State Sci.*, **2006**, 8, 197.
22. D. W Aldous, N. F. Stephens and P. Lightfoot, *Inorg. Chem.*, **2007**, 46, 3996.
23. N. F. Stephens, *Thesis*, University of St Andrews, 2006.
24. P. Dugat, M. El-Ghozzi, J. Metin and D. Avigant, *J. Solid State Chem.*, **1995**, 120, 187.
25. G. C. Hampson and L. Pauling, *J. Amer. Chem. Soc.*, **1938**, 2703.
26. H. Bode and G. Teufer, *Z. Anorg. Allg. Chem.,* **1956**, 283, 18.
27. R. M. Herak, S. S. Malcic and Lj. M. Manojlovic, *Acta Cryst*., **1965**, 18, 520.
28. M. A. Medkov, M. D. Davidovich, M. D. Rizaeva, I. P Kondratyuk and B. V. Bukvetski, *Izv. Akad. Nauk SSSR, Ser. Khim.*, **1980.**
29. B. Kojic-Prodic, S. Scavincar and B. Matkovic, *Acta Cryst. B*, **1971**, 27, 638.
30. B. V. Bukvetski, A. V. Gerasimenko and R. L. Davidovich, *Koord. Khim.*, **1992**, 18, 576.
31. G. Brunton, *Acta Cryst.* **1971**, B27, 1944.

32. C. Plitzko, *Thesis*, University of Hanover, 1996.
33. J. H. Burns, R.D. Ellison and H. A. Levy, *Acta Cryst.* **1968**, B24, 230.
34. L. A. Harris, *Acta Cryst*., **1959**, 12, 172.
35. E. G. Il'in, V. V. Kovalev, G. G. Aleksandrov and A. V. Sergev, *Dok. Akad. Nauk SSSR*, **2004**, 398, 639.
36. V. V. Tkachev, L. O. Atovmyan, V. B. Logvinova, and R. L. Davidovich, *Koord. Khim.*, **1996**, 22, 727.
37. A.I. Gusev, E. B. Chuklanova, V. Ya. Kuznetsov and D. L. Rogachev, *Z. Strukt. Khim.*, **1992**, 33, 195.
38. C. Plitzko, M. Strecker and G. Meyer, *Z. Anorg. Allg. Chem.,* **1997**, 623, 79.
39. C. Plitzko and G. Meyer, *Z. Anorg. Allg. Chem.,* **1998**, 624, 169.
40. J. L. Hoard and J. Martin, *J. Amer. Chem. Soc.*, **1941**, 63, 11.
41. M. B. Williams and J. L. Hoard, *J. Amer. Chem. Soc.*, **1942**, 64, 1139.
42. V. I. Pakhomov, T. A. Kiadalova, E. G. Il'in, *Koord. Khim.*, **1975**, 1, 37.
43. N. G. Furmanova, I. A. Verin, A. N. Zozulin and E. G. Il'in, *Kristallografiya*, **1997**, 37, 136.
44. T. A. Kiadalova, V. I. Pakhomov, and E. S. Panin, *Koord. Khim.*, **1976**, 2, 554.
45. N. F. Stephens and P. Lightfoot, *Acta Cryst.*, **2005**, C61, m334.
46. V. I. Pakhomov and T. A. Kiadalova, *Kristallografiya*, **1974**, 19, 733.
47. S. Carlson, A. K. Larsson and F. E. Rohler, *Acta Cryst.* **2000**, B56, 189.
48. J. L. Hoard, *J. Amer. Chem. Soc.*, **1939**, 61, 1252.
49. C. Grimberg, J. Straehle, J. P. Lavel, B. Frit, R. Sonntag and J. Ihringer, *Eur. J. Solid State Inorg. Chem.*, **1994**, 31, 449.
50. S. A. Brewer, A. K. Brisdon, J. Fawcett, P. J. Holliman, J. H. Holloway, E.G. Hope and D. R. Russel, *Z. Anorg. Allg. Chem.,* **2006**, 632, 325.
51. V. Gutmann and K. H. Jack, *Acta Cryst.*, **1951**, 4**,** 244.

7.0 General Summary, Conclusions and Further Work

One of the initial aims of this work was to try and synthesise SHG active materials, by using polar octahedral building units. As it became clear that the majority of samples being made were centrosymmetric and therefore not SHG active, the magnetic properties of these materials were studied with more interest, in addition to the synthetic aspects of the work.

Vanadium was the first metal explored and proved to be the most fruitful for the number of new structures and the variety of materials produced (29 in total). Initially, water content was examined as the main variable at 100 °C, with an increase in temperature being introduced to try and synthesise more condensed materials. This method worked as several materials were successfully synthesised and fully characterised through X-ray single crystal diffraction and magnetic data analysis. A final variable was investigated; the counter-cation to metal ratio. This produced three different materials and helped to establish the diversity of products that can be synthesised solvothermally. All pure products were investigated for their possible magnetic properties. Some of the materials synthesised which are of the greatest interest are:

- Several chain structures which have been shown to have antiferromagnetic interactions.[1]
- Vanadium oxyfluoride ladders[2] which are very similar in structure and physical properties to $(VO)_2P_2O_7$.
- A family of products all based on a “Y” shaped motif which show increased connectivity through an increase in tempertature.[3]
- A wide variety of oligomeric compounds.[4]

After some of these vanadium materials had been synthesised, niobium was investigated along with tantalum, to find the effects of periodicity upon the products at 100 °C. It became clear that the number of new structures being synthesised was a lot lower than the vanadium compounds and some of these were known phases. The effect of increased temperature upon synthesis was investigated but proved to have little effect upon the products formed.

In the case of niobium and tantalum, it is clear that the lack of variable oxidation states, and the reduced tendency towards condensation of polyhedral units, makes these systems less interesting than the vanadium analogues. Further metal sources were then investigated (titanium, zirconium and hafnium) with the group 4 metals being shown in the literature to produce a variety of structures. Reactions were again carried out at 100 °C with the increase of reaction temperature also being investigated with little success (only one hafnium system proved successful in producing a different product with a change of temperature). In total, 22 new crystal structures were synthesised ranging from isolated MF_6 and MF_7 monomers (where M is either Ti, Zr or Hf) to the infinite chain structure $[TiOF_4]^-$. All the metals except for

vanadium and molybdenum were not investigated for the effect of changes in cation ratio. This was due to time constraints and the number of experiments involved (over 2600 experiments were performed up to this point without the investigation of this variable on these metals).

Finally molybdenum was investigated, as it has a variety of stable oxidation states. Chromium was not investigated as the d^0 metal oxide is highly toxic and reduces instantaneously to Cr^{3+} under the reaction conditions being used, which would be unsuitable for SHG materials (which need to be d^0 or d^1). Molybdenum proved to be a rich source of novel products with nine new structures being synthesised. Changes in cation content and temperature also yielded different products in a similar manner to the vanadium compounds.

In total, 60 structures were synthesised which are comprised of 57 novel structures and three materials not previously made through hydrothermal synthesis. Some trends in the effect of temperature on the oxidation state of vanadium and molybdenum materials have been established, along with the increased covalent connectivity of the products. Several antiferromagnetic materials have been synthesised and the interactions for some of these materials have been modelled. Three known solid state materials[5-7] (KVF_4, $K_5V_3F_{14}$ and $NaVF_4$) have successfully been synthesised by the hydrothermal method which paves the way forward for more materials with interesting physical properties to be synthesised in this manner.[8]

7.1 Further Work

Although a large number of reactions were carried out in this thesis, a lot more would need to be performed before the full number of possible materials are synthesised, by systematic variations in the reactions conditions.

Firstly the Ti, Zr, Hf, Nb, Ta reactions need to have their cation ratios varied to see if this has an effect on the products formed. Also tungsten could be used as a metal source at elevated temperatures (as WO_3 does not dissolve in excess HF at 100°C).

The use of fluoro-organics may be a route to greater 3D connectivity. Organic moieties such as difluoroethane or difluorobenzene may act as bridging units to create novel 2D and 3D materials. In a similar way $[Cu(py)_4]^{2+}$ (py = pyridine), which has been used to great effect by the Poeppelmeier group[9-22] could be used as a linking agents to increase dimensionality. The first example of this is the preparation of a 3D-connected material $[CH_3NH_3]_8[Cu(Py)_4]_3[V_7O_6F_{30}]$.[23]

The trigonal chain compound (**V−28**) needs to be studied in greater depth to fully elucidate its magnetic structure. This could be performed through a neutron diffraction study if the sample could be successfully deuterated.

All novel materials should also be studied for the optical, electrical or magnetic properties, where appropriate. Perhaps the most exciting avenues to be explored are the methods of linking building units into 3D structures, and the preparation of further inorganic transition metal fluorides by solvothermal rather than solid state methods, in order to prepare potential multiferroics or other functional materials.

References

1. D. W. Aldous, N. F. Stephens and P. Lightfoot, *Inorg. Chem.,* **2007**, *46*, 3996-4001.
2. D. W. Aldous, R. J. Goff, J. P. Attfield and P. Lightfoot, *Inorg. Chem*., **2007**, *46*, 1277-1282.
3. D. W. Aldous, N. F. Stephens and P. Lightfoot, *Dalton Trans.*, **2007**, 4207-4213.
4. D. W. Aldous, N. F. Stephens and P. Lightfoot, *Dalton Trans.,* **2007,** 2271-2282.
5. D. Babel and B. Peschel., *Z. Anorg. Allg. Chem.*, **1997**, 623, 1614.
6. B. J. Garrard, S. H. Smith, B. M. Wanklyn and G. Garton, *J. Cryst. Growth*, **1975**, 29, 301.
7. B. M. Wanklyn, B. J. Garrard, F. Wondre and W. Davidson, *J. Cryst. Growth*, **1976**, 33, 165.
8. M. Yoshimura, M. Hidaka, T. Mizushima, J. Sakurai, T. Tsuboi and W. Kleeman, *J. Magn. Mag. Mater.,* **2006**, 299, 404.
9. P. Halasyamani, M. J. Willis, C. L. Stern, P. M. Lundquist, G. K. Wong and K. R. Poeppelmeier, *Inorg. Chem.*, **1996**, 35, 1367.
10. A. J. Norquist, K. R. Heier, C. L. Stern and K. R. Poeppelmeier, *Inorg. Chem.*, **1998**, 37, 6495.
11. P. Halasyamani, K. R. Heier, A. J. Norquist, C. L. Stern and K. R. Poeppelmeier, *Inorg. Chem.*, **1998**, 37, 369.
12. K. R. Heier, A. J. Norquist, C. G. Wilson, C. L. Stern and K. R. Poeppelmeier, *Inorg. Chem.*, **1998**, 37, 76.
13. A. J. Norquist, C. L. Stern and K. R. Poeppelmeier, *Inorg. Chem.*, **1999**, 38, 3448.
14. M. E. Welk, A. J. Norquist, C. L. Stern and K. R. Poeppelmeier, *Inorg. Chem.*, **2000**, 39, 3946.
15. A. J. Norquist, M. E. Welk, C. L. Stern and K. R. Poeppelmeier, *Chem. Mater.*, **2000**, 12, 1905.
16. P. A. Maggard, C. L. Stern and K. R. Poeppelmeier, *J. Amer. Chem. Soc.*, **2001**, 123, 7742.
17. M. E. Welk, A. J. Norquist, C. L. Stern and K. R. Poeppelmeier, *Inorg. Chem.*, **2001**, 40, 5479.
18. P. A. Maggard, A. L. Kopf, C. L. Stern and K. R. Poeppelmeier, *Inorg. Chem.*, **2002**, 41, 4852.
19. M. E. Welk, A. J. Norquist, F. P. Arnold, C. L. Stern and K. R. Poeppelmeier, *Inorg. Chem.*, **2002**, 41, 5119.
20. J. E. Kirsch, H. K. Izumi, C. L. Stern and K. R. Poeppelmeier, *Inorg. Chem.*, **2005**, 44, 884.
21. J. E. Kirsch, H. K. Izumi, C. L. Stern and K. R. Poeppelmeier, *Inorg. Chem.*, **2005**, 44, 4586.
22. M. E. Welk, C. L. Stern, K. R. Poeppelmeier and A. J. Norquist, *Crystal Growth & Design*, **2007**, 7, 956.

23. T. Mahenthirarajah and P. Lightfoot, *Chem. Commun.*, **2008**, 1401.